EPRI

Topical Report on Reactivity Initiated Accident: Bases for RIA Fuel and Core Coolability Criteria

Technical Report

Topical Report on Reactivity Initiated Accident: Bases for RIA Fuel and Core Coolability Criteria

1002865

Final Report, June 2002

EPRI Project Manager
R. Yang

EPRI • 3412 Hillview Avenue, Palo Alto, California 94304 • PO Box 10412, Palo Alto, California 94303 • USA
800.313.3774 • 650.855.2121 • askepri@epri.com • www.epri.com

DISCLAIMER OF WARRANTIES AND LIMITATION OF LIABILITIES

ORGANIZATION(S) THAT PREPARED THIS DOCUMENT

ANATECH Corp.
EPRI

ORDERING INFORMATION

Requests for copies of this report should be directed to EPRI Orders and Conferences, 1355 Willow Way, Suite 278, Concord, CA 94520, (800) 313-3774, press 2 or internally x5379, (925) 609-9169, (925) 609-1310 (fax).

CITATIONS

This report was prepared by

ANATECH Corp.
5435 Oberlin Drive
San Diego, CA 92121

Principal Investigator
R. Montgomery

EPRI
3412 Hillview Avenue
Palo Alto, CA 94304

Principal Investigators
N. Waeckel
R. Yang

This report describes research sponsored by EPRI.

The report is a corporate document that should be cited in the literature in the following manner:

Topical Report on Reactivity Initiated Accident: Bases for RIA Fuel and Core Coolability Criteria, EPRI, Palo Alto, CA: 2002. 1002865.

REPORT SUMMARY

Revised acceptance criteria have been developed for the response of light water reactor (LWR) fuel under reactivity initiated accidents (RIA). Development of these revisions is part of an industry effort to extend burnup levels beyond currently licensed limits. The revised criteria are proposed for use in licensing burnup extensions or new fuel designs.

Background

Early results from various RIA-simulation experiments with high-burnup fuel raised concerns that existing acceptance criteria defined in NUREG-0800 for the pressurized water reactor (PWR) rod ejection accident (REA) and the boiling water reactor (BWR) rod drop accident (RDA) may be inappropriate above a certain level of burnup. As a consequence, EPRI and the nuclear industry conducted an extensive review of data from such experiments to assess their applicability to the behavior of commercial LWR fuel during an REA or an RDA. Results of this review, which were summarized in EPRI TR-106387, determined that data from the RIA-simulation tests could not be applied directly. Rather, it is more appropriate to translate the data with analytical methods based on information from separate-effects tests to shed light on expected fuel response under realistic LWR conditions. Fuel failures could be explained as a result of loss of cladding ductility due to accumulation of hydrides from outside surface corrosion. Although drastic changes in criteria were not found to be necessary for current fuel designs, it became clear that a revision to the fuel failure and core coolability criteria would be needed for burnup extensions.

Objectives

- To conduct a comprehensive evaluation of all data relevant to the behavior of LWR fuel under transient conditions representative of an RIA.
- To evaluate the basis of current RIA criteria.
- To develop and propose revisions to core coolability limits and fuel failure thresholds appropriate for high-burnup fuel.

Approach

The investigators reviewed all well-characterized RIA simulation tests conducted on high-burnup fuel at different test facilities around the world. An extensive database was compiled consisting of in-pile observations and post-test examinations that can be used to evaluate phenomena and mechanisms that influence the transient performance of the fuel and cladding. Using results from separate-effects mechanical property tests, the investigators also developed a database of mechanical properties to represent the response of irradiated Zircaloy cladding and UO_2 fuel during an RIA event. RIA-simulation test data and mechanical property data were used to validate the transient fuel behavior code FALCON for the analysis of RIA events. This

comprehensive approach has (a) provided a mechanistic basis for understanding key phenomena that are operative in such tests, (b) qualified the use of a FALCON-based analysis for translating results from the non-prototypical RIA-simulation tests to prototypical LWR conditions and different cladding materials, and (c) provided a basis for developing RIA acceptance criteria for burnup extension.

Results

Technical insights gained from this deterministic evaluation approach were used to construct—as a function of rod average burnup—both a fuel rod failure threshold and a core coolability limit for use in the licensing analysis of LWR RIA events. Modifications to the current fuel failure threshold and core coolability limit are proposed for fuel with burnups above ~36 GWd/MTU. Above this burnup level, the fuel rod failure threshold decreases because of increased potential for cladding failure by pellet-cladding mechanical interaction. The core coolability limit decreases above 36 GWd/tU due to increased potential for UO_2 melting in the pellet periphery caused by local power and burnup peaking.

EPRI Perspective

Considerable insight has been achieved into the response of high-burnup fuel to an RIA-like event since the publication of EPRI TR-106387. The current work is part of an industry-wide effort under the Robust Fuel Program aimed at extending fuel rod average burnup levels above currently licensed limits. The work was performed under the direction of Working Group 2 (Response to Transients) of the Robust Fuel Program. In addition to developing revised RIA acceptance criteria, Working Group 2 also has supported development of a new three-dimensional neutron kinetics methodology for analyzing rod ejection accidents in commercial PWRs. This methodology (to be published in a separate EPRI report) will serve as a template that the industry can follow in licensing burnup extensions or new fuel types. Although the proposed revisions to the RIA acceptance criteria for high-burnup fuel are lower than the current criteria in NUREG-0800, the new three-dimensional neutron kinetics methodology is expected to demonstrate that the revised acceptance criteria will not be exceeded during a postulated RIA event in an LWR.

Keywords

Reactivity initiated accident
LWR fuel
Fuel reliability
Safety analysis
Burnup extension
Robust fuel

ACKNOWLEDGMENTS

The development of the RIA Topical Report was sponsored by the Robust Fuel Program under the direction of Working Group 2 – Response to Transients. The technical expertise and the experience provided by the members of Working Group 2 are gratefully acknowledged. Many individuals from Working Group 2 and the industry provided valuable contributions to the RIA Topical Report. In particular, the authors would like to acknowledge the efforts of:

Dr. A. Alapour from Southern Nuclear Operating Co.

Mr. W. Choe from TUX Electric

Mr. B. Dunn from Framatome ANP

Mr. G. Potts from Global Nuclear Fuel

Mr. M. Quecedo from ENUSA

Mr. T. Rieck from Exelon Corp.

Mr. D. Risher from Westinghouse

Mr. P. Garcia from Iberdrola

Considerable engineering analyses were used in establishing the technical bases for the criteria described in the report. The authors would like to acknowledge the efforts of Mr. D. Sunderland from ANATECH Corp. in conducting the FALCON fuel rod behavior analyses. Dr Y. Rashid and Mr. W. Lyon from ANATECH Corp. constructed the cladding integrity model used in the development of the fuel rod failure threshold. The efforts of Dr. N. Waeckel from EdF in providing data on the UO_2 melting temperature and cladding mechanical properties is gratefully acknowledged. The authors would like to thank Mr. G. Swindlehurst from Duke Power and Mr. R. Deveny from Framatome ANP for providing the results from multi-dimensional spatial kinetics analyses.

SUMMARY

S.1 Scope of Report

The purpose of this topical report is to describe the technical bases supporting a set of revised acceptance criteria for use in the safety analysis of the hot-zero power (HZP) and hot-full power (HFP) Reactivity Initiated Accidents (RIA) in Pressurized Water Reactors (PWRs) and Boiling Water Reactors (BWRs). The primary RIA events considered in this topical report are the postulated control rod ejection accident (REA) for PWRs and the postulated control rod drop accident (RDA) for BWRs. The revised RIA acceptance criteria have been developed as part of the on-going industry effort to extend fuel rod average burnup levels beyond the current limit of 62 GWd/MTU.

The revised acceptance criteria are shown in Figure S-1 and are defined in terms of the radial average peak fuel enthalpy and as a function of rod average burnup. Two separate criteria have been developed to 1) ensure long-term cooling of the reactor core after the accident and 2) account for radiological release to the environment following cladding failure. The strategy to develop two separate criteria is consistent with the approach in Regulatory Guide 1.77 which contains a limit on the maximum radial average fuel enthalpy to satisfy the requirements of 10 CFR 50 Appendix A – General Design Criterion 28 and a threshold to estimate the number of fuel rod failures.

The curves shown in Figure S-1 are applicable to:

- PWR: HZP and HFP REA
- BWR: HZP RDA
- Cladding materials: Zircaloy-4, Zircaloy-2, ZIRLO and M5
- UO_2 or UO_2-Gd_2O_3 fuel rods operated up to a target lead rod average burnup of 75 GWd/MTU
- PWR fuel rod designs: 17x17, 15x15, and 14x14
- BWR fuel rod designs: 8x8, 9x9, and 10x10
- Maximum cladding outer surface oxide thickness layers less than 100 microns
- No fuel rods with cladding outer surface oxide spallation sufficient to have a significant affect on the cladding mechanical properties

The revised RIA fuel rod failure threshold is applicable to advanced cladding designs provided the cladding material exhibits superior or equivalent ductility as Zircaloy cladding with the same outer surface oxide layer thickness. Since the development approach used material properties and corrosion rates based on low-Sn Zircaloy-4, the fuel rod failure threshold shown in Figure S-1 represents a lower bound for advanced fuel rod designs using low corrosion alloys. Application of the revised acceptance criteria to cladding material not addressed in the topical report will require the development of mechanical property data to demonstrate that the ductility relations used to derive the criteria represent a lower bound for the new cladding material.

As part of the limited scope LTA program to collect data at extended burnup (WCAP-15604-NP), industry surveillance programs will be used to demonstrate that the maximum oxide thickness data is bounded by the 100 micron oxide thickness value limit used to develop the fuel rod failure threshold.

The revised acceptance criteria shown in Figure S-1 are for use in the design basis analysis of the PWR REA and the BWR RDA to account for the number of estimated fuel rod failures and to demonstrate that the reactor core geometry remains amenable to cooling following the hypothetical accident. The method to utilize these criteria in the design basis methodology is as follows:

a) An accepted neutron kinetics analysis method is used to calculate the maximum deposited energy as a function of rod average burnup.

b) The radial average peak fuel enthalpy is calculated using an accepted fuel rod thermal analysis methodology

c) The radial average peak fuel enthalpy as a function of rod average burnup is compared to the fuel failure threshold shown in Figure S-1. All rods exceeding the fuel rod failure threshold should be considered failed.

d) The calculated radial average peak fuel enthalpy as a function of rod average burnup should be compared to the core coolability limit shown in Figure S-1. No fuel rods will have a maximum radial average peak fuel enthalpy that exceeds the limit shown in Figure S-1.

It is envisioned that the NRC will review the technical bases for the revised acceptance criteria and adopt them as generic criteria applicable to the design basis analysis of RIA events. One method to achieve generic usage of these criteria will be to use the technical bases described in this topical report to modify the appropriate sections in Regulatory Guide 1.77 and the Standard Review Plan Section 4.2.

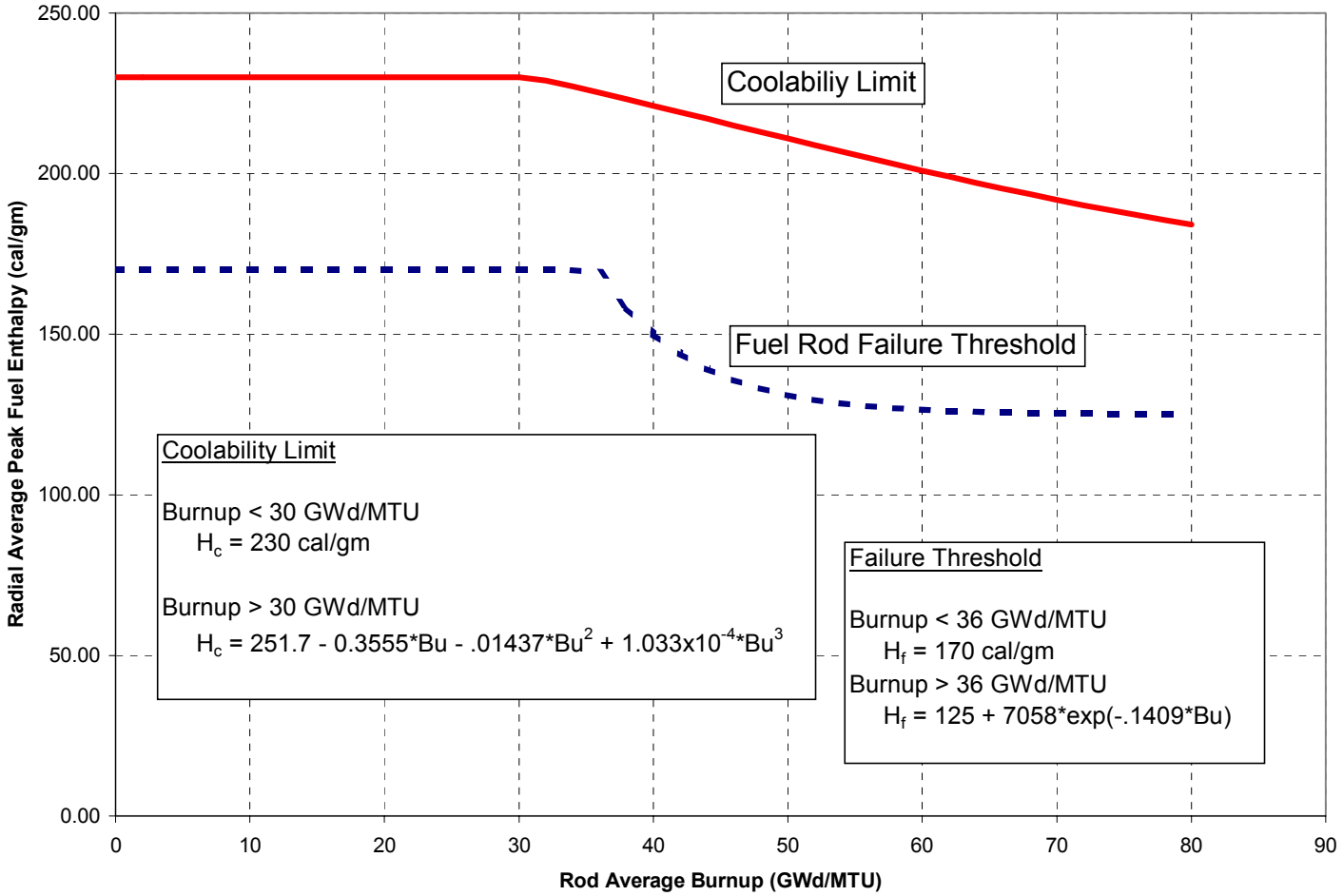

Figure S-1
Revised Acceptance Criteria for the PWR REA and BWR RD events. The criteria are defined in terms of the radial average peak fuel enthalpy as a function of rod average burnup.

S.2 Approach to Develop Revised Acceptance Criteria

The approach to develop the revised criteria used an evaluation methodology that combined both experimental data and analytical calculations to establish the influence of burnup on transient fuel rod behavior during reactivity initiated accidents. Used in the evaluation were experimental data from RIA-simulation tests on fuel segments extracted from commercial UO_2-Zircaloy cladding fuel rods irradiated to 64 GWd/MTU. These technical bases were then translated to the PWR REA application using the state-of-the-art fuel rod behavior analysis code FALCON as a means to establish the fuel rod failure threshold and core coolability limit as a function radial average fuel enthalpy and rod average burnup. The advantage of using a combined approach of analytical evaluations and experimental data to derive the revised acceptance criteria is that the methodology can be applied to other fuel rod designs and cladding materials to determine application specific criteria, if relaxation of the criteria is required.

To assure core coolability and to preclude damage to the reactor pressure vessel, a core coolability limit is established based on the maximum radial average peak fuel enthalpy that precludes incipient UO_2 pellet melting during power deposition. The fuel enthalpy required to produce incipient pellet melting was determined using a FALCON analysis to calculate the peak fuel pellet temperature as a function of both radial average peak fuel enthalpy and rod average burnup. The analytical approach considered the following effects:

- The influence of burnup on the UO_2 melting temperature
- Local power, burnup and temperature peaking
- Heat conduction from the pellet to the cladding
- Burnup-induced fuel-cladding gap closure
- The influence of burnup on the UO_2 thermal conductivity

The results of spatial kinetics analyses for both PWR and BWR RIA events show that the power pulse width will be greater than 10 milliseconds for typical power pulses. Experimental data demonstrate that the dispersal of finely fragmented solid pellet material occurs at pulse widths less than 10 milliseconds. However, limiting the peak fuel temperature in the rim to the melting temperature insures that most of the pellet material is well below the melting temperature in high burnup fuel. Such a restriction on the maximum radial average peak fuel enthalpy mitigates any significant consequences in the unlikely event that finely fragment solid pellet material is dispersed into the coolant.

Second, a threshold on the radial average peak fuel enthalpy is defined that represents the occurrence of fuel rod failure for use in off-site dose calculations. The fuel rod failure threshold below a rod average burnup of 36 GWd/MTU is established to preclude cladding failure by high temperature processes such as oxidation-induced embrittlement or clad ballooning and rupture. Experimental data from both RIA-simulation tests and power-coolant mismatch tests that operated in post-DNB heat transfer were used to justify a radial average peak fuel enthalpy below which peak cladding temperatures remained below the time-at-temperature threshold for oxidation-induced cladding embrittlement failure. Furthermore, experimental data from NSRR and IGR/BIGR were used to demonstrate that a positive pressure differential in excess of 1 MPa

at the start of the RIA event is required to cause ballooning and rupture in both Zircaloy and Zr-niobium alloys. At HZP conditions, it can be shown that the fuel rod internal pressure is less than the coolant pressure for low and intermediate burnup fuel rods, thus eliminating any potential for fuel rod failure by ballooning and rupture.

Beyond a rod average burnup of 36 GWd/MTU, the fuel rod failure threshold is based on cladding failure by pellet-cladding mechanical interaction (PCMI). The approach used a realistic evaluation of the fuel rod response during a RIA power pulse combined with a conservative estimation of the cladding ductility decrease with burnup to establish the fuel rod failure threshold. The FALCON PCMI analysis included the following effects:

- Pellet-cladding gap closure as a function of burnup
- Pellet to cladding heat conduction
- Cladding to coolant heat transfer
- Local power, burnup and temperature peaking
- Influence of burnup on the UO_2 thermal conductivity
- Pellet thermal expansion, cracking and plastic deformation
- Cladding elastic and plastic deformation

Cladding failure was established using the Critical Strain Energy Density (CSED) approach to describe the effects of irradiation and cladding outer surface oxidation on the cladding ductility. An upper bound cladding outer surface oxidation rate for low-Sn Zircaloy-4 was used in the evaluation to ensure conservatism in the failure threshold. The result is a lower bound fuel rod failure threshold as a function of rod average burnup.

ACRONYMS

BWR	Boiling Water Reactor
CABRI	French Test Reactor
CDC	Capsule Driver Core (at SPERT)
CEA	Commissariat a l' Energie Atomique (France)
CSED	Critical Strain Energy Density
CZP	Cold-Zero Power
DNB	Departure from Nucleate Boiling
DNBR	Departure from Nucleate Boiling Ratio
EdF	Elecricité de France
EOL	End of Life
EPRI	Electric Power Research Institute
ESCORE	EPRI Steady State Core Reload Evaluation Code
FALCON	Fuel Analysis & Licensing Code
FCI	Fuel-Coolant Interaction
FRAPTRAN	Fuel Rod Analysis Program, Transient
FREY	Fuel Rod Evaluation System
FSAR	Final Safety Analysis Report
FWHM	Full Width Half Maximum
HFP	Hot-Full Power
HZP	Hot-Zero Power
IFBA	Integral Fuel Burnuable Absorbers

IPSN	Institute for Protection and Nuclear Safety (France)
JAERI	Japan Atomic Energy Research Institute (Japan)
LOCA	Loss-of-Coolant Accidents
LWR	Light Water Reactor
MOX	Mixed Oxide Fuel
NB	Nuclear Boiling
NRC	Nuclear Regulatory Commission
NSRR	Nuclear Safety Research Reactor
PBF	Power Burst Facility (U. S.)
PCMI	Pellet-Cladding Mechanical Interaction
PIRT	Phenomena Identification & Ranking Table
PROMETRA	Program for Measuring the Mechanical Properties of the Cladding
PWR	Pressurized Water Reactor
RDA	Rod Drop Accident
REA	Rod Ejection Accident
REP	Pressurized Water Reactor (rectur a eau pressurisie)
RIA	Reactivity Initiated Accidents
SED	Strain Energy Density
SCANAIR	Code for describing the fuel behavior under an RIA Transient
SPERT	Special Power Excursion Reactor Test (U. S.)
TRANSURANUS	European Institute for Transuranium Element Fuel Rod Performance Code
TUBRNP	TRANSURANUS Burnup Model
UE	Uniform Elongation

CONTENTS

LIST OF FIGURES

LIST OF TABLES

1
INTRODUCTION

1.1 Background

The goal to achieve higher fuel rod burnup levels has produced considerable interest in the transient response of high burnup fuel. The database on transient fuel behavior is limited at burnup levels beyond 40 GWd/tU and is based on older fuel rod designs. Several experimental programs are currently underway to generate data on the behavior of high burnup fuel under transient conditions representative of Loss-of-Coolant Accidents (LOCA's) and Reactivity Initiated Accidents (RIA's) [Chung et al. 1996; Papin et al.1996; Fuketa et al.1996][1]. Such programs include the RIA simulation experiments performed at the CABRI facility in France and the Nuclear Safety Research Reactor (NSRR) in Japan. The purpose of these programs is to provide data that can be used to develop safety criteria for extended burnup levels applications and to validate analytical codes for high burnup fuel behavior.

The initial results from RIA-simulation tests on fuel rod segments with burnup levels above 50 GWd/tU, namely CABRI REP Na-1 (1993) and NSRR HBO-1 (1994), raised concerns that the existing licensing criteria defined in NUREG-0800 may be inappropriate beyond a certain level of burnup. As a consequence, EPRI and the nuclear industry conducted an extensive review and assessment of the observed behavior of high burnup fuel under RIA conditions which was summarized in EPRI TR-106387 [Montgomery and Rashid 1996; Ozer et al. 1996; Montgomery et al. 1997a] The objective of this program was to conduct a detailed analysis of the data obtained from RIA-simulation experiments and to evaluate the applicability of the data to commercial LWR fuel behavior during a REA or CRDA. The industry assessment included a review of the fuel segments used in the tests, the test procedures, in-pile instrumentation measurements, post-test examination results, and a detailed analytical evaluation of several key RIA-simulation tests using the EPRI-sponsored transient fuel behavior code FREY, which was an earlier version of the FALCON transient code used in this evaluation. Major conclusions from that industry assessment are:

- The RIA-simulation test conditions are not representative of those expected during a postulated in-reactor REA or CRDA. The experiments were conducted either in room-temperature, atmospheric-pressure water or in hot sodium coolant. The pulses were considerably more rapid (sharper and narrower) than anticipated LWR power pulses calculated using 3-D spatial kinetics methods.
- In many cases, the conditions under which the test rods were base-irradiated produced cladding corrosion and hydriding features that were not representative of commercial LWR

[1] References provided in brackets [ ] are listed in alphabetical order in Section 6.

fuel. This was most evident in early tests performed in SPERT-CDC and the JM Test Series in the NSRR facility

- Analytical evaluations and separate effects data are required to understand the key mechanisms operative in RIA-simulation tests and to translate the experimental results to LWR conditions and different cladding materials.
- Loss of cladding ductility due to localized hydrides was the major cause of failure for high burnup test rods during the RIA-simulation tests. Although, loss of cladding ductility may be a result of higher burnup, the causes are more related to adverse hydride content and distributions resulting from outer surface cladding oxidation anomalies such as spallation. The primary effect of burnup is to increase PCMI by gap closure effects such as solid fission product swelling.

Since the publication of EPRI TR-106387, the industry has continued the assessment and evaluation of the burnup impact on the behavior of high burnup fuel during a RIA. More recent RIA-simulation experiments have been conducted on high burnup PWR and BWR test rods and the analytical evaluations and post-test examinations have provided further insights into the behavior of high burnup fuel under transient conditions. The newer data continue to confirm the major conclusions summarized above. It is becoming apparent that our understanding of high burnup fuel behavior during a RIA event is sufficient and that most post-test observations can be explained.

As a logical next step in the process, Working Group 2 of the EPRI Robust Fuel Program, representing the nuclear industry, has developed a strategy to resolve the RIA licensing issues raised by the RIA-simulation experiments. The Industry strategy consists of: 1) development of revised RIA licensing criteria using experimental data and analysis methods, and 2) development of improved neutron kinetics methods to demonstrate compliance to the revised licensing criteria.

The approach employed to develop the revised licensing criteria by the Industry combines elements of experimental results and analytical evaluations to establish a fundamental understanding of fuel behavior during RIA events. The approach includes three major components:

1. Establish the transient behavior of intermediate and high burnup fuel rods using well-characterized RIA simulation tests. The RIA-simulation experiments in the previous evaluation, and the more recent tests on rods with burnup levels ranging from 45-65 GWd/MTU in the CABRI, NSRR and IGR/BIGR reactors, provide a database of in-pile observations and post-test examinations that can be used to evaluate the phenomena and mechanisms that influence the transient performance of the fuel and cladding. A summary of the RIA-simulation database is provided in Section 2.2

2. Define the cladding mechanical properties using data from separate effects tests. The database of Zircaloy cladding mechanical properties furnishes insights into the influence of irradiation damage, hydrogen content and distribution, and temperature on the capability of the cladding to accommodate the pellet loading during an RIA event. The database of separate effects tests on Zircaloy cladding mechanical properties is described in Section 2.3, as well as the methods used to develop a cladding integrity model.

3. Benchmark the RIA analysis capabilities in the transient fuel behavior code FALCON using experimental data from the database of RIA-simulation tests. FALCON, which is the most recent version of the FREY transient fuel behavior code, calculates the thermal and mechanical performance of a single fuel rod during transient power conditions. Performing fuel rod analyses of the RIA experiments provides a means to validate the predictive capabilities of the program and also provides insights into the mechanisms that influence the pellet and cladding transient performance. A description of FALCON and the fuel rod analyses performed using the code is included in Section 2.4.

This comprehensive approach has provided some key results: 1) a mechanistic basis for understanding the key phenomena that are operative in RIA-simulation tests and 2) qualified the use of FALCON for the translation of non-prototypical RIA-experimental results to both LWR conditions and different cladding materials. The industry has used the technical insights gained from this deterministic evaluation as the basis for developing the proposed revisions to the regulatory criteria used in the licensing analysis of RIA events. As will be discussed in this report, the proposed regulatory criteria are a combination of the best-estimate technical understandings of transient fuel behavior coupled with conservative assumptions to account for the uncertainties associated with high burnup fuel.

In addition to proposing revised RIA licensing criteria, Working Group 2 has also developed a new methodology for analyzing the PWR rod ejection accident based on a three-dimensional neutron kinetics approach. This methodology is intended to serve as a template, which the industry can follow in upgrading their analytical methods. Improvements in the compliance methodology are expected to be necessary to meet the revised regulatory criteria which unlike the existing criteria will decrease as a function of rod average burnup. A separate EPRI report will be submitted to the NRC to obtain generic review and approval of the methodology.

Combined with the NRC Phenomena Identification and Ranking (PIRT) review conducted on the PWR REA event, the technical assessment performed by the industry establishes a strong technical basis to develop revised licensing criteria for reactivity initiated accidents. The development of additional RIA test data will slow for the next several years as the CABRI facility is modified and upgraded to include a Water Loop [Papin et al. 2000]. Given that our current understanding of the important mechanisms is sufficient, it is appropriate at this time to propose revised licensing criteria for RIA events. The additional RIA-simulation tests on high burnup fuel rods with advanced cladding alloys planned as part of the International CABRI Water-Loop project and the NSRR test program will provide data at extended burnup and with advanced cladding materials that can be used to confirm the proposed regulatory criteria.

1.2 Scope of Topical Report

The focus of this report is to summarize the technical bases for the revised core coolability criteria and fuel rod failure threshold used in the licensing analysis of a PWR or BWR HZP and HFP RIA events. Section 2 summarizes the regulatory bases associated with reactivity initiated accidents, provides a review of the experiments performed to evaluate the behavior of irradiated fuel to RIA conditions, reviews the mechanical property tests used to describe the performance of irradiated cladding, and finally, summarizes the validation of the fuel rod analysis methodology used to analyze and interpret the RIA experiments. Section 3 summarizes the

current technical understanding of the fuel rod failure mechanisms during RIA transient conditions and describes the methodology used to develop the proposed fuel rod failure threshold. Section 4 summarizes the issues associated with maintaining core coolability and describes the approach used to develop the proposed core coolability limit.

2
DATABASE REVIEW

Section 2 summarizes the current licensing and technical bases related to RIA events. Included is a review of the regulatory background for the current licensing criteria, a review of the RIA-simulation test database, a review of the separate effects tests used to establish the mechanical behavior of high burnup cladding material, and a review of the RIA test analysis performed using FALCON.

2.1 Regulatory Basis

Section 4.2 of NUREG-0800 - Standard Review Plan for the Review of Safety Analysis Reports for Nuclear Power Plants (SRP) specifies two licensing criteria applicable to RIA events: a fuel coolability limit and a fuel rod failure threshold [U. S. Nuclear Regulatory Commission, 1981]. The fuel coolability limit was established to restrict the amount of energy deposition into the fuel rod during an RIA event as a means to preclude fuel melting, fragmentation and dispersal. Under certain conditions, the mechanical energy release resulting from dispersal of molten fuel material may be sufficiently large to destroy the cladding and the fuel assembly geometry and produce significant pressure pulses in the primary system. The fuel rod failure threshold was established to meet the requirements of fission product release during postulated accidents. The regulatory and technical bases for these criteria are outlined below.

2.1.1 Fuel Coolability Limit (Violent Expulsion of Fuel)

The fuel coolability limit was developed to satisfy regulatory requirements contained in General Design Criteria 28 (10 CFR Part 50 Appendix A). GDC 28 defined in 10 CFR Part 50 Appendix A specifies that reactivity control systems shall be designed to assure that the effects of a postulated reactivity accident neither (1) result in damage to the reactor coolant pressure boundary greater than limited local yielding, nor (2) sufficiently disturb the core, its support structures, or other reactor pressure vessel internals to cause serious impairment of core cooling capability. GDC 28 further specifies that reactivity initiated accidents shall include consideration of rod ejection (unless prevented by positive means), rod drop, steam line rupture, changes in coolant temperature and pressure, and cold water addition.

Regulatory Guide 1.77, "Assumptions Used for Evaluating a Control Rod Ejection Accident for Pressurized Water Reactors," outlines the acceptable assumptions and analytical methods that may be used in evaluating REAs for PWRs. Furthermore, Regulatory Guide 1.77 states that by using these assumptions and methods it should be shown that:

1. Reactivity excursions will not result in a radial average fuel enthalpy greater than 280 cal/g at any axial location in any fuel rod.

2. Maximum reactor pressure during any portion of the assumed transient will be less than the value that will cause stresses to exceed the Emergency Condition stress limits as defined in Section III of the ASME Boiler and Pressure Vessel Code.

Standard Review Plan Section 4.2 paragraph II.A.3.b also states that the PWR and BWR fuel coolability limit for violent expulsion of fuel should be a limit of 280 cal/gmUO_2 on the radial average peak fuel enthalpy.

The radial average peak fuel enthalpy limit of 280 cal/gUO_2 is based on a Regulatory staff review of the available data (prior to 1974) from the SPERT and TREAT experimental programs describing the fuel failure consequences following a high rate of reactivity insertion [Martinson and Johnson 1968; Miller and Lussie 1969; USAEC 1974]. The review found that there exists a potential at high fuel energy depositions for prompt rupture of a fuel rod and the rapid heat transfer from finely dispersed molten fuel material. Prompt fuel element rupture is defined in Regulatory Guide 1.77 as a rapid increase in internal fuel rod pressure due to extensive fuel melting, followed by rapid fragmentation and dispersal of molten fuel and cladding material into the coolant. The review concluded that the failure consequences of UO_2 fuel rods were insignificant for total energy depositions below 300 cal/g for both unirradiated and irradiated fuel rods. As a result, a peak radially averaged fuel enthalpy of 280 cal/g was considered to be a conservative maximum limit to ensure that core damage will be minimal and that both short-term and long-term core cooling capability will not be impaired.

The fuel coolability limit of 280 cal/gm for the maximum radial averaged peak fuel enthalpy, defined in Reg. Guide 1.77, was defined based on experiments performed on unirradiated test rods that experienced severe fuel and clad melting during the energy deposition. MacDonald, et. al. performed a review and re-assessment of the supporting data and found that although, the limit for violent expulsion of fuel is stated in terms of radial average peak fuel enthalpy, the data used to establish the limit was actually based on the total energy deposition for the tests [MacDonald et al. 1980]. The maximum radially averaged fuel enthalpy is less than the associated total energy deposition due to heat conduction from the fuel and energy deposition from delayed neutrons. Re-evaluation by MacDonald, et. al. of the tests performed in the SPERT and TREAT facilities using the maximum radially averaged fuel enthalpy shows that the consequences for enthalpies greater than 250 cal/gm were fragmentation and loss of rod geometry. These observations indicate that the 280 cal/gm may not be conservative with respect to maintaining fuel coolability. Based on the earlier re-evaluation, a revision of the fuel coolability limit to 230 cal/gm for the maximum radial average peak fuel enthalpy would provide margin to loss of rod geometry and would be a more limit appropriate at zero and low burnup (< 10 GWd/MTU).

2.1.2 Fuel Rod Failure Threshold (Excessive Fuel Enthalpy)

The fuel rod failure threshold for RIA events is specified in SRP Section 4.2 (II.A.2.f) and was established to meet the requirements of 10 CFR Part 100.11 and 10CFR50 Appendix A, GDC-19 as these relate to both on-site and off-site dose consequences. The fission product release resulting from fuel rod failure during a postulated accident is required by 10 CFR Part 100.11 to calculate the radiation dose for the exclusion area boundary (EAB) and low population zone (LPZ) boundary. Regulatory Guide 1.77 specifies that the offsite dose levels at the EAB and

LPZ for an RIA event must be well within the exposure guideline values in 10 CFR Part 100.11. Appendix A of Standard Review Plan section 15.4.8 and 15.4.9 defines "well within" as 25% of the 10 CFR 100.11 exposure guidelines. The assumptions used in calculating the source term activity for fuel rod failure are defined in Reg. Guide 1.77 Appendix B. For fuel rod failure, the accumulated fuel-cladding gap activity should be assumed to be 10% of the iodines and 10% of the noble gases accumulated at the end of core life, assuming continuous maximum full power operation. The activity inventory should take no allowance for radioactive decay prior to the accident.

The fuel rod failure threshold for PWR and BWR applications is as follows:

PWR

> Regulatory Guide 1.77 states "The number of fuel rods experiencing clad failure should be calculated and used to obtain the amount of contained fission product inventory released to the reactor coolant system." Clad failure should be assumed to occur when the calculated heat flux equals or exceeds the departure from nucleate boiling ratio (DNBR) for zero power, low power and full power RIA events in PWRs.

BWR

> The fuel rod failure threshold used in BWR's is defined in Standard Review Plan Sections 4.2 II.A.2.f) and 15.4.9. Cladding failure should be assumed for rods that experience a maximum radially averaged fuel enthalpy greater than 170 cal/g for RDA events initiated from zero or low power. The fuel enthalpy threshold for cladding failure established for zero or lower power RDAs was defined to be a surrogate for the Critical Power Ratio threshold traditionally used for BWR clad overheating. As will be seen in Section 2.2, zero or lower burnup fuel rods tested above 170 cal/g experienced clad overheating and subsequent cladding fracture following quenching. For rated power conditions, fuel rods that experience cladding dryout should be assumed to fail.

2.2 RIA Simulation Test Database

Experimental programs have been conducted worldwide since the early 1960's to evaluate fuel behavior during rapid energy deposition simulating a reactivity accident. Prior to the late 1980's. all of the relevant RIA simulation experiments were conducted in the US or Japan. In the US, the two main programs were the SPERT-CDC and the PBF RIA tests [Martinson and Johnson 1968; Miller 1970; MacDonald 1980]. The experiments in Japan were conducted by JAERI in the NSRR facility. The early RIA simulation tests in the US and Japan consisted of experimental programs on unirradiated tests rods or low burnup (< 30 GWd/MTU) test rods specially fabricated for testing and were pre-irradiated in material test reactors such as the Engineering Test Reactor [Miller 1970; Miller 1971] or the Japanese Materials Test Reactor [Ishikawa 1980; Fuketa 1997]. A primary goal of a majority of these tests was to investigate the post-failure consequences leading to coolant pressure pulse generation. As a consequence, these test rods were fabricated with reduced rod diameters and high ^{235}U enrichments to achieve high levels of energy deposition. Also, the pre-irradiation was accelerated to obtain the desired burnup in the shortest time possible. These conditions introduced complexities that make application of the

data to modern LWR fuel rod conditions difficult. As a result, most of these data are only applicable to zero burnup.

More recently, three experimental programs have been conducted to evaluate the behavior during RIA conditions of irradiated fuel rods from commercial reactors. These programs include the CABRI REP Na tests in France [Schmitz and Papin 1998; MacLachlan 2000a; MacLachlan 2000b], the NSRR tests in Japan [Fujishiro 1992; Fuketa 1996; Fuketa 1998; Fuketa 1999; Fuketa 2000], and the IGR/BIGR tests in Russia [Yegorova 1999; Bibilashvili et al. 2000]. A total of sixty-one (61) RIA simulation tests have been conducted on LWR-type test rods in the burnup range between 26-65 GWd/tU, including twenty-nine tests on PWR-type fuel rods, fourteen tests on BWR-type fuel rods, four tests on PWR MOX-type fuel rods, and fourteen tests on VVER-type fuel rods. These tests were performed in sodium coolant (280ºC and 0.5 MPa) in the CABRI program or in stagnant water (25ºC and 0.1 MPa) conditions in the NSRR and IGR/BIGR programs. All of the test rods were refabricated into short segments from full-length fuel rods extracted from fuel assemblies that had been irradiated in commercial PWR, BWR, or VVER power plants.

A summary of the most recent RIA simulation tests conducted using test rods from commercial fuel rods is shown in Table 2-1 through 2-4 for the CABRI, NSRR, and IGR/BIGR programs. A more detailed database of RIA experiments, including zero burnup tests in the US and Japan is contained in Appendix A.

Tables 2-1 through 2-4 highlight most of the key features of each experiment. The test segment burnup and oxide thickness are provided to describe the condition of the test rods. The fuel rod design and the pellet type (UO_2 vs. MOX) are also indicated in each table to show the wide variety of fuel designs tested. The two key parameters that define the power pulse characteristics namely, pulse width and maximum radial average fuel enthalpy (H_{max}), are also provided for each test. Finally, test results described by the fuel enthalpy at cladding failure (H_f) and the occurrence of fuel dispersal are provided for those tests that failed. In most cases, the fuel enthalpy at failure was obtained from in-pile instrumentation and the presence of fuel dispersal was determined by post-test examination techniques.

The attributes used to define an RIA experiment include the total energy deposition (E_p) and the maximum radial average fuel enthalpy (H_{max}). Normally, the result of RIA simulation experiments are reported in terms of E_p, which is obtained from the neutron physics analysis of post-test destructive examinations. The total energy deposition includes three components: the energy produced by prompt fissions during the power pulse, the energy from delayed neutron fissions, and the γ- and β-decay from fission products. The last two sources are the delayed energy components that occur during the power runout before reactor scram and therefore are not important contributors to the prompt fuel rod response. Unfortunately, the reporting of total deposited energy has not been consistent between the different test programs. Some organization report the prompt energy deposition, others have reported the total deposited energy, including the delayed energy deposition. This makes it difficult to compare the results reported from the different programs.

The maximum radial average fuel enthalpy is also determined by three components: the initial (or baseline) fuel enthalpy, the prompt energy deposition, and the amount of heat conduction that occurs during the power pulse. The maximum radial average fuel enthalpy is obtained through a

fuel rod analysis that accounts for the heat condition characteristics of the test rod and the rate of energy deposition. For power pulses with pulse widths of 10 milliseconds or less, the effect of heat conduction is minor and the maximum radial average fuel enthalpy is near the sum of the initial enthalpy (H_i) and the prompt energy deposition. Heat conduction effects become more prevalent for pulse widths greater than 20 milliseconds.

It should be noted that for tests at 280°C (CABRI), the initial fuel enthalpy is 16-17 cal/gm. For tests performed at atmospheric conditions (SPERT-CDC, NSRR). The initial fuel enthalpy is approximately zero.

The schematic in Figure 2-1 highlights the relationships between the power pulse, the energy deposition and the radial average fuel enthalpy. The energy deposition represents the integration of the power-time curve and reaches the total energy deposited once the power returns to zero. The radial average fuel enthalpy is calculated based on the UO_2 specific heat and the radial temperature profile. A maximum is reached near the late part of the power pulse as heat conduction effects begin to dominate. The relative response of these different parameters depends on the pulse width defined by the full-width half maximum (FWHM) of the power pulse.

Figure 2-2 contains a plot of the RIA-simulation tests from the US (CDC-SPERT/PBF), France (CABRI), and Japan (NSRR). Included in Figure 2-2 are several experiments from the database shown in Appendix A conducted on non-commercial test rods as well as test rods from commercial LWR fuel rods listed in Table 2-1 through 2-4. The maximum radial average peak fuel enthalpy is plotted as a function of the test rod burnup for more than 80 tests. Those tests that experienced cladding failure are indicated by a solid symbol and are plotted at the radial average fuel enthalpy at failure. The data show a general downward trend that is caused by a decrease in test segment reactivity with burnup. As shown in Figure 2-2, the rods that experienced cladding failure are interspersed amongst the rods where the cladding remained intact following the power pulse. Because of the fact that the failed and non-failed rods are interspersed when plotted as a function of burnup indicates that burnup is not the sole parameter that influences the cladding integrity, other parameters such as cladding temperature, the level of zirconium oxidation, and the cladding zirconium hydride content and distribution may also have an impact.

An extensive review and assessment of the test results developed in these experimental programs up to 1996 has been performed by the nuclear industry and reported in EPRI TR-106387. Since that review, additional tests have been conducted in these programs and the summary discussions below will highlight the results of these additional tests [Schmitz and Papin 1998; Fuketa 1998; Fuketa, 2000].

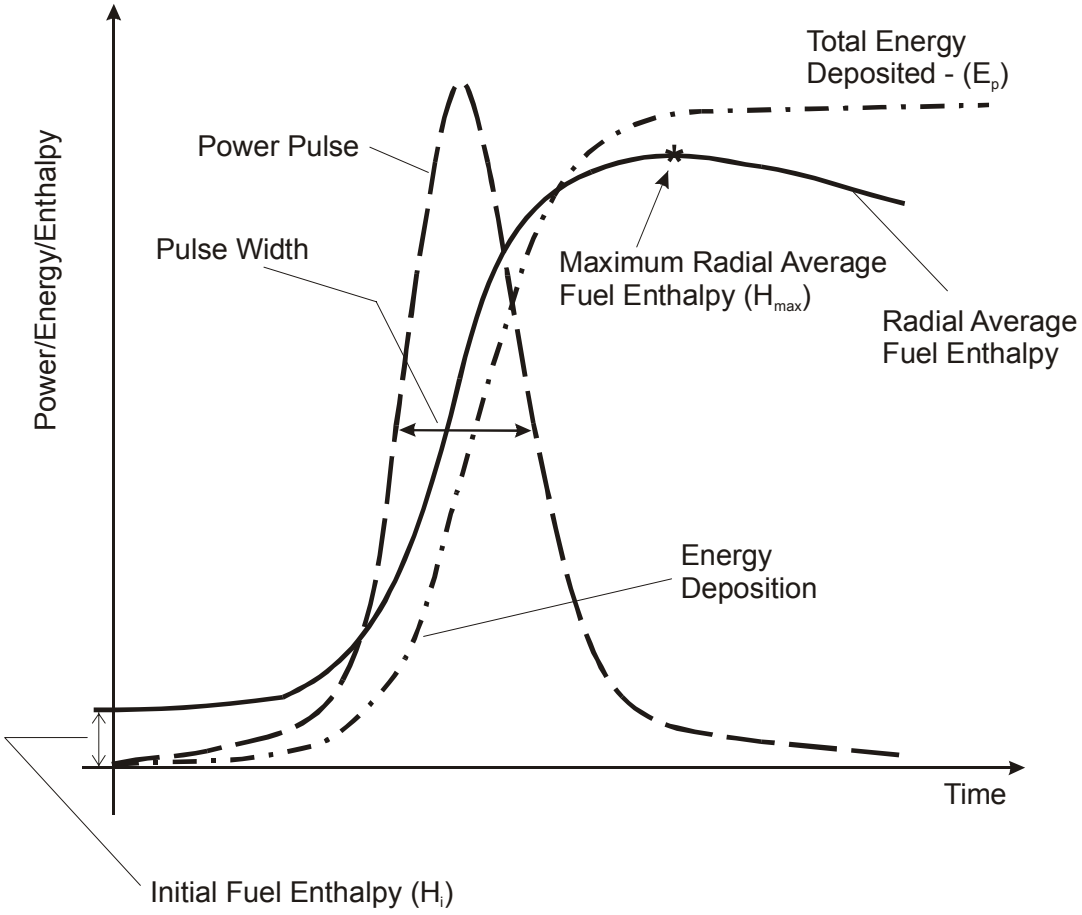

Figure 2-1
RIA power pulse schematic showing the relationship between power, energy deposition, and radial average peak fuel enthalpy.

Table 2-1
CABRI REP Na Test Rods
[Schmitz and Papin 1998; MacLachlan 2000a; MacLachlan 2000b]

Test	Peak Pellet Burnup (GWd/tU)	Oxide Layer (microns)	Fuel Type	Pulse Width (msec)	Max. H (cal/gm)	H at Failure (cal/gm)	Fuel Dispersal
Na-1	65	>80 – spall	17x17	9.5	115	30	Yes
Na-2	33	10	17x17	9.5	220		
Na-3	52	50	17x17	9.5	138		
Na-4	62	85	17x17	70	81		
Na-5	64	20	17x17	9.1	113		
Na-6	47	35	17x17 – Mox	35	138		
Na-7	55	50	17x17 – Mox	40	140	120	Yes
Na-8	60	130 - spall	17x17	78	105	83	No
Na-9	28	10	17x17 – Mox	34	203		
Na-10	64	>80 - spall	17x17	31	112	79	No
Na-11	64	~20	17x17 - M5	35	105		
Na12	65	~80	17x17 - Mox	65	~90		

Table 2-2
NSRR PWR Test Rods [Fujishiro 1992; Fuketa 1996; Fuketa 1997; Fuketa 1998; Fuketa 2000]

Test	Burnup (GWd/tU)	Oxide Layer (microns)	Fuel Type	Pulse Width (msec)	Max. H (cal/gm)	H at Failure (cal/gm)	Fuel Dispersal
HBO-1	50	40-50	17x17	4.4	73	60	Yes
HBO-2	50	30-40	17x17	6.9	37		
HBO-3	50	22	17x17	4.4	74		
HBO-4	50	18	17x17	5.4	50		
HBO-5	44	35-60	17x17	4.4	80	77	Yes
HBO-6	49	20-30	17x17	4.4	88		
HBO-7	49	30-50	17x17	4.4	88		
MH-1	39	5	14x14	5.3	47		
MH-2	39	5	14x14	5.0	55		
MH-3	39	5	14x14	4.8	67		
GK-1	42	10	14x14	4.8	93		
GK-2	42	10	14x14	4.8	90		
OI-1	39	N/A	17x17	4.4	106		
OI-2	39	N/A	17x17	4.4	108		
TK-1	38	7	17x17	4.4	125		
TK-2	48	15-35	17x17	4.4	107	60	Yes
TK-3	50	8	17x17	4.4	99		
TK-4	50	20	17x17	4.4	98		
TK-5	48	25	17x17	4.4	101		
TK-6	38	15	17x17	4.4	125		
TK-7	50	15-35	17x17	4.4	95	86	Yes

Table 2-3
NSRR BWR Test Rods [Nakamura 1994; Fuketa 2000]

Test	Burnup (GWd/tU)	Oxide Layer (microns)	Fuel Type	Pulse Width (msec)	Max. H (cal/gm)	H at Failure (cal/gm)	Fuel Dispersal
TS-1	26	6	7x7	6.7	55		
TS-2	26	6	7x7	6.2	66		
TS-3	26	6	7x7	5.6	88		
TS-4	26	6	7x7	5.0	84		
TS-5	26	6	7x7	4.5	98		
FK-1	45	11	8x8BJ	4.4	130		
FK-2	45	11	8x8BJ	5.3	70		
FK-3	41	15	8x8BJ	4.4	145		
FK-4	56	10	8x8	4.4	140		
FK-5	56	10	8x8	5.3	70		
FK-6	61	20	8x8	4.3	131	70	Yes
FK-7	61	20	8x8	4.3	129	62	Yes
FK-8	61	20	8x8	7.3	65		
FK-9	61	20	8x8	5.7	93	86	No

Table 2-4
IGR/BIGR Irradiated VVER Test Rods (Water 20°C and 0.1 MPa) [Yegorova 1999; Bibilashvili et al. 2000]

Test	Burnup (GWd/tU)	Oxide Layer (microns)	Fuel Type	Pulse Width (msec)	Max. H (cal/gm)	H at Failure (cal/gm)	Fuel Dispersal
H1T	48	5	1000	800	151		
H2T	48	5	1000	800	213	213	No
H3T	48	5	1000	800	252	252	No
H4T	48	5	1000	800	114		
H5T	48	5	1000	800	176	176	No
H6T	48	5	1000	800	87		
H7T	48	5	1000	800	187	187	No
H8T	48	5	1000	800	61		
BIGR-1	48	5	1000	3	142		
BIGR-2	48	5	1000	3	115		
BIGR-3	48	5	1000	3	138		
BIGR-4	61	5	440	3	125		
BIGR-5	48	5	1000	3	146		
BIGR-6	48	5	1000	3	153		

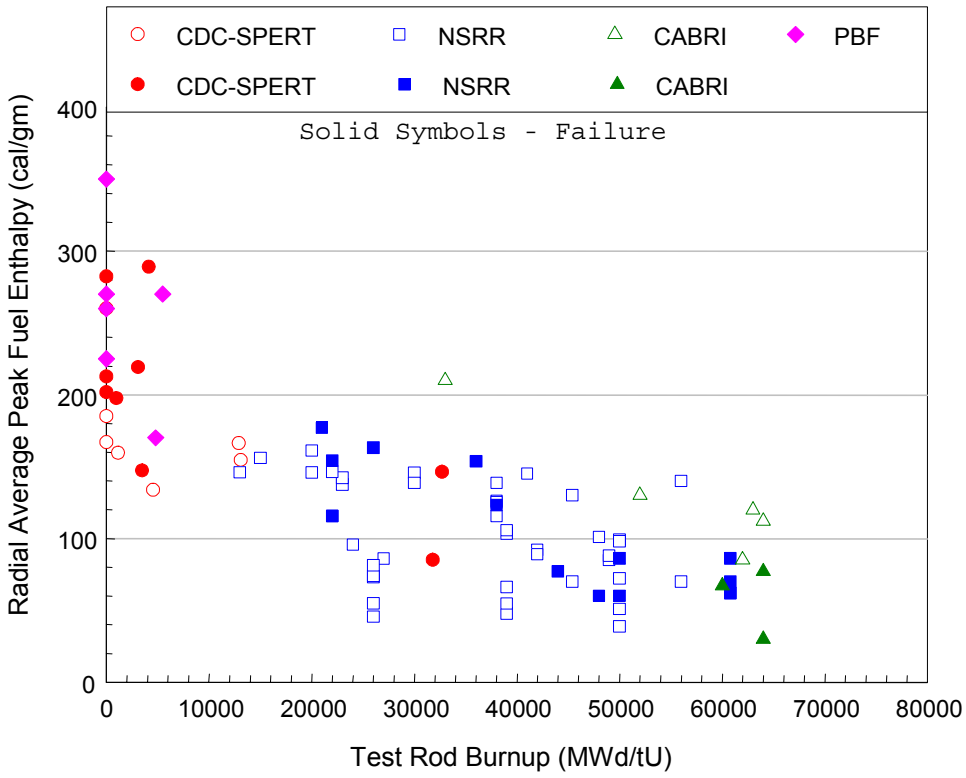

Figure 2-2
The radial average peak fuel enthalpy as a function of test rod burnup for RIA-simulation tests performed in the US, France, and Japan. Tests with cladding failure are indicated by solid symbols. The downward trend in the data is caused by the decrease in test rod reactivity with burnup accumulation.

2.2.1 CABRI REP Na Program

A review of the CABRI REP Na program on PWR fuel rods with non-spalled oxide layers at burnup levels up to 64 GWd/tU (see Appendix A for definition of oxide spallation) finds that these rods survived the RIA tests with minimum of consequences. The only tests on UO_2 fuel that experienced cladding failure in the CABRI REP Na program were Na-1, Na-8 and Na-10, which contained cladding with spalled outer surface oxide layers. Accompanying the spalled oxide layers in these tests were localized hydrides up to 50% of the cladding wall thickness, identified by neutron radiography and post-test metallography. Recent tests REP Na-8 and REP Na-10 failed at fuel enthalpy levels around 60 cal/gm and each rod had an additional energy deposition of ~30 cal/gm following cladding failure. Although these test rods contained extensive cladding spallation and hydride localization, only trace amounts of volatile fission products were released into the coolant, no fuel dispersal was experienced, and massive loss of cladding integrity was not observed even though an additional ~30 cal/gm was deposited after cladding failure. CABRI REP Na-8 and Na-10 further support the concept that loss of cladding ductility by formation of localized hydrides is the major cause of cladding failure during rapid

energy deposition events at elevated temperatures. Each of these tests exhibited brittle cladding cracks associated with localized hydrides.

The root cause of the low enthalpy failure of CABRI REP Na-1 continues to be unresolved. As a result, the International CABRI Water Loop Project has formed a special REP Na-1 Task Force with the objective of reaching a general consensus on the cause of cladding failure for this test. Members of the REP Na-1 Task Force have initially focused on the hypothesis of failure proposed by H. Chung at the recent ANS LWR Fuel Performance Topical Meeting [Chung 2000]. Chung has raised a concern that the pre-test initial conditions may have influenced the hydride morphology within the cladding and produced significant Zr-4 embrittlement. This embrittlement may then have influenced the fracture behavior of the cladding during the power deposition. The REP Na-1 Task Force has also reviewed the detection of the initial failure by the in-pile microphones to determine the reliability of the time of failure. The response of other in-pile measurements, such as the sodium flow rate and the pressure transducer response are being compared to the microphone data to confirm the time of cladding failure. However, it is the opinion of most members of the task force that REP Na-1 is an outlier test that need not be considered in the evaluation of high burnup fuel behavior during an RIA.

The results from the CABRI tests on MOX fuel irradiated between 28 and 47 GWd/tU show higher fission gas release and an increased PCMI loading from fission gas-induced pellet swelling [Schmitz and Papin 1999]. CABRI REP Na-7, which had a burnup of 55 GWd/tU, failed during the power pulse although the cladding corrosion layer was less than 50 microns [Schmitz and Papin 1999]. The Na-7 results suggest that a significant contribution of fission gas expansion or pressure loading was applied to the cladding during the power pulse to cause cladding failure.

2.2.2 NSRR Program

Since the mid-nineties, several additional RIA-simulation tests on PWR and BWR test rods have been performed in the NSRR facility. For PWR rods, an additional three tests have been conducted on the high-tin (~1.5% Sn) cladding material in the HBO series and a total of seven tests on low-tin (~1.3% Sn) cladding material have been conducted in the TK series. The burnup range for the test rods was between 38 and 50 GWd/tU. The NSRR facility has also conducted a total of nine tests on BWR rods refabricated from fuel rods previously irradiated in the Fukushima plant to a burnup range between 45 and 61 GWd/tU.

Evaluation of the PCMI-related failures in the PWR test rods HBO-1, HBO-5, TK-2 and TK-7 shows a correlation between the cladding outer oxide thickness and the potential for cladding failure. A plot of the peak fuel enthalpy versus the outer surface oxide layer thickness is shown in Figure 2-3. A failure boundary that has an oxide layer thickness dependency is indicated in the data. The curve shown in Figure 2-3 is just an engineering approximation. A more in-depth review of this data suggests that the cladding failure response in the NSRR tests is related to the hydride rim thickness. Post-test examinations on unfailed tests HBO-6 and HBO-7 found part-wall microcracks in the outer surface oxide and hydride rim layer that were blunted in the ductile Zircaloy substrate [Fuketa et al.1996]. Similar microcracks were also observed in the failed tests HBO-1 and HBO-5 in the vicinity of the through-wall cracks. The low initial cladding

temperature and the narrow pulse width in the NSRR tests magnify the influence of the hydride rim at the cladding outer surface on the effective cladding ductility.

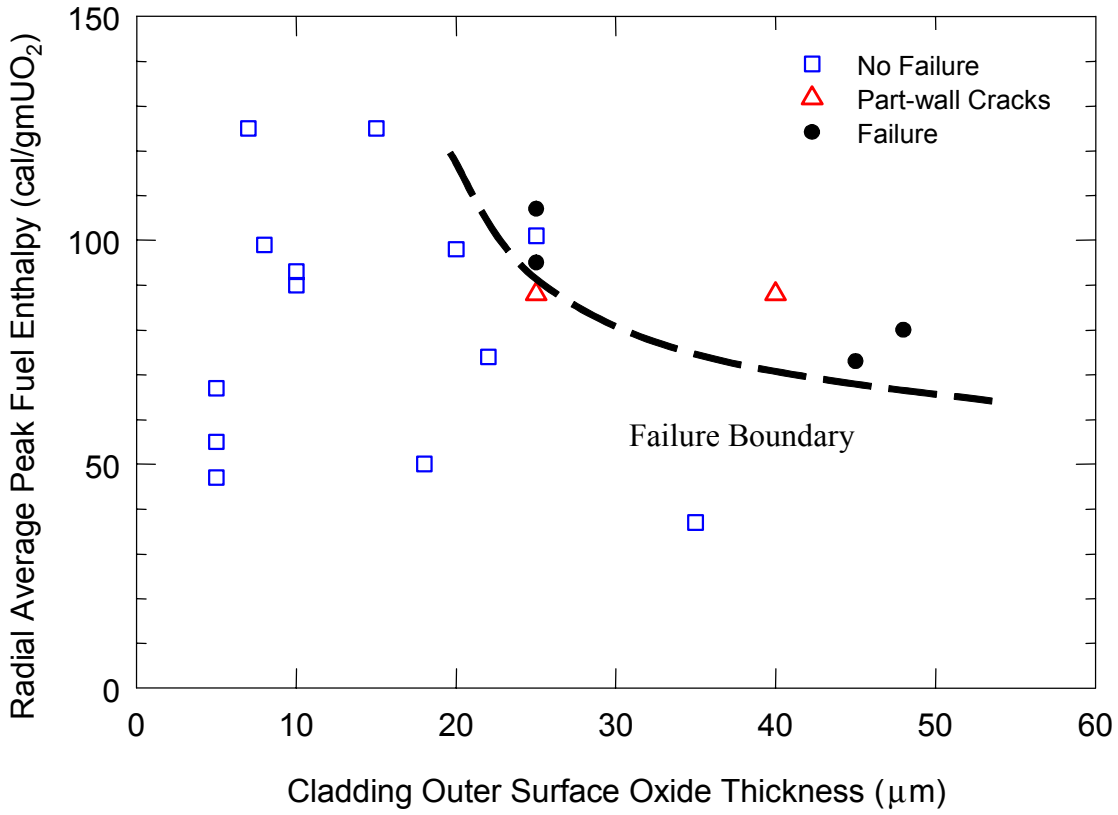

Figure 2-3
Peak Fuel Enthalpy versus Oxide Thickness from the NSRR Experiments

RIA-simulation tests using BWR rods have been performed on test rods refabricated from 8x8 zirconium liner cladding fuel rods irradiated to 61 GWd/tU. As shown in Table 2-3, no BWR test rods have failed below a burnup level of 56 GWd/tU up to peak fuel enthalpy levels of 140 cal/gm. A review of the tests finds no unusual behavior exhibited by the BWR test rods. The permanent cladding hoop strains are below 2% and the transient fission gas release is below 20%. This level of cladding strain is consistent with pellet thermal expansion during the energy deposition and does not indicate any enhancement of the PCMI loading from burnup-induced gaseous swelling or expansion. Compared to the PWR tests, these results are lower than the HBO and TK series. Recently, four tests have been performed on BWR rods at a burnup of 61 GWd/tU. Pre-test examinations show extensive fuel-clad bonding and almost complete gap closure. Tests FK-6 and FK-7 were tested to 130 cal/gm peak fuel enthalpy and each one failed between 60 and 70 cal/gm, broke into several pieces and dispersed finely fragmented fuel pellets into the coolant. FK-8 was tested with a wider pulse to peak fuel enthalpy of 65 cal/gm without cladding failure. Cladding failure may have been avoided in FK-8 because the wider pulse produces higher cladding temperature and thus, an increase in the cladding ductility. FK-9 also

included a wider pulse, but was tested to a peak fuel enthalpy of 90 cal/gm. Cladding failure was observed at 86 cal/gm from in-pile instrumentation. These results are still under investigation.

The test conditions (low initial coolant temperature and narrow pulse width) used thus far in the NSRR tests produce high cladding stress prior to any significant cladding heating by heat conduction from the pellet. At low temperature, the effective ductility of Zircaloy cladding containing non-uniform hydride layers is low and may be insufficient to accommodate fuel pellet expansion. The results obtained from tests conducted in the NSRR facility highlight the influence of the initial cladding temperature and the pulse width on the cladding failure response. Because these tests are conducted under room temperature coolant conditions, the test results are not representative of the fuel rod response for a HZP RIA event. Furthermore, these results require analytical evaluation to allow for comparison to other test programs, such as CABRI, and to assess the key mechanisms in the fuel rod response during an RIA event.

In the majority of the NSRR tests that resulted in cladding failure, a small amount of fuel dispersal was observed following cladding failure [Fuketa et al.1998]. The presence of fuel dispersal in the NSRR tests is related to the narrow pulse widths used in the RIA simulations. Since almost no heat conduction occurs during the energy deposition in NSRR, the pellet is under a large compressive stress state, particularly in the rim region. Upon cladding failure, the sudden removal of the confinement stress within the fuel produces local cracking and expulsion of small particles through the crack opening. The relevance of the NSRR tests with fuel particle dispersal will be discussed in more detail in Section 4.1.2.

2.2.3 IGR/BIGR Program

The IGR/BIGR program was performed in Russia to evaluate the failure mechanisms and failure thresholds for VVER fuel rods during RIA conditions [Asmolov 1996, Yegorova 1999, Bibilashvili 2000]. The program included approximately 200 tests on unirradiated VVER test rods and 14 tests on VVER test rods with burnup levels in the range of 50 GWd/tU to provide information on the effects of energy deposition, pulse width, initial rod internal pressure, and temperature. The VVER test rods differ from those tested in the French and Japanese programs in two ways: the use of Zr-1%Nb cladding material and the presence of a central hole in the fuel column. The IGR/BIGR test conditions are similar to those used in the NSRR test program and included three different coolant conditions: water at 20ºC and atmospheric pressure, air at 20ºC and atmospheric pressure, and water at 20ºC and 16 MPa pressure.

The mode of cladding failure for the tests on VVER rods was shown to depend on the pressure differential across the cladding. For tests with a positive pressure differential (prepressurized 1.5 MPa above the coolant pressure), the dominant fuel rod failure mechanism was high temperature ductile rupture (clad ballooning) and the cladding survived the lower temperature PCMI during the power pulse. The high cladding temperatures required to produce ballooning were a result of departure from nucleate boiling (DNB) that occurred either during the latter portion of the power pulse or after the completion of the power pulse. From analytical calculations, estimated peak cladding temperatures exceeded 1300 K in the high energy tests. For tests with a negative or zero pressure differential (prepressurization at or below coolant pressure), cladding failure was by melting due to interaction with molten UO_2 material.

The peak fuel enthalpy at failure depends on the initial conditions of the tests and is listed in Table 2-5.

Table 2-5
Summary of RIA-Simulation Tests on VVER Fuel in the IGR/GIRDA/BIGR Reactors

Type/Number of Tests	P_{rod} (MPa)	$P_{coolant}$ (MPa)	Pulse Widths (msec)	Radial Average Peak Fuel Enthaply (cal/gm)	Failure Threshold (cal/gm)
Unirradiated Unpressurized Rods (40)	0.1	0.1	2.75 - 1000	130 - 320	260 - 290
Unirradiated Pressurized Rods (129)	1.6 - 2.5	0.1	1.8 - 1000	20 - 500	160 - 180
Unirradiated Pressurized Rods (8)	2.5	16	440 - 600	175 - 250	250
Irradiated Pressurized Rods (14)	1.7	0.1	3 - 800	61 - 252	160 - 170

Almost no difference was observed between the failure response of the unirradiated and irradiated test rods to a burnup level near 50 GWd/tU because the Zr-1%Nb cladding material retains a significant amount of ductility at high burnup due to lower corrosion and less hydrogen absorption. As a consequence, the cladding can accommodate the PCMI loading during the energy deposition and prior to DNB. A comparison of the unirradiated and irradiated pre-pressurized tests performed in the IGR/BIGR test program with earlier tests performed in NSRR on pre-pressurized rods is shown in Figure 2-4. As can be seen, no large differences are observed between the failure threshold derived from the NSRR program using Zr-4 cladding and the IGR/BIGR program using Zr-1%Nb cladding. These results indicate that the high temperature failure response during an RIA event is the same for the two cladding types. Furthermore, these results demonstrate that the maximum fuel enthalpy at failure is primarily a function of positive pressure differential across the cladding. The cladding failure mode changes from a melt response to ballooning/rupture above a positive pressure differential of 1 MPa.

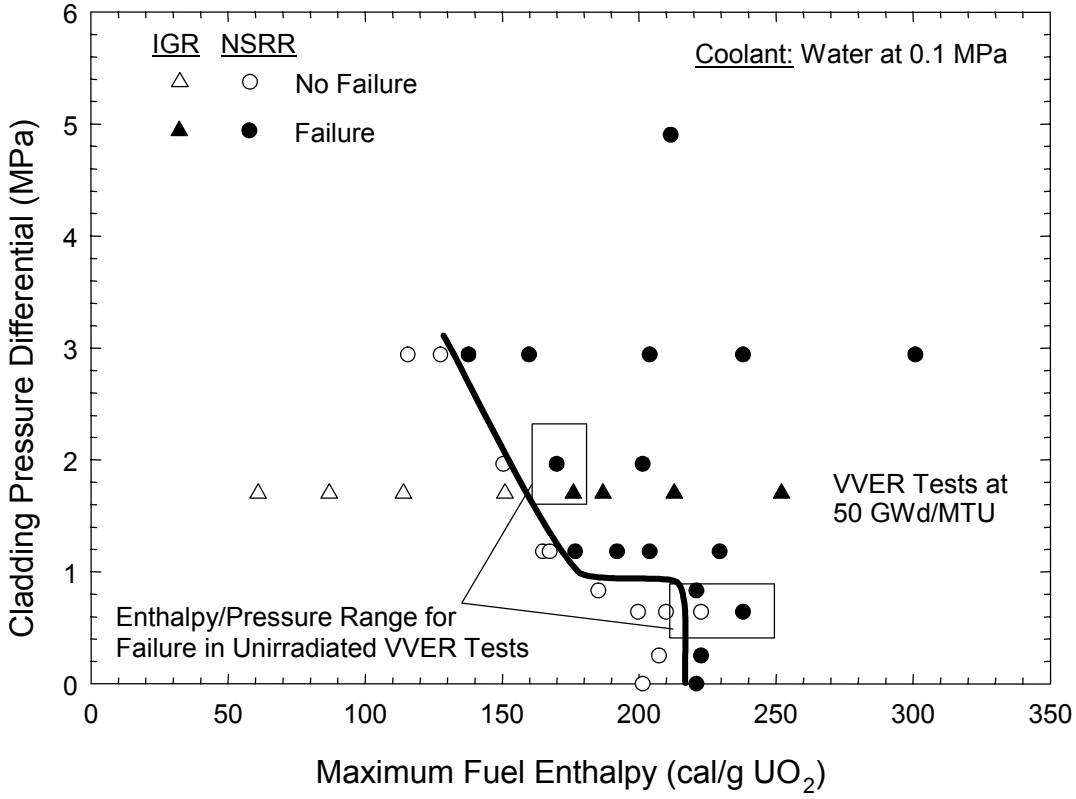

Figure 2-4
Initial Internal Pressure versus Energy Deposition for the NSRR and IGR/BIGR Tests

2.2.4 Summary

In tests conducted in NSRR and CABRI above 55 GWd/tU, the effect of burnup has been shown to increase the PCMI forces on the cladding by the gradual reduction of the fuel-cladding gap thickness during steady state irradiation. The CABRI REP Na-4, REP Na-5 and REP Na-11 tests at 60+ GWd/tU and the recent NSRR tests FK-4 and FK-5 at 56 GWd/tU did not fail after experiencing maximum fuel enthalpy increases between 70 and 140 cal/gm. These test rods had cladding material with sufficient ductility to accommodate the PCMI loading strains. The results from these tests demonstrate that the main load imposed on the cladding is from PCMI mechanisms caused by pellet thermal expansion combined with burnup related processes. The role of fission gas-induced transient swelling is much less for UO_2 fuel rods at the burnup and temperature conditions experienced by the tests.

The results from RIA-simulation tests on VVER rods at burnup levels near 50 GWd/tU demonstrate that the zirconium-niobium alloy cladding will survive the PCMI phase without failure. The primary failure mode is by high temperature processes that occur once heat conduction is initiated. For test rods with an internal pressure that exceeded the external pressure, ballooning and burst failure of the cladding was initiated at energy levels that produced cladding temperatures above 1200 K. Since the irradiated VVER fuel rod designs contain a central hole, the larger gas volume and the rapid axial gas communication was able to support

the clad ballooning deformations that led to failure. The tests on VVER fuel overestimate the impact of gas pressure on ballooning for high burnup LWR fuel rods, which have restricted axial gas communication due to gap closure and pellet-clad bonding. The cladding temperature at failure increases, as well as the peak fuel enthalpy, for low or negative pressure drops across the cladding. These results are consistent with similar tests conducted in NSRR during the 1970's.

In development of a failure threshold from all the data shown in Figure 2-2, the statistical failure/no failure method used to evaluate the data produces mixed results because of factors introduced during irradiation such as the decrease in fuel rod reactivity and the decrease in cladding ductility with fluence and corrosion for older cladding designs. In addition, variations in test conditions make it difficult to directly compare the results from different test programs. To more fully understand the contribution of burnup, cladding embrittlement and test conditions requires analysis of the test rods using sophisticated analytical capabilities coupled with data from separate effects tests to distinguish between the various effects. Through such an approach, the circumstances leading to fuel rod failure can be determined considering the parameters that influence the response of the fuel and cladding.

2.3 Separate Effects Tests

An important element in the evaluation and modeling of fuel behavior during an RIA event are the data from separate effects tests. The main separate effects tests used in the modeling and analysis of RIA-simulation experiments are the mechanical property tests on irradiated cladding material. The data obtained from cladding mechanical property tests and the method employed to utilize this data with the analytical methods for RIA-simulation experiments are described below.

2.3.1 Cladding Mechanical Properties Database

Data describing the effects of operation on the cladding material tensile strength and elongation are necessary to understand the behavior of irradiated test specimens during RIA-simulation tests and to evaluate the performance of irradiated fuel during a hypothetical RIA event. Similar data is also required to demonstrate adequate cladding performance during normal operation and anticipated operational occurrences. As a result, several post-irradiation test programs have been conducted to evaluate the effects of irradiation on the cladding mechanical properties. The outcome of such test programs has been to highlight the changes in cladding mechanical properties caused by fast neutron damage, absorption of hydrogen from the corrosion process, and temperature. An example of the mechanical tests used and results obtained for irradiated Zircaloy cladding is presented by Garde [Garde 1989].

Table 2-5 lists the mechanical property test programs used as part of the industry assessment of RIA fuel behavior to develop the strength, elongation and critical strain energy density relationships for irradiated Zircaloy cladding [Papazoglou and Davis 1983; Balfour et al. 1985; Newman 1986; Smith et al. 1994a; Smith et al. 1994b; Lemoine and Balourdet 1997; Hermann et al. 2000; Kuo et al. 2000]. The cladding material used in these test programs includes different cladding designs, e.g. 14x14 and 17x17, irradiation conditions, oxide layer thickness levels, and zirconium hydride distributions. The programs summarized in Table 2-5 include most of the

mechanical property tests conducted on high burnup Zircaloy-4 cladding material. As indicated, test results are included from samples that contained cladding outer surface oxide layers with cracking, flaking, and spallation.

In general, three types of mechanical property tests are used in the programs listed in Table 2-5: uniaxial tube tension tests, uniaxial ring tension tests, and biaxial tube burst tests. Uniaxial tube tension tests consist of tube samples approximately 125 mm long, with a central gauge section of ~50 mm. These specimens are tested by loading in the axial direction at strain rates of ~$5x10^{-5}$/sec in most cases. Uniaxial ring tension tests consist of a thin ring sample fabricated to widths between 2.5 and 7 mm and with or without a machined gauge section. Typical machined gauge sections are ~3 mm long and 1.5 mm wide. For specimen designs without a machined gauge section, the experimenters assumed that the gauge length was 20% of the mid-wall circumference in the calculation of the hoop strain [Garde et al. 1996]. The ring tension specimens are tested with special inserts to provide loading in the hoop direction. For uniaxial tube tension and ring tension samples obtained from fuel rods, the pellet material is removed by drilling and chemical etching. Biaxial tube burst tests are performed on 200 mm long tube samples using some type of hydraulic fluid to pressurize the sample. The pellet material is either completely or partially removed prior to testing. Closed-end burst tests are performed in most cases. The mechanical properties determined from the three different test types include yield stress, ultimate tensile stress, uniform elongation and total elongation.

2.3.1.1 Influence of Irradiation on Cladding Mechanical Properties

A review of the mechanical properties measured for irradiated cladding at burnup levels greater than 50 GWd/tU indicates that the effects of fast neutron damage (irradiation hardening) causes only an incremental increase from low burnup values in the yield stress and ultimate tensile stress. Saturation of the yield and ultimate tensile strength with fast neutron damage occurs below fluence values of 3-$4x10^{21}$ n/cm^2 (E > 1 MeV). The effect of fluence on the yield stress of CWSR Zircaloy-4 material is shown in Figure 2-5 for uniaxial tension tests. Similar results are obtained from burst specimens.

The uniform and total elongation values decrease with accumulation of fast neutron damage. The most significant reduction in uniform and total elongation occurs during the first cycle of operation at fast fluence levels approaching 3 to $4x10^{21}$ n/cm^2 (E > 1 MeV). After the first cycle of irradiation, the uniform elongation value for Zircaloy-4 SRA material is reduced from 4 to 5 % for unirradiated material down to values between 1 and 3% for irradiated material. The reduction of the uniform elongation is observed in all of the different mechanical property test methods. Similarly, the total elongation decreases from 20 to 30% for unirradiated material to values between 10 and 15% after 1 cycle of operation. The extent of the reduction depends somewhat on the type of mechanical property test (uniaxial or biaxial) and the susceptibility of test sample to develop bending within the gauge section. Beyond this level of fast fluence, the uniform and total elongation remain about constant until a fast fluence of $9x10^{21}$ n/cm^2 (E > 1 MeV).

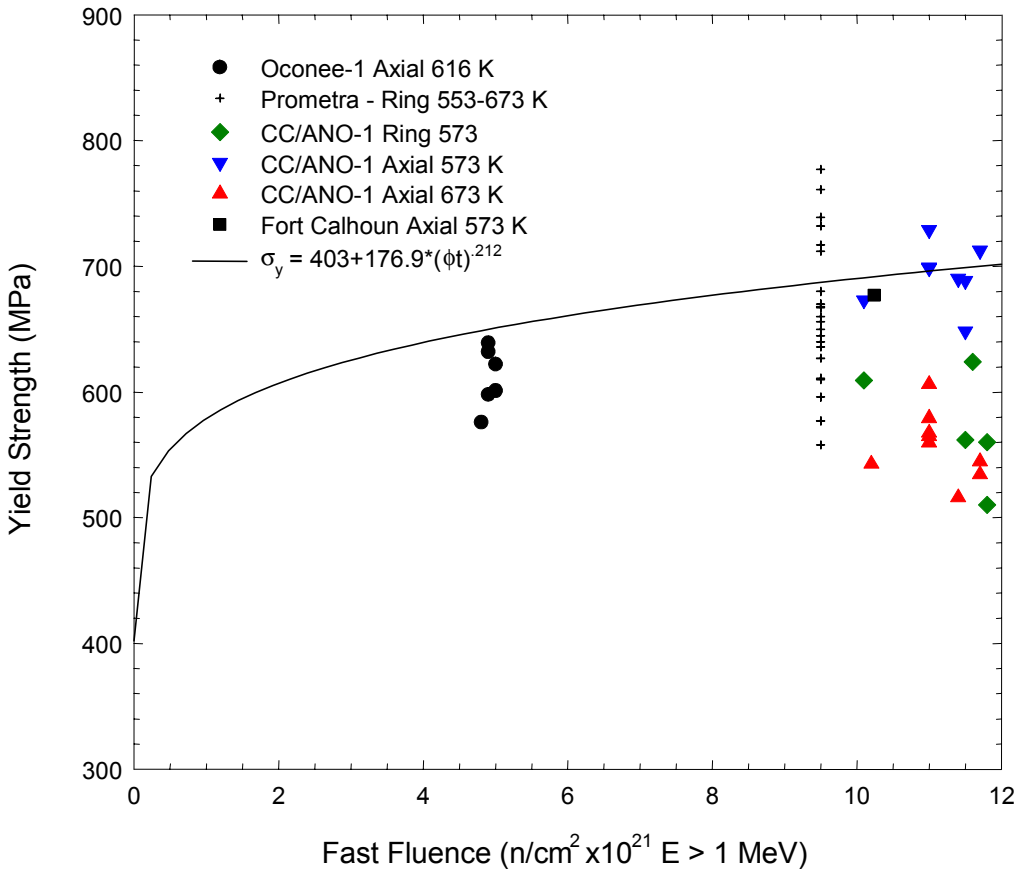

Figure 2-5
Cladding yield stress as a function of fast neutron fluence. Irradiation hardening saturates at fast fluence levels above $3x10^{21}$ n/cm^2 (E>1 MeV).

At the fluence levels corresponding to extended burnup ($\phi t > 9x10^{21}$ n/cm^2 E> 1 MeV), the concentration of zirconium hydrides and the zirconium hydride distribution in the cladding can further influence the cladding mechanical properties. Mechanical tests on cladding with hydrogen levels above 300 ppm begin to exhibit the effects of hydride precipitates on both the uniform and total elongation. The uniform elongation can be reduced below 1% and the total elongation can decrease to below 2% for biaxial burst tests.

Figure 2-6 contains the total plastic elongation measurements from axial tension, ring tension, and tube burst tests conducted on cladding material irradiated to fast fluence levels between 9 and $12x10^{21}$ n/cm^2 (E > 1 MeV). The current evaluation uses the oxide thickness to depict the influence of hydrides on the cladding mechanical properties. This approach was necessary because the methods employed to determine the hydrogen content for a given test sample were not consistent between the various test programs. Since the hydrogen within the cladding comes from the corrosion process, the oxide thickness can be assumed to represent the average hydrogen content within the cladding. Finally, the oxide thickness was normalized using the cladding wall thickness to account for the variation in cladding designs, i.e., 17x17 and 14x14.

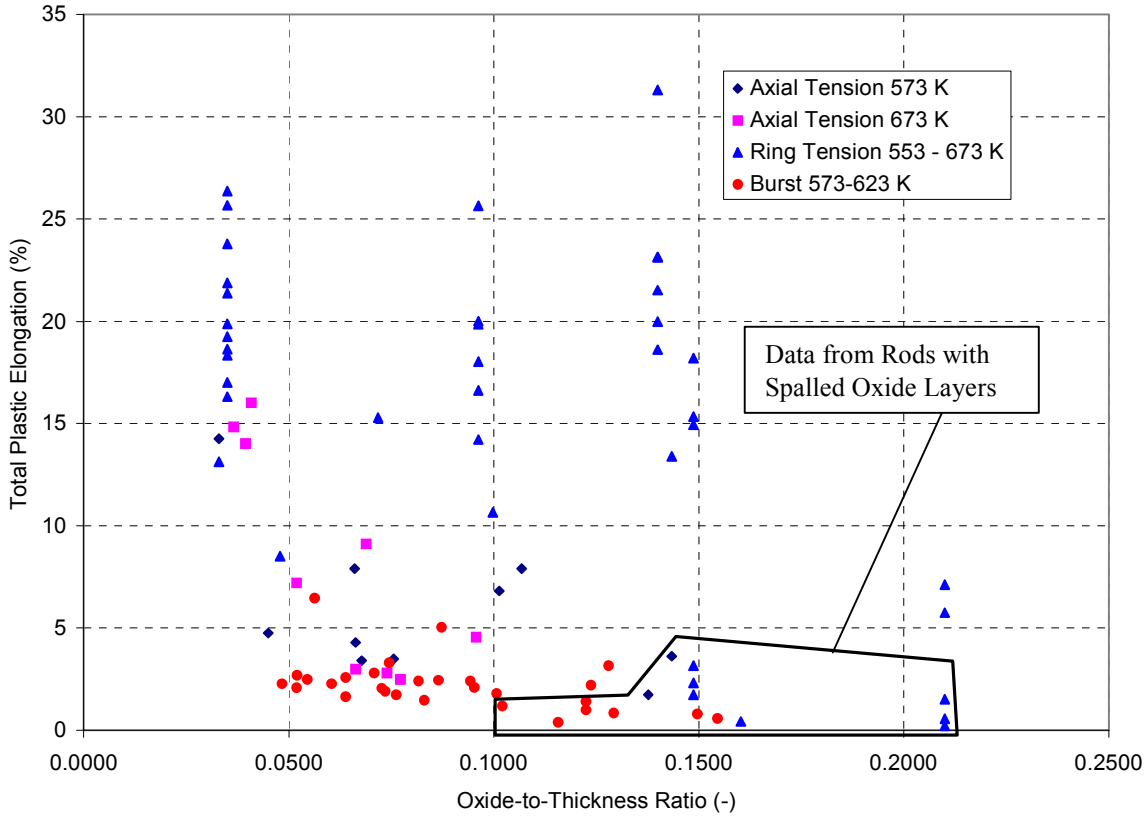

Figure 2-6
Total plastic elongation as a function of oxide-to-thickness ratio. Data obtained from uniaxial ring tension, uniaxial axial tension and burst tests on irradiated cladding at fluence levels above $9x10^{21}$ n/cm^2 (E > 1 MeV).

The total plastic elongation decreases as a function of the outer surface oxide thickness. Although only limited data is available, the effect of hydrogen is more pronounced in the axial tension data. The data shown in Figure 2-6 indicate that both the ring tension and the burst total plastic elongation data are independent of the hydrides in the cladding below oxide thickness-to-cladding thickness ratios of 0.1 to 0.12 at temperatures above 573 K. Above this oxide thickness, the potential to form localized hydrides increases and the total plastic elongation values begin to drop below 1% for samples with localized hydrides. Those test samples that came from rods with localized hydrides or were confirmed to have localized hydrides within the samples are indicated in Figure 2-6. The uniform plastic elongation data shown in Figure 2-7 also decreases as a function of outer surface oxide thickness. The influence of oxide thickness is observed in both the uniaxial and biaxial tests. Uniform plastic elongation values that are below 0.5% are associated with cladding with localized hydrides as indicated in Figure 2-7.

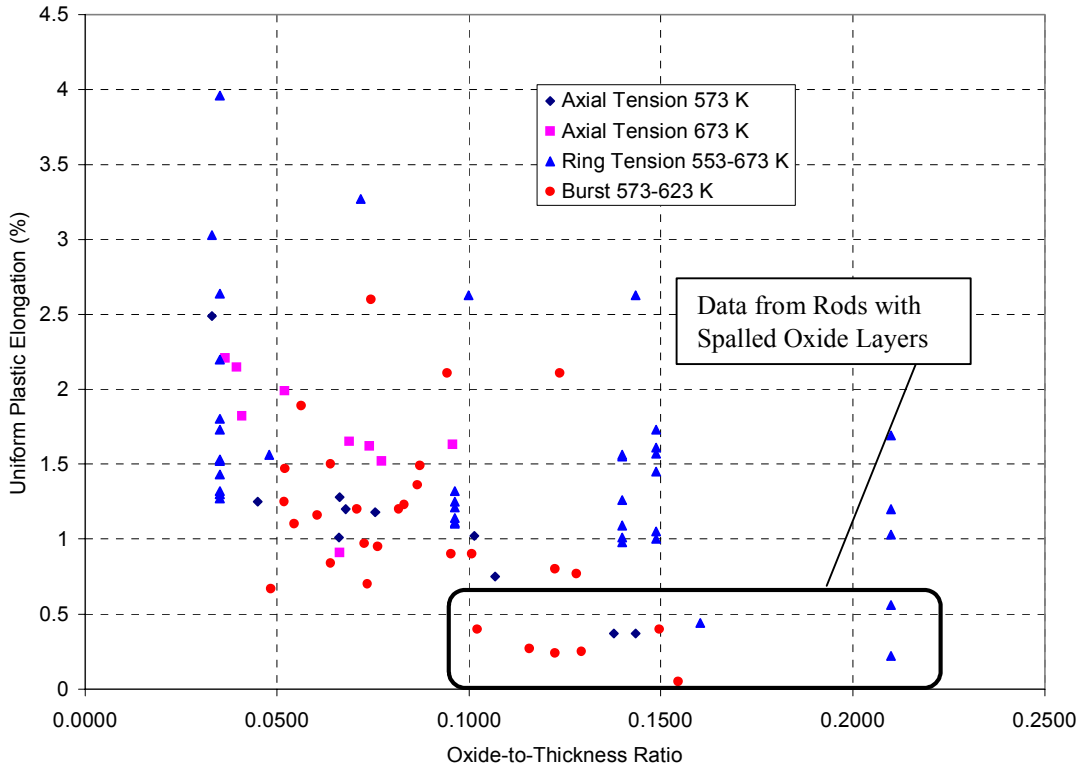

Figure 2-7
Uniform plastic elongation as a function of oxide-to-thickness ratio. Data obtained from uniaxial ring tension, uniaxial axial tension and burst tests on irradiated cladding at fluence levels above $9x10^{21}$ n/cm^2 (E > 1 MeV).

As shown in Figures 2-6 and 2-7, non-uniform zirconium hydride distributions corresponding to high hydrogen concentrations (> 700 ppm) can reduce the uniform and total plastic elongation, as well as, the ultimate tensile strength. Garde, et al. presented results on uniform and total plastic elongation measurements from cladding with localized hydride regions [Garde et al. 1996]. These data show that the cladding total plastic elongation can decrease to below 1% for cladding average hydride volume fractions above 80% in the vicinity of the fracture location. Formation of localized hydride accumulations leading to 80% volume fraction requires the migration of hydrogen under thermal gradients. Non-uniform oxide layers as a consequence of outer surface oxide spallation can cause the thermal gradients sufficient to promote hydrogen migration, depending on such factors as the oxide layer thickness and operating power level. Oxide spallation is addressed in Appendix B.

2.3.1.2 Sources of Data Scatter

The mechanical property data for irradiated cladding obtained from the different test methods contains a certain level of data scatter that is caused by two main sources. First, the testing methods introduce data scatter by such factors as specimen design and fabrication, loading and

heating conditions, and measurement uncertainties. Second, material variability arising from differences in initial cladding material fabrication (composition and heat treatment), cladding geometry (wall thickness and outer diameter), irradiation temperature, and hydrogen concentration also contribute to the scatter in the measured material strength and elongation values. An understanding of the sources of data scatter is important in the development of mechanical property dependencies on fast fluence, hydrogen content, and temperature.

The mechanical properties of irradiated cladding are measured using testing methods that inherently introduce some amount of data scatter. Developing a uniaxial test specimen from clad tubing is difficult and the specimen designs deviate from traditional uniaxial tension specimens. As a result, two main problems arise in the ring tension and axial tension tests. For the ring tension, the double-D loading method can introduce bending within the gauge section. The amount of bending is a function of the tolerances between the loading inserts and the sample and can affect the measured elongation values. Also, the gauge section in both the ring tension and axial tension test specimens is not well defined. This also can introduce uncertainties in the total elongation strains measured in the post-test examinations. Efforts are underway in the NRC-sponsored programs at ANL to improve the test specimens to eliminate bending and improve the strain measurements [Daum et al. 2001; Link et al. 1998]. However, the data scatter arising from the testing methods must be recognized to always be present in the data.

The condition or material characteristics of the cladding sample being tested also influence the measured mechanical properties of irradiated cladding. Variability in fabrication processes can influence the impurity content and/or the heat treatment of the cladding. Mechanical properties of cladding from different fuel vendors will always display some variability for unirradiated material. Irradiation further complicates the cladding mechanical properties because irradiation damage accumulation is influenced by the operating temperature of the cladding [Rowland 1984; Lyon et al. 2001]. Therefore, samples removed from the upper regions of the rod can have different irradiation hardening characteristics compared to the lower region of the rod because of the higher cladding temperature. These uncertainties are also inherent to the data and are difficult to account for in any modeling activity.

Because of the nature of irradiated cladding, data scatter will always be present in the mechanical properties reported. This must be recognized when developing material models for irradiated Zircaloy material.

Table 2-6
Mechanical Property Tests

Program	Fuel Type	Max. Bu (GWd/tU)	Max. Fast Fluence (n/cm^2)	Range of Oxide Thickness (μm)	Temperature Range (K)	Strain Rate (/sec)
ESEERCO Hot Cell Program on Zion Rods						
Burst	15x15	49	$9.4x10^{21}$	15 - 25	588	$2x10^{-5}$
ABBCE-DOE Hot Cell Program on Fort Calhoun Rods						
Burst	14x14	53	$8x10^{21}$	30 - 50	588	$6.7x10^{-5}$
EPRI-B&W Hot Cell Program on Oconee-1 Rods						
Axial Tension	15x15	25	$5x10^{21}$	< 20	616	$8x10^{-5}$
Ring Tension						
Burst						
EPRI-ABBCE Hot Cell Program on Calvert Cliffs-1 Rods						
Axial Tension	14x14	68	$12x10^{21}$	24 - 110‡	313 - 673	$4x10^{-5}$
Ring Tension				24 - 115‡	573	$4x10^{-5}$
Burst				36 - 110‡	588	$6.7x10^{-5}$
ABBCE-DOE Hot Cell Program on ANO-2 Rods						
Axial Tension	16x16	58	$12x10^{21}$	24 - 46	313 - 673	$4x10^{-5}$
Burst				24 - 46	588	$7x10^{-5}$
EdF-IPSN PROMETRA Program						
Ring Tension	17x17	63	$10x10^{21}$	20 - 120‡	298 - 673	.01 - 5
Nuclear Fuel Industry Research Program-III						
Burst	15x15	51	$9x10^{21}$	40 - 110‡	573 - 623	$5x10^{-5}$

‡ - Several samples were obtained from cladding with spalled oxide layers.

2.3.2 Cladding Integrity Model

A first approach to develop an integrity model for high burnup cladding subjected to an RIA event might be to use a simple strain-to-failure (ductility limit) criterion. This strain-to-failure criterion would be measured directly in a mechanical property test and can be a function of temperature, hydrogen content, strain rate etc. Unfortunately, however, strain is not a path independent response quantity and, consequently, does not uniquely characterize a failure state of the material; further, it depends on the rate of loading and the multi-axial condition of the imposed stresses. A practical difficulty in using a strain limit is the choice between the "uniform elongation" and the "total elongation". The latter is a uniaxial limit state that is subject to the restrictions outlined above, but the former is an apparent limit state that has significance only in describing the stress-strain test and plays no role in modeling and analysis. The uniform elongation is the strain at the point of maximum load in an engineering-stress-engineering-strain curve, and is assumed to be the onset of plastic instability. Thus, when the source of loading is purely pressure, it is often argued that the uniform elongation becomes the true failure measure. By contrast, PCMI is a displacement controlled loading, and thus could not be judged by such a strain measure. More importantly, the true-stress-true-strain curve is the material property relation used in RIA modeling and analysis where the calculated strain response is a single quantity with no possible way of identifying a uniform-elongation strain. It would seem, then, that the use of a strain criterion as a failure measure for judging RIA events is unworkable.

A stress-based criterion suffers from similar deficiencies, in that it does not recognize the state of deformations and does not distinguish between a load-controlled (pressure type) and a displacement controlled (PCMI type) loading events. Consequently, neither the strain state alone nor the stress state alone is sufficient to describe a failure state. The appropriate approach, then, is to develop a failure criterion that combines both the stress and the strain states, for which the strain energy density concept is best suited. The material resistance would be judged in terms of a critical value of the strain energy density (CSED), and the applied loading would be described in the calculated response in terms of the strain energy density (SED). The CSED is determined from material property tests as function of temperature, fast fluence, hydrogen content and other material conditions. The SED represents the accumulation of the total mechanical energy during mechanical loading of the cladding during an RIA event.

2.3.2.1 Theoretical Description of SED/CSED Model

The derivation of the SED model is described in detail in Rashid et al. 2000, but for continuity we give here a summary of the relevant material. The development is fashioned after the well-known path independent J-integral approach developed by Rice in the sixties (Rice 1968) for the analysis of strain concentration by notches and cracks, which revolutionized the field of Fracture Mechanics. It will be shown that an exact equivalence exists between the SED/CSED model and Rice's J/J_C formulation.

Consider a homogeneous body subjected to a two-dimensional deformation field, containing a defect or a crack that can be represented by a notch of the type shown in Figure 2-8.

Define the strain energy density $\overline{U}$:

$$\overline{U} = \int_{ij} d_{ij} \tag{2-1}$$

where $_{ij}$ and $_{ij}$ are the stresses and the strains respectively. The J-integral is defined by

$$J = \int \overline{U} dy - \int F \frac{u}{x} ds \tag{2-2}$$

In eq. 2-2, the integration is performed over the curve surrounding the notch tip. F is the traction vector such that it is positive in the direction of the outward normal along , i.e. $f_i = _{ij} n_j$, u is the displacement vector, and ds is an element of arc length along . The integral in eq. 2-2 is path independent; i.e., the value of J does not change if another contour enclosing the notch is chosen; proof of path dependence of the J-integral is given by Rice in his classic paper [Rice 1968].

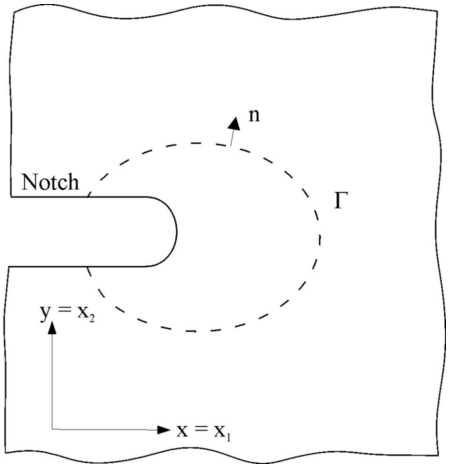

Figure 2-8
Flat Surface Notch in Two-Dimensional Deformation Field

The model development will now focus on a fuel rod geometry and material condition. During service, damage accumulation by two sources, fast-neutron fluence and hydrogen absorption affects the ability of the cladding to withstand mechanical loading by PCMI or pressure forces. The effects of irradiation damage is to homogenize the material, including reducing anisotropy, to increase the yield and ultimate strengths and to decrease the uniform and total elongation values. The damage caused by hydrogen, on the other hand, is heterogeneous and is of two types. The first type consists of circumferentially oriented hydride platelets distributed in the cladding in a radially varying concentration gradient. In some cases, the hydrides are driven towards the cladding outer region, under the effects of temperature and stress gradients, forming a narrow (<50 m) hydride-rich outer rim beneath the corrosion layer [Fuketa et al. 1996]. The hydrogen concentration in the hydride rim can exceed 2000 ppm, with the average hydrogen concentration decreasing to one or two hundred ppm closer to the inner surface. The second type

of damage is the formation of hydride lenses as a result of oxide spallation [Papin et al. 1996]. These hydride lenses are localized discontinuities, which under worst case conditions can penetrate to almost mid wall. They have the effect of a notch, causing strain concentration in the surrounding Zircaloy material. Such hydride concentration can be characterized as a notch-type discontinuity, which lends itself quite naturally to the application of the J-integral methodology. Other, but less severe, forms of discontinuities, which can be treated in the same way, are surface hydrides and small incipient cracks. Under high burnup, given the right loading condition, there is ample opportunity for cladding failure to initiate from one such discontinuity. Since the exact location and geometry of the offending discontinuity is not known a priori, other than that it exists somewhere in the cladding cross section, the adoption of a fracture-toughness based failure criterion would not be useful. Thus, the purpose is to formulate a failure model based on notch-type simulation of a discontinuity, but without having to prescribe the exact geometry or location of the notch.

To this end consider Figure 2-9, which is a cross-section of a fuel rod with a notch-type cladding defect. Owing to the path independence of the J-integral, we are free to take the contour shown by the dashed line, which encloses the entire cross section, consequently enclosing all possible discontinuities. The choice of a discrete notch-type form of damage is mainly to facilitate the mathematical derivations, but the exact form of the damage is not important. We wish to estimate the value of *J* without analyzing the cracked body. Now, for the contour line chosen, we have,

$$F = 0 \text{ at } r = r_o$$

$$F \approx 0 \text{ at } r = r_i$$

$$F^+ = F^- \text{ at } \theta \cong 0$$

Under internal pressure, the line integral of the traction term,

$$\oint_{\Gamma} F \cdot \frac{\partial u}{\partial x}\, ds = 0 \text{ at the closed ID surface.}$$

The traction term in eq. 2-2 drops out, and *J* becomes, using Green's theorem,

$$J = \oint_{\Gamma} \overline{U}\, dy = \int_{A} \frac{\partial U}{\partial x}\, dx dy \tag{2-3}$$

From eq. 2-3 it can be noted that, at the time of failure initiation, *J* becomes J_c (the fracture toughness), and correspondingly $\overline{U}$ becomes $\overline{U}_c$, which we designate as the critical strain energy density (CSED). Using the definition in eq.1, this can be written as,

$$\overline{U}_c = \int_{0}^{\varepsilon_f} \sigma_{ij}\, d\varepsilon_{ij} \tag{2-4}$$

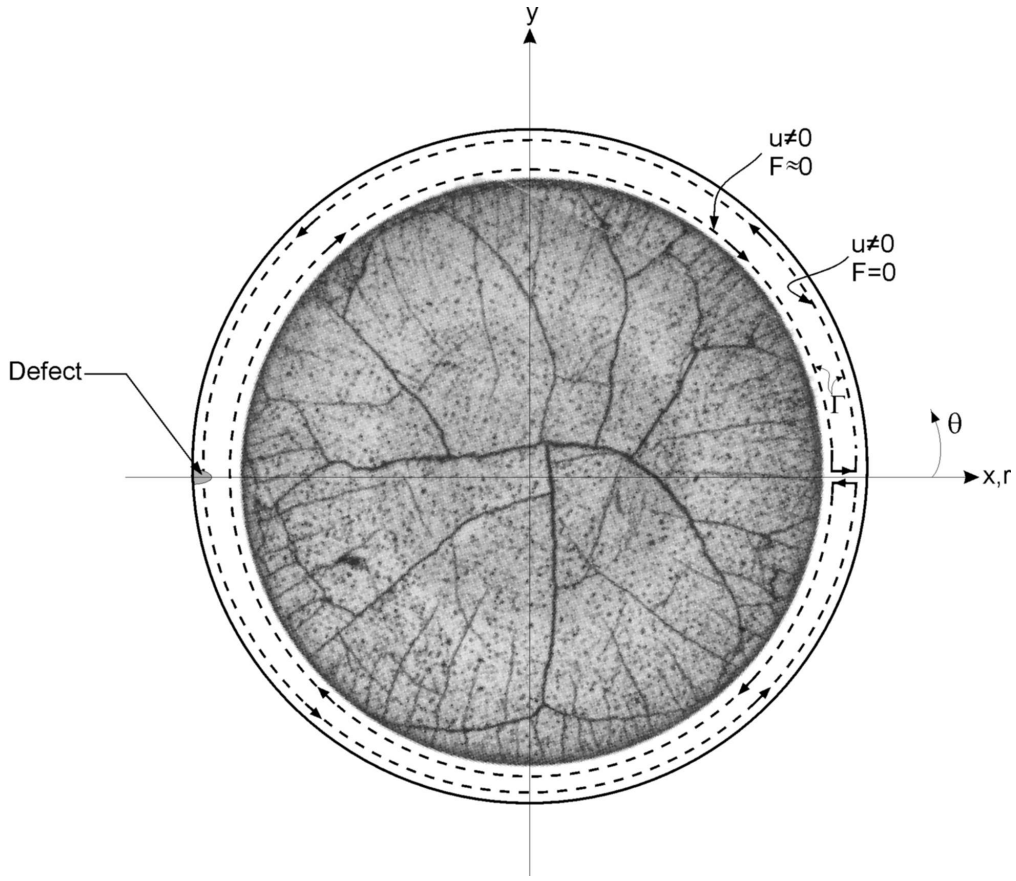

Figure 2-9
Cross-Section of Fuel Rod with Contour Line Surrounding Defect Tip

where ε_f is the material failure strain, which is the total elongation in a uniaxial test; in multi-dimensional tests, ε_f becomes a function of the biaxial or triaxial stress ratios. Having thusly established equivalence between CSED and J_c, we can henceforth concentrate on the development of the CSED as a failure model for cladding material. Equation 2-4 states that the CSED is quantified from stress-strain data obtained from material property tests. The functional dependence of CSED on damage mechanisms, such as hydride lenses, hydride rim, spalled oxide, ID or OD cracks, etc., is reflected in the material property data for irradiated cladding with representative corrosion and hydride conditions to those encountered in high burnup fuel rods.

2.3.2.2 Development of CSED for Irradiated Zircaloy Cladding

The critical strain energy density (CSED) is developed from material property tests as a function of material conditions, including temperature, fast fluence, outer surface corrosion, hydrogen concentration, and hydride morphology. The database of mechanical property tests on irradiated cladding material used to develop the CSED relations contains a variety of cladding designs, irradiation conditions, oxide thickness levels, and testing conditions (temperature and strain rate). These tests were conducted as part of fuel performance monitoring programs sponsored by EPRI and the U.S. Department of Energy (DOE) to evaluate intermediate and high burnup fuel

behavior [Newman 1986; Smith et al. 1994a; Smith et al. 1994b]. A summary of the important characteristics of the database is shown in Table 2-6. The test samples were obtained from fuel rods that had achieved fuel rod average burnup levels between 25 GWd/tU and 62 GWd/tU. A few samples extracted from high burnup rods exhibited oxide spallation and localized hydrides. Like the ultimate tensile strength and total elongation data from which it is derived, the CSED data obtained from mechanical property tests on irradiated cladding implicitly includes all the mechanical property degradation mechanisms caused by irradiation, such as fast neutron damage, zirconium hydride content and orientation, and localized hydride accumulations.

The CSED ($\overline{U}_c$) is obtained by calculating the contribution from each deformation regime (elastic and plastic) separately and adding them together to obtain the total CSED. The material parameters used in the calculation of the CSED are depicted in Figure 2-10, which shows a schematic of the stress-strain curve for Zircaloy.

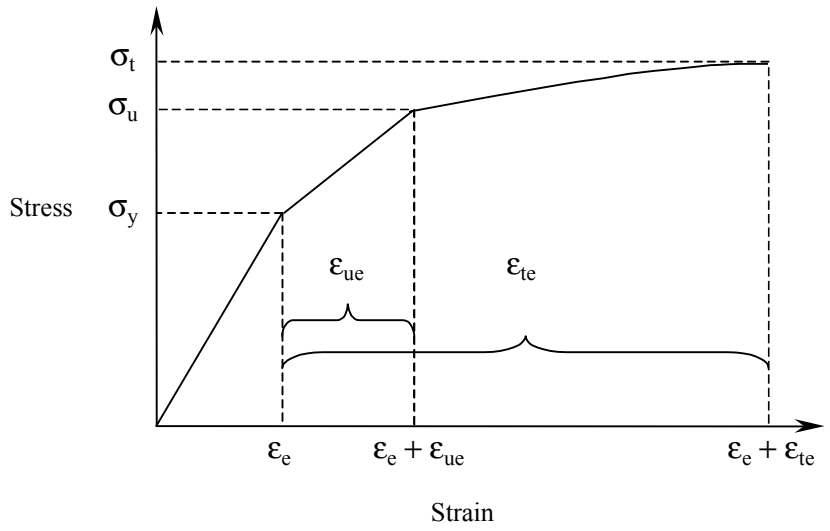

Figure 2-10
Schematic of the Stress-Strain Curve Illustrating CSED Calculations

The elastic strain energy component ($\varepsilon \leq \varepsilon_e$) is derived from Hooke's Law and is given by;

$$\overline{U}_e = \frac{\sigma_y^2}{2E} \tag{2-5}$$

where σ_y is the yield stress and E is Young's Modulus.

The calculation of the CSED in the plastic regime is based on the assumption that the material true stress-true strain curve can be represented by the following relationship from MATPRO [Hagrman1995]:

$$\sigma = K\varepsilon^{n}\left(\frac{\dot{\varepsilon}}{\dot{\varepsilon}_o}\right)^{m} \quad \text{for} \quad \varepsilon_e < \varepsilon < \varepsilon_e + \varepsilon_{te} \tag{2-6}$$

where σ is the true stress; ε is the true strain; $\dot{\varepsilon}$ is the strain rate; and K, n, and m are material constants obtained from MATPRO.

The total strain energy in the plastic regime ($\varepsilon > \varepsilon_e$) can be obtained by integrating eq. 2-6 between the elastic limit (ε_e) and the total elongation as shown in eq.2- 7.

$$\overline{U}_p = \int_{\varepsilon_e}^{\varepsilon_e+\varepsilon_{te}} K\varepsilon^{n}\left(\frac{\dot{\varepsilon}}{\dot{\varepsilon}_o}\right)^{m} d\varepsilon \tag{2-7}$$

This expression can be simplified by evaluating eq.2-6 at the elastic limit, which yields,

$$K\left(\frac{\dot{\varepsilon}}{\dot{\varepsilon}_o}\right)^{m} = \sigma_y^{1-n} E^{n} \tag{2-8}$$

Substituting eq. 2-8 into eq. 2-7, integrating and evaluating the result at the integration limits gives the plastic strain energy component as:

$$\overline{U}_p = \frac{\sigma_y^{1-n}E^{n}}{n+1}\left[(\varepsilon_e + \varepsilon_{te})^{n+1} - \varepsilon_e^{n+1}\right] \tag{2-9}$$

The total CSED is simply the sum of the elastic and plastic strain energy components, i.e.,

$$\overline{U}_c = \overline{U}_e + \overline{U}_p \tag{2-10}$$

2.3.2.3 Data Adjustment Factors

There are three important effects that must be considered before using the data from mechanical property tests to establish a CSED relation for irradiated Zircaloy cladding. These are material anisotropy, multiaxial stress-state, and strain rate effects.

Anisotropy: Irradiated Zircaloy exhibits significant reduction in anisotropy because of irradiation damage. Existing mechanical property data, obtained for temperatures below the level required to anneal irradiation damage, demonstrate that irradiated Zircaloy cladding exhibits isotropic or near-isotropic behavior [Murty and Mahmood 1991]. The effect of cladding anisotropy need be considered only when combining irradiated and unirradiated data.

Multiaxial Stress-State: PCMI-induced stresses are generally biaxial, a condition that needs to be accounted for in the CSED Model. Therefore, the total elongation values obtained from the uniaxial ring tension and axial tube tension tests were adjusted to account for biaxiality effects on ductility. The total elongation values from the uniaxial tests were reduced using an adjustment

factor developed based on material test data obtained by Koss and Andersson that show that effects of hydrogen content and stress ratio on total elongation [Fan and Koss 1985; Andersson and Wilson 1978].

The biaxiality adjustment factor used for the ring and axial tension data was developed from mechanical property tests reported by Koss on Zircaloy sheet material under different loading and hydrogen conditions. Figure 2-11 was used to develop a relationship between a strain reduction factor and hydrogen. It was assumed in the developing the adjustment factor that PCMI conditions are represented by a plane strain condition in the axial direction, i.e. $\varepsilon_z = 0$. The following relationship was developed from a numerical fit of the $\varepsilon_{2f} = 0$ data reported by Koss;

$$f_b = 0.33 \cdot e^{-.1.19x10^{-3} \cdot H_c} \tag{2-11}$$

where:

f_b is the biaxiality adjustment factor

H_c the average hydrogen content for the sample (ppm)

The adjusted total plastic strain for biaxial conditions is calculated using the following expression:

$$\varepsilon_c = \varepsilon_{uni} \cdot f_b$$

where

ε_c is the adjusted total plastic strain for biaxial conditions

ε_{uni} is the uniaxial total plastic strain measured in tube or ring tension tests

The adjusted strain values are used in the calculation for the CSED values and total elongation values, and are applied to transient PCMI conditions.

Strain Rate Effects: The rapid PCMI loading caused by RIA transients suggests that strain rate effects should be considered in the CSED development. High strain rates can reduce the ductility; however, the limited experimental data on irradiated Zircaloy above 288ºC show little effect of strain rate in the range observed in RIA tests. It should be mentioned, however, that the SED values calculated in FALCON using the MATPRO true-stress-true-strain equations are strain-rate dependent. This means that for the RIA events, where the strain rates are somewhat higher than the material property data used in the CSED correlation, FALCON calculates slightly higher SED values. Thus FALCON's predictions of RIA response would be conservative with respect to the CSED correlation.

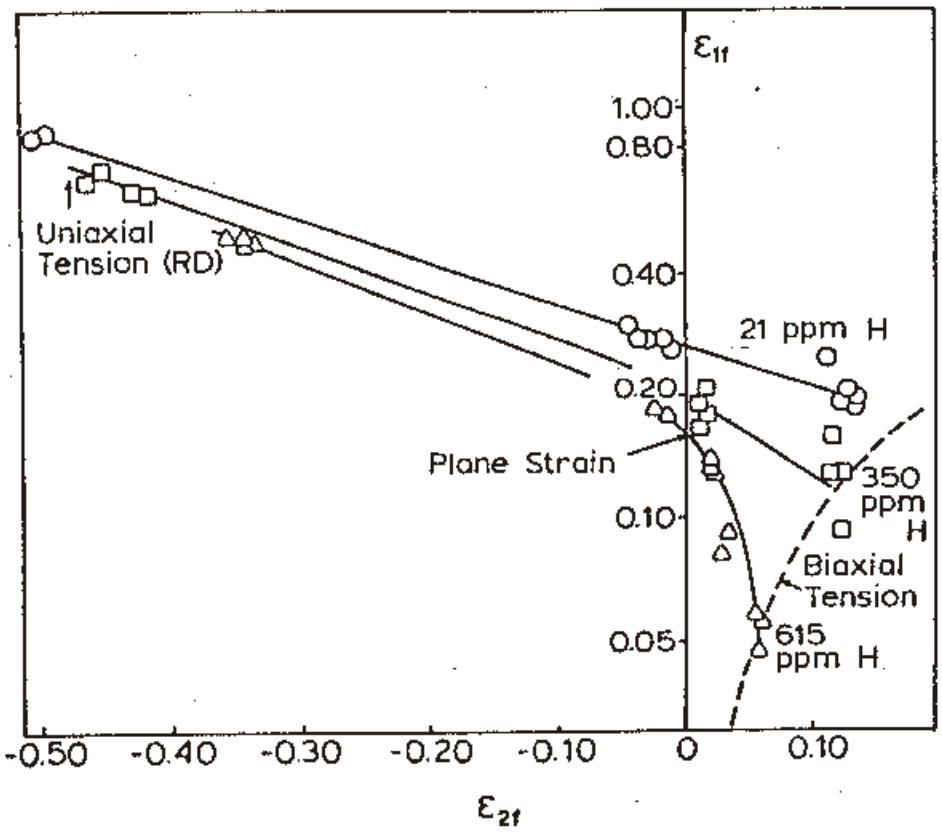

Figure 2-11
Zircaloy Sheet Ductility Data for Various Loading Conditions [Koss, et. al.]

2.3.2.4 CSED Correlation

The CSED correlation used as part of the cladding model for RIA events was determined from the results of the mechanical property tests as a function of temperature, fast fluence, and the hydrogen concentration, or alternatively the oxide thickness. For high burnup Zircaloy cladding, hydride content and distribution can have an important impact on the mechanical response. Hydrogen pickup from outer surface corrosion is the primary source of hydrogen in Zircaloy cladding. Consequently, the hydride content is generally proportional to the oxide layer thickness. In developing a CSED correlation for high burnup Zircaloy, the ratio of the sample oxide thickness to cladding thickness (R_{ox}) was used as the correlation parameter. By using this parameter to correlate the CSED results, it is possible to compare results for different initial cladding types, e.g. 14x14 vs. 17x17.

The CSED values from the mechanical property tests listed in Table 2-6 are shown in Figure 2-12 for temperatures above 280°C and in Figure 2-13 for temperatures below 150°C. The legend shown in Figure 2-12 designates which CSED values correspond with the axial tension tests, the uniaxial ring tension tests and the burst tests. A review of the data indicates that the CSED data

from the ring tension tests are generally larger than the burst and axial tension CSED data. The higher CSED values for the ring tension tests may be related to bending within the gauge section during the test, which will increase the measured total elongation for these specimens. Bending artifacts would be most notable in ductile samples. On the other hand, the CSED obtained from axial tension data generally reside below the ring and burst data. The CSED data from burst tests reside between the CSED values from ring and axial tension tests. All the different data sets display a decreasing trend as a function of R_{ox}. The data from samples with non-spalled oxide layers shown in Figure 2-12 does not show significant temperature dependence in the 280°C to 400°C range. However, only a limited number of tests were performed at the high temperature and insufficient data is available to fully quantify the effect of temperature on the CSED in the temperature range from 280°C to 400°C.

The CSED data obtained from mechanical property tests on samples with spalled oxide layers are indicated by the solid symbols. These data reside at R_{ox} values above 0.10 and the CSED values are generally below 10 MJ/m^3. As seen in Figure 2-11, the CSED data from samples with spalled oxide layers display a natural separation from the data with non-spalled oxide layers.

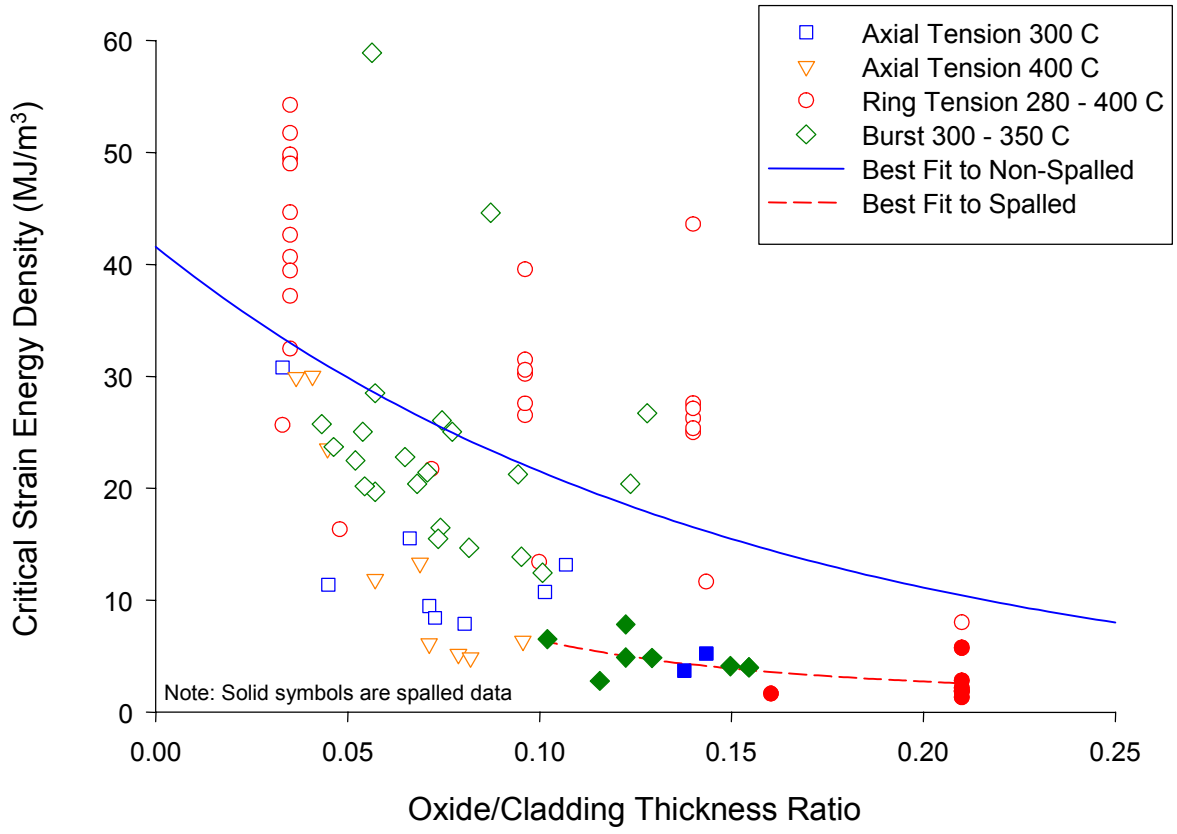

Figure 2-12
CSED data as a function of oxide-to-cladding thickness ratio developed from mechanical property tests at temperatures above 280°C on cladding irradiated to burnup levels between 50 and 65 GWd/tU. The data from samples with outer surface oxide spallation are indicated by the solid symbols. The best-fit correlations are shown for comparison.

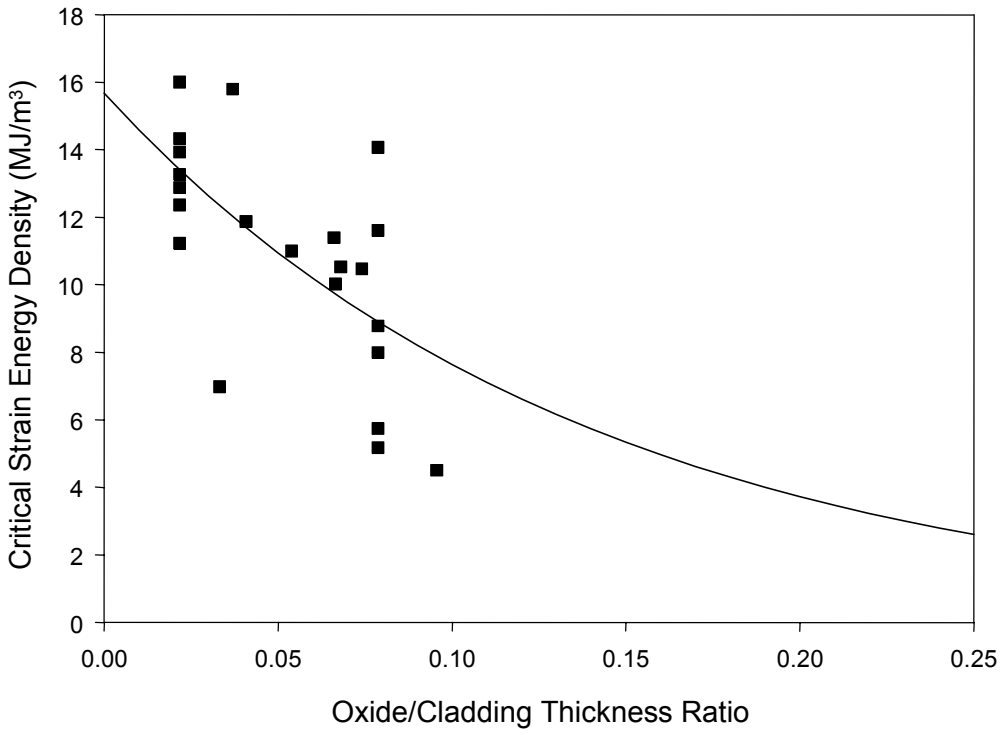

Figure 2-13
CSED data as a function of oxide-to-cladding thickness ratio developed from mechanical property tests at temperatures below 150°C on cladding irradiated to burnup levels between 50 and 65 GWd/tU. None of these data points were from cladding with spalled oxide layers. The best-fit correlations are shown for comparison.

A numerical fit to the data was conducted to develop a correlation between the CSED and oxide to thickness ratio (R_{ox}). To facilitate the fitting process, the data above 280°C were divided into two data sets that represent different material conditions: one for samples without oxide spallation and one for samples with oxide spallation. Best-fit curves were developed for each data set (non-spalled and spalled) by fitting to all the CSED data (ring, axial, burst) in each data set. For the CSED data from samples with non-spalled oxide layers, an exponential expression was used to obtain the functional form of CSED correlation. An exponential functional dependence was selected to allow for saturation of the CSED to a low, non-zero value when extrapolated to high R_{ox} values. Because the data from samples with spalled oxide thickness layers displays less of a dependence on R_{ox}, a power law was used to develop the CSED correlation.

The resulting numerical fits for the CSED of non-spalled and spalled cladding at temperatures above 280°C are:

For non-spalled cladding,

$$\overline{U_c} = 41.5 \cdot e^{-6.6 \cdot R_{ox}} \text{ with } 0.03 < R_{ox} < 0.23 \qquad (2\text{-}12)$$

For spalled cladding,

$$\overline{U}_c = 0.371 \cdot R_{ox}^{-1.24} \text{ with } 0.1 < R_{ox} < 0.23 \quad (2\text{-}13)$$

where

$\overline{U}_c$ is the critical strain energy density (MJ/m^3)

R_{ox} is the ratio of the outer surface zirconium oxide layer thickness to cladding thickness (unitless)

For non-spalled cladding loaded below 150°C, the CSED correlation is given by;

$$U_c = 15.67 \cdot e^{-7.19 \cdot R_{ox}} \quad (2\text{-}14)$$

Equations 2-12 through 2-14 represent best-fit correlations to all CSED values in each data set and the CSED data is scattered about these curves. As can be seen in Figures 2-12 and 2-13, the scatter in the data is large and is attributable to the variability in the material condition for irradiated cladding, test conditions such as temperature and loading direction, and sample artifacts such as bending within the gauge section. Unfortunately for irradiated material, this level of scatter is inherent to the data and improvements in future tests are needed to eliminate some of these sources of scatter. An attempt has been made to address data scatter caused by outer surface oxide spallation by separating the data into spalled and non-spalled specimens. As seen in Figure 2-12, the data show a natural separation in the CSED values between the data from non-spalled specimens and spalled specimens.

As a means to evaluate the influence of the data scatter within the non-spalled CSED data set on the best-fit correlation, two additional numerical fits were performed: a best-fit to the non-spalled CSED data from the tube burst tests and a lower bound fit to the non-spalled CSED data from the tube burst and ring tension tests. Tube burst tests and ring tension tests yield hoop direction mechanical properties. Since PCMI loading is primarily oriented in the hoop direction, it can be argued that ring and tube burst mechanical tests are more applicable to PCMI loading conditions. Furthermore, the burst test CSED data displays the least amount of data scatter and also represents the mechanical properties in the hoop direction under biaxial stress conditions. Unfortunately, the amount of data available for tube burst tests is limited making it more difficult to use this data to develop a versatile CSED model that can be applied to transient fuel rod analysis and data interpretation.

A comparison of the correlation in Equation 2-12 and the two alternative fits is shown in Figure 2-14. The lower bound fit to the non-spalled tube burst and ring tension CSED data is well below the best-fit Equation 2-12 or the best fit of the tube burst data. This correlation accounts for the lower bound scatter of the data and represents a conservative measure of cladding failure.

As seen in Figure 2-14, the best fit to the non-spalled tube burst data deviates only slightly from the best-fit to all the non-spalled data (Equation 2-12). The largest difference occurs at low

oxide thickness layers ($R_{ox} < 0.1$). For these conditions, the ductility exhibited by the ring tension tests is larger than that for the tube burst tests, even after the biaxiality correction factor is applied to the ring tension data. This could be caused by the influence of sample bending in the ring tension tests. However, at R_{ox} values greater than 0.1, very little difference exists between the two correlations. Such comparison supports the approach used to develop the correlation given by Equation 2-12.

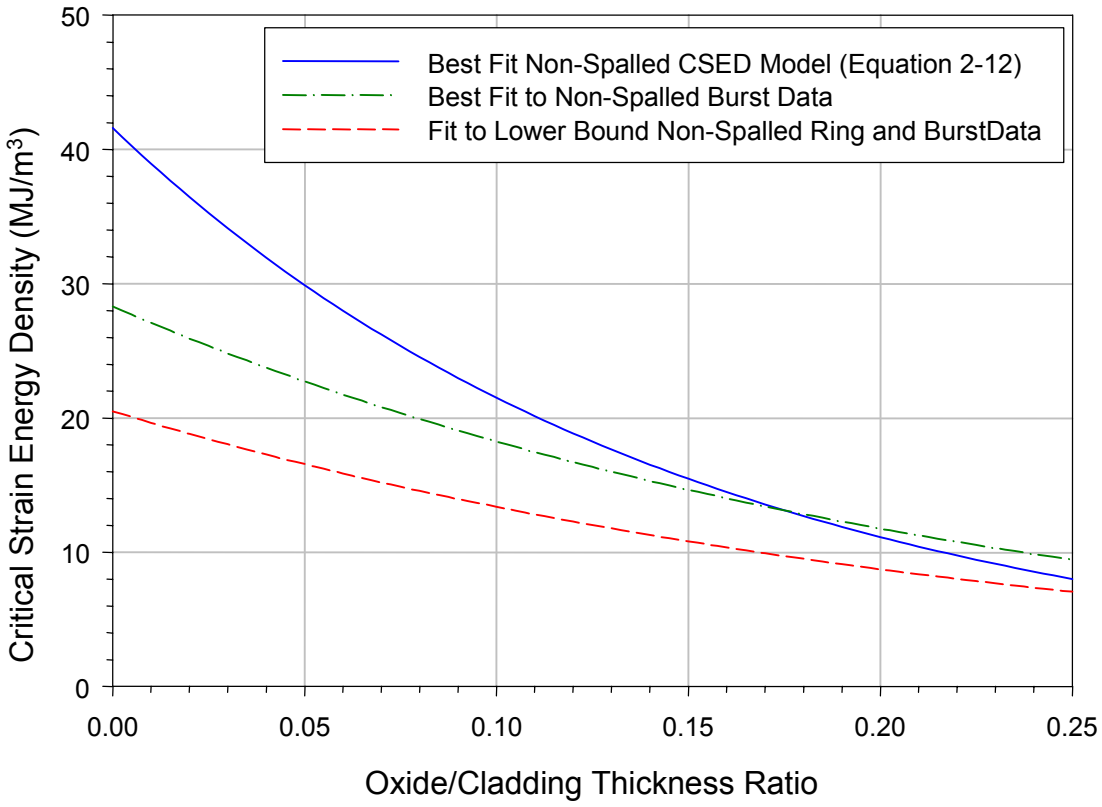

Figure 2-14
Comparison of the Best-Fit CSED model (T > 280°C) developed using all the data from tests on non-spalled oxide samples (Equation 2-12) with two alternative fits developed using the data from the tube burst and ring tension tests on non-spalled oxide cladding samples.

2.3.2.5 Total and Uniform Elongation Models

To compare the SED/CSED approach with other strain-based criteria, cladding integrity models based on the total elongation (TE) and uniform elongation (UE) strains have been developed from the same material property data used for the CSED correlation. In the case of the TE strain, the biaxiality adjustment factor shown in Equation 2-11 was applied to the data from uniaxial ring and axial tension tests. The elastic strain obtained from the elastic modulus and the yield stress was added to the total and uniform plastic strain values measured in the mechanical property tests. The TE strain data is shown in Figure 2-15 and the UE data is shown in Figure 2-16 as a function of the oxide-to-thickness ratio. The data from samples with spalled oxide layers has been separated from the non-spalled data for clarification. Also shown for comparison are

the correlations from the data fit exercise. As can be seen, the trend with oxide thickness is similar to the CSED correlation. The data scatter is equal to or greater than that for the CSED data shown in Figures 2-12 and 2-13. The ability of these models to separate failures from non-failed RIA-simulation tests is discussed in Section 2.4.3.

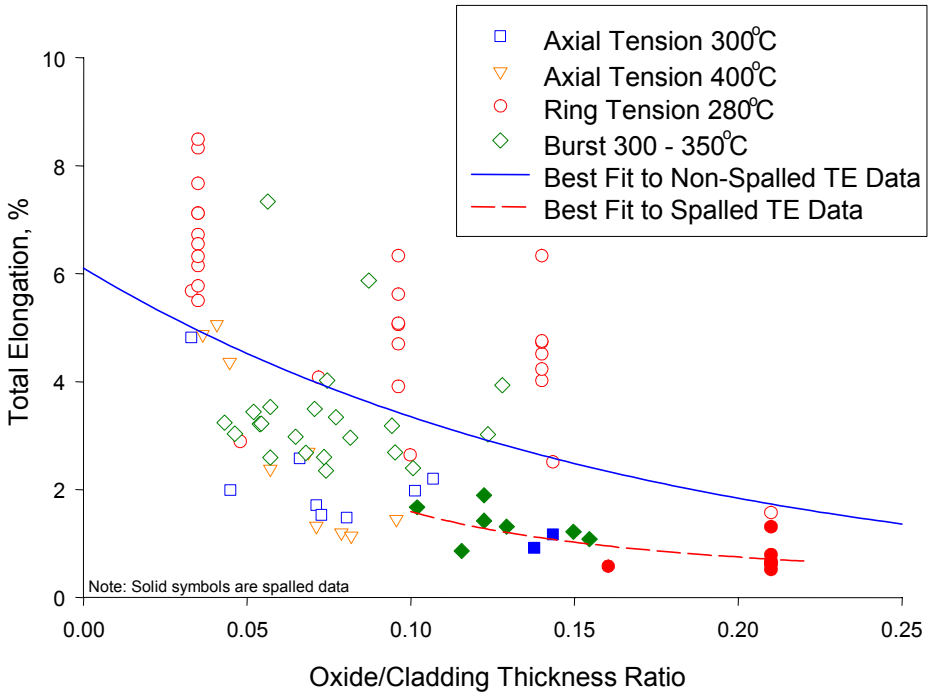

Figure 2-15
Total elongation (TE) data as a function of oxide-to-cladding thickness ratio developed from mechanical property tests on irradiated cladding at temperatures above 280°C. The data from samples with outer surface oxide spallation are indicated by the solid symbols. The best-fit correlations are shown for comparison.

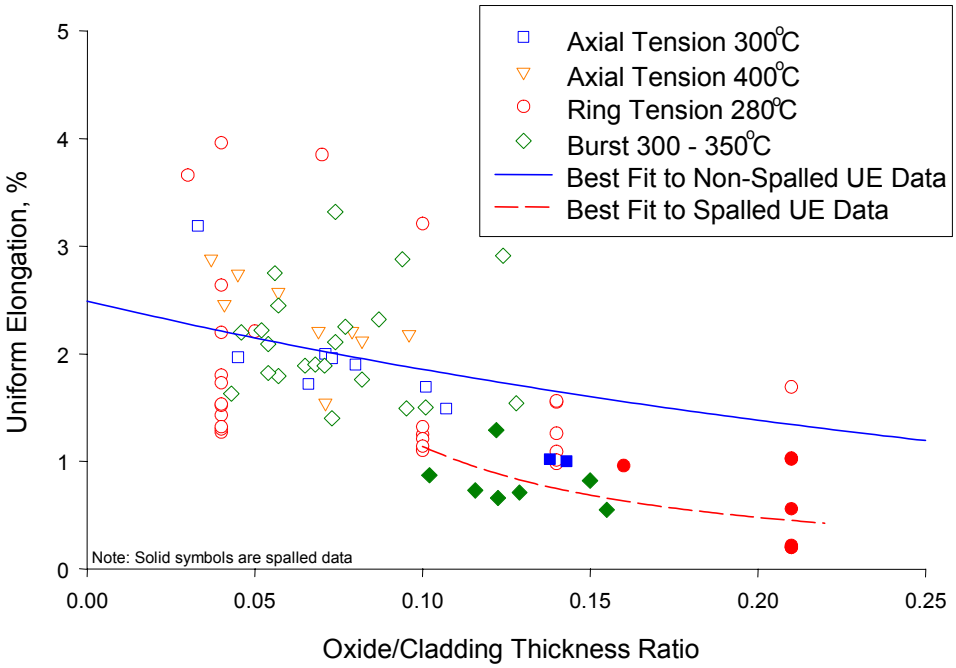

Figure 2-16
Uniform elongation (UE) data as a function of oxide-to-cladding thickness ratio developed from mechanical property tests on irradiated cladding at temperatures above 280°C. The data from samples with outer surface oxide spallation are indicated by the solid symbols. The best-fit correlations are shown for comparison.

2.3.2.6 Summary

A cladding failure model applicable to PCMI conditions under operational and accident transients has been developed for irradiated Zircaloy cladding based on the strain energy density (SED) concept. The SED/CSED model is derived from the J-integral methodology used in fracture mechanics evaluations, by establishing exact equivalence between SED and J, and CSED and J_c. It allows for the treatment of damaged material without explicitly modeling local defects or performing fracture mechanics analysis. A critical strain energy density (CSED), which defines the material limit for mechanical loading, was developed as a function of temperature and outer surface oxide layer thickness from mechanical property tests conducted on irradiated Zircaloy cladding. An important aspect of this approach is the fact that the mechanical property data used to derive the CSED includes material that contains incipient hydride and irradiation damage similar to that present in irradiated cladding.

2.4 Analysis of RIA-Simulation Experiments

Detailed fuel behavior analyses were performed for key RIA-simulation experiments using the EPRI fuel behavior code FALCON [Montgomery and Rashid 1996; Yang et al. 2000]. The objectives of these analyses can be separated into three different goals. First, these analyses were used to assist in the interpretation of the experimental results by providing insights into the

thermal and mechanical performance of the fuel and cladding. From the results of these analyses, it was possible to assess the evolution of cladding stresses and temperatures to determine the cladding state at the time of peak stress. Second, it was possible to demonstrate that the mechanisms important for understanding fuel behavior have been identified through comparison of the calculated results with the experimental observations and post-test examination results. The FALCON analyses of RIA experiments assisted in separating the effects of cladding ductility and fission gas swelling on the fuel behavior exhibited in the experiments. Third, these analyses were used to validate the analysis capabilities of FALCON.

2.4.1 FALCON Description

FALCON is a two-dimensional transient fuel behavior program developed to analyze the response of LWR fuel rods during RIA, LOCA and other transient conditions [Montgomery et al. 1997b]. FALCON, which is an improved version of FREY [Rashid et al. 1994], utilizes a coupled thermal and mechanical finite element methodology to represent the transient behavior of the fuel column, cladding, and gap. A complete fuel pellet mechanical constitutive model is used that includes pellet cracking, creep, plasticity, and thermal expansion. The effects of burnup and fast neutron fluence are included in the thermal and mechanical properties of the fuel and cladding, as well as, on the radial power distribution. Recently, modifications have been incorporated into FALCON to calculate the sodium coolant temperature heatup during the CABRI experiments. Earlier analyses used estimated heat transfer coefficients and coolant temperatures to model the fuel-sodium heat transfer.

At this time, FALCON does not include a gaseous swelling model in the high burnup rim region for rapid transients such as an RIA. It has been postulated by some that an additional rapid pellet expansion process exists that is driven by the large inventory of fission gas resident in the pellet periphery [Lemoine, 1997, Papin, 1996]. However, evidence supporting the potential for rapid gas bubble expansion in the rim region has not been found in post-test examinations of high burnup test rods such REP Na-4 and REP Na-5 [Lespiaux et al 1997]. Furthermore, validation of FALCON using RIA test results from UO_2 fuel rods demonstrates that pellet thermal expansion is the primary driving force for PCMI during rapid power deposition [Montgomery 1996a].

2.4.2 FALCON Validation for RIA Analysis

The RIA-simulation tests analyzed with FALCON are summarized in Table 2-7. The tests selected for the FALCON validation include tests conducted in the CABRI sodium loop at an initial temperature of 290ºC and the NSRR test capsule with 25ºC stagnant water. Tests with both narrow and wide pulses were selected to evaluate the influence of pulse width on the test rod response. Sodium temperature thermocouple measurements, in-pile cladding axial elongation and residual cladding hoop strains have been used to validate the FALCON capabilities for RIA analyses.

Table 2-7
RIA-Simulation Tests used in the FALCON Validation

Test	Peak Pellet Burnup (GWd/tU)	Oxide Layer (microns)	Fuel Type	Pulse Width (msec)	Maximum Radial Average Fuel Enthalpy (cal/gm)	Fuel Enthalpy at Failure (cal/gm)
CABRI REP Tests in 280°C Sodium at 0.5 MPa						
Na-1	65	>80 – spall	17x17	9.5	115	30
Na-2	33	10	17x17	9.5	220	
Na-3	52	50	17x17	9.5	138	
Na-4	62	85	17x17	70	81	
Na-5	64	20	17x17	9.1	113	
Na-8	60	120 - spall	17x17	78	105	83
Na-10	64	>80 - spall	17x17	31	112	79
NSRR PWR and BWR Tests in 25°C Water at 0.1 MPa						
HBO-1	50	40-50	17x17	4.4	73	60
HBO-2	50	30-40	17x17	6.9	37	
HBO-3	50	22	17x17	4.4	74	
HBO-4	50	18	17x17	5.4	50	
HBO-5	44	35-60	17x17	4.4	80	77
HBO-6	49	20-30	17x17	4.4	88	
TK-1	38	7	17x17	4.4	125	
TK-2	48	15-35	17x17	4.4	107	60
TK-4	50	20	17x17	4.4	98	
FK-1	45	20-40	8x8BJ	4.4	130	
FK-2	45	20-40	8x8BJ	5.3	70	
FK-4	56	~20	8x8	4.4	140	
FK-5	56	~20	8x8	7.3	70	
FK-6	61	~25	8x8	4.3	131	70
FK-7	61	~25	8x8	4.3	129	62
FK-8	61	~25	8x8	7.3	65	
FK-9	61	~25	8x8	5.7	90	86

A comparison of the CABRI REP Na-4 thermocouple response within the sodium coolant at 48 cm (near the top of the fuel stack) and the calculated sodium temperature at different locations in the FALCON model is shown in Figure 2-17. The peak sodium temperature measured by the two thermocouples located 120º azimuthally apart varied from 373ºC to 396ºC. The calculated sodium temperatures at 46 cm reached a peak of 383º C and the calculated sodium temperatures at 52 cm reached a peak at 388º C. The calculated results are within the scatter of the in-pile measurements.

The cladding axial elongation response measured using an in-pile LVDT device is shown in Figure 2-18 for CABRI REP Na-4. Also shown for comparison is the calculated cladding elongation. FALCON calculates a slightly lower peak cladding elongation (3.7 mm versus 4.2 mm), however, the calculated cladding elongation response is consistent with the overall trend in the cladding elongation measurements after the power pulse. The difference between the measured and calculated peak cladding elongation is 13% and is related to differences in the power pulse and axial power distribution used in the analysis and the actual experimental conditions.

A comparison of the calculated and measured permanent cladding radial displacements for REP Na-5 is shown in Figure 2-19 as a function of axial position. Two different azimuthal traces are shown to indicate the variation in the measured data. The calculated results reside in the mid-range of the experimental measurements in the peak power location. FALCON has a tendency to calculate slightly higher cladding radial displacements at the ends of the test specimen. This could be due to uncertainty in the axial power shape used in the analysis.

Figures 2-20 and 2-21 show a comparison between the measured and predicted residual cladding hoop strains (Figure 2-20) for the CABRI REP Na tests and the measured and predicted cladding and fuel axial elongation for the CABRI and NSRR tests analyzed with FALCON (Figure 2-21). The calculated and measured cladding hoop strain results shown in Figure 2-20 represent the mid-pellet strain at the maximum power location. The error bars shown in Figure 2-20 indicate the variation in the measured data based on the measurement uncertainty. Since most of the datapoints reside near the perfect agreement line (solid line), it can be concluded the FALCON calculates well the cladding radial and axial deformations.

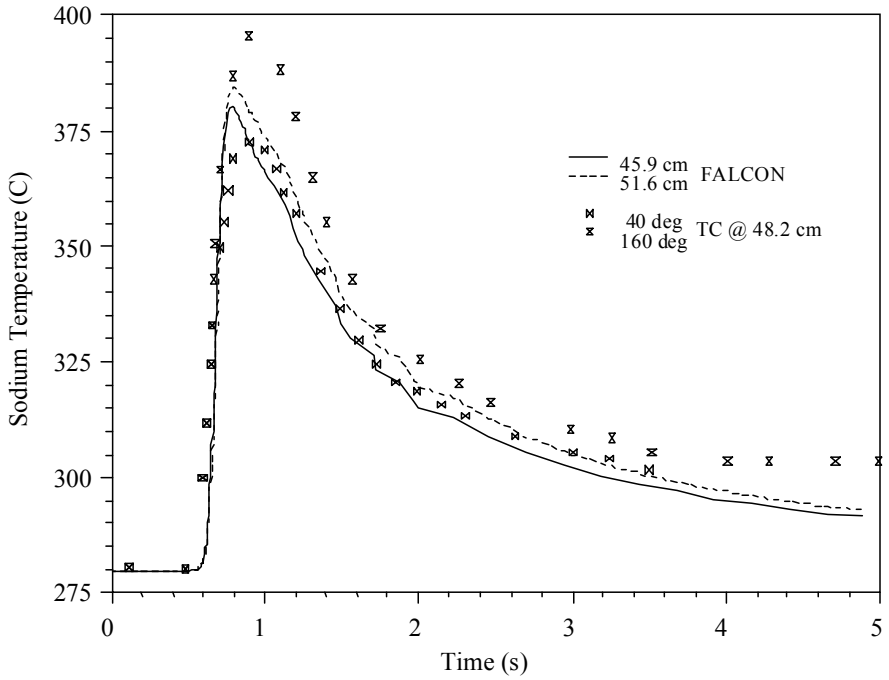

Figure 2-17
Sodium Coolant Temperature during CABRI REP Na-4

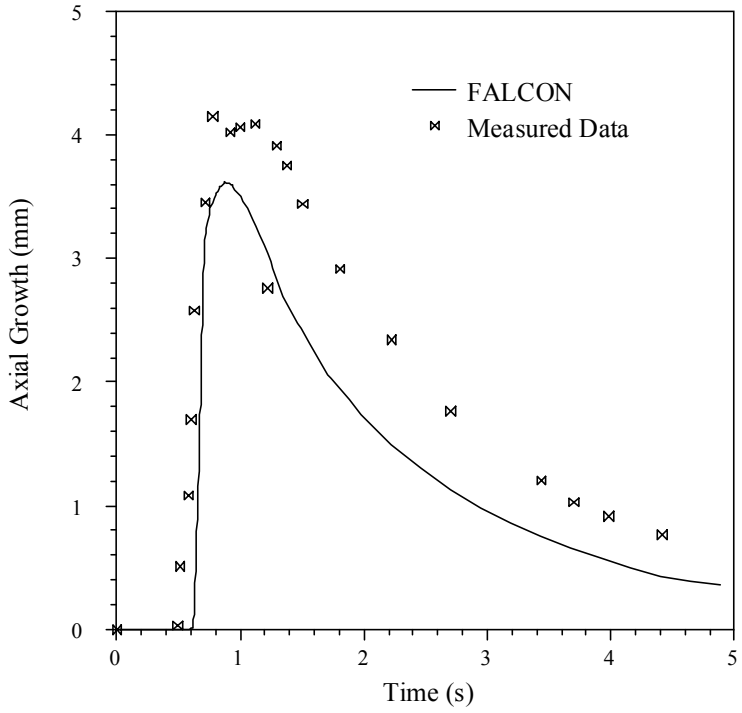

Figure 2-18
FALCON Results and Measured Data for the Time History of the Cladding Axial Elongation in CABRI REP Na-4

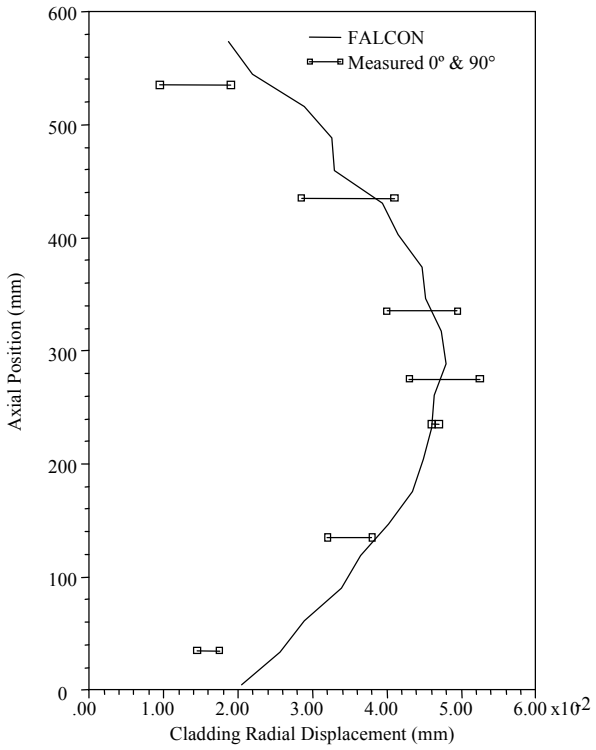

Figure 2-19
Comparison of FALCON and Measured Residual Cladding Radial Displacements for CABRI REP Na-5

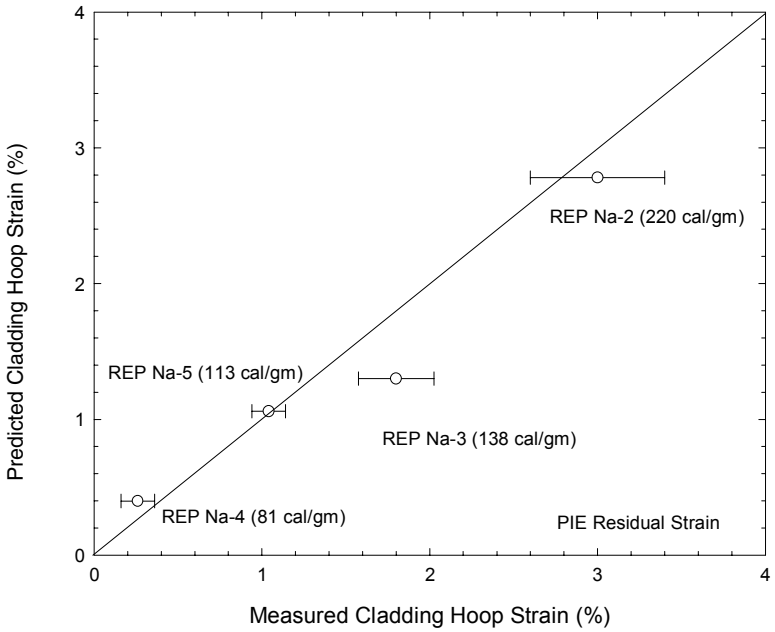

Figure 2-20
Predicted versus Measured Residual Cladding Hoop Strain for Selected CABRI REP Na Tests

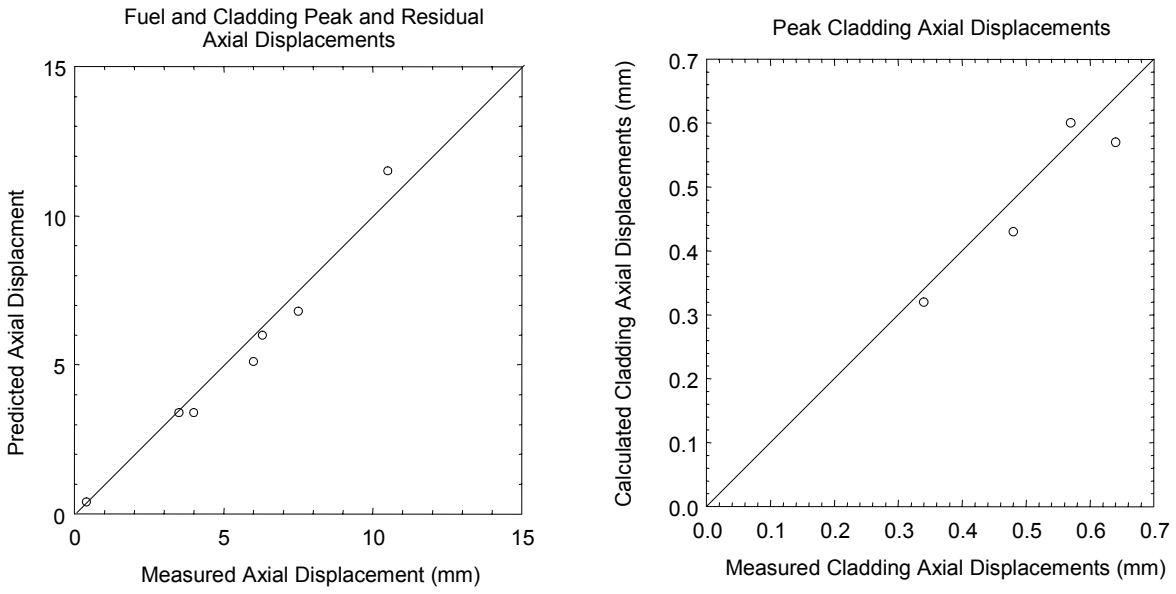

CABRI REP Na Tests

NSRR HBO and JM Tests

Figure 2-21
Predicted versus Measured Peak and Residual Axial Displacements for Selected CABRI REP Na and NSRR tests

2.4.3 Cladding Failure Analysis

The cladding failure evaluation performed within FALCON is based on the CSED/SED approach presented in Section 2.3.2. In this approach, cladding mechanical properties are used to develop the critical strain energy density (CSED) required to initiate material failure from mechanical property tests on irradiated Zircaloy cladding. As summarized in Section 2.3.2.2, the CSED is represented as a function of the material condition, temperature, and loading state. FALCON is then used to calculate the evolution of the strain energy density (SED) within the cladding as a function of cladding stress-state and temperature. An increase in the potential for cladding failure is assumed to occur at the point where the FALCON calculated SED exceeds the CSED for the given cladding condition defined by temperature and oxide thickness.

The SED throughout the cladding is calculated during the PCMI phase for each RIA-simulation test analyzed with FALCON. The SED model in FALCON performs a summation of the product of the stress and strain increment for the three coordinate stresses and strains (radial, axial, and hoop) at every location in the cladding. This quantity is then integrated over the time of the transient to provide the SED (U(t)) as a function of time, ie.;

$$U(t) = \int_0^t \left[\sum \sigma_i \cdot \Delta\varepsilon_i , i = r, \theta, z \right] dt \qquad (2\text{-}14)$$

The maximum calculated SED from Equation 2-14 at the time corresponding to the end of the power pulse or the time of cladding failure determined by in-pile instrumentation is shown in Figure 2-22 for the sodium tests (T > 280°C) and Figure 2-23 for the stagnant water tests (T < 150°C). Also shown for comparison are the appropriate best-fit CSED curves from Figure 2-12 (Equation 2-12) and Figure 2-13 (Equation 2-13) presented in Section 2.3.2. Equation 2-12 represents a best-fit to all the non-spalled CSED data and Equation 2-13 represents a best-fit to all the spalled CSED data. In addition, two alternative non-spalled CSED correlations were developed in Section 2.3 and these correlations are also shown in Figure 2-22 for comparison.

The tests in sodium coolant on rods with non-spalled oxide layers lie below the best-fit CSED curve for non-spalled cladding (Equation 2-12), indicating a low potential for cladding failure. No tests at 300°C using UO_2 rods with non-spalled oxide layers have failed in the CABRI sodium loop. However, the two tests on rods with spalled oxide layers (REP Na-8 and Na-10) reside either on or above the best CSED curve for spalled cladding (Equation 2-12), indicating a high potential for cladding failure. As indicated in the figure (solid symbols), REP Na-8 and REP Na-10 were identified to have experienced cladding failure during the power pulse by in-pile instrumentation and post-test examinations. These results indicate that the presence of significant oxide layer spalling and corresponding localized hydride formation has embrittled the cladding sufficiently to cause cladding failure by PCMI under RIA conditions.

The two alternative CSED fits discussed in Section 2.3 are also shown in Figure 2-22. Both of these curves are only applicable to RIA tests using test rods with non-spalled oxide layers. The lower bound curve does not adequately differentiate between the failed and non-failed rods for the CABRI REP Na tests using UO_2 fuel rods. As shown in Figure 2-22, the lower bound CSED curve predicts that REP Na-2 and REP Na-3 would have failed in the CABRI tests when compared to the calculated SED values for the REP Na experiments. Neither of these rods showed any indication of cladding failure during the experiment or in post-test examinations. Based on these observations, the lower bound CSED correlation does not adequately differentiate between failed and non-failed UO_2 rods tested in the CABRI REP Na program. As a result, this CSED correlation does not represent an alternative to Equation 2-12.

The best-fit of the non-spalled tube burst CSED data resides at the upper boundary of the non-failed CABRI REP Na tests on UO_2 rods. This curve represents an envelope of success based on the CABRI REP Na tests and could serve as an optional lower bound alternative to the Equation 2-12.

Similarly in Figure 2-23, the SED results for the NSRR tests that did not fail reside below the CSED curve for low temperature conditions. It should be noted that the NSRR tests shown in Figure 2-23 are PWR rods because the CSED curve is only applicable to PWR rods tested in NSRR. Tests that experienced failure or contained micro-cracks in the outer region of the cladding reside near or above the CSED curve. Based on these results, the coupled FALCON/SED model displays a reasonable level of success in separating failed and non-failed tests using a CSED limit developed from cladding mechanical property tests on irradiated cladding.

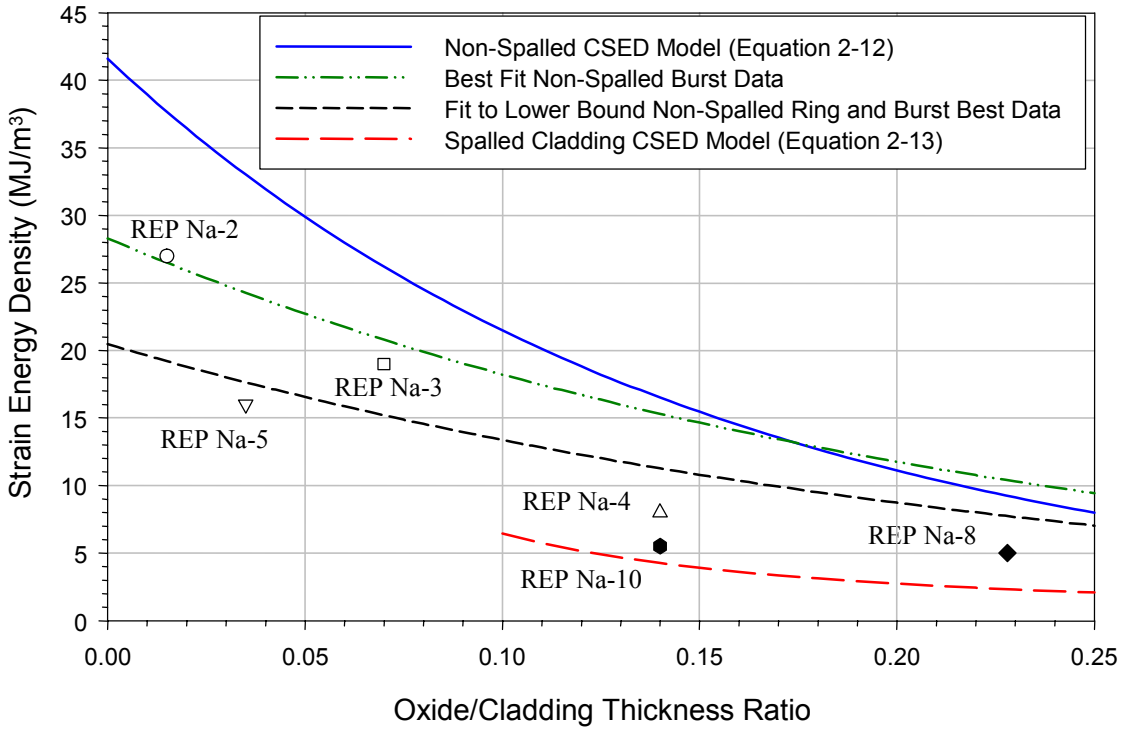

Figure 2-22
Strain energy density results calculated by FALCON for the CABRI REP Na UO_2 test rods. The non-spalled and spalled CSED models for temperatures greater than 280°C are also shown for comparison.

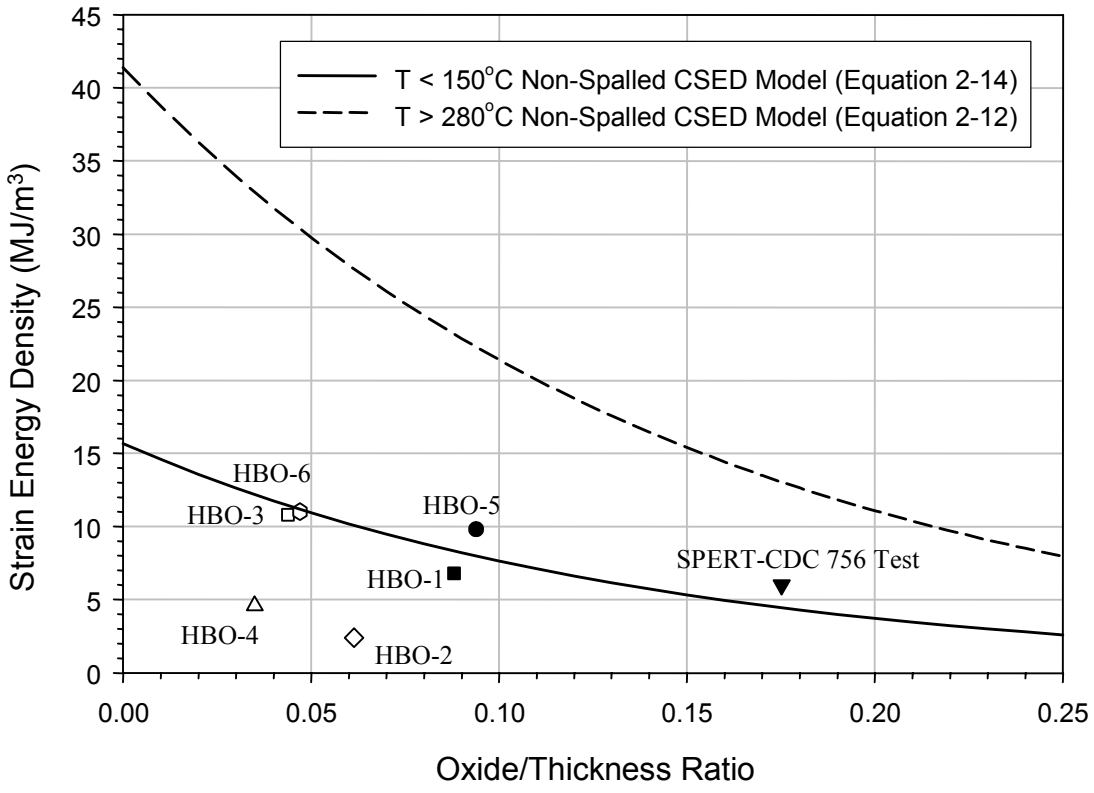

Figure 2-23
Strain Energy Density Results Calculated by FALCON for Selected NSRR Test Rods. The CSED models for non-spalled cladding at T < 150°C and T > 280°C are shown for comparison. It should be noted that part-wall cracks were observed in HBO-3 and HBO-6 in post-test examinations.

Two other methods to develop a cladding integrity model based on cladding strain limits have been evaluated using the FALCON analysis. As discussed in Section 2.3.2, failure curves based on a numerical fit of the total elongation data and uniform elongation data have been constructed from mechanical property tests performed at temperatures above 300°C. These failure curves were compared to the maximum cladding hoop strain calculated by FALCON for the CABRI REP Na tests summarized in Table 2-6. The results of the comparison are shown in Figure 2-24 for the total elongation limit and Figure 2-25 for the uniform elongation limit. For the total elongation curve, the maximum cladding hoop strains calculated by FALCON are below the curves for both unspalled and spalled cladding. Using the total elongation as a basis for developing a cladding integrity model does not separate between the non-failures and failures. In the case of the uniform elongation limit, REP Na-3 is predicted to fail using the non-spalled curve. Only REP Na-8 is predicted to fail using the spalled curve. REP Na-10 resides below the failure limit based on the uniform elongation for spalled cladding. The inability of using the either the total elongation or uniform elongation to predict cladding failure arises from two issues. First, the total elongation overestimates the capacity of the cladding to withstand the PCMI loading because of biaxiality effects. Even though the total elongation data have been corrected using a biaxiality correction factor, this correction factor is not consistent with the PCMI biaxial stress conditions calculated by FALCON. These differences diminish when the mechanical property data are formulated in terms of critical strain energy density values.

Second, the uniform elongation does not necessarily represent a failure limit for displacement control loading conditions, especially for material with some level of ductility. These results further support the coupled FALCON/SED approach for use in predicting cladding failure during the analysis of RIA-simulation experiments.

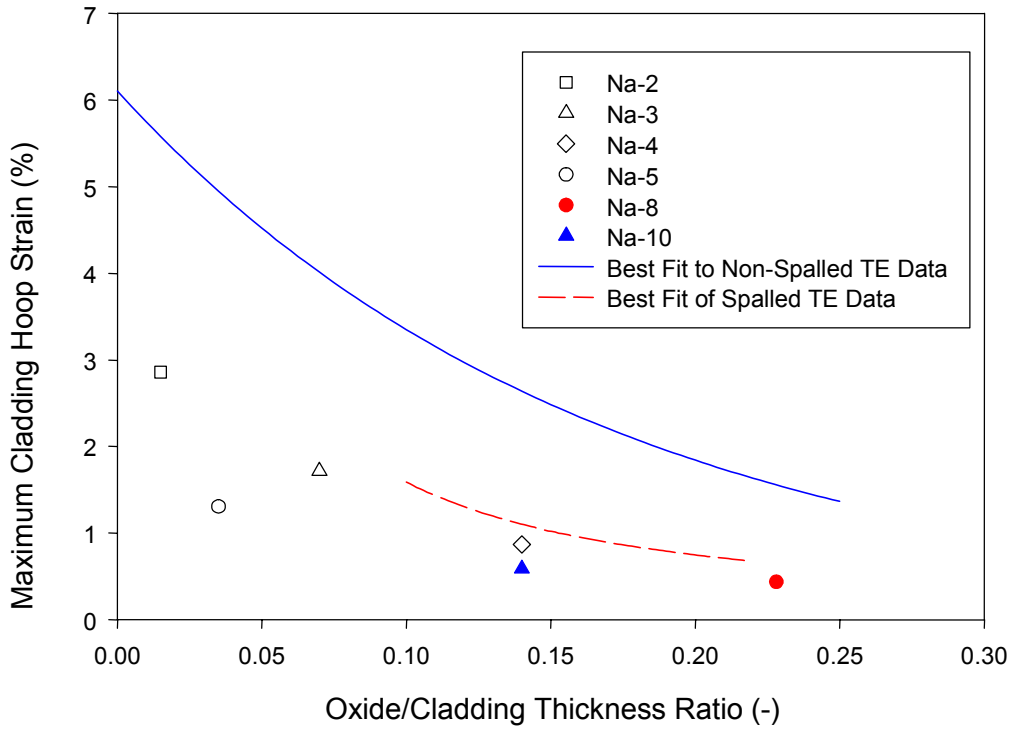

Figure 2-24
Maximum cladding hoop strain calculated by FALCON for the CABRI REP Na tests. Total elongation (TE) limit curves for spalled and non-spalled cladding are shown for comparison.

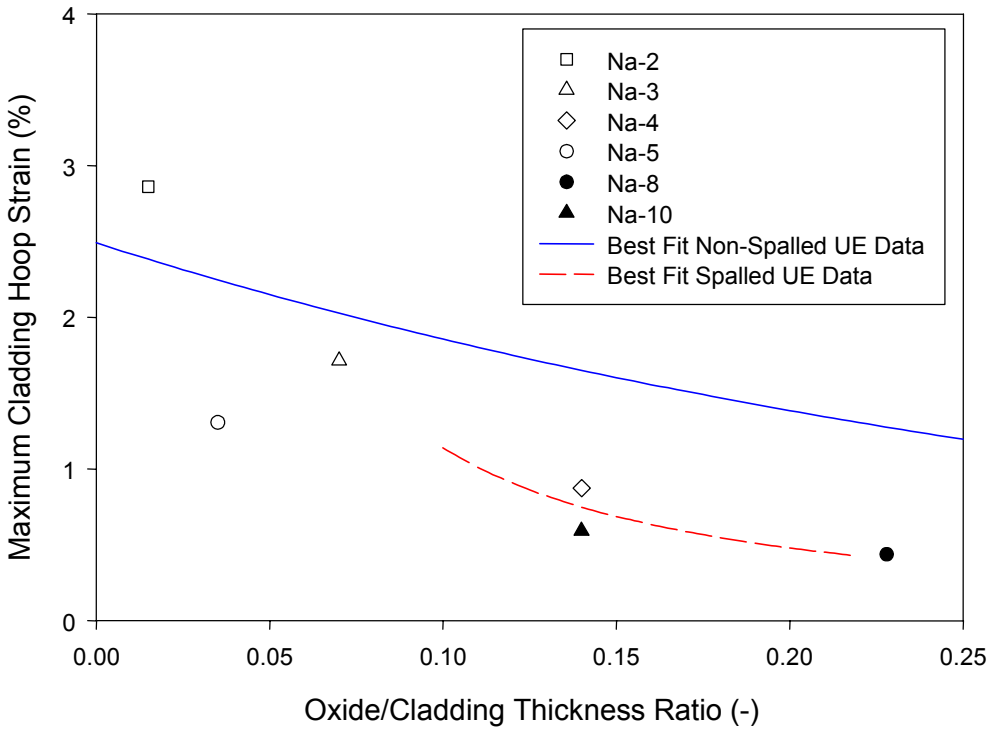

Figure 2-25
Maximum cladding hoop strain calculated by FALCON for the CABRI REP Na tests. Uniform elongation (UE) limit curves for spalled and non-spalled cladding are shown for comparison.

2.4.4 Summary

These results demonstrate the capability of FALCON to conservatively model the complex thermal and mechanical behavior of high burnup fuel during rapid energy depositions corresponding to a RIA event. As summarized in Table 2-7, the validation of FALCON for RIA analyses includes pulse widths between 4 milliseconds and 60 milliseconds, both 20°C and 300°C coolant temperature conditions, and different fuel rod types.

Analysis of the CABRI and NSRR tests find that an analytical translation is required to correct for the variation in the initial coolant temperature before a comparison of the fuel enthalpy levels is performed. The FALCON methodology provides for this translation through the calculation of the cladding SED response, and combined with CSED at the appropriate temperature condition, establishes a basis for a comparison. Furthermore, the analytical evaluation suggests that the CABRI tests performed in high temperature sodium represent well the PCMI phase of a postulated in-reactor RIA event and require only limited analysis to translate the results to PWR conditions. On the other hand, the NSRR tests conducted in room temperature stagnant water and under extremely narrow power pulses require analytical translation to PWR conditions before the results can be used to evaluate the fuel rod failure licensing bases.

3
RIA FUEL ROD FAILURE THRESHOLD

Section 3 summarizes the technical bases for revisions to the RIA fuel rod failure threshold described in NUREG-0800 Standard Review Plan Section 4.2 and Regulatory Guide 1.77 to incorporate the effects of burnup [NRC 1981; AEC 1974]. The revisions are developed for the failure threshold used in zero power reactivity events in both a PWR and BWR. These events include the hot-zero power control rod ejection accident in a PWR and the hot-zero power control rod drop accident in a BWR. For at-power events in both a PWR and BWR, the use of DNB for the fuel rod failure threshold should continue to be used in licensing analyses.

Section 3 begins with a summary of the current understanding of the fuel rod failure mechanisms active during zero-power reactivity accidents, including both high temperature post-DNB failure and PCMI-induced failure. The summary focuses on the influence of burnup or burnup related processes on the mechanisms that lead to fuel rod failure during or following a reactivity-initiated power pulse.

Section 3 also presents a description of the methodology and approach used to develop the revised fuel rod failure threshold as a function of burnup. A total of three different fuel rod designs were used in the approach to develop the failure threshold. A generic fuel rod failure threshold is presented that represents the lower bound of the different fuel designs. The fuel rod failure threshold is defined in terms of the radial average fuel peak enthalpy as a function of rod average burnup and is applicable to 75 GWd/MTU.

3.1 Current Understanding of Failure Mechanisms

RIA-simulation experiments conducted in the 1960's and 1970's using zero or low burnup test rods have shown that cladding failure at low burnup occurs primarily by either thermal quench following excessive cladding temperatures caused by post-DNB operation or by cladding contact with molten fuel [Martison and Johnson 1968; Miller and Lussie 1969; Zimmermann et al. 1979]. These observations formed the basis for the current failure threshold of DNB used for PWR control rod ejection accident analyses or a peak radial average fuel enthalpy of 170 cal/gm used for BWR control rod drop accident analyses. However, a transition from cladding failure dominated by high cladding temperatures to cladding failure by PCMI is observed in recent RIA-simulation tests at burnup levels beyond 30 GWd/tU (See Section 2). Beyond 30 GWd/MTU, the fuel-cladding gap thickness has decreased such that contact is initiated between the fuel and cladding during the power pulse. As a result, failure by PCMI is possible prior to DNB because heat conduction from the pellet is required to produce sufficient surface heat fluxes to exceed the critical heat flux. This heat conduction generally takes place after the pulse (for pulse widths less than 20 milliseconds), whereas, the PCMI loading happens during the power pulse.

Detailed examination of the results from RIA-simulation experiments on irradiated test rods has revealed that, while the level of PCMI loading from the fuel pellet thermal expansion and fuel matrix fission gas swelling can depend on burnup, the actual mechanisms leading to cladding failure are more related to cladding ductility [Montgomery and Rashid 1996; Yang et al. 2000, Montgomery et al. 1996]. Mechanical properties tests have shown that the ductility of irradiated cladding is mainly a function of the fast neutron damage, the hydrogen concentration and distribution, the temperature and the loading conditions (strain rate and biaxiality) [Garde 1989, Garde et al. 1996]. As a consequence, the cladding failure response of irradiated fuel during a RIA event is less dependent on burnup and more dependent on the operating environment such as the power level, irradiation time, and coolant temperature and the cladding corrosion characteristics. This is supported by the CABRI database on LWR UO_2 test rods which shows that no cladding failure has occurred up to 64 GWd/tU for rods with non-spalled oxide layers up to 80 microns.

Based on these observations from RIA experiments, the cladding failure mechanisms active during a reactivity-initiated accident can be divided into two main categories;

1) Operation in post-DNB heat transfer for low burnup fuel

2) Pellet-Cladding Mechanical Interaction (PCMI) for high burnup fuel

3.1.1 Departure from Nucleate Boiling

The current fuel rod failure threshold for RIA's specifies that PWR rods that exceed the Departure from Nucleate Boiling Ratio (DNBR) must be considered to undergo cladding failure. However, experience has shown that exceeding the DNBR does not result in immediate cladding failure, but represents a transition from high heat transfer rates to low heat transfer rates from the rod [Collier 1972]. This generally causes a cladding surface temperature excursion to temperature levels exceeding 800ºC, depending on the power level (heat flux) and coolant conditions. Cladding surface temperature measurements from the NSRR facility find that operation in post-DNB heat transfer lasts between 5 to 15 seconds for high energy power pulses.

A fuel failure threshold based on exceeding the DNBR has traditionally been used as a conservative threshold for cladding failure in steady state and Final Safety Analysis Report (FSAR) Chapter 15 transients to limit high temperature operation under film boiling conditions [NRC 1981]. Most events described in Chapter 15 occur over time periods that range from seconds to minutes and therefore the potential to be in film boiling heat transfer conditions is possible. Operation at high cladding temperatures for extended periods of time can lead to cladding failure by several high temperature mechanisms. However, the transient conditions for most FSAR Chapter 15 accidents are considerably longer than an RIA event.

Observations from integral transient tests to simulate power-coolant mismatch conditions leading to DNB [Van Houten 1979], as well as high power RIA-simulation tests [Zimmermann et al. 1979; MacDonald et al. 1980], find that cladding failure by post-DNB operation occurs by two different modes: oxidation-induced embrittlement and ballooning/burst. Each of these cladding failure modes is described below.

3.1.1.1 Cladding Failure by Oxidation-Induced Embrittlement

At temperatures above 700ºC, Zircaloy material experiences a rapid steam oxidation reaction that can cause cladding embrittlement. The extent of embrittlement has been shown to be a function of the amount of oxygen absorbed by the cladding during the oxidation process [Hobbins 1977; Chung et al. 1978]. These results demonstrate that the temperature level and the time-at-temperature are important elements in the embrittlement of Zircaloy cladding, since these parameters influence the oxygen uptake and diffusion in the material. Van Houten has reviewed the experimental data from five separate test programs, including over 600 BWR and PWR type test rods and test conditions and evaluated the consequences of operating in post-DNB film boiling on cladding failure [Van Houton 1979]. A summary of the experimental results reviewed by Van Houten is shown in Figure 3-1. The plot in Figure 3-1 contains the Equivalent Clad Temperature as a function of the time after DNB. Van Houten defines the Equivalent Clad Temperature as the isothermal temperature of the cladding to produce the equivalent amount of oxidation observed in the experiment. Evident from the data is a failure boundary indicated by the dashed line that is a function of temperature and time-at-temperature. Above the failure boundary, the cladding temperature is sufficiently high to produce cladding failure by oxidation induced-embrittlement.

Recently, in-pile dryout tests on fuel rods pre-irradiated between 22 and 40 GWd/MTU have been conducted in the Halden test reactor to evaluate fuel behavior at high cladding temperatures [McGrath et al. 2001]. The rods from Halden test IFA-613 experienced numerous temperature excursions beyond 1000 K caused by high power and low coolant flowrate conditions. The data from the Halden IFA-613 are also included in the plot shown in Figure 3-1. The results are consistent with the failure boundary based on results from earlier tests.

Cladding temperature measurements from RIA experiments indicate that the temperature excursion associated with post-DNB operation can produce cladding temperatures ranging from 850 K to 1500 K at peak radial averaged fuel enthalpy levels below 170 cal/gmUO_2. The temperature excursions can be 10 to 15 seconds long before nucleate boiling heat transfer is re-established by re-wetting of the cladding surface. The peak cladding temperature and the duration of film boiling conditions have been shown to be a function of the energy deposition, the coolant subcooling, the water to fuel ratio, and the coolant flow rate [Ishikawa and Shiozawa 1980]. Typical cladding surface temperature time histories from RIA tests performed in the NSRR facility are shown in Figure 3-2 for several different peak fuel enthalpy levels [Ishikawa and Shiozawa 1980]. From this type of data, Saito was able to develop a relationship between the peak cladding surface temperature, initial pellet-cladding gap size, and the fuel enthalpy [Ishikawa and Shiozawa 1980]. These results are shown in Figure 3-3 along with the temperature results from the RIA 1-2 tests and recent results from NSRR on high burnup test rods. The relationship developed by Saito for the peak cladding temperature as a function of energy deposition works well for both high burnup fuel rods and tests performed in other test reactors. These results demonstrate that the peak cladding temperature for RIA conditions does not exceed 1500 K at fuel enthalpy levels below 170 cal/gmUO_2.

Included in Figure 3-1 are the peak cladding temperatures determined from post-test cladding metallography for the RIA 1-2 experiment conducted in the INEL Power Burst Facility [Cook et al. 1981]. A comparison of cladding temperature from RIA-simulation tests with the failure boundary from Figure 3-1 indicates that cladding failure by oxidation-induced embrittlement

following an RIA event is unlikely at fuel enthalpy levels below 170 cal/gm. Experimental results from tests on zero and low burnup rods conducted in the SPERT-CDC and the NSRR programs show that the fuel enthalpy is above 200 cal/gm for cladding failure under high temperature conditions [MacDonald et al. 1980; Ishikawa and Shiozawa 1980].

In-pile thermocouple measurements and post-test examinations of the cladding after RIA-simulation tests demonstrate that the cladding temperature will remain below the temperature-time threshold to cause oxidation-induced embrittlement of the cladding at fuel enthalpy levels below 170 cal/gmUO_2. These results further show that the time and temperature domain for RIA conditions is considerably smaller than for a loss-of-coolant accident where oxidation-induced embrittlement is important. Finally, the range of maximum cladding temperatures expected based on improved neutron kinetics calculations for a REA event, which is shown in Figure 3-1, is well below the time-temperature threshold for cladding failure.

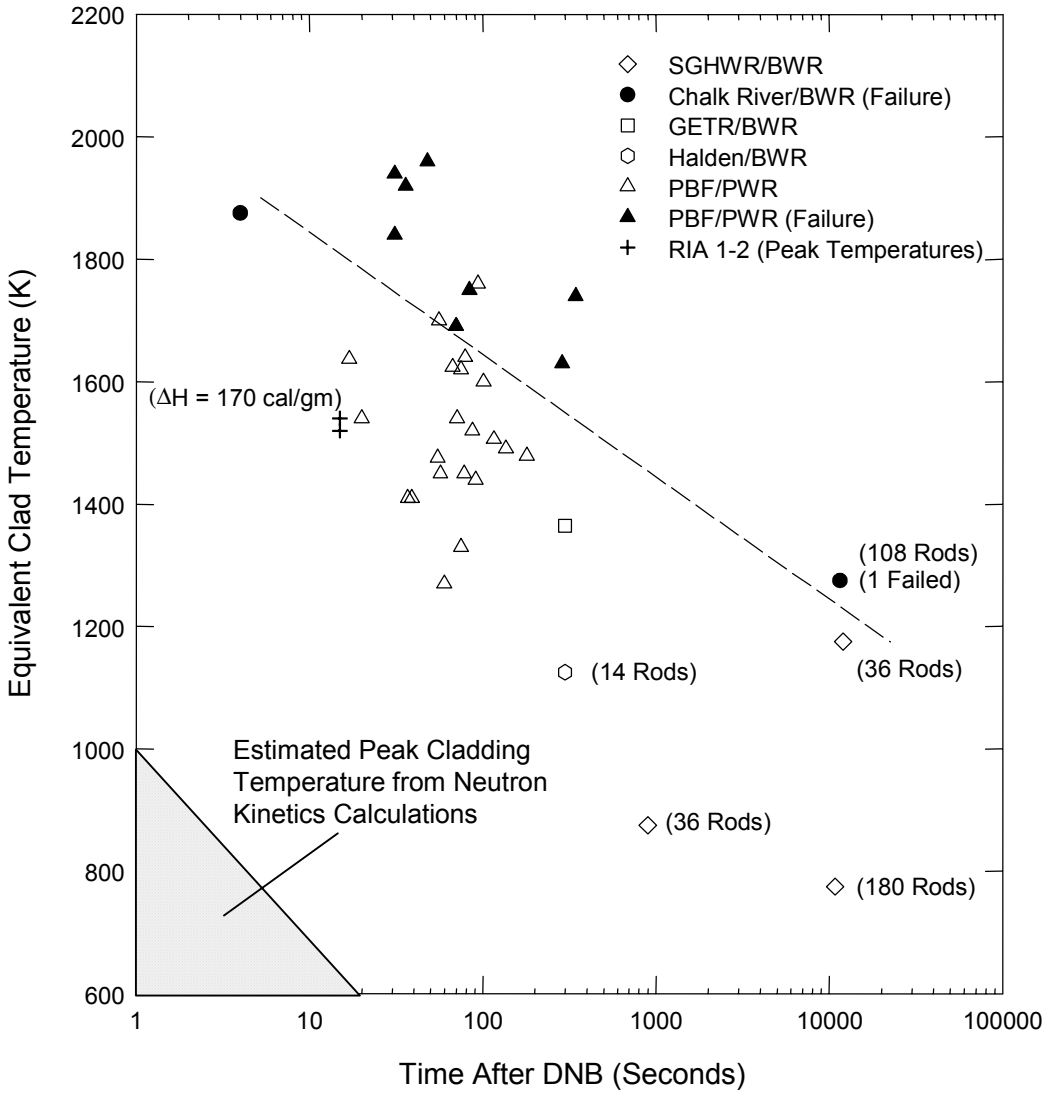

Figure 3-1
Equivalent Clad Temperature versus Time After DNB from In-Reactor Experiments [Van Houten 1979]. These date define a time and temperature threshold for oxidation-induced embrittlement. Results from RIA experiments and neutron kinetics calculations show that the maximum cladding temperatures and times are well below this threshold.

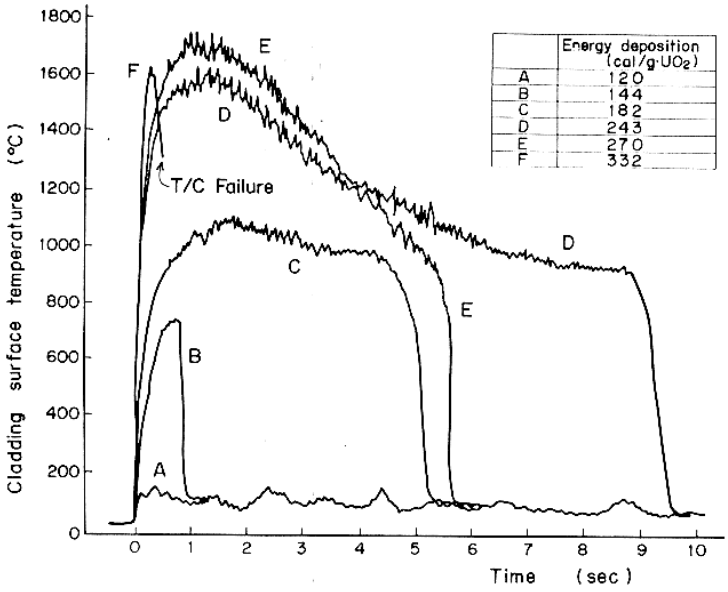

Figure 3-2
Cladding Surface Temperature Histories from NSRR Experiments with Post-DNB Operation [Ishikawa and Shiozawa 1980]. Results show that maximum cladding temperatures remain below 1300ºC for fuel enthalpy levels below 200 cal/gmUO_2.

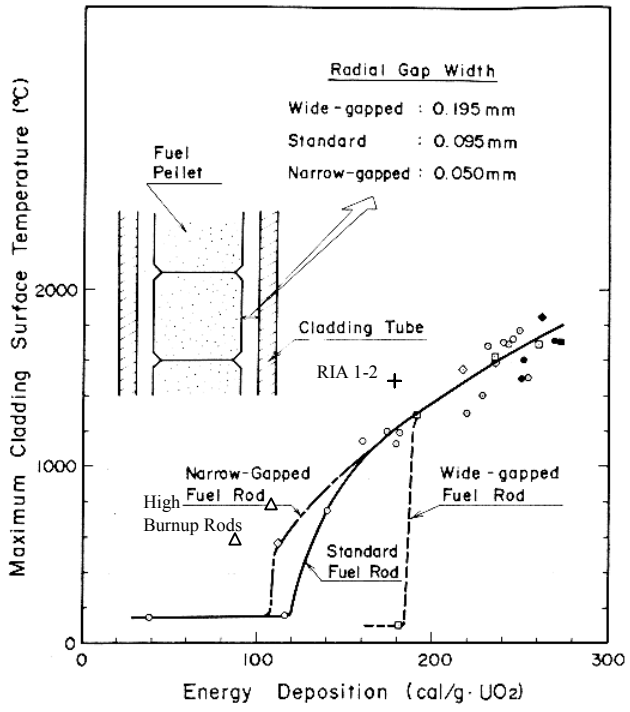

Figure 3-3
Maximum Cladding Surface Temperature as a Function of Energy Deposition [Ishikawa and Shiozawa 1980]

3.1.1.2 Cladding Failure by Ballooning and Burst

The second possible cladding failure mode for post-DNB operation during an RIA is cladding rupture by ballooning and burst. To produce cladding rupture, the rod internal pressure at the initiation of the event must exceed the external coolant pressure i.e., the rod must have a positive pressure differential across the cladding. Experiments have been performed to evaluate the effects a positive pressure differential on the cladding failure response during an RIA-simulation test [Ishikawa and Shiozawa 1980; Yegorova 1999]. Figure 3-4 contains results from experiments conducted in the NSRR and IGR/BIGR programs using unirradiated PWR-type rods with CWSR Zircaloy-4 cladding and unirradiated and irradiated VVER-type rods with Zr-1%Nb cladding [Ishikawa and Shiozawa 1980; Yegorova 1999]. The fuel rod failure threshold is similar to unpressurized rods at a positive pressure differential below 1 MPa. Above a positive pressure differential of 1 MPa, the fuel enthalpy at failure decreases as a function of the amount of the positive pressure differential. The IGR/BIGR results for Zr-1%Nb cladding are consistent with the experimental data from the NSRR program and indicate the ballooning and burst response of Zr-1%Nb cladding material is similar to standard CWSR Zircaloy-4 cladding.

The cladding deformations observed in the post-test examinations appear similar to rods tested under LOCA conditions. In fact, the cladding temperature and burst pressures from the NSRR program [Ishikawa and Shiozawa 1980] and the IGR/BIGR programs [Yegorova 1999] are consistent with out-of-pile LOCA burst tests on standard (1.5% Sn) CWSR Zircaloy-4 material [Chung and Kassner 1978]. As shown in Figure 3-5, the burst temperature and pressure data obtained from RIA experiments resides within the data scatter from transient-heating burst tests conducted on unirradiated Zircaloy-4 cladding. Also, it should be noted that the tests performed in the IGR/BIGR program were from fuel rods with Zr-1%Nb cladding material irradiated to 50 GWd/MTU. The results shown in Figure 3-5 indicate that irradiation damage in the cladding appears to have no impact on the ballooning and burst behavior of the IGR/BIGR tests. For the VVER fuel rods, the gas loading conditions are the same for zero or high burnup fuel rods because the large central hole along the length of the fuel column allows for the rapid gas communication required to support ballooning.

The tests with a positive internal pressure differential indicated that the high temperature ballooning and burst behavior during an RIA event could be evaluated using the large database of cladding mechanical properties obtained from LOCA experiments.

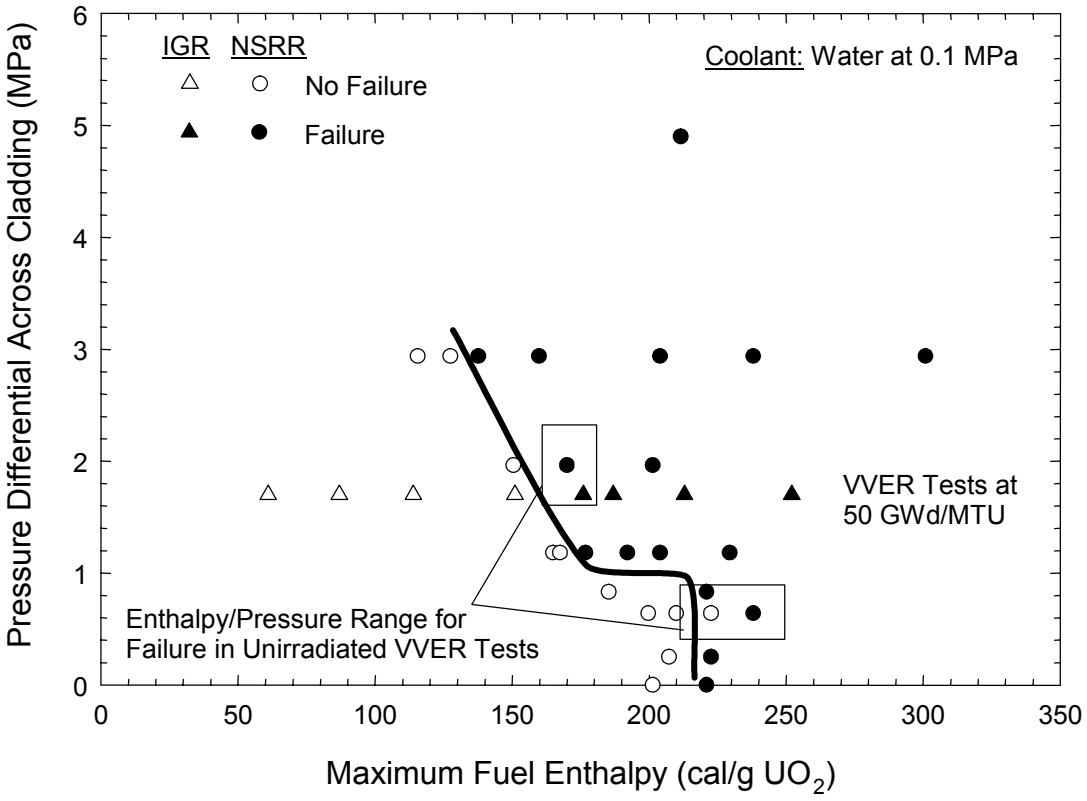

Figure 3-4
Initial Internal Pressure versus Energy Deposition from NSRR and IGR/BIGR Experiments [Ishikawa and Shiozawa 1980; Yegorova 1999]. The threshold between failed and non-failed tests decreases with higher initial internal pressure. Tests on irradiated and unirradiated VVER fuel rods with Zr-1%Nb cladding show results that are similar to tests with standard CWSR Zr-4 cladding.

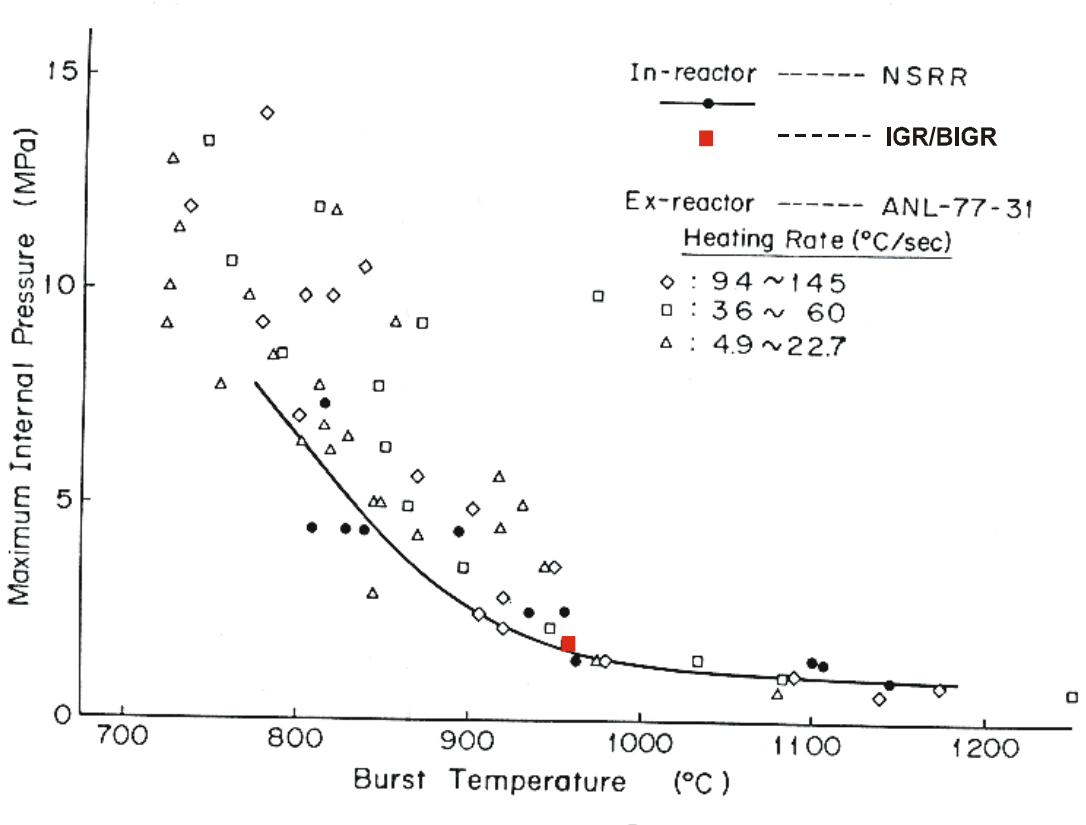

Figure 3-5
Comparison of Burst Data for Standard (1.5% Sn) CWSR Zircaloy-4 Cladding from In-Reactor and Ex-Reactor Experiments [Ishikawa and Shiozawa 1980; Yegorova 1999]. The burst behavior of RIA tests is consistent with out-of-pile burst tests performed for LOCA.

Failure by ballooning and burst below a peak radially averaged fuel enthalpy of 200 cal/gm requires a fuel rod positive internal pressure differential of above 1 MPa as shown by the experimental data in Figure 3-4. To achieve this condition, the fuel rod internal pressure at hot zero power would have to be16 to17 MPa for PWR fuel rods and 8 to 9 MPa for BWR rods. This is well above the initial rod pressure at beginning of life (BOL) conditions. During normal operation, increases in rod internal pressure occur due to a decrease in the fuel rod internal gas volume and an increase in the amount of gas content present in the fuel rod. Typical changes in rod internal gas volume range from 20 to 30% of the as-manufactured conditions based on EOL post-irradiation examinations. Furthermore, normal steady-state operation to 20 to 40 GWd/tU results in less than 5% fission gas release. In contrast, it can be shown that the fission gas release must exceed 30% to cause a positive internal pressure differential at HZP for a 40 GWd/tU fuel rod.

For fuel utilizing Integral Fuel Burnable Absorbers (IFBA) pellets with boron coating, helium release can also cause the rod internal pressure to increase. However, the large initial internal gas volume and the lower initial pre-pressurization offset some of the helium release on the rod pressure. Also, the fission gas release is lower for IFBA fuel at low to intermediate burnup because of the lower operating power levels. As a result, the rod internal pressure should be below the system pressure at hot-zero power conditions for IFBA fuel rods. These results show

that low to intermediate burnup fuel rods have insufficient fission gas release to produce a positive pressure differential at zero power conditions and therefore would not be susceptible to failure by ballooning and burst. This conclusion is supported by post-irradiation examination results from rods irradiated to 53 GWd/MTU in Fort Calhoun that show that the fuel rod internal pressure is between 3.5 and 4 MPa at room temperature [Garde 1986]. Using this data, PWR fuel rods below 50 GWd/MTU have rod internal pressure levels below 7 or 8 MPa at hot zero power conditions, which is well below system pressure for PWR coolant conditions.

The results from the CABRI and NSRR programs on test rods near 30 GWd/tU have not shown a propensity to fail by ballooning and burst although cladding temperatures have reached 700 to 800ºC and transient fission gas release can approach 30% for high burnup fuel rods [Fuketa et al. 2000; Waeckel et al. 2000]. Although the cladding yield stress decreases dramatically above 600ºC, CABRI REP Na. 2, Na-6, Na-9, and NSRR FK-4, which experienced maximum cladding temperatures above 600ºC showed no indications of ballooning or burst behavior in the cladding. These results demonstrate that transient fission gas release will not promote cladding ballooning and burst.

Cladding failure by ballooning and rupture at peak radial average fuel enthalpies near 170 cal/gm have been observed in the IGR/BIGR tests on fuel rods at 50 GWd/tU (See Section 2.2.4). However, these rods were tested with an initial positive pressure differential of 1.7 MPa. Another key difference the IGR/BIGR test rods and PWR fuel rods is the unimpeded axial gas flow present due to the large central hole in the fuel stack. The unrestricted axial gas communication allows the plenum gas supply to participate in maintaining the pressure at the local burst region. In contrast, high burnup LWR fuel rods have a limited gas inventory within the fuel column. This arises because of the reduced gas volume caused by gap closure and dish volume shrinkage by fuel swelling. At the high radial average peak fuel enthalpy levels required to reach cladding temperatures above 600°C, pellet thermal expansion would cause the pellet-cladding gap to close during the power pulse of an RIA. The restricted axial gas flow resulting from gap closure and fuel-clad bonding limits any gas resident in the plenum from supporting the ballooning deformations. Restricted axial gas flow in fuel rods is well demonstrated in the gas flow experiments in Halden reactor [refer]. As a consequence, a majority of the internal gas resides in the upper plenum and the restricted gas flow limits the participation of the plenum gas in maintaining the local pressure in the vicinity of the ballooning and burst deformations.

The experimental data demonstrate that cladding failure by ballooning and burst is unlikely below 200 cal/gm for PWR and BWR fuel rods two main reasons:

1) Low to intermediate burnup fuel rods have internal gas pressures below the system pressure and therefore the driving forces are insufficient to produce ballooning deformations.

2) It is not possible to rule out overpressure conditions in high burnup fuel rods due to the potential for transient fission gas release. However, high burnup fuel rods have a reduced gas inventory within the fuel-cladding gap to support ballooning deformations in the cladding because of the restricted axial flow within the fuel rod. This isolates the local balloon region from the gas plenum that contains a majority of the pre-transient gas inventory.

With regards to advanced cladding alloys such as ZIRLO and M5, the ballooning and burst behavior displayed by Zr-1%Nb cladding used in VVER fuel rod designs is consistent with the

standard (1.5% Sn) CWSR Zircaloy-4 material from out-of-pile burst tests. In support of this conclusion, high temperature burst tests on advanced cladding alloys have show that ZIRLO and M5 have similar burst temperatures and pressures as standard (1.5% Sn) CWSR Zircaloy-4 (Davidson and Nuhfer 1990; Forgeron et al. 2000). These observations indicate that advanced alloy cladding material would exhibit similar behavior as standard (1.5% Sn) CWSR Zircaloy-4 cladding during the high temperature phase of an RIA event. Furthermore, the experimental data from IGR/BIGR shows little impact of irradiation on the behavior of Zr-1%Nb fuel rods test up to rod average burnup of 50 GWd/tU.

3.1.1.3 Industry Position on Potential for Post-DNB Fuel Rod Failure

Based on the experimental data from high energy deposition tests on low and intermediate burnup test rods, the potential for cladding failure at fuel enthalpy levels below 200 cal/gm by post-DNB failure modes such as oxidation-induced embrittlement or ballooning and burst is very low in modern fuel designs irradiated under current operating conditions. Therefore, the current maximum radial average enthalpy threshold of 170 cal/gm used for cladding failure for BWR RIA events is also applicable to low and intermediate burnup PWR rods and provides a margin to cladding failure. At maximum radial average fuel enthalpy levels below 170 cal/gmUO_2, the cladding temperatures will remain well below the conditions to produce failure by oxidation-induced embrittlement. For ballooning and burst, the fuel rod internal gas pressure for low to intermediate burnup PWR fuel rods is well below the system pressure at hot standby conditions and is therefore insufficient to produce large cladding deformations that could lead to failure. The restricted axial gas flow and the small fuel-cladding gap limit the amount of gas inventory available to cause ballooning deformations in high burnup fuel rods. As a result, cladding failure by ballooning and burst in high burnup fuel rods is unlikely below a maximum fuel enthalpy of 170 cal/gmUO_2. Based on these observations, it can be concluded that cladding failure of UO_2 fuel below fuel enthalpy levels of 170 cal/ gmUO_2 is only possible by pellet-cladding mechanical interaction.

3.1.2 Pellet-Cladding Mechanical Interaction

As discussed in Section 2, RIA-simulation tests on pre-irradiated test rods conducted in CABRI and NSRR found that cladding failure during the power pulse was caused by PCMI related mechanisms, not by high temperature mechanisms. The process of failure by PCMI is a combination of two main elements: (1) the loading imposed on the cladding by fuel expansion and (2) the ability of the cladding to accommodate the fuel expansion strains. Irradiation influences both of these components to varying degrees, leading to the apparent burnup dependency of fuel rod failure as exhibited by the RIA-simulation test data.

3.1.2.1 Fuel Pellet Expansion and Cladding Contact

At intermediate and high burnup levels, fuel pellet swelling and cladding creepdown during irradiation causes closure of the fuel-cladding gap. The residual pellet-cladding gap at burnup levels beyond 40 GWd/tU is generally less than 20% of the as-manufactured gap. As a consequence, fuel pellet thermal expansion resulting from a rise in fuel enthalpy during an RIA event can produce PCMI stresses that strain the cladding. Another potential contributor to

increased PCMI stresses is related to the high burnup pellet rim region. Neutron absorption due to self-shielding increases the local Pu concentration and power production in the outer 100-200 μm near the pellet surface [Lassmann et al. 1994; Cunningham et al. 1992; Guedeney, P. et al. 1991]. Local burnup in this region can exceed 100 GWd/tU, producing high concentrations of fission gases that reside in a complex network of intergranular and intragranular bubbles. The almost adiabatic energy deposition during a RIA causes the pellet rim temperature to exceed normal operating temperature levels by 4 to 5 times due to the sharply peaked power distribution across the fuel pellet. The high temperature in the rim region can cause expansion of the fission gas bubbles, leading to gaseous swelling effects that may increase the PCMI forces on the cladding [Cunningham et al. 1992].

The combination of fuel thermal expansion and gaseous swelling causes the pellet to expand outward and imposes a displacement controlled loading on the cladding. Although fuel thermal expansion is burnup independent, the intensity of the overall PCMI loading depends on burnup due to the decrease in the pellet-cladding gap caused by steady state operation and the dependency of gaseous swelling on burnup.

Other important factors that can influence the PCMI forces on the cladding include the rate of loading from pellet expansion and the fuel and cladding interfacial friction. Depending on the power pulse width, the increase in cladding stress by PCMI can occur at a rate that is faster than the temperature rise in the cladding by heat conduction from the fuel pellet. Hence, the maximum loading can occur at low cladding temperatures, which can influence the ability of the cladding to accommodate the PCMI deformations. For high burnup fuel rods, the friction coefficient between the fuel and cladding is high or fuel-clad bonding may be present. This leads to axial stresses in the cladding that are about 70 to 80% of the hoop stresses. The biaxial stress and strain conditions in the cladding caused by PCMI in high burnup fuel also influences the ability of the cladding to accommodate the PCMI deformations.

Cladding failure occurs by PCMI when the fuel pellet expansion and gaseous swelling effects produced during the power pulse exceed the ductility capacity of the cladding. Therefore, the controlling component in the PCMI failure mechanism is the cladding ductility and how the ductility is influenced by irradiation.

3.1.2.2 Clad Ductility

Other than the fabrication characteristics, the tensile strength, uniform elongation, and total elongation of irradiated cladding depends on the fast fluence, hydrogen content and distribution, temperature and loading conditions. Mechanical property tests on irradiated cladding material show that the yield stress and ultimate tensile stress increase as a function of fast fluence. The increase in yield and ultimate tensile stress reaches saturation after one cycle of irradiation for PWR cladding [Papazoglou and Davis 1983; Pettersson et al. 1979; Newman 1986]. However, the effect of irradiation on cladding ductility is more complex due to the combined effects of fast fluence accumulation and zirconium hydride formation. Initially, fast fluence causes a decrease in the total and uniform elongation that saturates after 1 or 2 cycles of operation [Newman 1986]. The amount of decrease is a function of the initial cladding fabrication characteristics, i.e., degree of recrystallization. At extended burnup and fast fluence, the largest influence on the cladding ductility is the presence of zirconium hydrides. The impact of hydrogen on cladding

ductility depends on the hydrogen content, the distribution and orientation of the hydride platelets, and the temperature level.

Irradiated PWR cladding with uniform oxide layers generally show hydride concentrations that vary across the cladding thickness, with higher concentrations near the outer radius and low concentrations at the inner radius. The extent of hydrogen through-thickness variation depends on the cladding oxide layer thickness, power level and irradiation time. As the level of through-thickness variation increases, a region of hydride concentration (hydride rim) develops near the cladding outer surface that has a hydrogen content above 2000 ppm [Fuketa et al. 1996]. The presence of a hydride rim near the cladding outer surface can decrease the effective cladding ductility due to the formation of incipient cracks in the brittle hydride rim region that can propagate through the cladding [Fuketa et al. 2000; Daum et al. 2001b, Bates 1998]. The effect of the hydride rim on cladding ductility is a function of temperature and appears to be largest at room temperature [Fuketa et al. 2000; Daum et al. 2001b, Bates 1998]. The only cladding failures during RIA-simulation tests that may be linked to a decrease in cladding ductility by the hydride rim have been observed in tests on PWR samples with burnup levels near 50 GWd/tU from the NSRR program. In these experiments, the test capsules use 25ºC water as coolant.

As the cladding outer surface oxide layer grows during irradiation, the build-up of internal forces within the oxide layer due to volume expansion increases the possibility of crack formation in the oxide layer. Once cracks in the oxide layer have developed to a certain level, the oxide layer may delaminate into pieces and flake off from the cladding outer surface, causing a non-uniform oxide layer to form. The process of cladding oxide loss observed at higher oxide thickness levels is generally referred to as oxide spallation. A detailed description and definition of oxide spallation is contained in Appendix B. Only limited information is available to identify the operating conditions that influence the development of oxide spallation. The main variables that may influence oxide spallation include the oxide morphology and thickness, the oxidation rate, the cladding heat flux, and the coolant water chemistry.

Fuel rod profilometry with significant local axial and azimuthal variations in oxide layer thickness (>50%) are generally referred to as containing regions of spalled oxide. Spalled oxide layers influence the cladding-to-coolant heat transfer and can produce locally reduced cladding temperatures at regions where the oxide has flaked off. Analytical evaluations have shown that the temperature perturbations are less that 5ºC for uniform oxide layer levels less than 50 microns. However, spallation of uniform oxide layers above 100 microns can produce local cold spots that are 20-30ºC below the average cladding temperature. Non-uniform temperature distributions will induce hydrogen diffusion in the cladding and the formation of zirconium hydrides at the local cold spots.

Hydride redistribution caused by oxide layer spallation can result in regions of heavy hydride concentrations or localized hydrides [Garde et al. 1996]. The presence of localized hydrides impacts the effective cladding ductility because the brittle nature of zirconium hydride (ZrH_2) decreases the load bearing thickness of the cladding in the vicinity of the localized hydride. Mechanical property tests on cladding samples with spalled oxide layers show a significant decrease in the effective cladding ductility when localized hydrides are present in the gauge section of the sample. Test samples that were removed from spalled cladding regions that contained more uniform hydride concentrations displayed less impact of spallation on ductility. The decrease in cladding ductility, as defined by total elongation, caused by non-uniform hydride

distributions is evident in the CSED data presented in Section 2. These data reside well below the total elongation and CSED results from tests on cladding containing uniform hydride concentrations.

The only RIA-simulation tests on irradiated PWR test rods performed at 280ºC that failed contained cladding with spalled oxide layers. Tests CABRI REP Na-1, REP Na-8 and REP Na-10 all exhibited cracks in the cladding coincident with localized hydrides and displayed brittle mode fracture characteristics [Schmitz and Papin 1998; Schmitz and Papin 1999]. On-line instrumentation indicated that cladding failure occurred during power deposition, when fuel pellet expansion increases the PCMI forces on the cladding. Conversely, three tests above 60 GWd/tU have been tested at fuel enthalpy levels above 90 cal/gm without indications of failure. CABRI REP Na-4 performed successfully with an 80 micron non-spalled oxide layer and 600-700 ppm hydrogen content that only exhibit minor through thickness variation. Two tests with hydrogen contents below 200 ppm, the low-Sn Zr-4 rod CABRI REP Na-5 and the M5 rod CABRI REP Na-11, also performed well and did not display any adverse effects of burnup on the rod performance.

3.1.3 Summary

The results from the RIA-simulation tests and analytical evaluations have shown that the fuel rod failure mechanisms can be separated in two main categories: (1) high temperature cladding failure caused by post-DNB operation and (2) cladding failure by a combination of PCMI forces and loss of cladding ductility. Failure by high temperature oxidation-induced embrittlement or ballooning/burst is limited to high radial average fuel enthalpy levels and high internal overpressure conditions. Low burnup fuel is most susceptible to failure by oxidation-induce embrittlement above 170 cal/gmUO_2. High burnup fuel may develop high internal overpressure conditions, however, the restricted axial gas flow limits the effects of the overpressure on cladding deformations. For fuel rod average burnup levels below 40 to 50 GWd/MTU, a radial average fuel enthalpy of 170 cal/gmUO_2 bounds the high temperature failure mechanisms.

Whereas the high temperature failure mechanisms are active after the power pulse, PCMI-induced cladding failure occurs during the power pulse when the PCMI forces are greatest. PCMI-induced failure is unlikely below 40 GWd/MTU because the wider fuel-cladding gap thickness decreases the PCMI forces and the cladding ductility is sufficient to accommodate the pellet expansion. At higher burnup levels, changes in cladding ductility caused by the effects of hydriding, fast fluence and increased PCMI forces can cause the cladding to fail. Data from the RIA-simulation tests show that hydride-induced cladding embrittlement controlled by the cladding temperature and hydride distribution were the main causes of cladding failure due to PCMI. The main role of fuel rod burnup is to decrease the fuel-cladding gap and increase the PCMI loading by pellet expansion.

These conclusions are consistent with the outcome of the NRC-sponsored Phenomena Identification and Ranking Table (PIRT) process conducted to assist the NRC in addressing research requirements for modeling fuel behavior and defining fuel damage limits [Meyer 2001]. The panel of experts reviewed the phenomena and processes that influence fuel rod behavior during a PWR control rod ejection accident. From their review, phenomena with a high importance factor related to cladding failure included burnup, hydride distribution, cladding-to-

coolant heat transfer conditions, and power pulse width. Each of these phenomena influence the fuel rod behavior in various degrees and dictate the manner in which the cladding fails.

The propensity for cladding failure by PCMI is controlled by the cladding temperature, hydride distribution and PCMI loading conditions. Because of the complex interplay of these variables, it is difficult to develop an explicit relationship between fuel rod average burnup and the fuel enthalpy level at cladding failure. A more appropriate method to define the fuel rod failure threshold for PCMI cladding failure as a function of fuel rod average burnup is to use a combination of experimental data and analytical evaluations.

3.2 Methodology to Develop Fuel Rod Failure Threshold

The following summarizes the methodology used to develop the revised fuel rod failure threshold defined in terms of radial average fuel enthalpy as a function of rod average burnup. The approach is based on the observations from the RIA-experiments performed on test rods extracted from fuel rods irradiated in commercial reactors as well as fuel rod behavior analyses.

The review of the RIA-simulation experiments on commercial reactor fuel summarized in Section 2 found that the data could not be used directly to define a fuel rod failure threshold as a function of burnup because of the role of cladding ductility. Figure 3-6 contains the results of the RIA-simulation experiments on both commercial reactor fuel and non-commercial test rods and is a plot of the radial average peak fuel enthalpy as a function of test segment burnup. The rods that developed cladding failure during the power pulse are indicated by the solid symbols. As shown in Figure 3-6, the rods that experienced cladding failure are interspersed amongst the rods where the cladding remained intact following the power pulse. Because of the fact that the failed and non-failed rods are interspersed when plotted as a function of burnup indicates that burnup is not the sole parameter that influences the cladding integrity, other parameters such as cladding temperature, oxidation and hydride content also have an impact. These factors make it difficult to develop a failure threshold that is a function of burnup using this data directly.

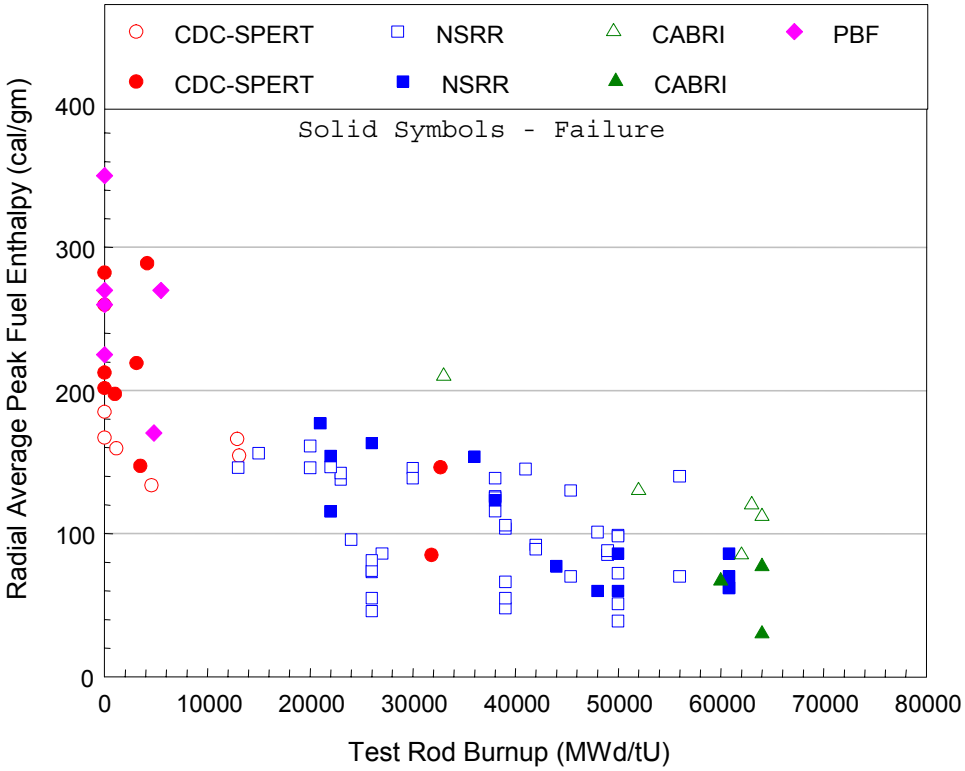

Figure 3-6
The radial average peak fuel enthalpy as a function of test rod burnup for RIA-simulation tests performed in the US, France, and Japan on previously irradiated test rods. Tests with cladding failure are indicated by solid symbols. Failed and non-failed rods are interspersed when plotted as a function of burnup.

Similarly, developing a criteria based on fuel enthalpy at failure as a function of oxide thickness directly from the data as proposed by some is complicated by variations in the test temperature and oxide spallation that make it difficult to develop a clear trend with oxide thickness [Meyer 2001; Yang 2000; Meyer 1997]. Also, developing a failure threshold as a function of oxide thickness would deviate from the typical licensing methodology that is performed on a burnup basis.

Since it was not possible to construct a failure enthalpy as a function of burnup directly from the experimental data, an alternative approach was developed based on a combination of experimental data and analytical evaluations. The methodology uses experimental data for the following purposes:

- Separate effect data on cladding oxidation and mechanical properties are used to describe the changes in cladding ductility caused by burnup accumulation.
- Selected integral RIA tests are used to understand the mechanisms active during RIA conditions and to validate the analytical methods that calculate the fuel rod behavior.
- The database of RIA tests is used to demonstrate the application of the failure threshold.

The fuel rod behavior analysis method is used to calculate the thermal and mechanical fuel rod response during the power pulse of a RIA event. Examples of fuel rod codes that can be used for this application include FALCON, SCANAIR, and FRAPTRAN. Within the approach to develop the fuel rod failure threshold, the analysis method is used to evaluate and interpret the RIA-simulation tests and to calculate as a function of rod average burnup the fuel rod response during a RIA event representative of a PWR hot-zero power control rod ejection accident.

The approach to develop the fuel rod failure threshold for a PWR control rod ejection event contains five major steps:

Step 1. Utilize data from mechanical property tests on Zr-4 material to define the cladding ductility (expressed as CSED) as a function of outer surface oxide layer thickness.

Step 2. Utilize cladding corrosion data for low tin Zr-4 to define oxide thickness as a function of burnup.

Step 3. Use results from Step 1 and Step 2 to develop the cladding ductility change as a function of burnup.

Step 4. Use a fuel rod analysis code validated with selected RIA-simulation tests to calculate the increase in cladding stress and strain (expressed as SED) during the power pulse of a control rod ejection accident as a function of burnup and fuel rod radial average fuel enthalpy.

Step 5. Combined the results from Step 3 and Step 4 to develop the fuel enthalpy at cladding failure as a function of burnup.

A schematic highlighting these five steps is shown in Figure 3-7. The following summarizes each of the steps.

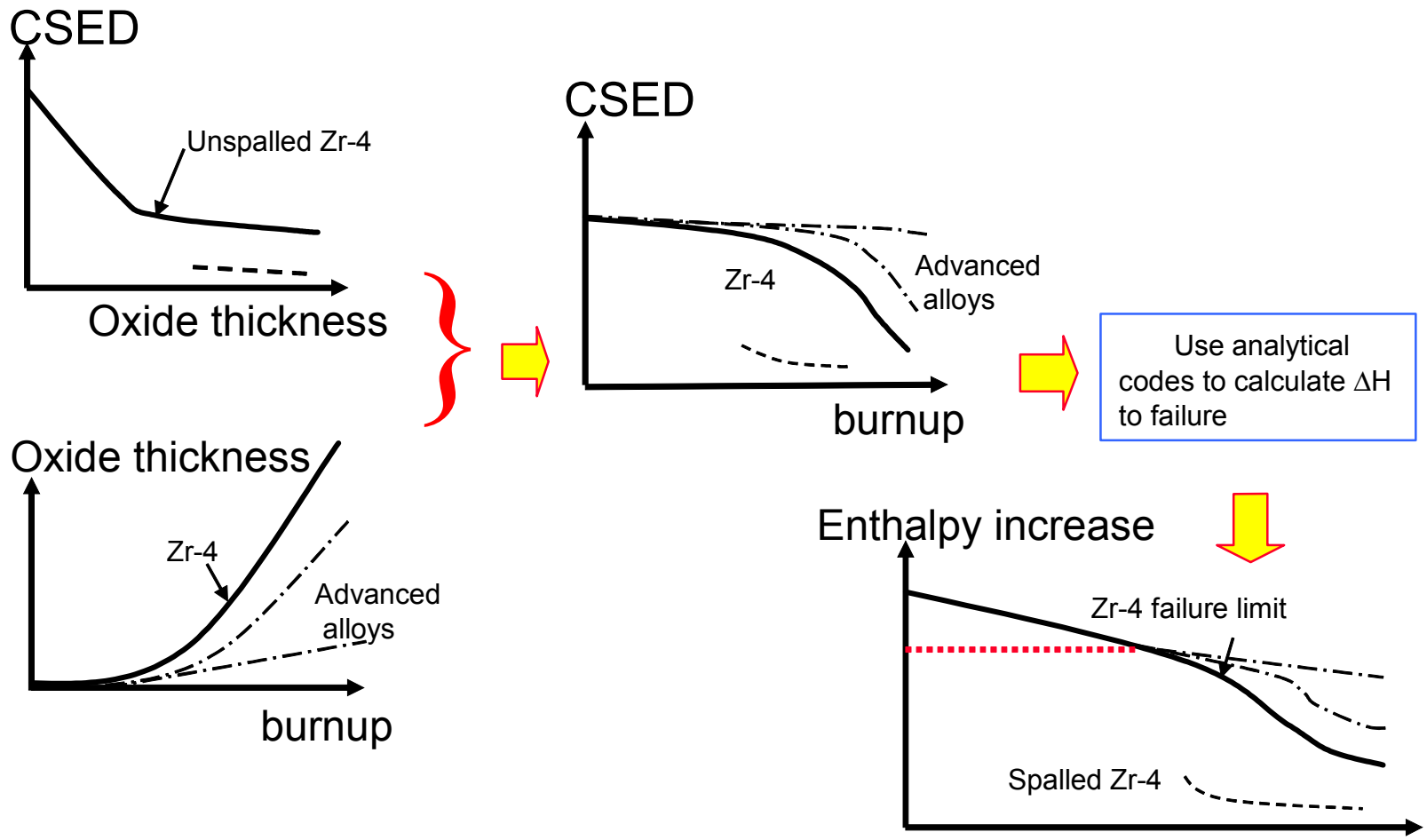

Figure 3-7
Schematic outlining the steps to develop the fuel rod failure threshold for RIA transient analysis

3.2.1 Step 1: Cladding Ductility as Function of Cladding Condition

For the evaluation of the cladding failure threshold for the PWR control rod ejection accident, the cladding ductility was correlated as a function of the outer surface oxide thickness. In this evaluation, it is assumed that the zirconium hydride content and distribution resulting from cladding oxidation is the main contributor to changes in the cladding ductility during burnup accumulation.

The mechanical property data summarized in Section 2.3.1 indicate that the cladding ductility is influenced by several factors, namely, the fast neutron fluence, the temperature during mechanical loading, and the hydrogen content and hydride distribution. The impact of fast fluence on elongation and strength of Zircaloy-4 material is most dominant at fluence levels below 3-4x10^{21} n/cm^2 and saturates during further fluence accumulation. However, as fluence levels exceed 9x10^{21} n/cm^2, the variability in the total elongation increases due to the effects of cladding hydrogen content and hydride distribution [Garde et al. 1996]. Although the fast fluence effect can decrease the cladding elongation by as much as 50%, even at high fluence levels, Zr-4 material has sufficient strength and elongation capacity to accommodate the PCMI loading during an RIA event at hot zero-power conditions, provided that no hydride lens (or hydride localization) caused by oxide layer spallation are present [Garde et al. 1996; Daum et al. 2001; Lespiaux et al. 1997].

In addition to the cladding condition at the time of loading, the PCMI loading conditions defined by the strain rate and the stress state can also influence the cladding ductility. As discussed in Section 2.3.2, experimental data indicate that the effect of strain rate on cladding ductility is largest at room temperature for average hydrogen contents less than 500 ppm. The stress-state in the cladding caused by the PCMI forces can decrease the cladding ductility depending on the amount of biaxiality present and the hydrogen content. Because of the strong biaxiality component in the PCMI loading for RIA conditions, the stress biaxiality effect is included in the cladding ductility. The biaxiality correction factor used in the development of the cladding ductility function is described in Section 2.3.2.3.

Three key mechanical properties can be used to represent the cladding ductility: uniform elongation, total elongation and the critical strain energy density. As described in Section 2.3.2, the critical strain energy density was selected in this methodology to represent the cladding ductility as a function of cladding condition. Application of the critical strain energy density to the analysis of RIA-simulation experiments demonstrated that this mechanical property best discriminated between failed and non-failed rods.

A critical strain energy density (CSED) relationship was constructed by performing a best fit of the mechanical data as a function of oxide thickness-to-cladding thickness ratio (R_{ox}). This method is described in detail in Section 2.3.2. The CSED curve shown in Figure 3-8 (Equation 2-12) is based on a best fit of the CSED data developed from mechanical property tests at or above 280ºC on irradiated Zircaloy-4 obtained from fuel rods with non-spalled oxide layers and various hydrogen contents [Papazoglou and Davis 1983; Balfour et al. 1985; Newman 1986; Smith et al. 1994a; Smith et al. 1994b; Lemoine and Balourdet 1997; Hermann et al. 2000; Kuo et al. 2000]. The CSED curve shown in Figure 3-8 decreases with increasing R_{ox} due to the

higher hydrogen content, the clad wall thinning with oxide formation, and an increase in the non-uniformity of the ZrH_2 distribution.

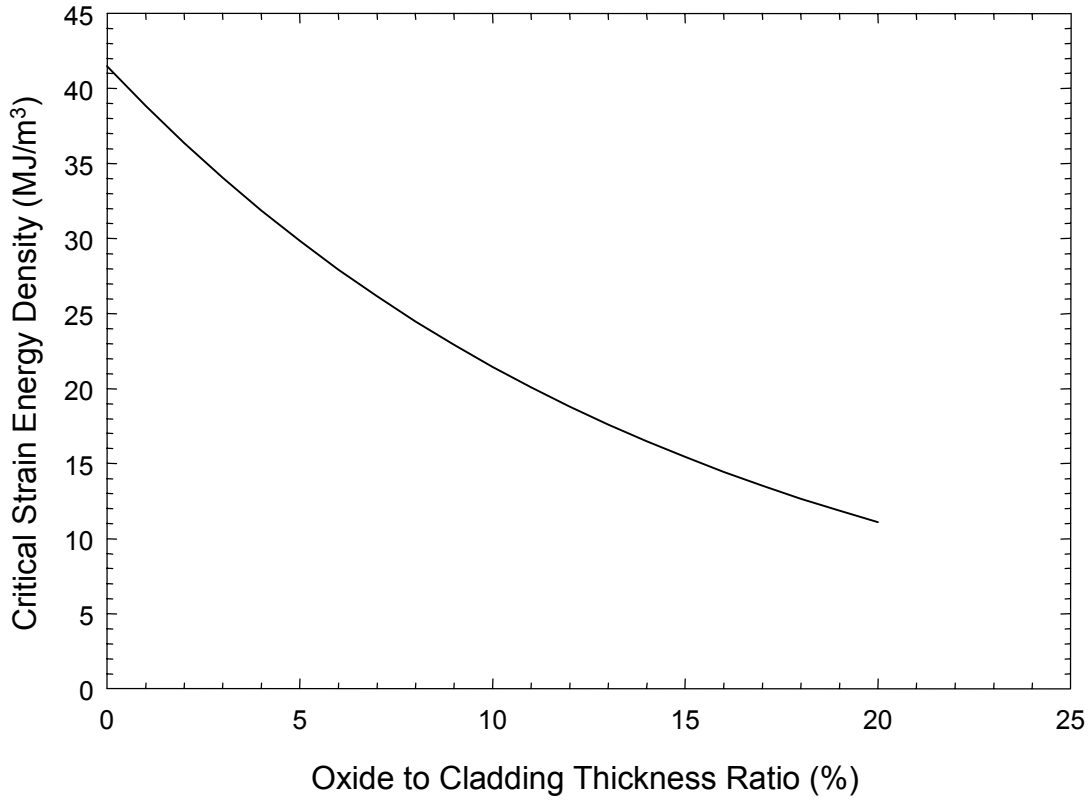

Figure 3-8
The critical strain energy density (CSED) as a function of oxide thickness-to-cladding thickness ratio for temperature levels above 300ºC. The expression shown was developed from mechanical property tests on Zircaloy-4 material.

3.2.2 Step 2: Cladding Outer Surface Oxidation as Function of Burnup

Since the cladding ductility is correlated with oxide layer thickness, a method is required to relate the maximum oxide thickness to the rod average burnup. The resulting relationship defines the evolution of the cladding ductility with fuel rod burnup. To develop an oxide thickness versus burnup relationship, maximum oxide thickness data were collected from poolside examinations on low-Sn Zircaloy-4 fuel cladding irradiated to rod average burnup levels of 64 GWd/MTU. Maximum oxide thickness is defined as the azimuthally averaged oxide layer thickness over a 1" axial section.

The corrosion kinetics of low-Sn Zircaloy-4 has been shown in out-of-pile corrosion tests and in-reactor examinations to have a higher rate than the newer cladding alloy designs currently being implemented by most fuel vendors [Corsetti et al. 1997; Mardon et al. 1997; Sabol et al. 1997; Willse 2000; Wilson et al. 1997; Woods and Klinger 1997]. Therefore, using oxidation data from low-Sn Zircaloy-4 represents an upper bound of the oxide thickness accumulation for the

advanced cladding alloy materials that are currently used or planned for high burnup applications.

Low-Sn Zr-4 oxide thickness data obtained from ~4400 poolside examination measurements on rods irradiated up to an average burnup of 64 GWd/MTU were used to develop the maximum oxide thickness accumulation as a function of rod average burnup (Willse 2000). These data are shown in Figure 3-9. The general trend shows that the maximum oxide thickness increases with rod average burnup. Figure 3-9 demonstrates that the maximum oxide thickness increases with a non-linear dependency on burnup and significant scatter is present in the data. Factors that contribute to the data scatter include the operating conditions such as coolant temperature, power level and water chemistry, variability between different fabrication methods for the cladding material, integrity of the oxide layer, and measurement uncertainties.

A bounding oxidation rate curve was developed for use in the fuel rod failure methodology. The main constraint in developing the curve was to encompass the single 100 micron oxide layer thickness data point at 40 GWd/MTU. The polynomial expression is given by:

$$Ox\Big|^{b} = a + b \cdot Bu + c \cdot Bu^{2} + d \cdot Bu^{3} \qquad (3\text{-}1)$$

where: $Ox\Big|^{b}$ is the bounding average maximum oxide thickness in microns

Bu is the rod average burnup in GWd/MTU

a = 6

b = 0.35

c = -1.35×10^{-2}

d = 1.613×10^{-3}

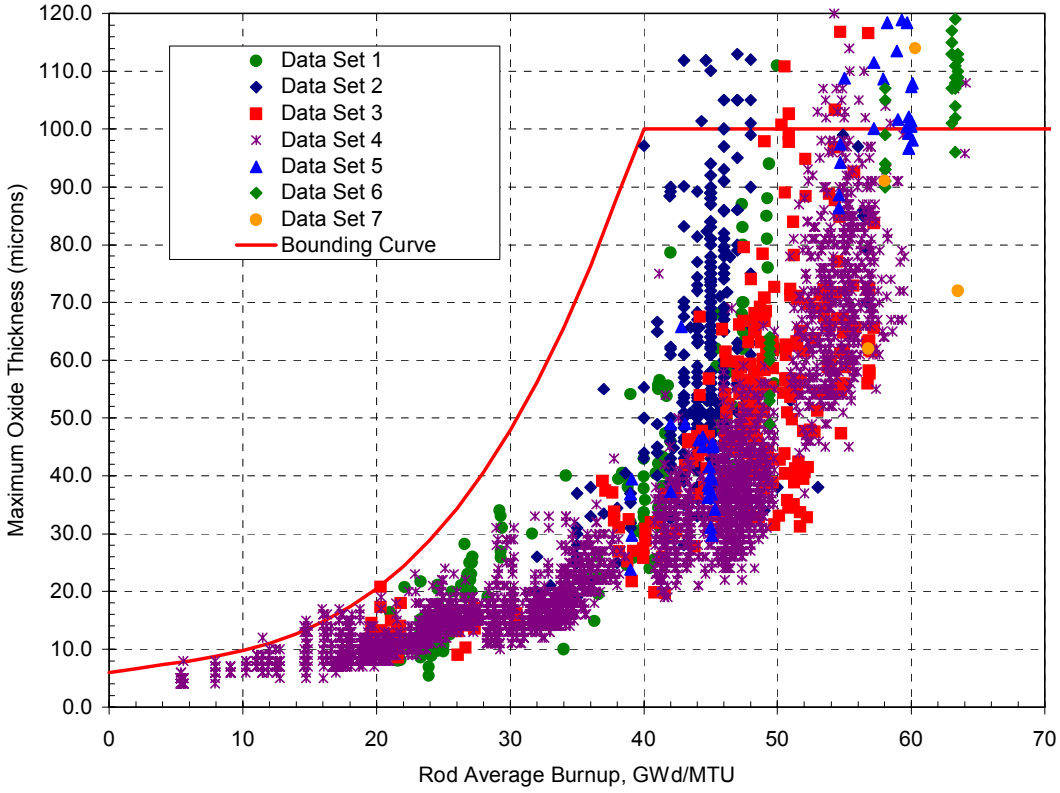

Figure 3-9
Maximum oxide thickness as a function of rod average burnup from low-Sn Zr-4 cladding. Upper bound polynomial expression is shown for comparison.

The maximum oxide thickness from Equation 3-1 is limited to 100 microns to preclude the effects of oxide spallation on the formation of localized hydrides and degradation of the cladding mechanical properties. The bounding oxidation rate given by Equation 3-1 provides conservatism to account for the uncertainties in cladding oxide thickness formation and resulting impact on cladding ductility. When combined with the CSED function shown in 3.2.1, the resultant cladding ductility function is a lower bound for Zr-4 with non-spalled oxide layers. Such an approach should bound the material ductility of advanced cladding alloy materials that have lower outer surface oxidation and hydrogen accumulation rates.

3.2.3 Step 3: Cladding CSED as Function of Burnup

The evolution of the cladding ductility with rod average burnup is obtained by combining the results from Step 1, cladding CSED as a function of oxide thickness, and Step 2, the cladding oxide thickness as a function of rod average burnup. The outcome is a relationship between the cladding CSED as a function of rod average burnup based on mechanical property tests on Zr-4 material and oxidation data on low-Sn Zr-4 cladding. Because of the higher rate of oxidation for low-Sn Zr-4 material, this approach yields a much stronger decrease in cladding ductility as a function of burnup than would be expected for newer cladding alloy designs. For the application

to extended burnup, it is anticipated that maximum oxide thickness values will not exceed 100 microns. Therefore, the upper bound oxidation model given in Equation 3-1 was limited to a maximum of 100 microns.

Combining the CSED and the oxide thickness functions from Step 1 and Step 2 yields the CSED versus rod average burnup shown in Figure 3-10. In Step 1, the CSED is a function of the oxide thickness to cladding thickness ratio (Rox). As a result, two different curves are shown in Figure 3-10, representing a 760 micron wall thickness 15x15 cladding design and a 575 micron wall thickness 17x17 cladding design, respectively. The function shown in Figure 3-10 indicates that the CSED decreases as the rod average burnup accumulates due to the impact of oxide thickness buildup on cladding ductility. A minimum CSED value is reached once the outer surface oxide thickness reaches 100 microns. The functional form shown in Figure 3-10 represents a conservative estimate of the decrease in cladding ductility as a function of rod average burnup. This conservative approach will bound the uncertainties in the decrease in cladding ductility caused by oxide thickness accumulation and irradiation damage.

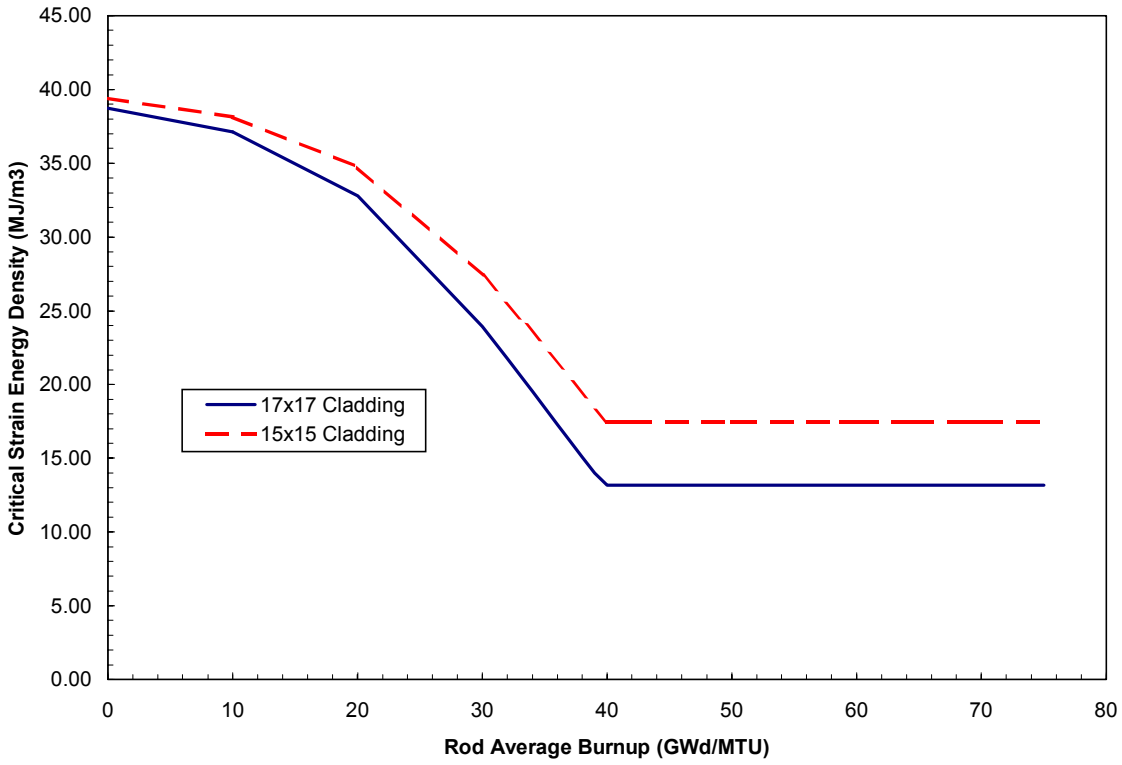

Figure 3-10
Critical strain energy density (CSED) as a function of rod average burnup developed for two different low-Sn Zircaloy-4 cladding designs.

3.2.4 Step 4: Analysis of Cladding Response During a PWR Hot Zero Power Control Rod Ejection Accident

The fourth step in the development of a fuel rod failure threshold for the PWR HZP Control Rod Ejection Accident is the analytical evaluation of the cladding thermal and mechanical response during the power pulse. The objective of the analysis is to calculate the amount of transient-induced cladding deformation caused by PCMI during an RIA power pulse as a function of rod average burnup. The approach used within this evaluation employed the steady-state and transient fuel behavior code FALCON to calculate the fuel and cladding behavior during both normal operation and the RIA power pulse [Montgomery and Rashid 1996, Yang et al. 2000]. The analysis approach described herein could also be performed using most any steady state and transient fuel rod analysis methods that accommodate the effects of burnup on the fuel and cladding thermal and mechanical response. Transient codes such as SCANAIR or FRAPTRAN could be initialized based on the results of steady state fuel performance analysis codes and then be used to calculate the evolution of the cladding deformation as a function of fuel rod burnup [Cunningham et al. 2000; Lespiaux et al. 1997; Papin et al. 1997; Stelletta and Waeckel 1997; Federici, E. et al. 2000].

The fuel behavior analysis methodology includes the following steps:

Steady state analysis of a full-length fuel rod geometry to rod average burnup levels between 10 and 70 GWd/MTU were performed to obtain the initial fuel rod condition for the transient analysis. The average linear power history and axial power shapes used in the analysis are shown in Figures 3-11 and 3-12. The fuel rod power history was developed to represent three 18-month cycles of irradiation at power levels near the upper range expected for fuel rods irradiated to high burnup levels.

A power ramp at increments of 10 GWd/MTU was included, representing a reactor shutdown to hot-zero power conditions at burnup levels between 0 and 70 GWd/MTU.

At each burnup increment, a transient analysis was conducted using a gaussian-shaped power pulse with a 20 millisecond full-width half maximum pulse at deposited energy levels between 120 and 220 cal/gm. A pulse width of 20 milliseconds was selected as a representative lower bound value for power pulses in an RIA event. An example of the RIA power pulse is shown in Figure 3-13.

This analysis procedure was conducted using three different fuel rod designs:

- 17x17 V5H-type with 570 micron wall thickness
- 15x15 OFA-type with 610 micron wall thickness
- 15x15 Siemens-W-type with 760 micron wall thickness

For each fuel rod design, the transient-induced cladding deformation was obtained from the FALCON analysis as a function of the radial average fuel enthalpy at each burnup increment. The cladding deformation is expressed in terms of the strain energy density (SED), which is simply an integration of the stress and strain response during the power pulse as discussed in Section 2.4.3. A summary of the FALCON results for the three different fuel designs is shown

in Table 3-1 as a function of rod average burnup and maximum radial average peak fuel enthalpy.

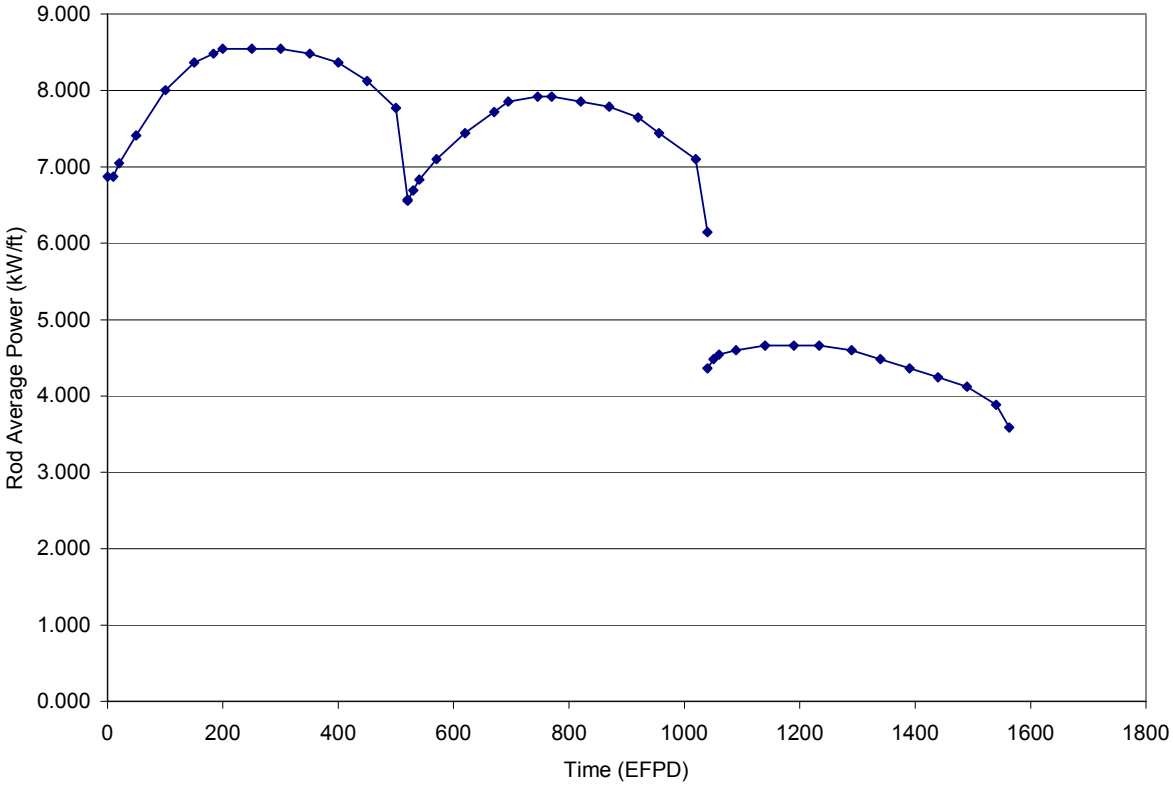

Figure 3-11
The idealized fuel rod average power history used in the burnup calculation. The results of the burnup calculation define the initial fuel rod condition for the RIA transient analysis.

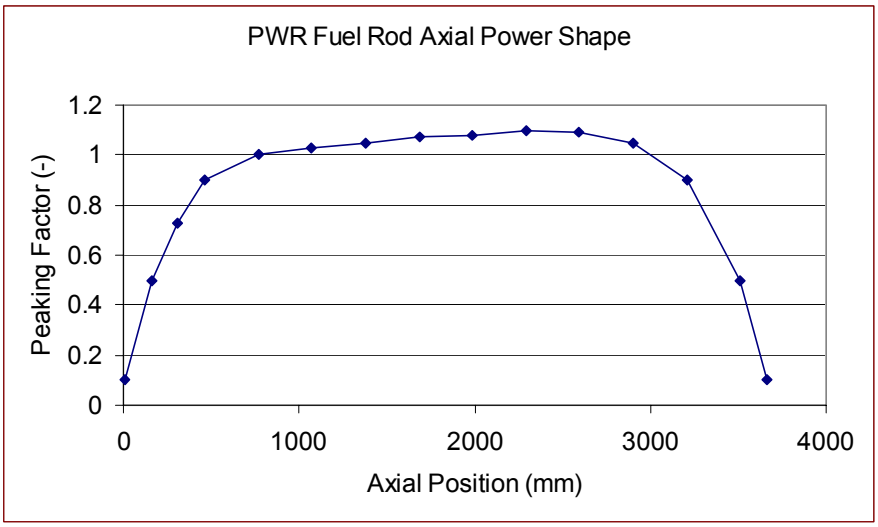

Figure 3-12
Idealized fuel rod axial power shape used in the burnup calculation.

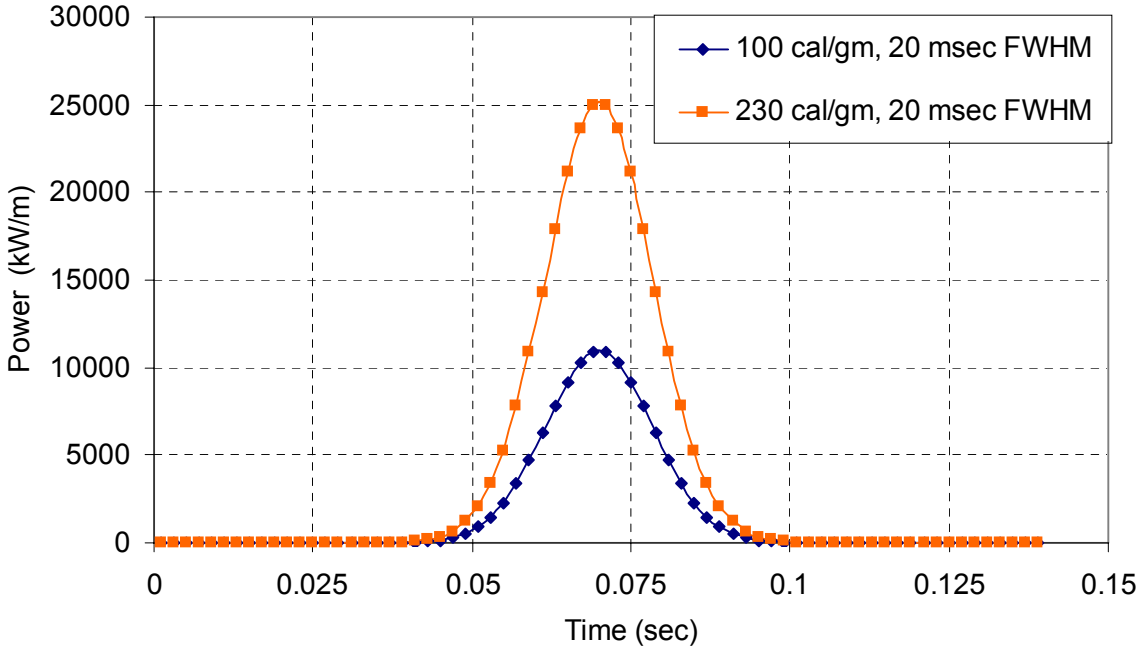

Figure 3-13
RIA power pulse shape used in the FALCON analysis of the PWR REA. The full-width half maximum (FWHM) for each pulse is 20 milliseconds.

Table 3-1
FALCON Analysis Results for Transient-Induced Cladding Deformations

Rod Average Burnup (GWD/MTU)	Maximum Fuel Enthalpy (Cal/gm)	Max. SED Design 1 (MJ/m^3)	Max. SED Design 2 (MJ/m^3)	Max. SED Design 3 (MJ/m^3)
0	238	13.1	13.0	14.8
10	230	17.3	22.2	17.7
20	230	21.5	21.1	21.5
30	230	23.5	23.4	23.1
40	230	23.5	25.7	23.8
50	190	19.9	21.7	19.3
60	170	20.9	21.5	18.9
70	160	19	21.1	19.5
75	130	14	14.5	14.4

3.2.5 Step 5: Maximum Radial Average Fuel Enthalpy at Cladding Failure as Function of Burnup

The final step in the fuel rod failure threshold development is the combination of the results from Step 3 and Step 4 to produce the maximum radial average fuel enthalpy at cladding failure. The result from Step 3 is the critical strain energy density as a function of fuel rod average burnup. The curves shown in Figure 3-10 represent the cladding ductility threshold and the methodology assumes that the maximum radial average fuel enthalpy that causes the cladding mechanical response during an RIA power pulse, given by the results of Step 4, to exceed this threshold will result in cladding failure by PCMI.

Figure 3-14 is a plot of the CSED curve from Step 3 and calculated SED curve from the fuel rod analysis in Step 4 as a function of rod average burnup for one of the fuel rod designs evaluated with the methodology. As can be seen, the FALCON SED curve remains beneath the CSED curve at fuel rod average burnup levels less than 30 GWD/MTU. The results below 30 GWD/MTU demonstrate that cladding failure by PCMI is only possible above a radial average fuel enthalpy of 230 cal/gm. It has been demonstrated earlier that above 170 cal/gmUO_2, cladding failure may occur by high cladding temperature mechanisms such as oxidation induced embrittlement or ballooning and burst. The SED curve crosses and exceeds the CSED curve beyond 30 GWD/MTU indicating a potential for cladding failure by PCMI.

To establish the maximum radial average fuel enthalpy threshold to preclude cladding failure beyond 30 GWd/MTU, the analytical results from FALCON are interpolated to determine the

radial average fuel enthalpy that produces a cladding mechanical response (given by the calculated SED) corresponding to the CSED curve. This produces a fuel rod failure threshold that is defined in terms of the radial average fuel enthalpy. For the low and intermediate burnup regimes where the SED does not exceed the CSED curve, the maximum radial average fuel enthalpy is established to be 170 cal/gm to preclude failure by high temperature mechanisms such as oxidation-induced embrittlement or ballooning/burst.

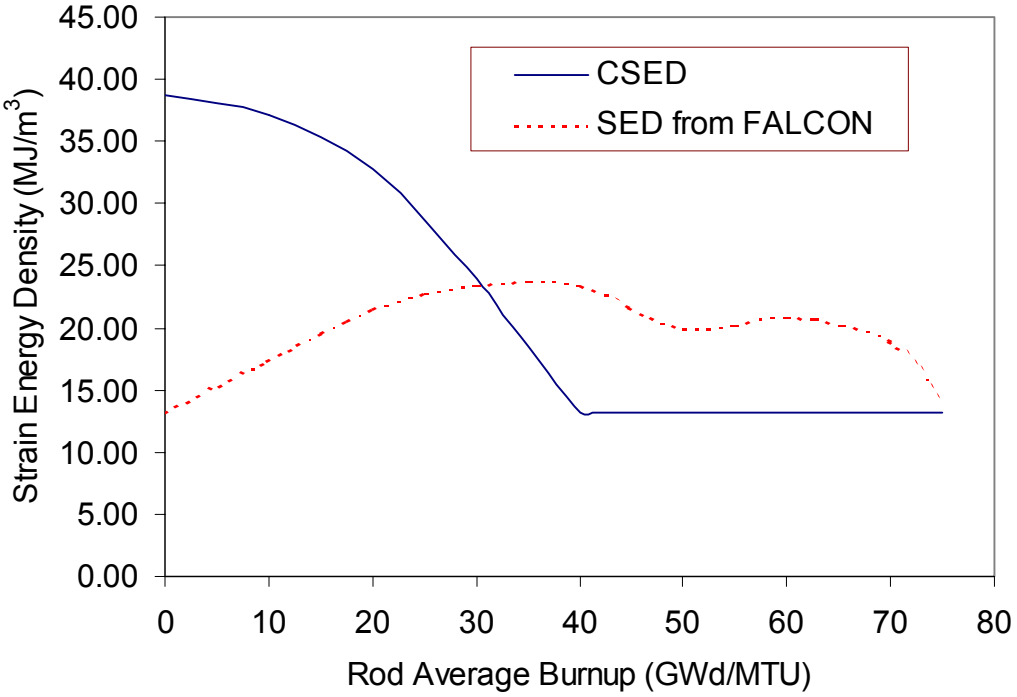

Figure 3-14
Strain energy density from fuel rod analysis (Step 4) and critical strain energy density from mechanical properties and oxidation (Step 3). Cladding failure by PCMI is possible once SED exceeds CSED curve.

The resultant fuel rod failure threshold for PWR HZP RIA events defined in terms of radial averaged fuel enthalpy is shown in Figure 3-15 as a function of rod average burnup for the three different PWR fuel rod designs evaluated using the described methodology. The thresholds shown in Figure 3-15 are applicable to low-Sn Zircaloy-4 cladding material without oxide spallation or similar types of material such as niobium-based cladding alloys with equivalent or improved ductility.

The lowest of the three curves shown in Figure 3-15 is compared to the results of RIA experiments performed using commercial reactor fuel in Figure 3-16. Shown in Figure 3-16 is the maximum radial average peak fuel enthalpy as a function of test segment burnup for tests from the CABRI REP Na UO_2 rod test series and the NSRR tests. For the CABRI REP Na tests, only the rods with non-spalled oxide layers are included in the comparison. Also included in the high burnup data from CABRI is REP Na-11 which was a test using a rodlet with M5 cladding.

Although the curve shown in Figure 3-16 was developed for Zr-4 cladding material, REP Na-11 with M5 cladding supports the use of this failure threshold as conservative threshold for some advanced cladding alloys.

The NSRR tests shown in Figure 3-16 include rods from both the JMTR series and the PWR series (See Appendix A). Since the failure threshold has been developed for initial coolant temperatures near 290ºC, the NSRR tests shown in Figure 3-16 have been translated from cold to hot coolant conditions using the analysis methodology described in Section 2. This was accomplished by performing an analysis of the NSRR experiments in which the coolant temperature was increased from ~25ºC to 290ºC and using the appropriate CSED curve (see Section 2).

It should be noted that the abscissa shown in Figure 3-16 is peak burnup because the burnup values reported for the experiments are the uniform values for the short test segment. The axial power shape shown in Figure 3-12 was used to relate the rod average to the rod peak burnup values for the fuel rod failure threshold curve. The fuel failure threshold bounds most of the experiments that survived without cladding failure to a burnup of 64 GWd/MTU. Several test rods reside at or above the fuel rod failure threshold using this methodology. These rods exhibited no evidence of failure or incipient cladding cracking. The fact that several rods reside above the failure threshold demonstrates the conservative nature of the approach used to develop the failure threshold

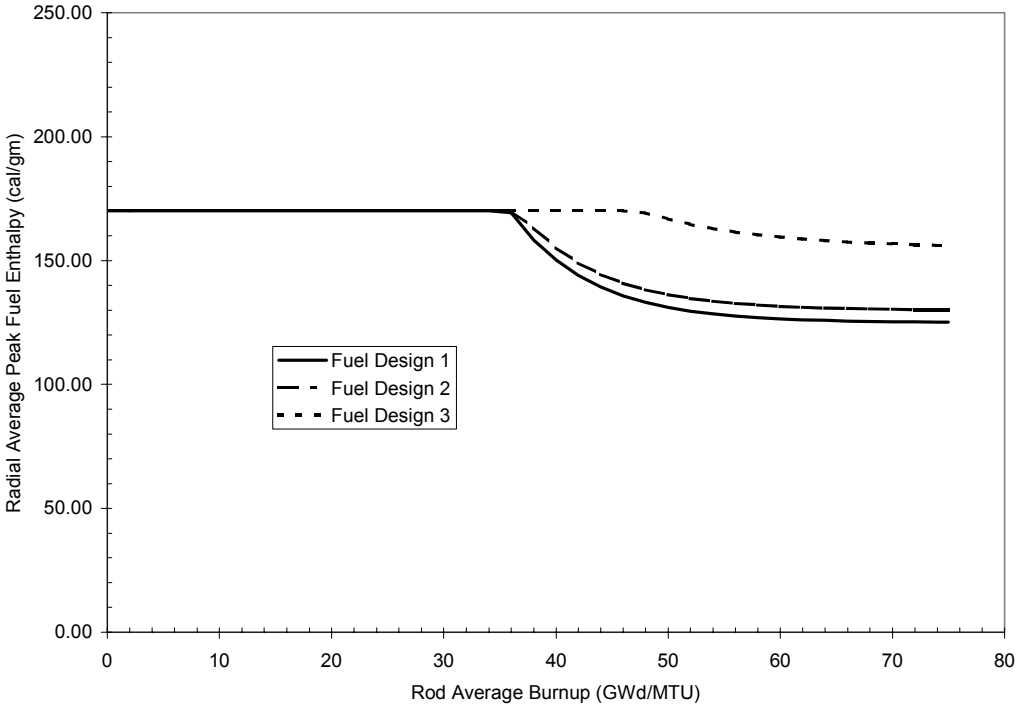

Figure 3-15
Fuel rod failure threshold for three different fuel rod designs determined using analysis methodology. The failure threshold is defined in terms of radial average peak fuel enthalpy.

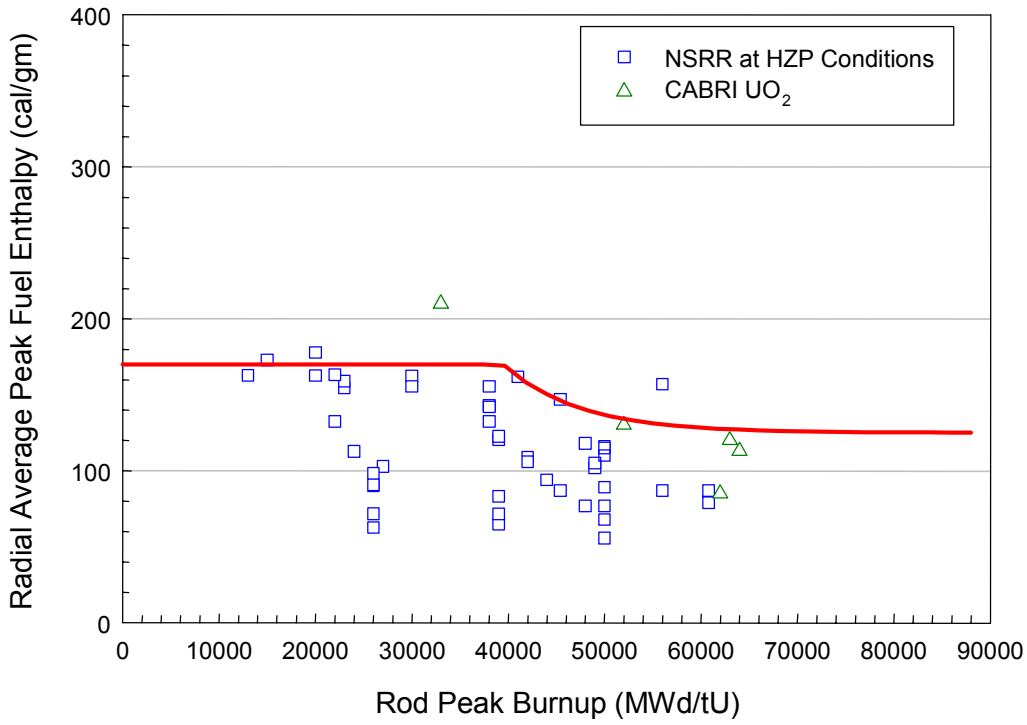

Figure 3-16
Comparison of fuel rod failure threshold to the results of RIA-simulation experiments from NSRR and CABRI on irradiated commercial reactor fuel rods. The abscissa is rod peak burnup since this represents the burnup for each test segment.

3.3 Revised Fuel Rod Failure Threshold

The curve shown in Figure 3-17 is the revised fuel rod failure threshold for non-spalled Zircaloy-4 cladding and is defined as a maximum value for the radial average peak fuel enthalpy in cal/gmUO_2 as a function rod average burnup. The fuel rod failure threshold is applicable to non-spalled Zircaloy-4 clad fuel rods irradiated to a rod average burnup of 75 GWd/MTU with a maximum oxide thickness less than 100 microns. The revised fuel rod failure threshold is applicable to fuel rod designs with a cladding wall thickness greater than 570 microns. The constant threshold of 170 cal/gm for the radial average peak fuel enthalpy below a rod average burnup of 36 GWd/MTU is established to preclude cladding failure by either high temperature or PCMI mechanisms. Above 36 GWd/MTU, the threshold is established to preclude PCMI cladding failure. At rod average burnup levels beyond 60 GWd/MTU, the fuel rod failure threshold saturates at a maximum radial average enthalpy of 125 cal/gm.

The fuel rod failure threshold (H_f) shown in Figure 3-17 is represented by the following expression.

For a fuel rod average burnup < 36 GWd/MTU

$$H_f = 170 \text{ cal/gm}$$

For a rod average burnup (Bu) > 36 GWd/MTU

$$H_f = 125 + 7058*\exp(-.1409*Bu)$$

The revised fuel rod failure threshold is supported by RIA-simulation tests performed on test segments with a maximum burnup level of 64 GWd/MTU. The analysis methodology presented in Section 3.2 was used to extrapolate the fuel rod failure threshold to a rod average burnup of 75 GWd/MTU. The conservative assumptions used to define the influence of burnup on the cladding ductility will accommodate the effect of burnup for the fuel designs targeted for extended burnup applications. As the results of tests planned for CABRI and NSRR on high burnup fuel rods become available, these results can be used to confirm the applicability of the revised fuel rod failure threshold beyond 64 GWd/MTU.

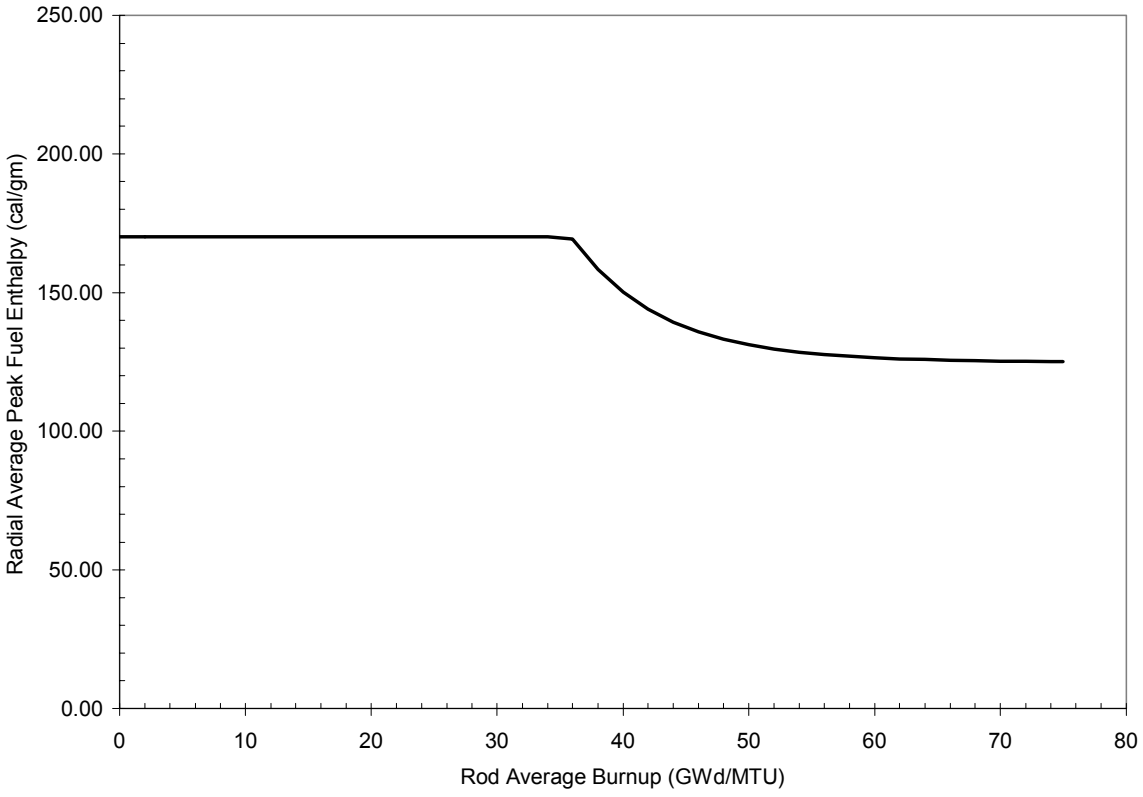

Figure 3-17
Revised fuel rod failure threshold for the licensing analysis of HZP RIA events. The curve is applicable to non-spalled low-Sn Zircaloy-4 clad fuel rods.

The threshold shown in Figure 3-17 is applicable to the PWR HZP Control Rod Ejection accidents and is based on the lower bound of the three fuel designs used in the methodology. The maximum radial average fuel enthalpy results from plant transient analyses would be compared to the curve in Figure 3-17 to estimate the number fuel rod failures for radioactivity dose calculations. The fuel rod failure threshold for at-power RIA events (core power greater

than 2%) should continue to be DNB as defined in Standard Review Plan Chapter 4.2 and Chapter 15.

3.3.1 Impact of Advanced Alloys

Since it is expected that advanced cladding alloys will exhibit superior material ductility at higher burnup values, the threshold shown in Figure 3-17 represents a conservative lower bound for these materials and therefore is valid for use with advanced alloys. The threshold curve shown in Figure 3-17 can be modified for advanced alloy cladding material by using the appropriate mechanical property tests to redefine the CSED as a function of oxide thickness (Step 1) and/or using oxidation data to define the oxide thickness as a function of burnup (Step 2).

Redefining the cladding CSED as a function of oxide thickness requires ultimate tensile strength and total elongation data from ring tension and cladding burst tests on the advanced alloy material. These data should be used to calculate the CSED using the approach described in Section 2.3.2. The new CSED function is then used in Step 1 of the fuel rod analysis methodology. Similarly, oxidation data for fuel rods with advanced cladding material can be used to develop an oxide thickness accumulation as a function of rod average burnup. The new relationship is then used in Step 2 of the fuel rod analysis methodology. The combination of the CSED and oxide thickness relationships yields an improved CSED versus burnup curve in Step 3 of the fuel rod analysis methodology.

Using data representative of advanced alloys would result in a fuel rod failure threshold curve that would be higher than the low-Sn Zircaloy-4 curve for a rod average burnup above 30 GWd/MTU.

3.3.2 Applicability to the BWR Control Rod Drop Accident

The Rod Drop Accident (RDA) is the design basis reactivity initiated accident for BWRs. As discussed in Section 2.1, the current fuel rod failure threshold for BWR RDAs is defined in Standard Review Plan Section 4.2 as a maximum radial average peak fuel enthalpy of 170 cal/gm for events that initiate at zero and low power. This threshold is based on cladding failure due to high temperature mechanisms associated with post-DNB operation and is assumed to be independent with burnup. Rods that are calculated to exceed a maximum radial average fuel enthalpy of 170 cal/gm are used to calculate the number of fuel rod failures for demonstrating compliance to on-site and off-site dose requirements.

Even though the fuel rod failure threshold shown in Figure 3-17 was developed using experimental data and analytical evaluations primarily from PWR fuel rod conditions, the curve is also applicable to the HZP BWR RDA event. Mechanical property tests have shown that irradiated BWR Zircaloy-2 cladding exhibits material ductility that is equal to or greater than irradiated PWR Zircaloy-4 cladding at temperatures above 280°C [Wisner 1998]. One reason for this is the lower level of outer surface cladding corrosion and the lower hydrogen content present in BWR Zircaloy-2 cladding. Therefore, the mechanical property data used to develop the curve shown in Figure 3-17 would represent a lower bound of BWR cladding ductility at

temperatures above 280°C, which corresponds to BWR HZP conditions. As a result, the revised fuel rod failure threshold also serves as a lower bound failure threshold for the HZP RDA event at rod average burnup levels above 35 GWd/tU.

Initial coolant temperature and pressure conditions lower than HZP are possible for the BWR RDA event because of the reactor startup process [Heck 1995]. These conditions include cold zero power (CZP) at temperatures between 20°C and 100°C and a coolant pressure less than 1 MPa. The failure mechanisms for BWR fuel rods are different at lower coolant temperature and pressure conditions and therefore, the fuel rod failure threshold shown in Figure 3-17 is not necessarily applicable to the BWR RDA event initiated below HZP conditions.

Several evaluations have been conducted to estimate the probability that a BWR control rod drop accident would result in unacceptable consequences [Rusche 1976, Thadani 1987, Diamond 1998]. All these evaluations have demonstrated that the overall frequency of occurrence for an RDA event to cause unacceptable consequences is less than $1x10^{-7}$/reactor-year. BNL has previously defined $1x10^{-7}$/reactor-year as a cutoff below which the frequency of the event is inconsequential [Diamond 1998]. It should also be noted that the probability for an RDA event at CZP is even lower than for HZP conditions because, in the case of CZP, less control rods have been withdrawn from the core.

Because of the low frequency of occurrence for the BWR RDA event, it is suitable to use a more realistic analysis approach to calculate the worth of the dropped control rod, to define the conditions at the time of the RDA event, and to calculate the characteristics of the power pulse and energy deposition. Such an analyses would show that the BWR HZP RDA event is typically the limiting RDA event because 1) control rod worths are generally higher at HZP and 2) the fraction of prompt energy deposition (defined as the energy associated with the gaussian power pulse) is considerably higher at HZP. Combined together, these factors produce larger radial average peak fuel enthalpy levels and greater thermal and mechanical demands on the cladding as compared to a CZP RDA event.

3.3.3 Fuel Rod Failure Threshold for At-Power RIA Events

The fuel rod failure threshold shown in Figure 3-17 was developed based on the HZP REA event. The energy deposition from the HZP REA event generally bounds all other reactivity initiated accidents in the reactor design basis safety analysis report. In addition, all the experimental test programs have focused on the HZP CEA event in developing the power pulse characteristics, initial power levels, and coolant conditions. However, the fuel rod failure threshold defined in SRP Section 4.2 also includes the HFP REA event and is defined as DNB for both PWR and BWR accidents. The industry position is that DNB should remain the fuel rod failure threshold for at-power or HFP RIA event in PWR's. At-power conditions are defined as all reactor states above 2% full power.

Because of the thermal-hydraulic conditions under at-power operation, the radial average peak fuel enthalpy to initiate DNB is 70-80 cal/gm. This is typically 20-50 cal/gm above the fuel rod stored energy at HFP conditions. To ensure that fuel rod failure by PCMI would not occur below this level of fuel enthalpy, a limited FALCON analysis was conducted at 50 GWd/MTU for HFP conditions. The results of that analysis are summarized in Table 3-2. The results demonstrate

that the radial average peak fuel enthalpy required to produce a certain level of SED by PCMI for at-power conditions is the same as for HZP. Because of the initial stored energy of the fuel is 27 cal/gm, the deposited energy is less for the at-power condition. The fuel rod stored energy to initiate DNB is well below the radial average peak fuel enthalpy shown in Table 3-2 and therefore, DNB would be initiated at a considerably lower deposited energy for the at-power event.

Neutron kinetics calculations show that the control rod worths and the deposited energy levels are lower for the at-power RIA event because of the increased doppler coefficient [Stelletta and Waeckel 1997; Stelletta and Moreau 1996]. It is unlikely that the radial average peak fuel enthalpy will reach or exceed the failure threshold developed in Section 3.2. As discussed in Section 3.1.1 fuel rod failure by DNB occurs by time at temperature processes such as oxidation induced embrittlement or ballooning/burst. The rapid nature of an RIA event decreases the potential of fuel rod failure by these mechanisms. Therefore, using DNB as the fuel rod failure threshold for at-power RIA events is bounding.

Table 3-2
Results of at-power analysis for a fuel rod average burnup 50 GWd/MTU

Power Level (%)	Initial Fuel Rod Stored Energy (cal/gm)	Deposited Energy (cal/gm)	Radial Average Peak Fuel Enthalpy (cal/gm)	SED (MJ/M^3)
0	16.9	140	143	13.2
50	27.1	130	143	13.5

3.3.4 Fuel Rod Failure Threshold Uncertainty Evaluation

An assessment has been made to evaluate the impact of uncertainties within the analytical approach used to establish the PCMI portion of the fuel rod failure threshold curve shown in Figure 3-17. The PCMI portion of the failure threshold corresponds to rod average burnup levels above 30 GWd/MTU. An important component of this approach is the FALCON calculations used to determine the amount of PCMI that occurs during an RIA power pulse. Since these calculations are subject to some uncertainties, it is appropriate to address the impact of these uncertainties on the analytical results. Also, uncertainties exist in the cladding integrity model used to establish the fuel enthalpy at failure and the impact of this uncertainties should be assessed. The sources of uncertainties in the analytical approach that were evaluated include;

1) The as-manufactured fuel rod dimensions and power history used to establish the initial conditions at the start of the power pulse

2) Initial enrichment and gadolinia content

3) Power pulse width

4) Critical strain energy density model

The uncertainty evaluation consists of both a qualitative assessment based on past experience in fuel rod analysis modeling and a quantitative assessment using analytical calculations to determine the impact of a particular model or variable. Where possible, the impact of the uncertainty in terms of change in the cal/gm of the fuel rod failure threshold is provided.

3.3.4.1 Fuel rod condition at start of the transient analysis

The fuel rod conditions at the start of the RIA transient analysis were established using a steady state analysis up to the fuel rod burnup level that the transient was postulated to occur, i.e., a rod average burnup of 40 GWd/tU. The key initial conditions that influence the calculated fuel rod thermal and mechanical response during the power pulse include the residual fuel-cladding gap, the radial burnup and power distribution, and the cladding condition. The residual fuel-cladding gap and the radial burnup and power distribution were obtained from the steady state analysis. The cladding condition was defined through the cladding integrity model and is based on an upper bound outer surface oxidation rate.

The steady state analysis performed using FALCON includes the effects of pellet densification, fission product induced solid swelling, pellet relocation, and cladding creep on the calculation of the residual pellet-cladding gap used in the transient analysis. Experience has shown that the combination of these mechanisms cause gap closure in PWR fuel at burnup levels ranging between 15 and 20 GWd/tU. At burnup levels beyond gap closure (> 20 GWd/tU), the residual fuel-cladding gap at HZP represents mostly the thermal contraction caused by the decrease from full power to hot zero-power conditions. Such HZP residual pellet cladding gap thicknesses are dependent on the power level prior to shutdown and are generally less than 20 microns as shown PIE observations. Uncertainties in the models used to calculate the residual pellet-cladding gap influence the burnup level at which gap closure occurs. However, once gap closure occurs these fuel behavior models have less of an impact on the residual pellet-cladding gap. Since the PCMI portion of the failure threshold occurs above a rod average burnup of 30 GWd/tU, gap closure at operating conditions is present in the peak burnup region and the impact of model uncertainties on the residual pellet-cladding gap at hot-zero power are decreased. This conclusion is supported by the NRC PWR RIA PIRT review that assigned a knowledge ranking of 82 (out of 100) to the residual pellet-cladding gap at the start of the transient [Boyack, et.al. 2001]. The knowledge ranking provided by the PIRT panel is an indication of how well known a particular parameter is understood. The knowledge ranking of 82 demonstrates that the PIRT panel felt that fuel rod analysis methods could provide a good estimate of the residual pellet-cladding gap thickness and that the uncertainties for this value are low.

Furthermore, variations in the residual pellet-cladding gap of 100% will not significantly impact the calculated thermal and mechanical response of the fuel rod during an RIA power pulse. The amount of fuel pellet thermal expansion caused by a radial average fuel enthalpy level above 100 cal/gm far exceeds a variation in the residual pellet-cladding gap of 5 to 10 microns.

Other sources of uncertainty in the initial fuel rod condition at the start of the transient power puluse include variations in the as-fabricated fuel rod dimensions. At burnup levels beyond 30 GWd/tU, the impact of fuel rod fabrication tolerances will be small on the transient thermal and mechanical response during an RIA power pulse.

Based on these points, it can be argued that the uncertainty in the failure threshold shown in Figure 3-17 associated with variations in the residual pellet-cladding gap at the start of the power pulse is small.

3.3.4.2 Initial ^{235}U Enrichment and Gadolinia Content

The analytical evaluation defined the initial ^{235}U enrichment at 4.8% in the fuel rod cases used to establish the failure threshold shown in Figure 3-17. No analyses were conducted using gadolinia burnable poison absorber. Sensitivity evaluations were conducted using the TUBRNUP model to establish the impact of different ^{235}U enrichment and gadolinia oxide (Gd_2O_3) contents on the radial power and burnup distribution. Uranium-235 enrichments between 3.8% and 4.95% and gadolinia contents of 8 wt% were evaluated to determine the sensitivity of the radial power and burnup distributions to variations in these parameters. In addition, a select number of FALCON calculations were performed to determine the impact on the radial temperature distribution of variations in initial ^{235}U enrichment.

The detailed results of the enrichment and gadolinia sensitivity evaluation are presented in Section 4.3.1.2. Depending on the enrichment level, the radial power and burnup distribution can vary by 10 or 20% from that used in the PCMI analysis. However, it can be concluded from the FALCON calculations that variations in the radial temperature distribution are below 100°C over the range of enrichments and gadolinia content evaluated. These variations have a no significant impact on the PCMI loading of the cladding. As a result, the fuel rod failure threshold shown in Figure 3-17 is applicable to enrichment levels up to 4.95% and gadolinia contents of 8 wt%.

3.3.4.3 Sensitivity to Power Pulse Width

The power pulses used in the FALCON analyses to establish the fuel rod failure threshold were generated with a pulse width of 20 milliseconds. However, the power pulse width determined from the results of neutron kinetics analyses, which are used to compare to the failure threshold, can vary between 10 and 30 milliseconds. A series of sensitivity calculations were performed with FALCON to assess the impact of pulse width on the PCMI fuel rod failure threshold shown in Figure 3-17. The FALCON calculations were performed at rod average burnup levels of 40 and 75 GWd/tU and power pulse widths of 10, 15, and 30 milliseconds. The FALCON calculations incorporate the impact of pulse width through the heat conduction processes, which influence the radial temperature profile and the cladding temperature. No additional fission gas bubble expansion or dynamic gas loading effects were included in the PCMI analysis.

The results of the pulse width sensitivity analysis are shown in Figure 3-18 for a rod average burnup of 40 GWd/tU and 75 GWd/tU. Shown in Figure 3-18 is the radial average peak fuel enthalpy to produce cladding failure by PCMI as a function of pulse width. The FALCON calculations demonstrate that the fuel rod failure threshold decreases by about 5 to 10 cal/gm for pulse widths below 20 milliseconds. Above a pulse width of 20 milliseconds, the failure threshold at both 40 and 75 GWd/tU saturate to values very close to those shown in Figure 3-17.

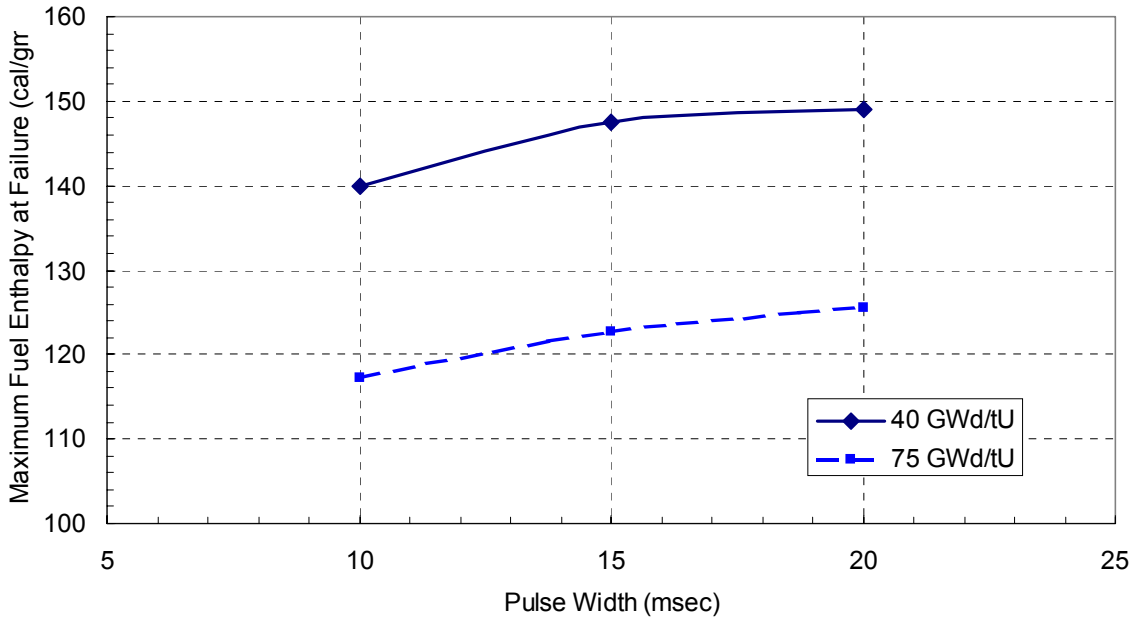

Figure 3-18
The Radial Average Peak Fuel Enthalpy at Cladding Failure as a Function of Power Pulse Width for Rod Average Burnup Levels of 40 GWd/tU and 75 GWd/tU.

3.3.4.4 Critical Strain Energy Density Model

The Critical Strain Energy Density (CSED) model is developed from mechanical property tests on irradiated cladding material with variations in material condition. As discussed in Section 2.3, the mechanical property data used to develop the CSED model is subject to data scatter caused by the test techniques used to measure the properties and variations in material condition. Because of the data scatter within the mechanical property results such as total elongation and yield stress, uncertainties arise in the CSED model derived from this data. The CSED model used in the development of the failure threshold shown in Figure 3-17 represents a best-fit to all the available CSED data from mechanical property tests on irradiated cladding with non-spalled outer surface oxide layers (as shown in Figure 2-11). The data used in the model development included ring tension tests, axial tension tests, and tube burst tests. Since a best-fit approach was used to develop the CSED model correlation, the CSED data from the different tests are scattered about the correlation.

The data scattered about the CSED correlation can be viewed as an indication of the uncertainties within the CSED model. This is not exactly true because of the method used to construct the database of mechanical properties. Since the amount of data was insufficient in any one data set to develop a consistent CSED correlation, it was necessary to combine data from different test methods (ring tension versus axial tension tests) and different test temperatures (300°C versus 400°C). This gives an impression of large data scatter where in actuality; the data scatter in any given data set is considerably less.

To address the issue of data scatter and uncertainty in the CSED model, two different data fits were developed from the CSED database. First, a data fit was developed using the lower bound of the non-spalled ring tension and tube burst CSED data. It can be argued that ring and tube burst mechanical tests are more applicable to PCMI loading conditions since these tests primarily measure the mechanical properties in the hoop direction. The resulting CSED correlation represents a lower bound curve. As discussed in Section 2.4, this curve however does not adequately differentiate between the failed and non-failed rods for the CABRI REP Na tests using UO_2 fuel rods. Using such a lower bound mechanical integrity curve combined with the conservative upper bound oxidation rate model described in Section 3.2.2 would produce an excessively conservative failure threshold. Therefore, the CSED model based on the lower bound of the non-spalled data was not considered further.

Second, a CSED correlation data fit was developed using a best-fit to the non-spalled burst test data. The burst test CSED data displays the least amount of data scatter and also represents the mechanical properties in the hoop direction under biaxial stress conditions. Unfortunately, the amount of data available for tube burst tests is limited. As discussed in Section 2.4, a comparison to the calculated SED values for the REP Na tests with the CSED curve developed from the burst data shows that this curve resides at the upper boundary of the non-failed CABRI REP Na tests. The CSED correlation based on the burst data is somewhat below the CSED based on the entire database of non-spalled data at oxide layer thickness to cladding thickness ratios below 0.10. This difference would result in a 5 to 10 cal/gm decrease in the failure threshold in the 25 to 40 GWd/tU burnup range. At oxide layer thickness to cladding thickness ratios above 0.12 to 0.13, the best-fit to the tube burst data and the original CSED correlation display very close agreement. As a consequence, the impact of using a CSED correlation based on the tube burst data on the failure threshold shown in Figure 3-17 is small at fuel rod average burnup levels above 40 GWd/tU.

3.3.5 Advantages of Revised Fuel Rod Failure Threshold

The revised fuel rod failure threshold is based on an analytical approach supported by experimental data from post-irradiation examinations, separate effects mechanical tests, and integral RIA-simulation tests. The technical foundation of the threshold includes the most current understanding of both low and high burnup fuel rod transient behaviors available from experimental programs and analysis methods. In the low burnup regime, the fuel rod failure threshold is consistent with the current limit used in licensing, i.e., the threshold is established based on failure by high cladding temperature mechanisms such as oxidation-induced embrittlement or ballooning/burst. Above 30 GWd/MTU, the fuel rod failure threshold is defined based on the PCMI failure mechanism controlled by the evolution of cladding ductility with increasing burnup.

It is anticipated that no new data from RIA-type tests will become available to further develop the revised failure threshold until 2002 or beyond. As already mentioned, the methodology used to construct the failure threshold is based on a strong technical understanding of the fuel behavior during an RIA event. The results of over 50 RIA-simulation tests have been used to establish the knowledge of fuel behavior during RIA power pulses. The combined approach of integrating the experience from separate effects mechanical property tests with the experience from integral RIA-simulation tests has yielded a robust methodology from which a fuel rod

failure threshold can be derived. As new RIA-simulation tests are performed on high burnup fuel rods, this data can be used to confirm the revised failure threshold at extended burnup.

The approach used to develop the fuel rod failure threshold is consistent with the conclusions of the NRC-sponsored Phenomena Identification and Ranking activity conducted for the PWR Control Rod Ejection accident and the methods proposed by NRC to resolve the RIA issue [Meyer 2001]. The effects of burnup on the different fuel rod phenomena identified in the RIA PIRT have been included in the evaluation used to develop the fuel rod failure threshold. In the NRC proposed method to resolve the RIA issue, several steps were outlined including:

- the establishment of a failure threshold that bounds the experimental data
- the adjustment of the failure threshold for advanced alloys using mechanical property tests and analytical methods
- the use of new RIA-simulation tests on high burnup fuel rods with advanced alloys to confirm the threshold.

These steps are also included in the Industry approach outlined above to establish the revised fuel rod failure threshold.

4
RIA CORE COOLABILITY LIMIT

Section 4 summarizes the technical bases for revisions to the RIA core coolability limit described in NUREG-0800 Standard Review Plan Section 4.2 and Regulatory Guide 1.77 to incorporate the effects of burnup [NRC 1981; AEC 1974]. The revisions are developed to include the effect of burnup on the core coolability limit used in both zero and full power PWR and BWR reactivity events. The core coolability limit is expressed in terms of the radial average peak fuel enthalpy as a function of rod average burnup.

Section 4 begins with a summary of the current understanding of fuel dispersal and fuel-coolant interaction issues as they relate to loss of fuel rod geometry. Included in the summary is a review of both the zero and low burnup RIA tests conducted in the US and Japan that resulted in fuel dispersal and fuel coolant interaction. These tests demonstrate that molten fuel is an important precursor to fuel-coolant interaction. The recent tests on high burnup fuel that resulted in solid particle fuel dispersal are also reviewed. The effect of fuel pellet burnup, pulse width, and the high burnup rim structure on the behavior the fuel pellet during the energy deposition is presented.

Section 4 also presents a description of the methodology and approach used to define the revised core coolability limit as a function of burnup. The revised limit on the radial average peak fuel enthalpy is established to preclude incipient fuel pellet melting and was determined using analytical methods and experimental data. The methodology included the effects of burnup on the radial power and burnup distribution, the effect of burnup on the UO_2 melting temperature, the effect of post-DNB heat transfer, and the influence of full power operation. The revised core coolability limit is applicable to 75 GWd/MTU.

4.1 Current Understanding of Fuel Coolability Issues

There are two primary safety concerns raised in connection with the rapid energy deposition and the resulting excessive fuel enthalpy of a reactivity initiated accident: (1) disruption of the core geometry to impair long-term coolability and (2) local yielding of the pressure vessel [AEC 1974]. Under postulated accident conditions, it may be possible to cause the insertion of sufficient reactivity to produce prompt criticality and rapid deposition of energy into the fuel. Because of the heat transfer characteristics of UO_2 fuel, this energy is momentarily stored in the fuel pellet and may damage the fuel rods by fuel pellet fragmentation and melting. At high energy densities, the possibility exists for prompt dispersal of fuel material into the coolant. The rapid dispersal of high energy fuel material into the coolant may produce coolant pressure pulses that could create destructive forces on the fuel assemblies or reactor vessel, thereby causing changes in the reactor core geometry and deformation of the reactor vessel [Tsuruta et al. 1985; Tompson 1964].

The main events that can interfere with maintaining a coolable core geometry and ensuring the reactor vessel integrity are the rapid dispersal of fuel material into the coolant and the subsequent fuel-coolant interaction (FCI). In defining safety limits to preclude core damage, it is important to understand the mechanisms controlling fuel dispersal and FCI under accident conditions. Results from experiments on unirradiated and irradiated test rods show that the factors that influence fuel dispersal and FCI include such mechanisms as the reactivity insertion characteristics, the fuel enthalpy, the coolant conditions, and the fuel rod burnup [Ishikawa and Shiozawa 1980].

4.1.1 Fuel Dispersal from Unirradiated Rods

Early experiments performed in the US and Japan to study transient fuel performance using unirradiated test rods demonstrated that at energy depositions above 250 cal/gm, the fuel enthalpy reached levels that produced molten fuel, energetic dispersal of molten fuel particles, and the conversion of nuclear energy to mechanical energy [Ishikawa and Shiozawa 1980; Martison and Johnson 1968; Miller and Lussie 1969]. Based on these experiments, the NRC established a limit of 280 cal/gmUO_2 on the radial average fuel enthalpy to preclude the potential for the dispersal of molten fuel particles during an RIA event [AEC 1974]. The objective of the NRC in establishing this limit was to eliminate the potential for molten fuel-coolant interaction and the generation of coolant pressure pulses that could damage the reactor core or pressure vessel [AEC 1974, MacDonald et al. 1980].

Most of the experimental data on the transient fuel behavior at high energy depositions have been obtained from unirradiated test rods in early test programs in the US and Japan. In these programs, more than 50 tests have been performed at radial average fuel enthalpies above 200 cal/gmUO_2 (See Table 4-1) [Miller 1970; Miller 1971; Ishikawa and Shiozawa 1980; Tsuruta et al. 1985]. The experimental results from these tests show that the test rods began to fragment into several large pieces near radial average fuel enthalpies of 250 cal/gmUO_2. Above 200 cal/gmUO_2, some tests displayed partial clad melting, and in a subset of these tests, the clad melting contributed to the fuel rod fractures. However, these failures resulted in little post-failure consequences such as fuel material dispersal, fuel coolant interaction, or coolant pressure pulses. In tests above a radial average fuel enthalpy of 280 cal/gmUO_2, prompt dispersal of molten fuel particles was observed along with the development of fuel-coolant interaction and coolant pressure pulses. The magnitude of the fuel-coolant interaction increased with deposited energy levels above 350 cal/gmUO_2. At these energy levels, the UO_2 fuel material begins to melt during the energy deposition, and at high enough fuel enthalpy levels, fuel vaporization is initiated. The high fuel temperatures and fuel phase changes cause large rod internal pressures during the energy deposition and lead to cladding rupture (below the Zircaloy melting temperature) and the rapid dispersal of molten fuel into the coolant.

Table 4-1
RIA Tests with Energy Deposition Above 200 cal/gm

	No. of Tests	**Deposited Energy**	Energy at **Cladding Failure**	**Mechanical Energy Conversion**
SPERT-CDC	>33	195 - 590 cal/gm	300 - 425 cal/gm	0 - 0.2%
NSRR	>25	265 - 555 cal/gm	220* - 350 cal/gm	0 - 1.3%

* - tests with rod internal pre-pressurization greater than 3 MPa

Table 4-2
RIA Tests with Energy Deposition After Failure (ΔH less than 200 cal/gm)

Test	Burnup	Pulse Width	Fuel Enthalpy Increase at Failure	Maximum Fuel Enthalpy Increase	Enthalpy Increase after Failure	Fuel Dispersal After Failure	Mech. Energy Conversion.
NSRR JMH-5	30	4.4	185	210	25	Yes	Yes (.4%)*
NSRR HBO-1	50	4.4	60	73	13	Yes*	No
NSRR HBO-5	44	4.4	77	80	3	Yes	No
NSRR TK-2	48	4.4	60	107	47	Yes	Yes (.5%)*
NSRR TK-7	50	4.4	86	95	9	Yes	No
NSRR FK-7	61	4.3	62	129	67	Yes	Yes (.3%)
NSRR FK-6	61	4.4	62	129	67	Yes	Yes (?)
REP Na-1	65	9.5	15	100	85	Yes	Yes (?)
CDC 859	32	17	85	154	69	No	No
PBF RIA 1-2	5	20	125	170	45	No	No
CDC 568	3.5	26	147	161	14	No	No
REP Na-10	64	31	67	95	28	No	No
REP Na-8	60	70	57	92	35	No	No

* Based on amount of material dispersed.

4.1.2 Fuel Dispersal for High Burnup Rods

Recently, RIA-simulation experiments on test rods refabricated from previously irradiated commercial fuel rods have shown that a potential exists for the dispersal of non-molten fuel material following cladding failure at energy deposition levels well below that required to produce fuel melting [Sugiyama 2000; Schmitz and Papin 1999]. As has been demonstrated in tests on unirradiated fuel rods, dispersal of fuel pellet material may lead to coolability concerns due to the potential for coolant channel flow blockage, loss of coolable geometry, or pressure pulse generation (See Section 4.1). However, the development of these coolability concerns depends on the amount, particle size, and the thermal energy of the pellet material dispersed in the coolant, as well as the coolant conditions.

A total of eight rods with burnup levels ranging from 30 to 65 GWd/MTU experienced cladding failure and then dispersal of fuel material into the coolant. The power pulses for each of these rods contained additional energy deposition after cladding failure. A summary of these rods is shown in Table 4-2, along with five other test rods that had energy deposition after cladding failure, but did not disperse fuel material. Post-test examinations have found that the pellet material dispersed into the coolant in these tests was finely fragmented with mean diameters between 10 and 50 microns. In all cases, the temperature of the pellet material dispersed into the coolant was below the UO_2 melting temperature. No evidence of prior melting such as spherical particles with smooth surfaces was seen in the micrographs of the dispersed material [Tsuruta et al. 1985; Sugiyama 2000]. In the case of four tests with fuel dispersal, thermal to mechanical energy conversion was measured by in-pile instrumentation. For the other tests with fuel dispersal, either no mechanical energy conversion was measured by the in-pile instrumentation or no instrumentation was available for monitoring the energy release.

Dispersal of non-molten fuel material is a function of the energy deposition after cladding failure, the pellet burnup, and the pulse width of the energy deposition. A plot of energy deposition after cladding failure versus the power pulse width is shown in Figure 4-1 for the tests listed in Table 4-2. As can be seen, fuel dispersal occurred only at pulse widths between 4.3 and 9.5 milliseconds. No fuel dispersal was observed for tests with pulse widths above 10 milliseconds and burnup levels above 60 GWd/MTU, even with energy depositions after failure of 69 cal/gmUO_2.

The propensity for dispersal of pellet material from fuel irradiated beyond 40 GWd/MTU is related to the development of the pellet rim, and is governed by two main factors: (1) the local temperature and stress peaking in the rim during the rapid energy deposition and (2) the fine-grained structure of the pellet rim material and the tendency of the rim material to fracture into small (<20 micron) particles. Analytical evaluations and post-test examinations have shown that the pulse width of the energy deposition influences the thermal and mechanical behavior of the pellet rim region during the power pulse [Montgomery and Rashid 1996]. For energy deposition with narrow pulse widths, heat conduction from the rim region is low. This leads to higher local temperatures in the rim due to the radial power peaking in the rim region. Energy deposition with wider pulses allows for heat conduction from the pellet to the cladding, thus minimizing the temperature peaking in the pellet rim.

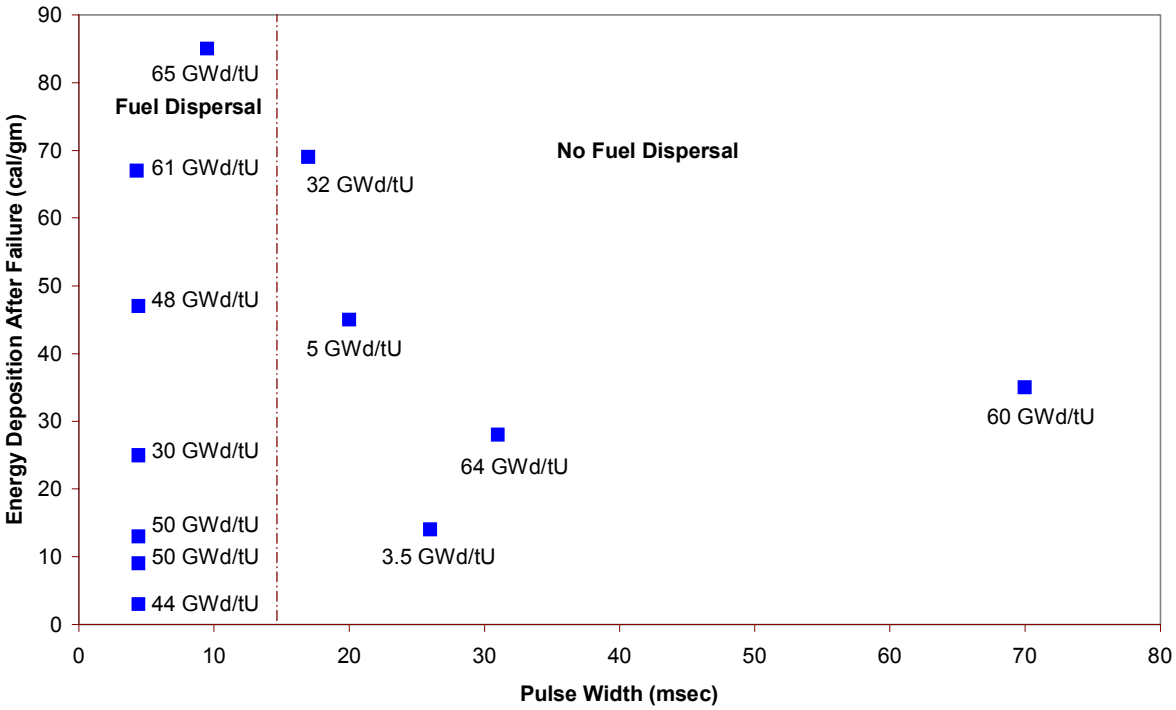

Figure 4-1
High burnup test rods with energy deposition after cladding failure versus full-width half maximum of the power pulse. No fuel dispersal observed for power pulse widths greater than 17 milliseconds.

Fuel rod thermo-mechanical calculations have shown that for pulse widths less than 10 milliseconds and burnup levels greater than 50 GWd/MTU, the peak temperature in the pellet rim is 1.7-2.0 times the centerline temperature. Compared to during normal operating conditions, the rim temperature is 3 - 5 times the pellet periphery temperature [Montgomery and Rashid 1996]. The large temperature peaking occurs over the outer 200-400 microns of the fuel pellet, establishing steep thermal gradients. The main consequences of the thermal behavior in the rim for narrow pulses are the development of large compressive stresses locally in the fuel matrix and the overheating of the fission gas bubbles in the pellet rim. The combination of the compressive stresses in the fuel pellet and the high gas pressure in the fission gas bubbles represents a large amount of stored potential energy that is available for release as kinetic energy upon cladding failure, propelling high temperature fuel particles from the rim region.

The same type of calculations using pulse widths greater than 10 milliseconds show that heat conduction from the pellet rim to the cladding becomes important for the thermal and mechanical behavior of the pellet rim region. The pellet rim to centerline temperature peaking factor is reduced to 1.2 to 1.5 and the thermal gradients in the rim region are reduced by an order of magnitude because of the increased heat conduction to the cladding [Montgomery and Rashid 1996]. Another key outcome of a wide pulse is that the peak temperature in the fuel occurs at a radial location that is a greater distance from the pellet surface than for narrower pulse widths. The lower temperature peaking in the rim region also decreases the temperature of the fission gas

bubbles. The combination of these factors decreases the likelihood of fuel material dispersal upon cladding failure.

Post-test examinations of the CABRI REP Na-4 and Na-5 tests identified several key features that provide insights into the thermal and mechanical behavior of the pellet rim region [Lespiaux et al. 1997]. The CABRI REP Na-4 test had a ~65 millisecond pulse width and the CABRI REP Na-5 test used a 9.5 millisecond pulse width. Cermography results from the pellet rim regions of the REP Na-5 test rod show an extensive network of radial and circumferential cracks in the outer 400-500 microns of the pellet. The pellet rim remained intact and attached to the cladding, but numerous radial and circumferential cracks were observed in the rim region. The fine porosity within the rim region associated with the grain restructuring and fission gas bubbles remained observable in the high magnification cermographies. A high density of cracks was evident in the fuel region adjacent (r/r_o ~ 0.95) to the pellet rim. Grain boundary decohesion, preferentially oriented in the tangential direction also accompanied the pellet cracking in the fuel material adjacent to the rim region. The grain boundary decohesion may have been caused by the presence of high pressure fission gas bubbles on the grain boundaries that expanded due to reduction in confinement during the heat conduction phase of the event. These post-test features provide an indication of the severe thermal and mechanical conditions experienced during the test. In comparison, the cermography results from the wider pulse test CABRI REP Na-4 showed only an increase in the radial cracks in the pellet periphery with almost no circumferential crack development or grain boundary decohesion. Estimates of the total crack length in the pellet periphery that developed during the power pulse test show that the REP Na-5 experienced about 3 times the extent of cracking as REP Na-4. In both Rep Na-4 and Na-5, the physical characteristics of the inner 80% of the fuel pellet remained unchanged as compared to the pre-test condition.

The combination of the post-test examinations and the thermo-mechanical fuel rod calculations provides a clear picture of the effect of the pulse width on the response of the pellet rim during a power pulse. REP Na-5 with a 9.5 millisecond pulse width experienced significant temperature peaking, high thermal gradients, and large stresses that produced fragmentation of the outer 5%-10% of the fuel pellet. The fragmentation of the outer pellet periphery into particles less than 100 microns would increase the potential for dispersal of most of this material into the coolant by entrainment within the escaping fill and fission gases upon cladding failure. However, REP Na-4 with the ~65 millisecond pulse width displayed only slight pellet fragmentation in the outer pellet periphery. Dispersal of fuel material into the coolant by entrainment within the escaping fill and fission gases would have been unlikely for cladding failure in REP Na-4. These conclusions are consistent with the experimental observations summarized in Table 4-2.

4.1.3 Fuel-Coolant Interaction

The rapid generation of vapor resulting from molten fuel-coolant interaction (FCI) may generate pressure pulses within the reactor core that, if of a sufficient magnitude, can produce significant forces on the fuel assemblies and reactor vessel walls. Out-of-pile experiments conducted to simulate the behavior of molten fuel during a severe core accident [Fletcher 1987] and in-pile experiments conducted to evaluate fuel behavior at high energy depositions during an RIA have identified the mechanisms associated with molten fuel-coolant interactions [Fuketa et al. 1993; Martison and Johnson 1968; Miller and Lussie 1969]. Those experiments have shown that the

rapid generation of vapor leading to large coolant pressure pulses depends on the particle size of the dispersed material, the energy of the dispersed material, and the coolant conditions, primarily, the amount of water to fuel ratio and the coolant subcooling [Fletcher 1987; Fuketa et al. 1993; Martison and Johnson 1968; Miller and Lussie 1969; Vaughan 1979].

The presence of molten fuel material, both in out-of-pile simulation tests and high energy RIA tests, was shown to be a key element in the FCI process. The rapid ejection of molten fuel through the cladding into the coolant causes the fuel to fragment into fine particles due to the hydrodynamic forces between the molten fuel and the coolant [Fuketa et al. 1993; Vaughan 1979]. This process increases the surface area of the molten fuel and enhances the energy transfer rate to the coolant. Also, the heat transfer rate from the fuel particles to the coolant increases with the temperature of the fuel [Tsuruta et al. 1985].

The fragmentation of molten fuel into fine particles has been shown to be a function of the energy deposition and the initial internal gas pressure [Fuketa et al. 1993; Tsuruta et al. 1985]. These factors affect the release mode of the molten fuel from the cladding. The release mode is partially defined by the temperature and velocity of the molten fuel jet exiting the cladding. For low initial internal pressure, energy depositions above 350 cal/gm are required to produce sufficient vapor pressure of UO_2 within the fuel rod to expel the molten fuel through the cladding at the necessary velocity to produce fine fragmentation of the molten material and FCI [Tsuruta et al. 1985; Martison and Johnson 1968; Miller and Lussie 1969]. Experiments with high initial rod internal pressures (> 5 MPa) have shown that finely fragmented molten particles and FCI can develop at fuel enthalpy levels near 275 cal/gm [Fuketa et al. 1993].

One method to assess the level of FCI under rapid power transients is to use the thermal to mechanical energy conversion efficiency defined by the ratio of mechanical energy generated in the coolant to thermal energy in the fuel [Tsuruta et al. 1985; Martison and Johnson 1968; Miller and Lussie 1969; Fuketa et al. 1993]. This ratio is determined based on estimates of the mechanical energy generated in the coolant caused by fuel-coolant interaction. The experimental techniques to detect the mechanical energy generation in the early US and Japanese RIA experiments using test capsules with stagnant ambient water included measuring the upward velocity of the water column or the pressure response of the cover gas [Tsuruta et al. 1985; Martison and Johnson 1968; Miller and Lussie 1969]. This information was then used to calculate the kinetic energy of the water column (E_k) or the compression work of the cover gas (E_c).

The mechanical energy conversion ratio (η_m) is given by:

$$\eta_m = \frac{E_k}{Q_n} \tag{4-1}$$

where Q_n is the total energy deposited in the fuel rod.

The mechanical energy conversion ratios for both CDC-SPERT and NSRR tests [IDO, Tsuruta] with molten fuel are shown in Figure 4-2 as a function of the mean fuel particle size observed in post-test examinations (d_{32}). As can be seen, the mechanical energy conversion ratio is

proportional to $1/d_{32}^{n}$ for tests with molten fuel. In the case of the dispersal of molten fuel during an RIA experiment, n varies between 0.8 and 1.3. This is consistent with molten fuel-coolant interaction experiments performed to study the effects of steam explosions during severe core accidents [Fletcher 1987; Vaughan 1979]. In Figure 4-3, the steam explosion yields as a function of particle size from a series of molten fuel-coolant interaction experiments by Fletcher are shown as a function of the post-test mean particle size [Fletcher 1987]. The explosion yield results also display a dependency with the inverse of the particle size. The exponent n from these experiments is between 0.8 and 0.9.

The results from both RIA experiments and severe core accident experiments that contained molten fuel indicate that the FCI efficiency as defined by the thermal to mechanical energy conversion is approximately proportional to the inverse of the fuel particle size. This is consistent with the theoretical approach proposed by Vaughan which showed that for molten fuel coolant interactions, the efficiency should be proportional to the inverse of the particle diameter [Vaughan 1979].

As mentioned previously, measurable fuel-coolant interaction has also been observed in four tests in high burnup fuel rods. In these tests, no evidence was found to indicate that the particles were molten prior to dispersal into the coolant. The fuel particles collected from the coolant following the tests were irregularly shaped with faceted surfaces, suggesting fracture [Sugiyama 2000]. Previously molten fuel particles dispersed into the coolant generally have a spherical geometry and a smooth surface finish [Tsuruta et al. 1985].

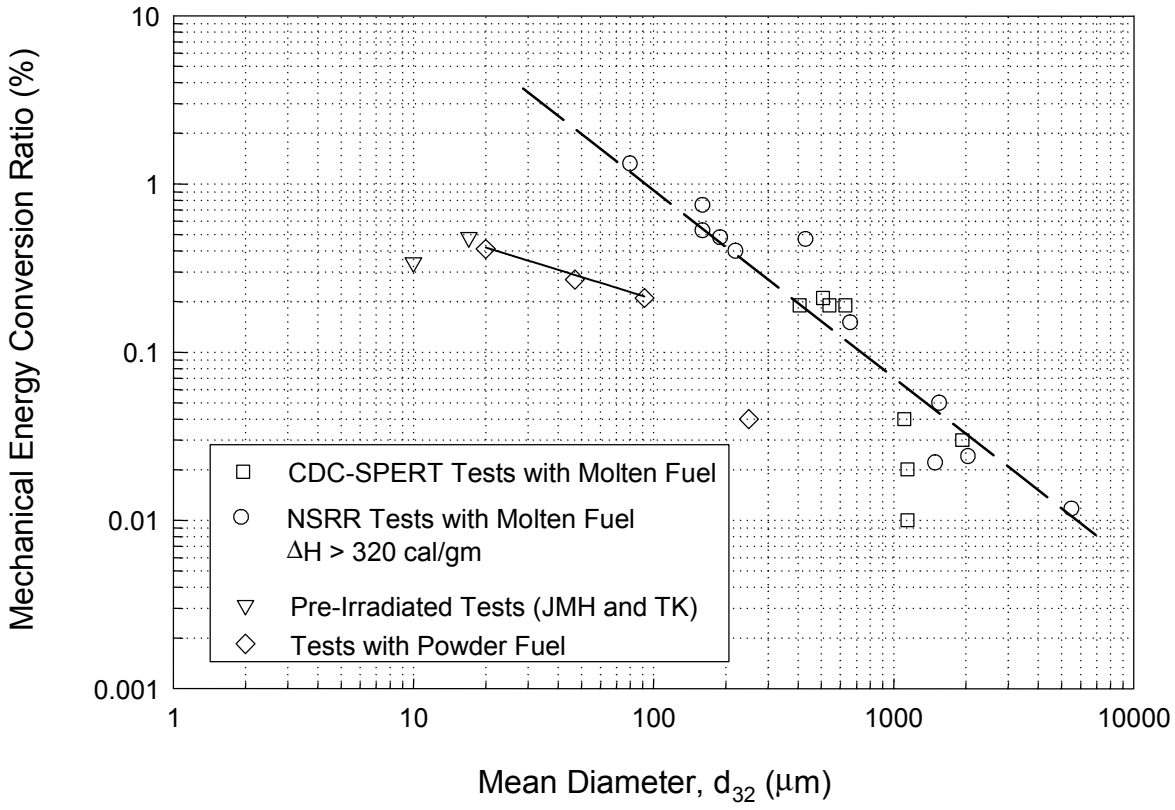

Figure 4-2
Mechanical energy conversion ratio as a function of the mean diameter of fuel particles dispersed into the coolant. Data show inverse dependence on particle mean diameter ($1/d_{32}^{n}$) with the exponent n between 0.8 and 1.3. Tests with dispersal of non-molten fuel particles are less efficient as compared to tests with molten fuel as evident in the lower slope (n varies between 0.4 and 0.5).

The mechanical energy generated during the power pulse was measured in two of the tests using water column velocity measurements. From these measurements, the mechanical energy conversion ratios were determined for each of these tests and are reported by Sugiyama. These results are shown in Figure 4-2 along with recent experiments using powderized fuel packets to evaluate the FCI behavior of finely fragmented material [Sugiyama 2000]. The mechanical conversion energy ratios reported by Sugiyama for JMH-5 and TK-2 were calculated based on the total energy deposited in the dispersed material, whereas those reported in the experiments with molten fuel were calculated based on the total energy deposited in the fuel rod as shown in Equation 4-1. If the JMH-5 and TK-2 mechanical energy conversion ratios are recalculated based on the total energy deposition, the reported values would decrease by about one order of magnitude.

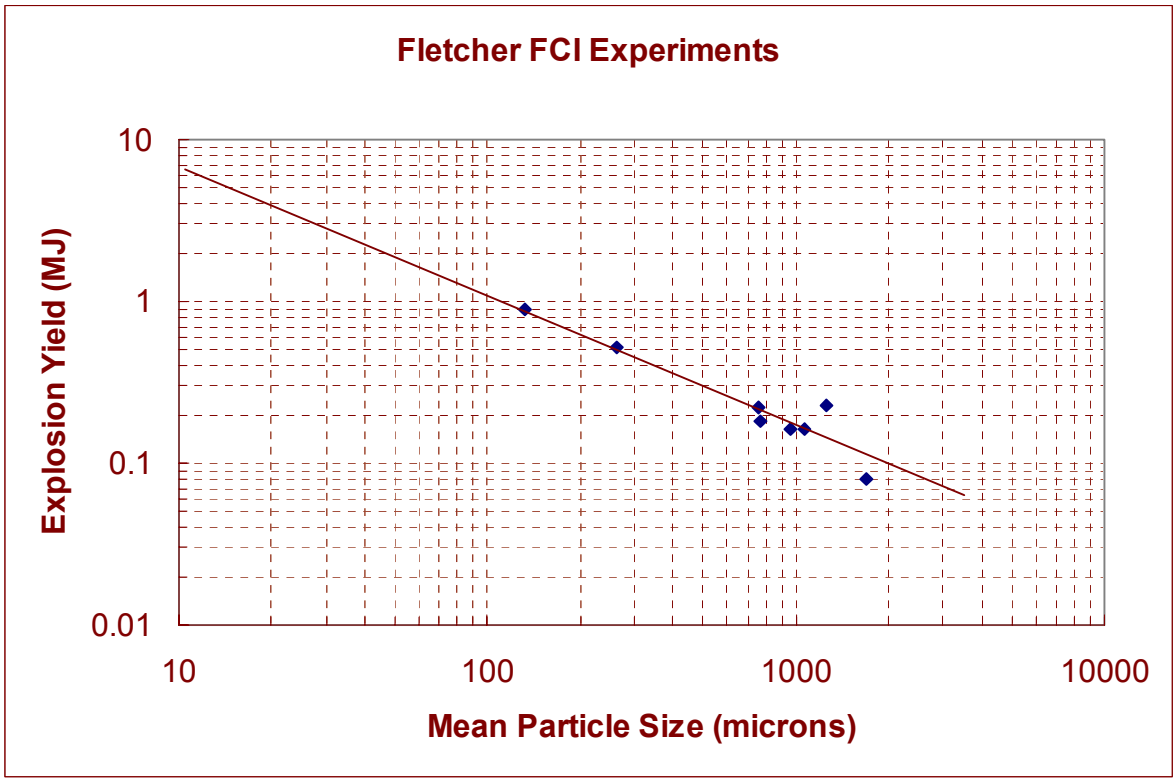

Figure 4-3
Steam explosion yield as a function of mean fuel particle size from severe core accident molten fuel experiments. Results display the same ($1/d_{32}^{n}$) dependency as the RIA tests with molten fuel with n approximately 0.8 to 0.9.

The mechanical energy conversion ratios for the RIA tests that dispersed highly fragmented non-molten fuel material are also shown in Figure 4-2 as a function of the mean particle diameter. Similar to molten fuel dispersal, the results for these experiments also display an inverse dependency on the mean particle size. However, the mechanical energy conversion ratios are below those for molten fuel and the dependence on particle size is lower. The exponent n in Equation 4-1 is between 0.4 and 0.5 in the fragmented fuel tests. These results demonstrate that although it may be possible to disperse into the coolant a small fraction of the fuel pellet as finely fragmented particles, the dispersal of non-molten material is less efficient in converting the thermal energy in the fuel particles to mechanical energy in the coolant. The lower energy densities and slower heat transfer rates of the dispersed solid material are the main reasons that the mechanical energy conversion ratios are less than for the dispersal of molten fuel particles. It also should be noted that the energy level of the pellet rim material is 1.5 to 2.0 times the average pellet energy. The dispersal of material from the central part of the fuel pellet would be even more inefficient at mechanical energy generation because of the lower stored energy and the much larger particle size.

In summary, fuel-coolant interaction has been observed in RIA experiments on both unirradiated and irradiated test rods. For the unirradiated rods, the generation of molten fuel at fuel enthalpy levels above 350 cal/gm leads to rapid dispersal of molten material into the coolant and the

generation of mechanical energy. Mechanical energy levels approaching 600 J and mechanical energy conversion ratios up to 1% were observed in these tests. The results from these tests with molten fuel show that the mechanical energy conversion ratios depend on the inverse of the dispersed particle size. Only a small number of previously irradiated fuel rods have resulted in fuel dispersal and FCI. A total of four tests on rods with burnup levels ranging from 30 to 60 GWd/MTU have had measurable mechanical energy generation. The mechanical energy levels generated by the FCI ranged from 20 to 60 J (150 J for the FK-7 test which dispersed all the fuel material). Mechanical energy conversion ratios estimated using the thermal energy of the dispersed material show maximum ratios of about 0.5%. The results from these tests show that the mechanical energy conversion ratio depends on the inverse square-root of the dispersed particle size. Based on these results, the dispersal of non-molten material is less efficient in converting the thermal energy in the fuel particles to mechanical energy in the coolant.

4.2 Development of the Revised Core Coolability Limit

The core coolability limit for RIA represents the ultimate safety limit to ensure that the consequences of the accident do not lead to impairment of the long-term capability to cool the core or threaten the integrity of the reactor vessel. The core coolability limit represents a "no-go" condition and as a result should not be exceeded. Therefore it is important to establish a limit that both ensures a conservative margin to the conditions that could lead to unwanted consequences and yet does not unnecessarily impose undue restrictions on operating conditions. To meet these objectives, it is important to understand both the regulatory requirements that the limit must satisfy and the technical issues that are associated with the consequences. The regulatory requirements are defined in the General Design Criteria contained in 10CFR50 Appendix A and have been summarized in Section 2. This section will focus on the technical issues associated with the consequences and how the revised core coolability limit precludes these consequences. The following summarizes the technical bases for the revised core coolability limit for RIA and describes the methodology used to develop the limit.

4.2.1 Basis of the Revised Limit

The consequences of high energy depositions and high fuel enthalpy levels during a reactivity accident are the potential for loss of fuel rod geometry and the generation of coolant pressure pulses by fuel-coolant interaction. The loss of fuel rod geometry caused by a large amount of fuel dispersal and/or massive clad fragmentation can lead to impairment of long-term core cooling, depending on the extent of the damage. Similarly, fuel-coolant interaction leading to mechanical energy generation may produce large coolant pressure pulses that can damage the core sufficiently to impair core cooling and also impose loads on the reactor vessel. The revised regulatory acceptance criterion for RIA must be established to preclude these consequences.

As discussed in Section 4.1.1, the potential for zero or low burnup fuel to develop loss of rod geometry or dispersal of fuel material is controlled by the melting response of the fuel pellet and cladding. Gross clad melting may lead to loss of fuel rod geometry since the cladding provides the fuel rod structural support. Melting of the fuel pellet may lead to rapid fuel dispersal and molten fuel coolant interactions. The propensity to generate mechanical energy after dispersal of fuel particles is increased for molten fuel.

Figure 4-4 shows the maximum radial average fuel enthalpy for a number of the zero or low burnup tests with high energy deposition. The tests have been separated into three different categories based on post-test visual examinations. The three categories are: (1) rods that remained in a rod geometry after the tests, (2) rods that contained partial melting of the cladding with one or two axial cracks but remained in a rod-like configuration, and (3) rods that had fuel melting and fragmented into small particles. These results show that although partial clad melting can occur it generally doesn't lead to loss of rod geometry. Loss of rod geometry occurs at fuel enthalpy levels where the fuel pellet begins to melt during the energy deposition and only limited heat conduction has developed to increase the cladding temperature. Under these conditions, the internal pressure caused by melting within the pellet causes fuel rod fragmentation.

The data from zero or low burnup tests indicate that by restricting the fuel enthalpy level to values below that necessary to produce fuel pellet melting would ensure that the fuel rod would maintain a rod geometry throughout an RIA evident. This has been confirmed by recent tests on fuel rods with burnup levels between 30 and 40 GWd/MTU. Both the CABRI REP Na-2 (33 GWd/MTU) and NSRR JMH-5 (30 GWd/MTU) tests reached peak fuel enthalpy levels above 200 cal/gmUO_2 without loss of rod geometry at the completion of the power pulse [Papin et al. 1996; Sugiyama 2000]. Furthermore, test rod JMH-5 maintained a geometry amenable to long-term cooling that contained more the 80% of the UO_2 material within the cladding, even though the cladding failed by a long PCMI-induced axial crack and dispersed a small amount of solid fuel material into the coolant.

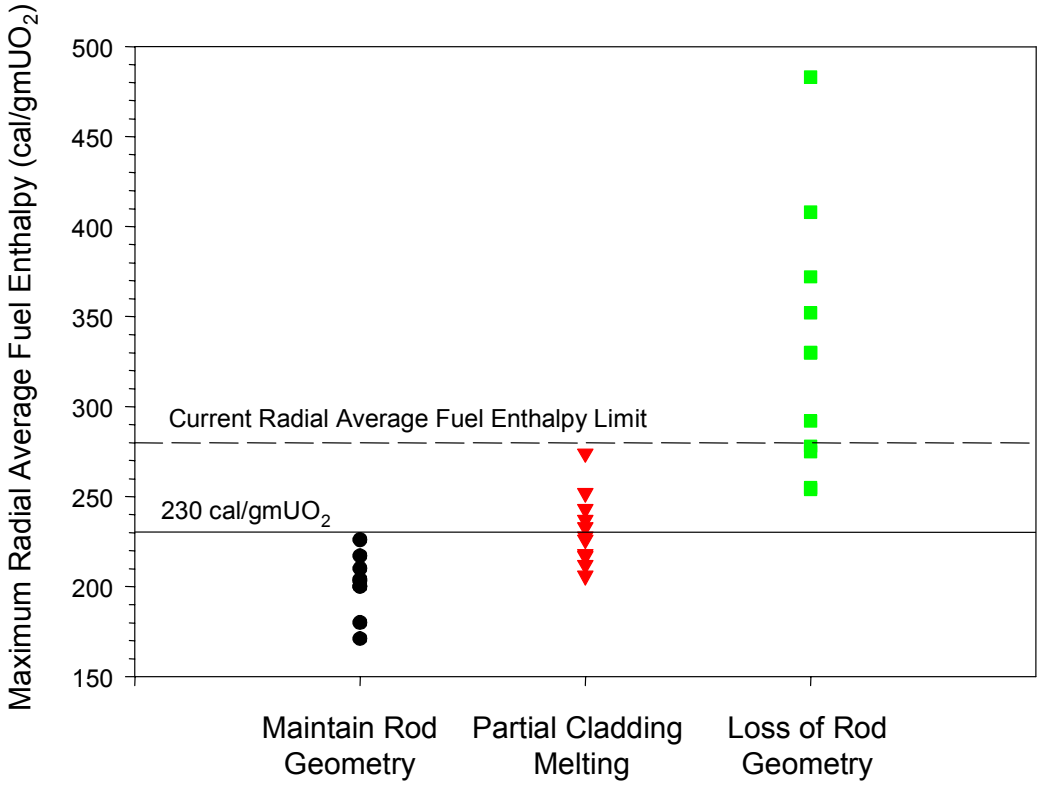

Figure 4-4
Maximum radial average fuel enthalpy for tests above 150 cal/gmUO$_2$ at zero or low burnup. The data has been separated into three categories: tests that maintained a rod geometry, tests that experienced partial clad melting and cracking, and tests that had total loss of rod geometry. Loss of rod geometry is initiated at a radial average fuel enthalpy of 250 cal/gmUO$_2$.

Beyond 40 GWd/tU, the experimental data indicate that dispersal of finely fragmented solid fuel material may occur after cladding failure depending on the pulse width, fuel rod burnup and energy deposition after failure. A summary of the data and the mechanisms associated with fuel dispersal is discussed in Section 4.1.2 for high burnup fuel rods. However, the experimental data also shows that the dispersal of a small quantity of finely fragmented fuel particles into the coolant does not lead to loss of rod geometry or the generation of forces that could damage the reactor core or pressure vessel.

The dispersal of finely fragmented fuel particles from high burnup fuel is not a coolability issue for the following technical reasons:

1). <u>No fuel dispersal is expected after cladding failures for pulse widths above 10 milliseconds</u>

Based on the experimental data from CABRI and NSRR, post-test examinations of both narrow and wide pulse test rods, and fuel behavior analytical evaluations, the potential is extremely low for the dispersal of significant amounts of finely fragmented solid fuel material for pulse widths greater than or equal 10 milliseconds.

2). <u>The amount of material that is available for dispersal is small:</u>

For the tests in which end effects did not influence the test outcome, the material dispersed from the test rod came from the outer 10% of the fuel pellet [Sugiyama 2000]. This was confirmed by the small mean diameters of the material retrieved from the test capsules and post-test examinations of the fuel pellet.

The axial power distribution during a control rod ejection event is sharply peaked in the upper regions of the fuel assembly. An example of the axial power distribution obtained from core neutronics calculations is shown in Figure 4-5. Typical axial power peaking factors range from 2 to 3, with the peak of the power pulse at the 130 inch (330 cm) elevation [Swindlehurst and Deveny 2001]. The localized axial power shape limits the region affected by the energy deposition to the upper 25% of the fuel rod length. The restricted region of power deposition confines the axial extent of any PCMI-induced cladding failure. Experimental data show that PCMI cracks remain narrow, even under RIA conditions because of the strain controlled loading mechanisms. The development of a narrow axial crack over 25% of the fuel rod will not lead to the rapid dispersal of a large amount of fuel material because of the limited size of the crack opening. The overall result is a maximum of 3 to 6% of the total fuel material in a high burnup fuel rod may be dispersed upon cladding failure.

The power deposition for a control rod ejection accident is a localized event that impacts a limited number of fuel assemblies in the vicinity of the ejected control rod assembly [Montgomery and Rashid 1996]. This further restricts the quantity of fuel rods influenced by the event.

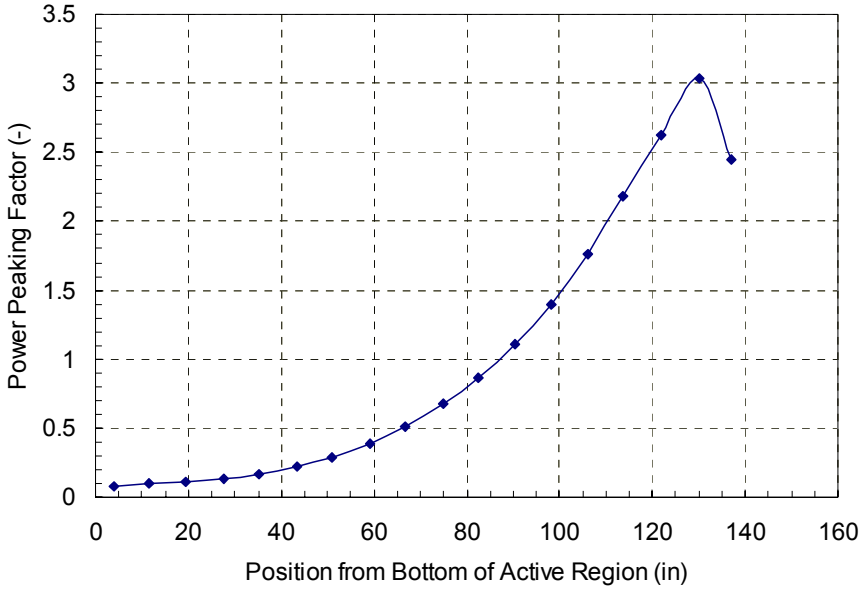

Figure 4-5
Representative axial power shape from a PWR Control Rod Ejection Accident. The peak to average ratio is about 3 and the power peak is localized in the upper region of the fuel rod. The localized power peak limits the region of the fuel rod impacted by the rod ejection event.

3). The mechanical energy conversion is less efficient

Experimental data shows that the mechanical energy conversion ratio for the dispersal of non-molten finely fragmented material is lower by a factor of 5 than that for the dispersal of molten material (See Figure 4-2). The inefficiency of dispersed finely fragmented solid material is a result of the lower energy of the dispersed material and the limited amount of material that is available for interaction with the coolant.

4). FCI is less efficient in reactor conditions

Experimental data show that as the fuel volume to coolant volume ratio increases, the mechanical energy conversion ratio decreases [Tsuruta]. At fuel to water volume ratios representative of in-reactor conditions, the mechanical energy conversion ratio decreases by a factor of 10 as compared to the RIA-simulation tests conducted in NSRR or CDC-SPERT.

Based on these technical points, it can be stated that the consequence of dispersing a small amount of the fuel pellet as finely fragmented non-molten material into the coolant is a radiological release issue, not a coolability issue. Unlike low burnup fuel rods, no tests on high burnup fuel have produced molten fuel and the subsequent loss of fuel rod geometry and significant mechanical energy generation observed in the high energy tests used to define the current core coolability enthalpy limit. Tests on high burnup fuel rods have shown multiple cladding cracks and, in a few instances, cracking of the test rod end caps that can be attributed to end effects related to test artifacts. Although limited dispersal of finely fragmented non-molten fuel material has been observed for narrow power pulse tests, the consequences of these tests as defined by the mechanical energy generation are an order of magnitude less than low burnup tests with molten fuel. An appropriate approach to define a core coolability limit for high burnup fuel is to assume that melting of the fuel pellet may lead to unwanted consequences associated with loss of rod geometry, and to therefore limit the peak fuel enthalpy to a level below that to induce fuel melting.

The industry position to define a core coolability limit that precludes the consequences of high energy depositions is to establish a limit based on incipient fuel pellet melting. Because of the sharply peaked radial power distribution across the pellet and the almost adiabatic energy deposition, limiting the peak pellet temperature to the melting temperature ensures that 99% of the fuel pellet remains well below melting. The pellet radial peaking factors are about 1.1 - 1.2 for low burnup fuel and increase to 1.8 - 2.5 for high burnup fuel [Montgomery and Rashid 1996; Yang et al. 2000; Lassmann et al. 1994]. Also, the power and temperature peaking is localized over the outer 20% to 30% of the fuel pellet, so that the volume average temperature is well below the melting temperature. Ensuring that the fuel pellet remains in the solid state will significantly limit the mechanical energy conversion efficiency in the unlikely event cladding failure occurs and some fuel material is dispersed into the coolant.

4.2.2 Approach to Develop Core Coolability Limit

To define the core coolability limit, the radial average peak fuel enthalpy to initiate incipient fuel pellet melting was determined as a function of rod average burnup. The radial average peak fuel enthalpy to induce melting was identified by performing fuel rod calculations for a 20

millisecond pulse width at increasingly larger energy deposition levels until a single radial location in the fuel pellet reached the melting temperature.

The FALCON transient fuel behavior program was used to calculate the temperature response of the fuel pellet during the power deposition. RIA events at both zero and full power were included in the analysis to include the effect of at power operation on the fuel pellet melting response. Since the cladding to coolant heat transfer can influence the heat conduction from the fuel pellet, cladding-to-coolant heat transfer coefficients representative of nucleate boiling and post-departure from nucleate boiling (DNB) were used in the analysis. The calculation was performed throughout the entire rod average burnup range at increments of 10 GWd/MTU to develop the radial average peak fuel enthalpy as a function of burnup. The effect of burnup on the UO_2 melting temperature and the radial power distribution was also included in the analysis.

4.2.2.1 FALCON Analysis Methodology

In the development of the core coolabilty limit, FALCON was used to calculate the evolution of the fuel pellet temperature distribution during the energy deposition phase of an RIA event. To simplify the analysis, the fuel pellet temperature calculations were performed at the peak burnup axial position within the fuel rod. This assumes that the radial average peak fuel enthalpy (the peak power) occurs at the axial location of the peak burnup. The fuel pellet temperature calculation was performed at rod average burnup levels between 0 and 75 GWd/MTU at 10 GWd/MTU increments. The analysis assumed an axial peaking factor of 1.1 for the ratio of fuel rod peak to average burnup. This burnup peaking factor is representative of intermediate to high burnup fuel.

To define the initial fuel rod conditions such as the thickness of the fuel-to-cladding gap and the fission gas inventory in the gas volume at the time of the RIA event, a full length steady state fuel rod analyses was performed using FALCON as described in Section 3.4.2 and the key information was transferred to the local model.

The FALCON RIA analysis for the fuel pellet temperature was conducted using the radial slice model shown in Figure 4-6. A total of twelve (12) fuel elements and three (3) cladding elements were used to obtain an accurate description of the radial temperature distribution. A refined grid was used near the pellet periphery to capture the power and temperature peaking during the energy deposition.

The analysis was performed for several different fuel rod designs to evaluate the sensitivity of the radial average peak fuel enthalpy to induce fuel melting on fuel rod design variables. Fuel rod dimensions spanning BWR 9x9 to PWR 17x17 fuel rod designs were used in the analysis and are summarized in Table 4-3

Table 4-3
Range of Fuel Rod Dimensions used in FALCON Analysis

Fuel Rod Property	Value
Cladding OD	9.14 - 11.18 mm
Cladding ID	8.00 - 9.75 mm
Pellet OD	7.84 - 9.55 mm
Pellet Density	96.2 - 97.0 % TD

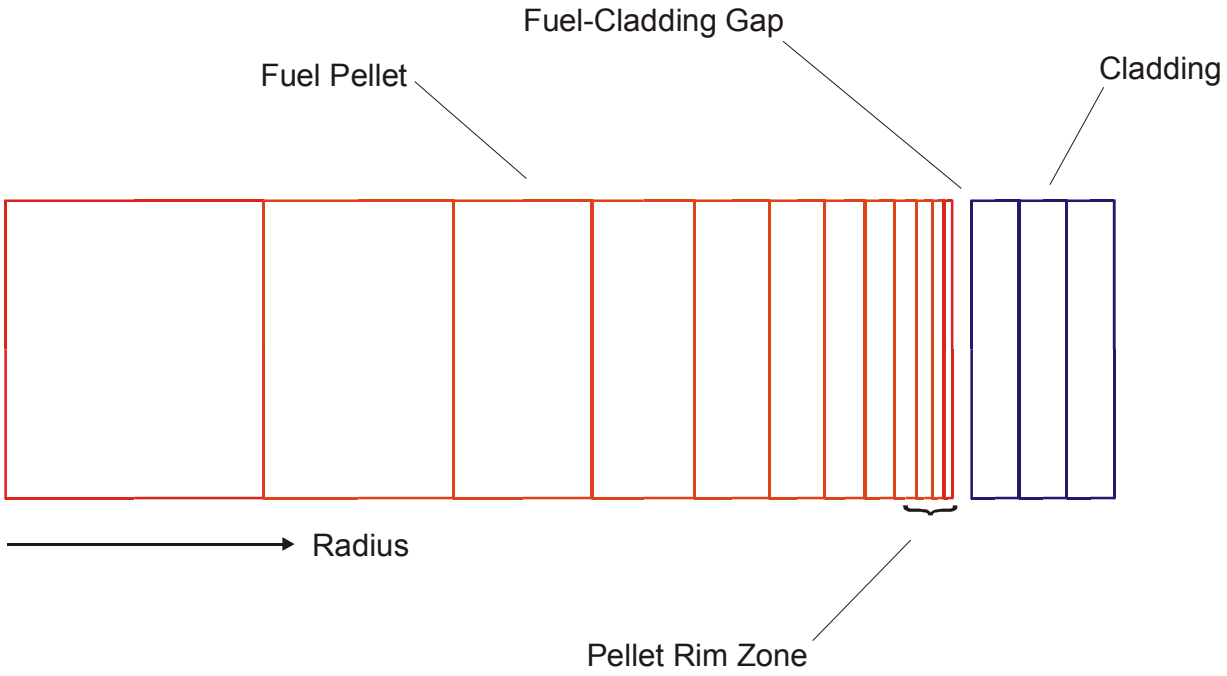

Figure 4-6
Finite element model used in FALCON for the fuel temperature analysis. Refined spatial resolution in the fuel pellet to calculate the temperature peaking caused by the radial power distribution in the fuel pellet.

4.2.2.2 Effect of Burnup on UO_2 Melting Temperature

The effect of local burnup on the UO_2 melting temperature was included in the calculation of the fuel temperatures. A recent review of the UO_2 melting temperature data by Philipponeau at CEA and experiments by Yamanouchi and Komatsu from NFD have shown that burnup has only a limited impact on the fuel melting temperature [Yamanouchi 1988; Komatsu et al. 1988]. Measurements by Yamanouchi on UO_2 and UO_2-2wt%Gd_2O_3 fuel samples irradiated to 30 GWd/MTU found no decrease in the UO_2 melting temperature with burnup. Komatsu conducted measurements on mixed oxide UO_2-20wt% PuO_2 fuel specimens up to a burnup 200

GWD/MTM. A slight decrease of the melting temperature was observed above 50 GWd/MTM for the mixed oxide material. Figure 4-7 shows a comparison of the Yamanouchi UO_2 data with earlier measurements by Christensen [Christensen 1964] and Figure 4-8 shows a comparison of the UO_2-20wt% PuO_2 from Komatsu with earlier data from Krankota and Craig [Krankota and Craig 1969].

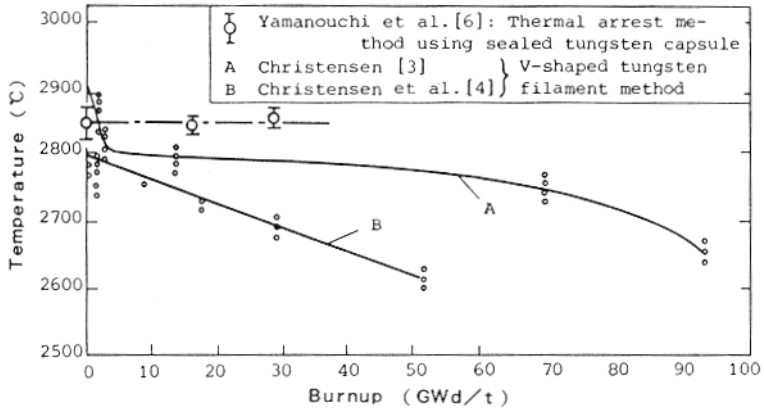

Figure 4-7
Comparison of Yamanouchi UO2 melting temperature data to earlier measurements by Christensen [Christensen 1964]. References in figure are defined in Reference *. Yamanouchi measurements display no burnup dependency out to 30 GWd/MTU.

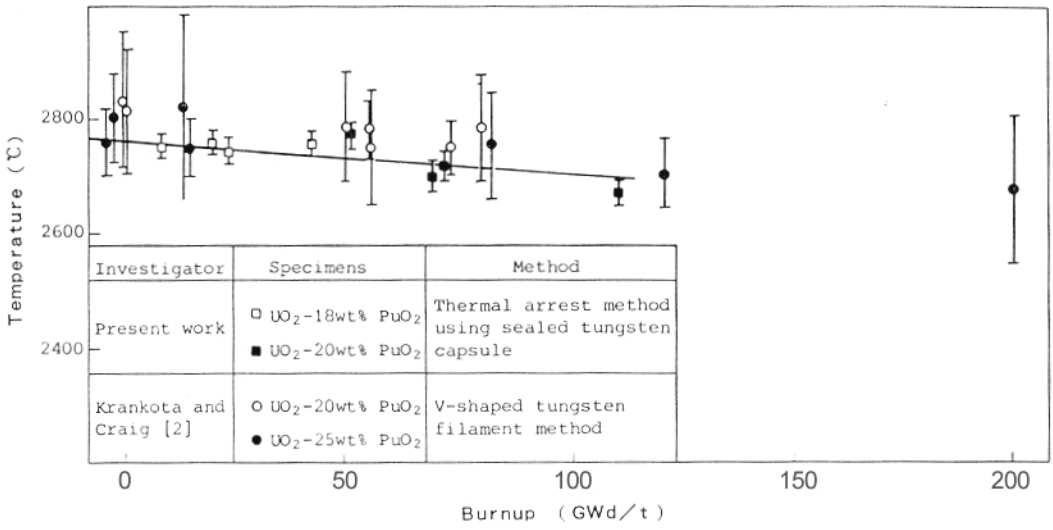

Figure 4-8
Comparison of Komatsu data for mixed oxide melting temperature data to earlier measurements by Krankota and Craig [Krankota and Craig 1969]. The data show a slight burnup dependency beyond a burnup of 50 GWd/MTU.

Phillipponeau conducted a theoretical evaluation using mixed chemical composition of U, Pu, and fission products (Phillipponeau 2; Phillipponeau 27). Using the ideal solid solution method to evaluate the melting temperature of a mixed chemical composition material, Phillipponeau was able to evaluate the separate effects of solid fission products and Pu on the melting temperature. For UO_2, the decrease in the melting temperature was determined to be -7.6ºC/10 GWd/MTU. In comparison to the data for both UO_2 and UO_2-20wt%PuO_2, the decrease in burnup determined by Phillipponeau appears to over-estimate the burnup impact on the UO_2 melting temperature. The UO_2 melting temperature expression recommended by Phillipponeau is given by:

$$T_m(UO_2) = 2847ºC - 7.6ºC/10\ GWd/MTU \quad (4\text{-}2)$$

Equation 4-2, which is shown in Figure 4-9 as a function of burnup, was used in the FALCON analysis to calculate the UO_2 melting temperature as a function of local burnup. The uncertainty of the melting temperature for unirradiated material is reported to be ± 30°C.

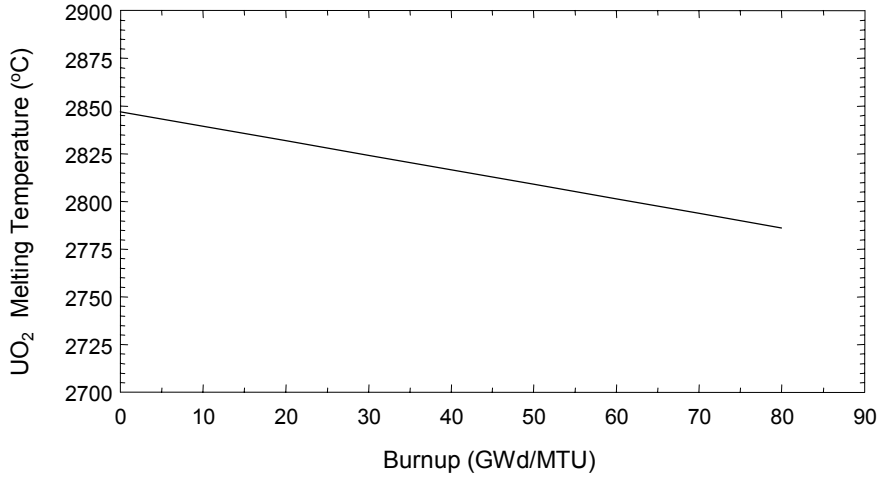

Figure 4-9
UO_2 melting temperature as function of burnup from the expression developed by Phillipponeau using a solid solution mixing method [Phillipponeau 2; Phillipponeau 27].

4.2.2.3 Radial Power and Burnup Distribution

The pellet radial burnup and power distribution is calculated in FALCON using the TUBRNP model developed by Lassmann, et. al. for the TRANSURANUS fuel performance code [Lassmann et al. 1994]. This model represents an improvement of the RADAR model that has been used extensively in the past for modeling the radial power and burnup distribution across the fuel pellet. TUBRNP includes an improved representation of the changes in the Pu isotope inventory with burnup, which allows for better definition of the power and burnup peaking in the pellet rim region. The TUBRNP model has been compared with measured radial Pu and burnup distributions from pellets irradiated to 64 GWd/MTU [Lassmann et al. 1994]. For the analyses performed with FALCON, the pellet was divided into eighty (80) radial locations for calculating the radial power and burnup distribution with the TUBNRP model. This level of radial refinement is required to capture the local peaking in the pellet rim region.

A comparison of the radial power and burnup distributions obtained from the TUBRNP model is shown in Figure 4-10 for two different pellet average burnup conditions. The power and burnup distributions for the 65 GWd/MTU pellet burnup show the characteristic peaking in the pellet periphery.

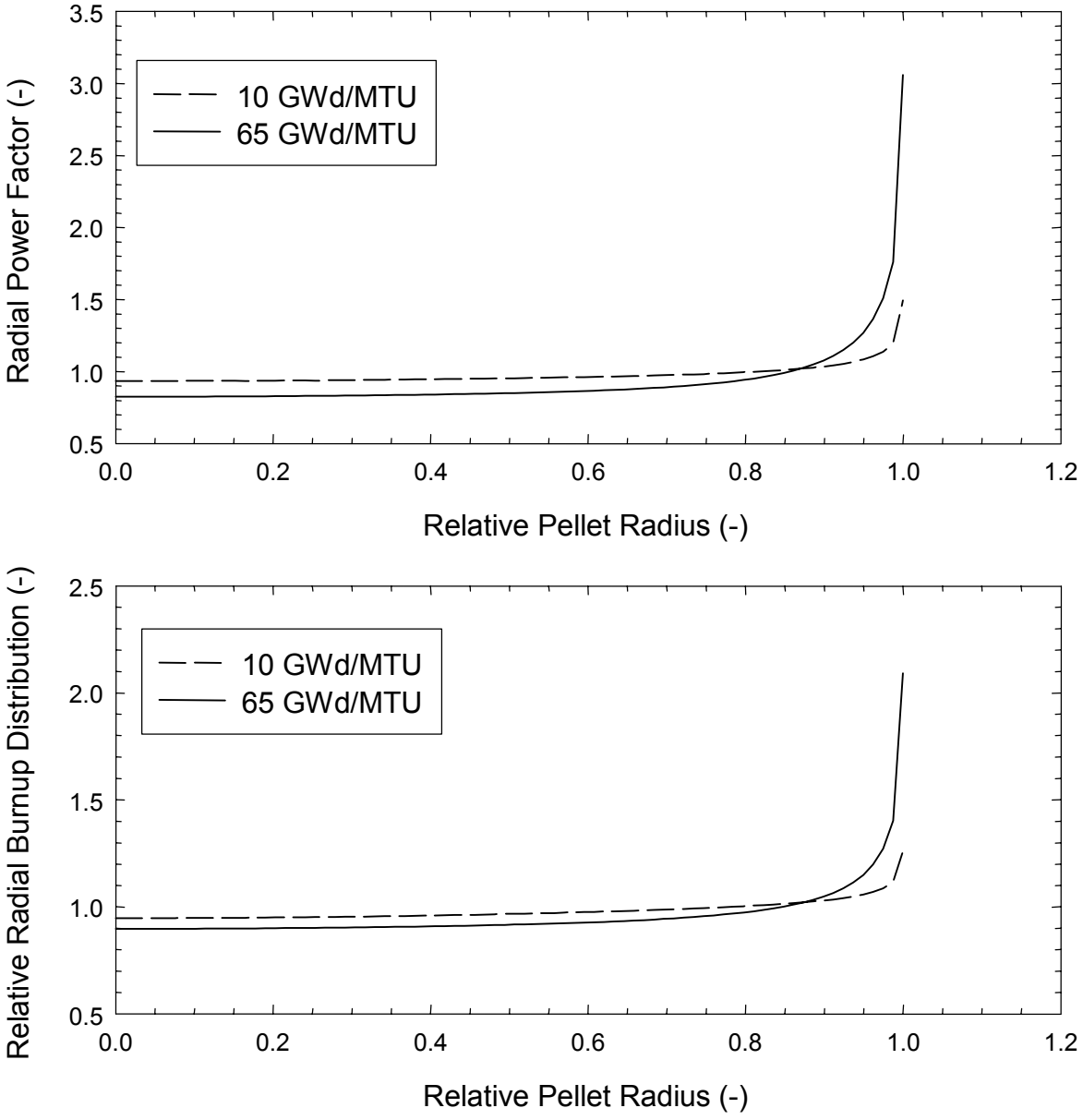

Figure 4-10
Comparison of radial power and radial burnup distribution calculated by TUBRNP model for a pellet average burnup of 10 GWd/MTU and 65 GWd/MTU.

4.2.2.4 Initial Power Level Conditions and Power Pulse Shape

At each burnup level, the FALCON temperature analysis was performed for both hot-zero power and hot-full power conditions using power pulses with a fixed pulse width of 20 milliseconds. The deposited energy of the pulses was increased between 100 and 230 cal/gm until the maximum temperature in the fuel pellet reached the melting temperature. Examples of two different power pulses used in the analysis are shown in Figure 4-11. The shape of the power pulses shown in Figure 4-11 differ somewhat from the power pulse shapes reported for PWR REA events calculated using neutron kinetics methods [Johansen 1995, Dias, 1995]. The power pulses shown in Figure 4-11 were developed assuming a gaussian shape for the power versus time function. Because of delayed neutrons/delayed fissions and the time of reactor scram, most PWR REA power pulses have a low power runout period following the pulse. This power tail is one to two orders of magnitude smaller than the peak of the power pulse. Although this decreases the contribution of the power tail to the total energy deposited, some energy deposition occurs during this part of the power pulse because of the relatively long time (1 to 2 seconds). This energy deposition has little influence of the fuel rod thermal and mechanical response because most of this energy is lost due to heat conduction from the pellet to the cladding.

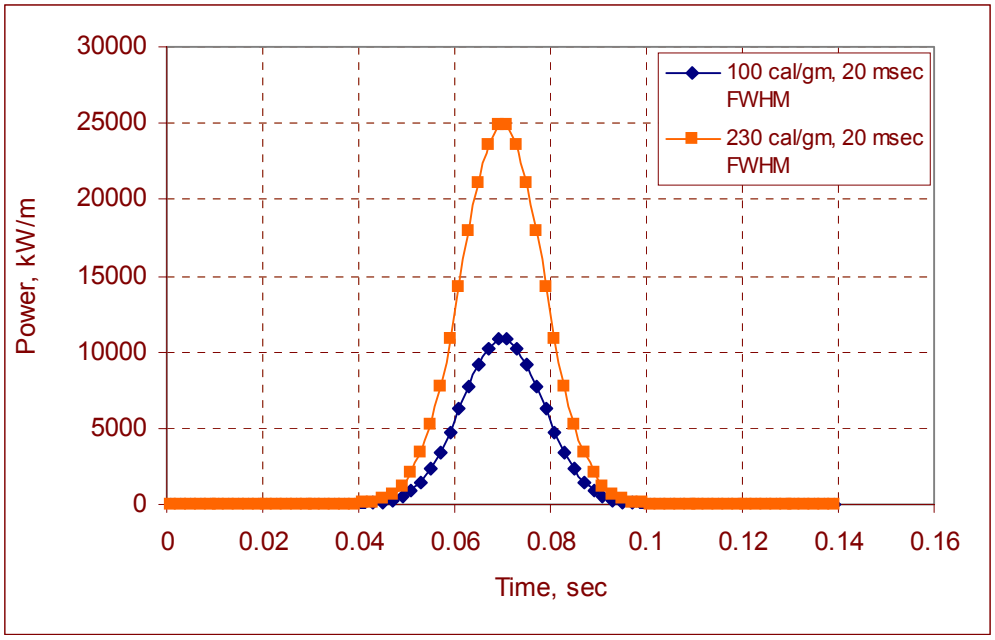

Figure 4-11
Example of RIA power pulses used in fuel temperature analysis with 100 cal/gm and 230 cal/gm deposited energy. Both pulses have a full-width half maximum of 20 milliseconds.

The HZP analyses were conducted assuming zero power at the start of the power pulse. For the hot-full power analyses, the initial fuel rod peak power levels are shown in Table 4-4 as a function of the rod average burnup. As shown in Table 4-4, a range of initial power levels were evaluated at a given burnup to identify the effects of the initial pellet temperature distribution on the evolution of the transient pellet temperature.

4.2.2.5 Heat Transfer Boundary Conditions and UO_2 Thermal Conductivity

Outer surface heat transfer boundary conditions used to represent the cladding to coolant heat transfer characteristics are summarized in Table 4-5 for both the HZP and HFP analyses. For the HZP analysis, the impact on the pellet temperature evolution of three different heat transfer conditions was evaluated: 1). high heat transfer representing nucleate boiling (NB) on a clean cladding surface, 2). Moderate heat transfer representing NB with 100 microns of outer surface oxide layer thickness, and 3). Low heat transfer representing DNB. For the cases using the DNB heat transfer rates, DNB was assumed to exist at the initiation of the RIA event (or the beginning of the analysis).

Table 4-4
Peak LHGRs for HFP RIA Analysis

Rod Average Burnup (GWd/MTU)	Peak Linear Heat Generation Rate (kW/m)	Initial Fuel Rod Stored Energy (cal/gm)
0 - 30	32.3 - 24.8	63 - 44
40	29.3 - 26.5	48 - 45
50	28.4 - 24.9	47 - 42
60	20 - 16.8	37 - 34
70 - 75	18.7 - 14.2	36 - 31

Table 4-5
Clad to Coolant Heat Transfer Conditions

RIA Event	Cladding to Coolant Heat Transfer Coefficient	Coolant Temperature
Hot-Zero Power		
Nucleate Boiling (NB)	40,000 W/m^2- K	290 °C
NB plus oxide	9,000 W/m^2- K	290 °C
DNB	3,000 W/m^2- K	290 °C
Hot-Full Power		
Nucleate Boiling	40,000 W/m^2- K	315 °C

The pellet to cladding gap conductance during the RIA event was calculated using the FALCON best-estimate gap conductance model [Rashid et al. 1994]. The gap conductance calculated by FALCON is a function of the gap thickness, gas conductivity, and the contact pressure. The gap thickness and internal gas constituents were initialized at the beginning of the RIA event from the full-length steady state FALCON analysis results. Fission gas release during the RIA event was not considered in the FALCON calculations.

The effect of burnup on the pellet thermal conductivity is included in FALCON through a burnup reduction factor applied to the UO_2 thermal conductivity value from MATPRO. The burnup reduction factor is based on Halden centerline thermocouple measurements and was developed for use in the ESCORE fuel performance code [Kramman and Freeburn 1987; Freeburn et al. 1991]. Figure 4-12 shows the evolution of the burnup reduction factor as a function of pellet average burnup. A maximum reduction factor of 14% is reached after a burnup of 30 GWd/MTU. The burnup reduction factor shown in Figure 4-12 is based on centerline temperature measurements from Halden on rods with centerline temperature values below 1600°C [Freeburn et al. 1991]. This is well below the high temperature conditions near melting and therefore the use of the burnup reduction factor is an extrapolation of the UO_2 thermal conductivity degradation observed in Halden.

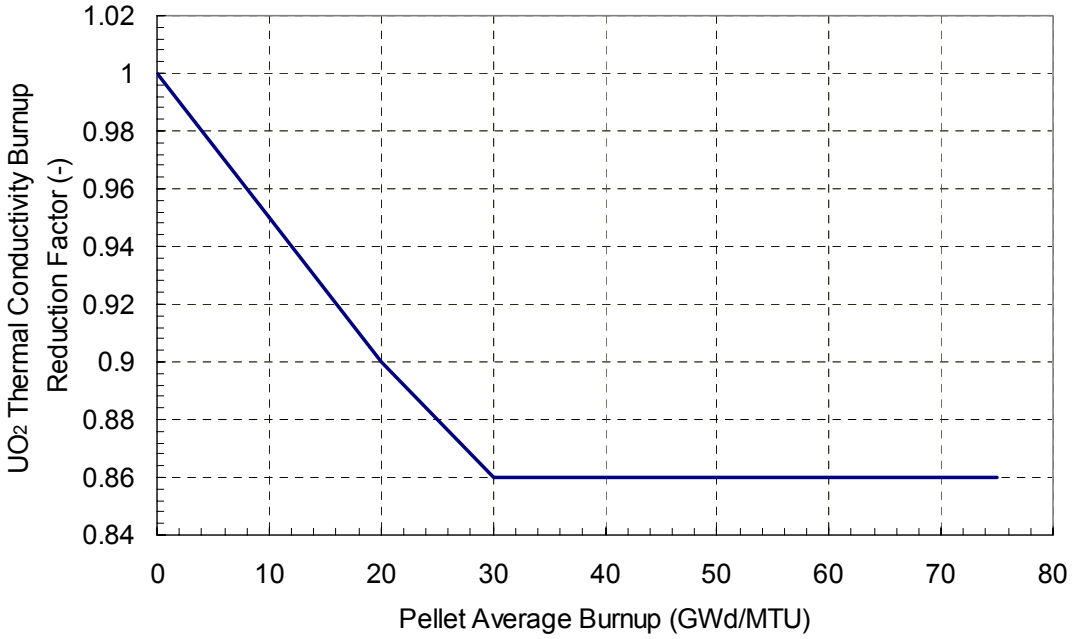

Figure 4-12
UO_2 thermal conductivity burnup reduction factor used in the FALCON analysis.

Typical UO_2 thermal conductivity models add the low temperature phonon-phonon scattering term (K_s) and the high temperature electron transport term (K_e) together to obtain the total thermal conductivity, i.e.,

$$K(T) = K_s(T) + K_e(T) \tag{4-3}$$

where

$$K_s(T) = \frac{1}{A + BT} \tag{4-4}$$

$$K_e(T) = \frac{C}{T^2} \cdot \exp\left(-\frac{W}{kT}\right) \tag{4-5}$$

The coefficients A, B, C, and W are determined by numerical fitting techniques using UO_2 thermal diffusivity or thermal conductivity measurements. Although alternatives exist, these empirical formulations have been used by many to describe the decrease in UO_2 conductivity with temperature in the phonon-phonon regime and the increase of UO_2 conductivity with temperature in the electron transport regime [Delette 1994, Turnbull 1996].

Data describing the effect of burnup on the UO_2 thermal conductivity has been primarily obtained at temperature levels below 1650°C. Therefore, most models used in fuel rod analysis only consider the effect of burnup on the phonon-phonon scattering term below 1600°C [Baron 1998, Sontheimer 1998, Wiesenack 1996, Lassmann 2000]. Generally, the burnup effect is incorporated in the A and B coefficients shown in Equation 4-4 [Baron 1998, Wiesenack 1996, Lassmann 2000]. The transition to high temperature UO_2 thermal conductivity by the electron (or Frenkel defect) transport contribution used in most models does not consider the effect of burnup. Recent thermal diffusivity measurements up to 1800°C on irradiated UO_2 specimens show that the effect of burnup decreases as the temperature increases [Amaya 2000]. The burnup degradation observed in experiments on 60 GWd/tU pellet material was about 40% at 800°C and less than 20% at 1800°C. At 1800°C, the electron transport contribution is less than a third of the total UO_2 thermal conductivity, however, this appears to be sufficient to offset some of the burnup degradation in the phonon-phonon scattering term. As the temperature increases, the electron transport contribution also becomes more dominant and the burnup degradation diminishes further. Unfortunately, no UO_2 measurements are available above 1800°C to determine the effect of burnup on the electronic heat conduction. When the burnup effects are incorporated into Equation 4-4 and then combined with Equation 4-5 to obtain the total UO_2 thermal conductivity, this approach results in only a slight decrease cause by burnup in the thermal conductivity above 1800°C. However, the burnup reduction factor used within FALCON results in a 14% lower UO_2 thermal conductivity at high temperature than for unirradiated conditions. Using the reduction factor ensures that the UO_2 thermal conductivity calculated by FALCON includes some impact of burnup, even at high temperature.

For the analyses used to determine the conditions for incipient melting, the FALCON calculated pellet temperatures are below 1800°C only during the early part of the power pulse when energy deposition is nearly adiabatic. At these conditions, the power level and the fuel specific heat control the pellet temperatures. Some heat conduction at the pellet surface occurs during the later part of the power deposition because of the high pellet-cladding gap conductance. However, this heat conduction only affects the outer 50 to 100 microns of the pellet where the fuel is above 1600°C. The majority of the heat conduction occurs after the peak temperature is reached in the pellet periphery. Since only limited heat conduction occurs during the energy deposition, the calculated temperatures are not sensitive to the value of the UO_2 thermal conductivity. As a result, the functional form of the thermal conductivity degradation factor used in the analysis will not strongly affect the peak pellet temperature.

Gadolinia additives have also been shown to decrease the pellet thermal conductivity [Sontheimer 1998, Amaya 2000]. As with burnup, the effect of gadolinia additives is considered in the low temperature phonon-phonon scattering contribution (Equation 4-4). The effect of gadolinia on the pellet thermal conductivity diminishes at temperatures levels above 1800°C when the electron transport contribution becomes more dominant [Sontheimer 1998]. Because of this, the temperature calculations using FALCON are also applicable gadolinia fuel.

4.2.2.6 FALCON Analysis Results

The FALCON results consist of temperature distributions within the pellet as a function of time during and following the power pulse. A schematic of the pellet temperature distribution for the HZP RIA event is shown in Figure 4-13 for a high burnup fuel rod. As can be seen in the schematic, the power peaking in the pellet rim region causes the temperature to reach a maximum in this region as well.

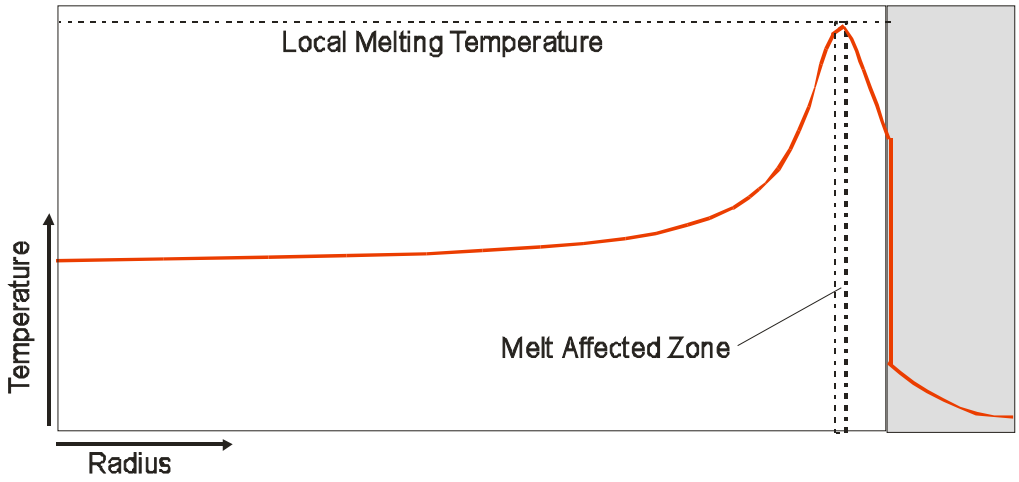

Figure 4-13
Schematic of Radial Temperature Distribution

In the case of the HFP RIA, the parabolic temperature distribution at the start of the power pulse causes the maximum temperature to occur at the centerline for fuel rod burnup levels below 40 GWd/MTU. At higher burnup levels, the influence of the initial parabolic temperature distribution decreases because of the lower initial LHGR and the power peaking in the pellet periphery. For burnup levels greater than 40 GWd/MTU, the peak temperature occurs in the outer pellet periphery similar to the HZP results.

Three-dimensional surface plots showing the evolution of the fuel pellet temperature as a function of time and pellet radial position is shown in Figure 4-14 for both the HZP and HFP RIA events at rod average burnup levels of 40 and 70 GWd/MTU. In these plots, the pellet surface is at 4.095 mm. The temperature peaking in the rim region is evident in the HZP cases, particularly for the 70 GWd/MTU analysis.

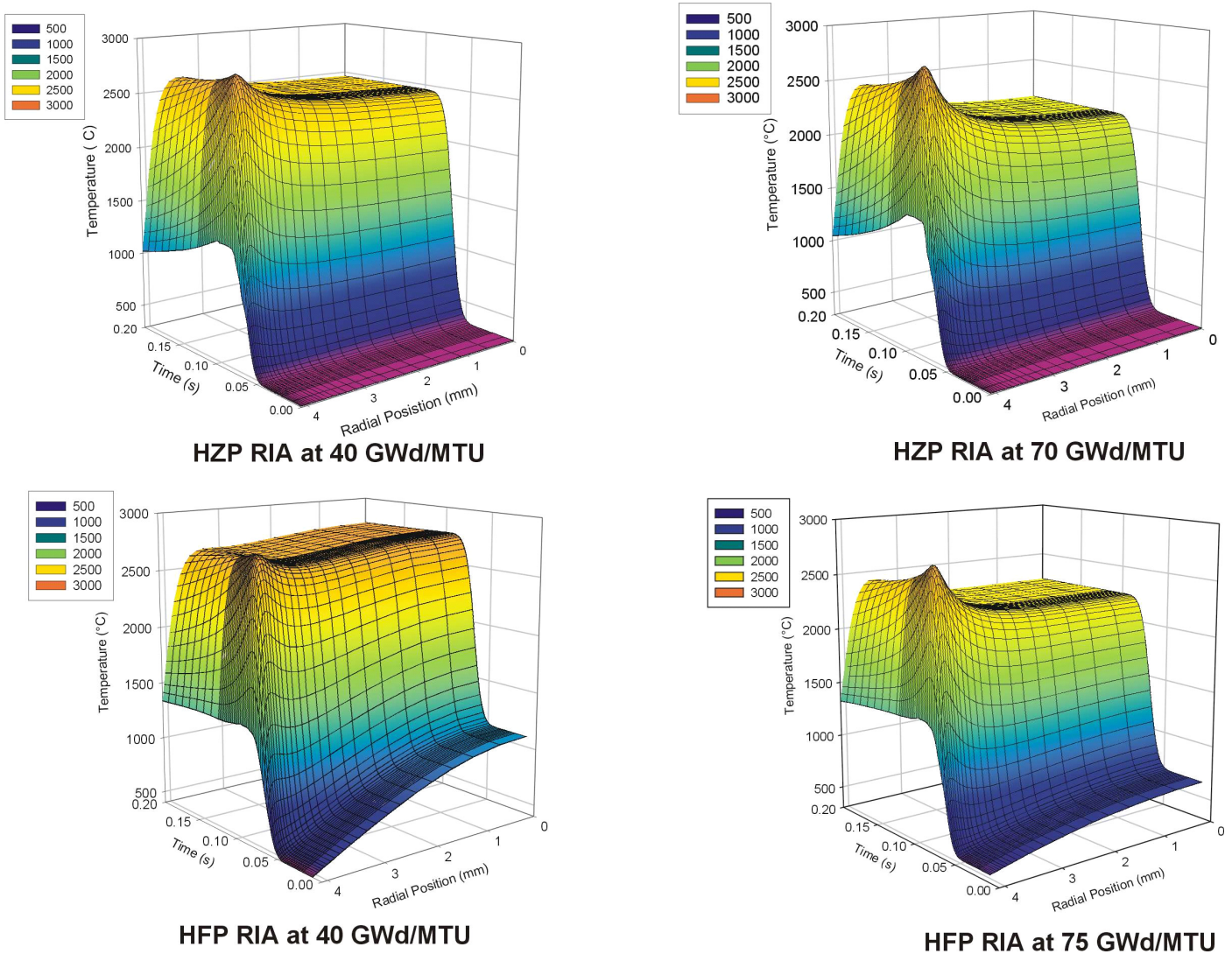

Figure 4-14
Fuel temperature surface plots from FALCON showing evolution of pellet temperature with position and time.

Table 4-6
FALCON results for the HZP RIA analysis

Rod Average Burnup (GWd/MTU)	Pellet Average Burnup (GWd/MTU)	Local Burnup @ Max. Temperature Location (GWd/MTU)	UO_2 Melting Temperature (°C)	Maximum Temperature in FALCON (°C)	Radial Average Peak Fuel Enthalpy (cal/gmUO_2)
0	0	0	2848	2829	252.6
10	11	11.3	2838	2822	245.6
20	22	22.9	2830	2818	238.4
30	33	34.7	2821	2817	232.7
40	44	48.1	2810	2799	222.1
50	55	60.6	2801	2782	210.8
60	66	75.7	2789	2775	199.8
70	77	89.6	2779	2764	191.3
75	82.5	98.2	2772	2763	188.7

Table 4-7
FALCON results for the HFP RIA analysis

Rod Average Burnup (GWd/MTU)	Pellet Average Burnup (GWd/MTU)	Local Burnup @ Max. Temperature Location (GWd/MTU)	UO_2 Melting Temperature (°C)	Maximum Temperature in FALCON (°C)	Radial Average Peak Fuel Enthalpy (cal/gmUO_2)
0	0	0.0	2848	2832	239.7
10	11	10.4	2840	2833	244.0
20	22	20.5	2832	2824	238.1
30	33	34.7	2821	2819	250.1
40	44	48.1	2811	2791	240.2
50	55	60.6	2801	2802	232.0
60	66	75.7	2801	2736	206.7
70	77	89.6	2789	2748	198.8
75	82.5	97.2	2779	2725	196.5

The parabolic temperature distribution is clearly evident at the initiation of the HFP RIA analysis. The initial temperature distribution has some impact on the evolution of the temperature distribution at low burnup levels as shown in the 40 GWd/MTU case. However, for the high burnup case, the initial temperature distribution has only a minor influence on the radial location and peak temperature reached during the power pulse.

Because of the temperature peaking in the pellet periphery, the amount of the fuel pellet material that approaches the melting temperature is a small fraction of the total pellet volume. In fact, for pellet burnup levels above 40 GWd/MTU, the pellet average temperature is 400 to 800ºC below the peak temperature.

Tables 4-6 and 4-7 summarize the FALCON results for the HZP and HFP analysis. Shown in the tables is the local pellet burnup at the maximum temperature location, the local UO_2 melting temperature, the maximum temperature, and the radial average peak fuel enthalpy. These results indicate that the radial average peak fuel enthalpy necessary to cause local incipient melting decreases as a function of rod average burnup. This trend is a result of the combined effects of burnup on the UO_2 melting temperature and the pellet radial power distribution. The results also show that the HZP RIA event bounds the HFP RIA event radial average peak fuel enthalpy at rod average burnup levels greater than 30 GWd/MTU.

Sensitivity studies to evaluate the effects of outer surface oxide thickness or DNB heat transfer demonstrated that the variations in cladding to coolant heat transfer conditions had no impact on the radial average peak fuel enthalpy necessary to cause local incipient melting. The heat transfer conditions at the cladding outer surface did influence the heat conduction period later in the RIA event well after the time of maximum temperature in the pellet.

The radial average peak fuel enthalpy to induce incipient melting obtained from the HZP results shown in Table 4-6 were used to develop the core coolability limit for HZP and HFP RIA events. The FALCON results were correlated to rod average burnup and a polynomial fit was constructed as shown in Figure 4-15. The resulting expression for the maximum radial average peak fuel enthalpy as a function of rod average burnup is given by:

$$H_{max} = 251.7 - 0.3555 \cdot B - 0.0144 \cdot B^2 + 1.033 \times 10^{-4} \cdot B^3 \qquad (4\text{-}6)$$

where

H_{max} - radial average peak fuel enthalpy at incipient melting (cal/gmUO_2)

B - rod average burnup (GWd/MTU)

Reasonable correlation with the FALCON results is obtained from the expression shown in Equation 4-6. To be consistent with the recommendations of MacDonald, et al, the maximum radial average peak fuel enthalpy given by Equation 4-6 is restricted to 230 cal/gmUO_2 at rod average burnup levels below 30 GWd/MTU.

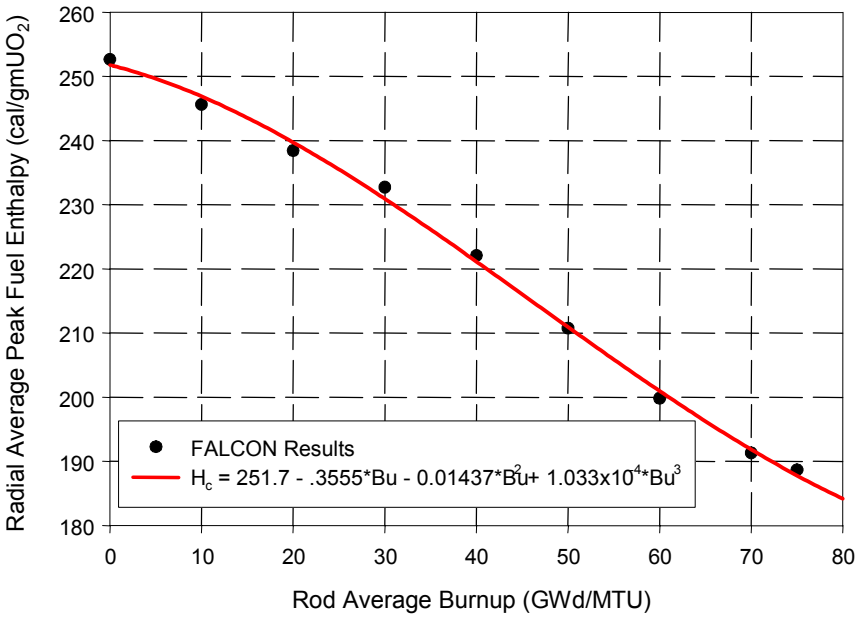

Figure 4-15
Regression analysis of FALCON results for the HZP RIA.

The results of the incipient fuel melting analysis to define the radial average peak fuel enthalpy as a function of rod average burnup is compared to the results of high energy deposition RIA tests in Figure 4-16. The limit of 230 cal/gm shown in Figure 4-16 is well below the radial average fuel enthalpy that leads to loss of rod geometry as observed in earlier tests at zero burnup. For tests on rods with burnup levels above 20 GWd/MTU, the curve resides at the upper boundary of the highest tested rods. As indicated in the figure, these rods remained in a rod-like geometry.

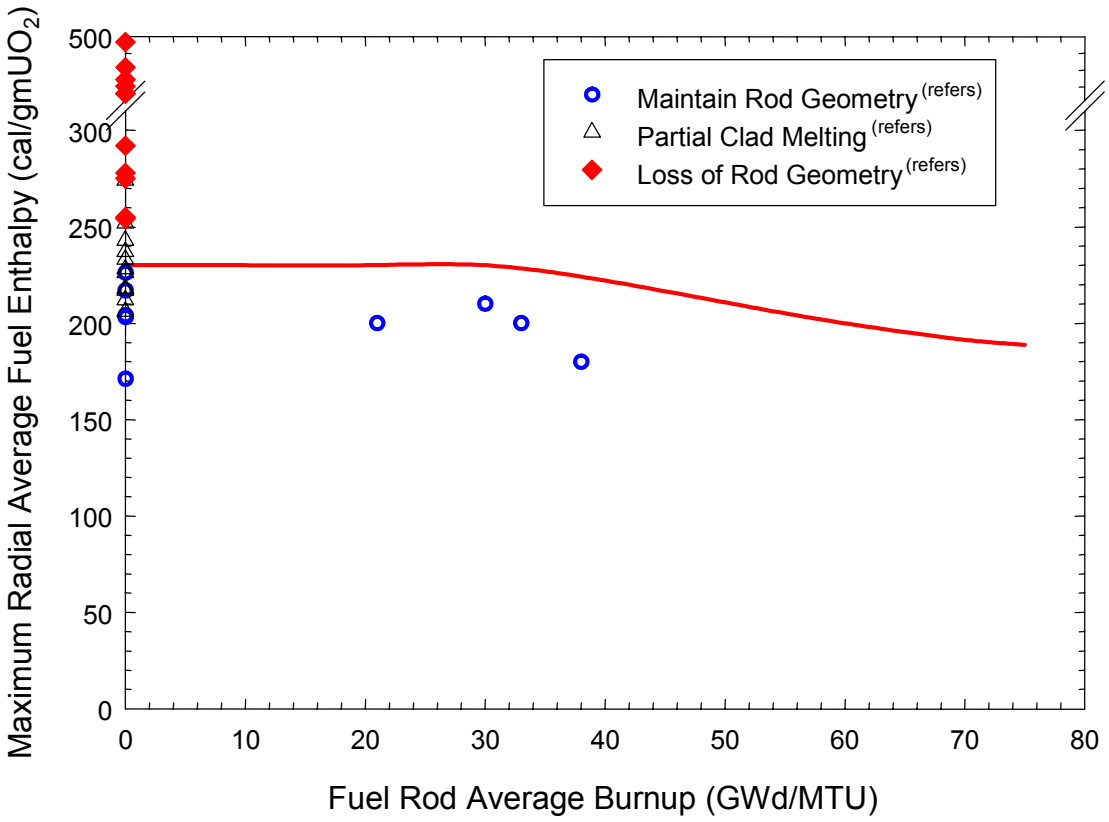

Figure 4-16
Maximum radial average fuel enthalpy to produce incipient fuel melting as a function of rod average burnup. Shown for comparison are the results of RIA-simulation tests [Martison and Johnson 1968; Miller and Lussie 1969; MacDonald et al. 1980; Tsuruta et al. 1985; Sugiyama 2000]

4.3 Revised Core Coolability Limit

The radial average fuel peak enthalpy versus rod average burnup curve shown in Figure 4-16 represents the industry revised core coolability limit for HZP and HFP RIA conditions and is established to preclude loss of rod geometry and generation of coolant pressure pulses. The core coolability limit is a separate criterion from the fuel rod failure threshold discussed in Section 3 and is defined to serve as the safety limit for the RIA event. The curve represents the maximum allowable radial average peak fuel enthalpy at HZP and HFP conditions to preclude incipient fuel melting in both PWR and BWR fuel designs.

A maximum value of 230 cal/gmUO_2 for the radial average fuel enthalpy was used as the basis for establishing the zero burnup limit. This value is somewhat below the current regulatory maximum allowable radial average peak fuel enthalpy of 280 cal/gmUO_2. MacDonald, et. al. performed a review and re-assessment of the data used by the NRC to establish the fuel coolability limit of 280 cal/gm for the maximum radially averaged fuel enthalpy as defined in Reg. Guide 1.77 [AEC 1974]. It was found that although the fuel coolability limit is stated in terms of radially average fuel enthalpy, the data used to establish the limit was actually based on

the total energy deposition for the tests [MacDonald et al. 1980]. The maximum radial averaged fuel enthalpy is less than the associated total energy deposition by 15-20% due to heat conduction from the fuel and energy deposition from delayed neutrons. As stated Section 4.1.1 and shown in Figure 4-4, the consequences of radial average fuel enthalpies greater than 250 cal/gm were loss of rod geometry and dispersal of molten fuel, which is well below the current radial average fuel enthalpy limit of 280 cal/gm. Re-evaluation by MacDonald, et. al. of the tests performed in the SPERT and TREAT facilities using the maximum radial average fuel enthalpy shows that a value of 230 cal/gm for the maximum radial average peak fuel enthalpy would provide margin to loss of fuel rod geometry and would be more appropriate for the fuel coolability limit at zero and low burnup.

The maximum radial average fuel enthalpy curve shown in Figure 4-16 decreases as a function of rod average burnup. As the rod average burnup increases, the effects of burnup on the UO_2 melting temperature and radial power distribution combine to decrease the radial average fuel enthalpy to produce incipient melting. These factors lead to the burnup dependency shown in Figure 4-16. The curve shown in Figure 4-16 is applicable to 75 GWd/MTU.

The revised limit on the radial average fuel enthalpy ensures that fuel melting does not occur during the energy deposition phase of a reactivity initiated accident. This approach prevents the dispersal of molten fuel that is a precursor for loss of rod geometry and fuel-coolant interaction leading to generation of damaging pressure pulses. Furthermore, the potential is very low to disperse finely fragmented non-molten fuel particles into the coolant from high burnup fuel for pulse widths larger than 10 milliseconds. It has been demonstrated that the power pulse widths for representative LWR reactivity initiated accidents are larger than 10 milliseconds. The combination of maintaining a pulse width greater than 10 milliseconds and solid UO_2 material during an RIA event guarantees that the reactor will remain amenable to long-term cooling and the reactor vessel integrity will not be compromised during a reactivity initiated accident.

4.3.1 Core Coolability Uncertainty Evaluation

An assessment has been made to evaluate the impact of uncertainties within the analytical approach used to establish the core coolability limit shown in Figure 4-16. An important part of this approach was the FALCON analyses used to calculate the radial average peak fuel enthalpy that resulted in incipient pellet melting. Since these calculations are subject to some uncertainties, it is appropriate to address the impact of these uncertainties on the analytical results. The sources of uncertainties in the analytical approach that were evaluated include;

1) The as-manufactured fuel rod dimensions and power history used to establish the initial conditions at the start of the power pulse

2) Initial enrichment and gadolinia content

3) Transient pellet-cladding gap conductance

4) Power pulse width

The uncertainty evaluation consists of both a qualitative assessment based on past experience in fuel rod analysis modeling and a quantitative assessment using analytical calculations to determine the impact of a particular model or variable. Where possible, the impact of the uncertainty in terms of change in the cal/gm of the core coolability is provided.

4.3.1.1 Fuel rod condition at start of the transient analysis

The fuel rod conditions at the start of the RIA transient analysis were established using a steady state analysis up to the fuel rod burnup level that the transient was postulated to occur, i.e., a rod average burnup of 40 GWd/tU. The key initial conditions that influence the calculated fuel rod thermal response during the power pulse include the residual fuel-cladding gap and the radial burnup and power distribution. The residual fuel-cladding gap and the radial burnup and power distribution were obtained from the steady state analysis.

The steady state analysis performed using FALCON includes the effects of pellet densification, fission product induced solid swelling, pellet relocation, and cladding creep on the calculation of the residual pellet-cladding gap used in the transient analysis. Experience has shown that the combination of these mechanisms cause gap closure in PWR fuel at burnup levels ranging between 15 and 20 GWd/tU. At burnup levels beyond gap closure (> 20 GWd/tU), the residual fuel-cladding gap represents mostly the thermal contraction caused by the decrease from full power to hot zero-power conditions. The residual pellet cladding gap thickness is dependent on the power level prior to shutdown and is generally less than 20 microns as shown PIE observations. Uncertainties in the models used to calculate the residual pellet-cladding gap influence the burnup level at which gap closure occurs. However, once gap closure occurs these fuel behavior models have less of an impact on the residual pellet-cladding gap. This conclusion is supported by the NRC PWR RIA PIRT review that assigned a knowledge ranking of 82 (out of 100) to the residual pellet-cladding gap at the start of the transient [Boyack, et.al. 2001]. The knowledge ranking provided by the PIRT panel is an indication of how well known a particular parameter is understood. The knowledge ranking of 82 demonstrates that the PIRT panel felt that fuel rod analysis methods could provide a good estimate of the residual pellet-cladding gap thickness and that the uncertainties for this value are low.

The residual pellet-cladding gap can have an influence on the evolution of the gap thermal conductivity during the power deposition. However, gap closure and the development of hard solid contact between the pellet and cladding establishes a high gap thermal conductivity that is rather insensitive to the size of the residual gap. Furthermore, during the power deposition, the pellet heats up in a nearly adiabatic condition and variations in the gap thermal conductivity of 20 to 50% will not have a significant impact on the peak temperature as discussed later in this section.

Other sources of uncertainty in the initial fuel rod condition at the start of the transient power pulse include variations in the as-fabricated fuel rod dimensions. At the high energy depositions required to produce incipient pellet melting, the impact of fuel rod fabrication tolerances will be small on the transient thermal and mechanical response during an RIA power pulse.

Based on these points, it can be argued that the uncertainty in the core coolability shown in Figure 4-16 associated with variations in the residual pellet-cladding gap at the start of the power pulse is small.

4.3.1.2 Initial ^{235}U Enrichment and Gadolinia Content

The analytical evaluation defined the initial ^{235}U enrichment at 4.8% in the fuel rod cases used to establish the core coolability limit shown in Figure 4-16. No analyses were conducted using gadolinia burnable poison absorber material. Sensitivity evaluations were conducted using the TUBRNP model to establish the impact of different ^{235}U enrichment and gadolinia oxide (Gd_2O_3) contents on the radial power, burnup, and UO_2 melting temperature distributions across the pellet [Lassmann 1994]. Uranium-235 enrichments between 3.95% and 4.95% and gadolinia contents of 8 wt% were evaluated to determine the sensitivity of the radial power, burnup, and UO_2 melting temperature distributions to variations in these parameters. In addition, a select number of FALCON calculations were performed to determine the impact on the radial temperature distribution of variations in initial ^{235}U enrichment.

The radial power distribution for ^{235}U enrichment levels ranging between 3.95% and 4.95% are shown in Figure 4-17 at three different peak pellet burnup levels: 20, 40, and 75 GWd/tU. Shown in Figure 4-17 is the radial power peaking factors as a function of pellet radius in the outer 1 mm of the pellet periphery. It can be seen that the radial power peaking factors differ by less than 5% over the range of ^{235}U enrichments from 3.95% to 4.95%. These results indicate that the peak temperature calculated by FALCON would vary by 5 to 10°C for the range of ^{235}U enrichments used in high burnup fuel rod designs. A key point to note is that the maximum radial power peaking factor decreases with increasing ^{235}U enrichment. Therefore, the peak temperatures calculated by FALCON for a ^{235}U enrichment of 4.8% will be 5-10°C higher than for a case of 4.95% enrichment.

The radial burnup distribution is also influenced by the initial ^{235}U enrichment. This distribution is important since it controls the local fuel pellet material properties, in particular the UO_2 melting temperature used in the FALCON calculation to define incipient melting. The TUBRNP results for the radial power distribution is shown in Figure 4-18a and 4-19a for a pellet average burnup of 40 GWd/tU and 75 GWd/tU, respectively. Again, the radial burnup distribution is shown for the outer 1 mm of the pellet to highlight the main variations between the different enrichment levels. The largest variation occurs at the pellet periphery where the local burnup can vary by as much as 13% with the highest local burnup occurring in the 3.95% enrichment case. The variation in the local burnup between the different ^{235}U enrichment levels decreases to less than 1% at a pellet radial positions less than 3.5mm.

A comparison of the UO_2 melting temperature for the three different ^{235}U enrichments evaluated is shown in Figure 4-18b and 4-19b for a pellet average burnup of 40 GWd/tU and 75 GWd/tU, respectively. The radial distribution of the UO_2 melting temperature was calculated using Equation 4-2 and the radial burnup distributions shown in Figure 4-18a and 4-19a. The distribution is shown for the outer 1 mm of the pellet periphery to highlight the main differences. The UO_2 melting temperature distribution varies as a function of the initial ^{235}U enrichment due the local burnup differences. However, the variations are less than 20°C at the pellet periphery where the burnup differences are the largest. The variation in UO_2 melting temperature

decreases to only a few degrees C at a distance of 0.2 mm from the pellet edge. Since the peak fuel temperatures calculated by FALCON occur at 0.2 to 0.5 mm from the pellet edge, the differences in UO_2 melting temperature caused by a variation in initial ^{235}U enrichment are less than a couple of degrees C. This is well within the uncertainty of the UO_2 melting temperature measurements on irradiated fuel samples.

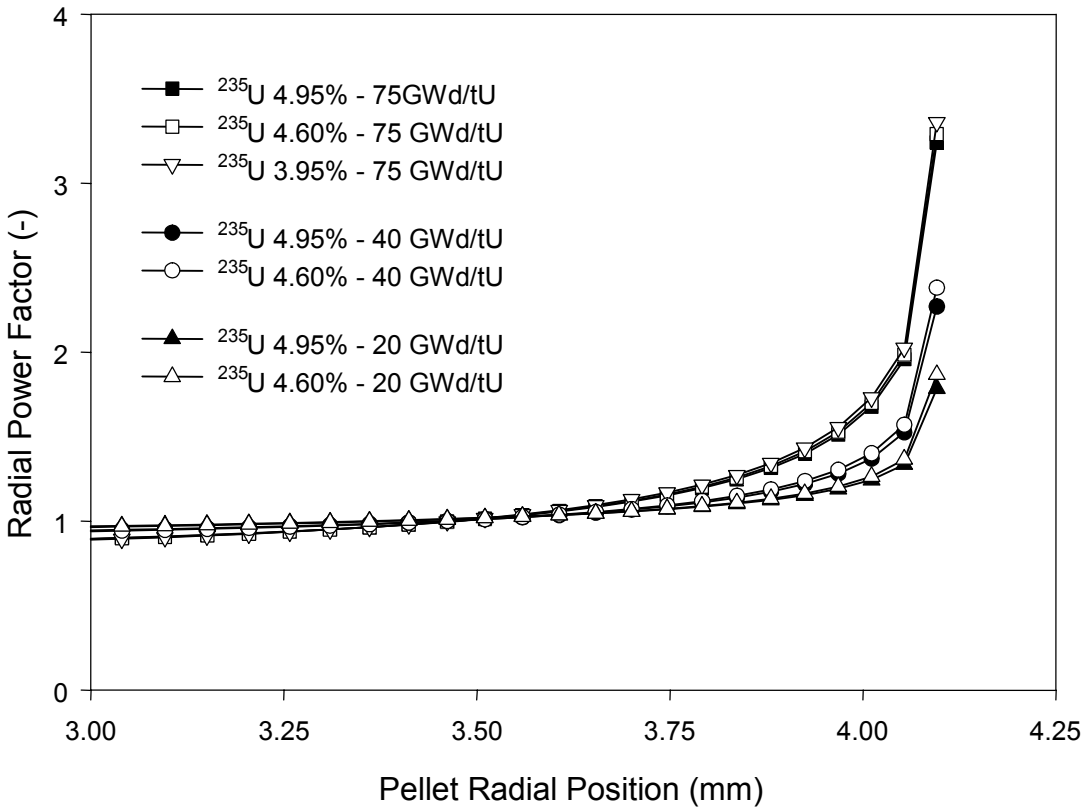

Figure 4-17
Radial Power Factors calculated by the TUBRNP model for different levels of ^{235}U enrichment and burnup.

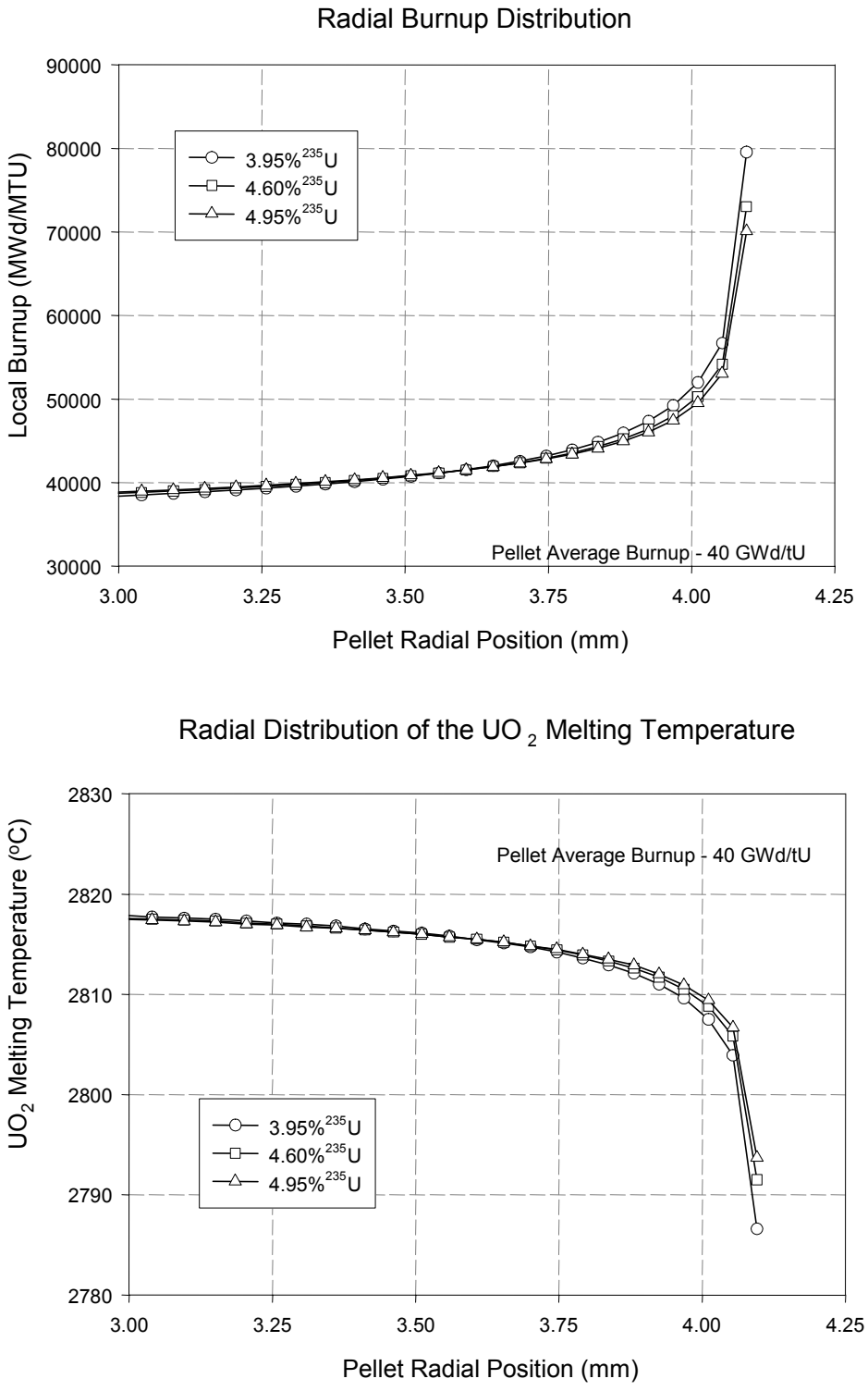

Figure 4-18
The TUBRNP calculated radial burnup distribution (a) and the radial distribution of the UO_2 melting (b) are shown as a function of pellet radial position and ^{235}U enrichment at a pellet average burnup of 40 GWd/tU.

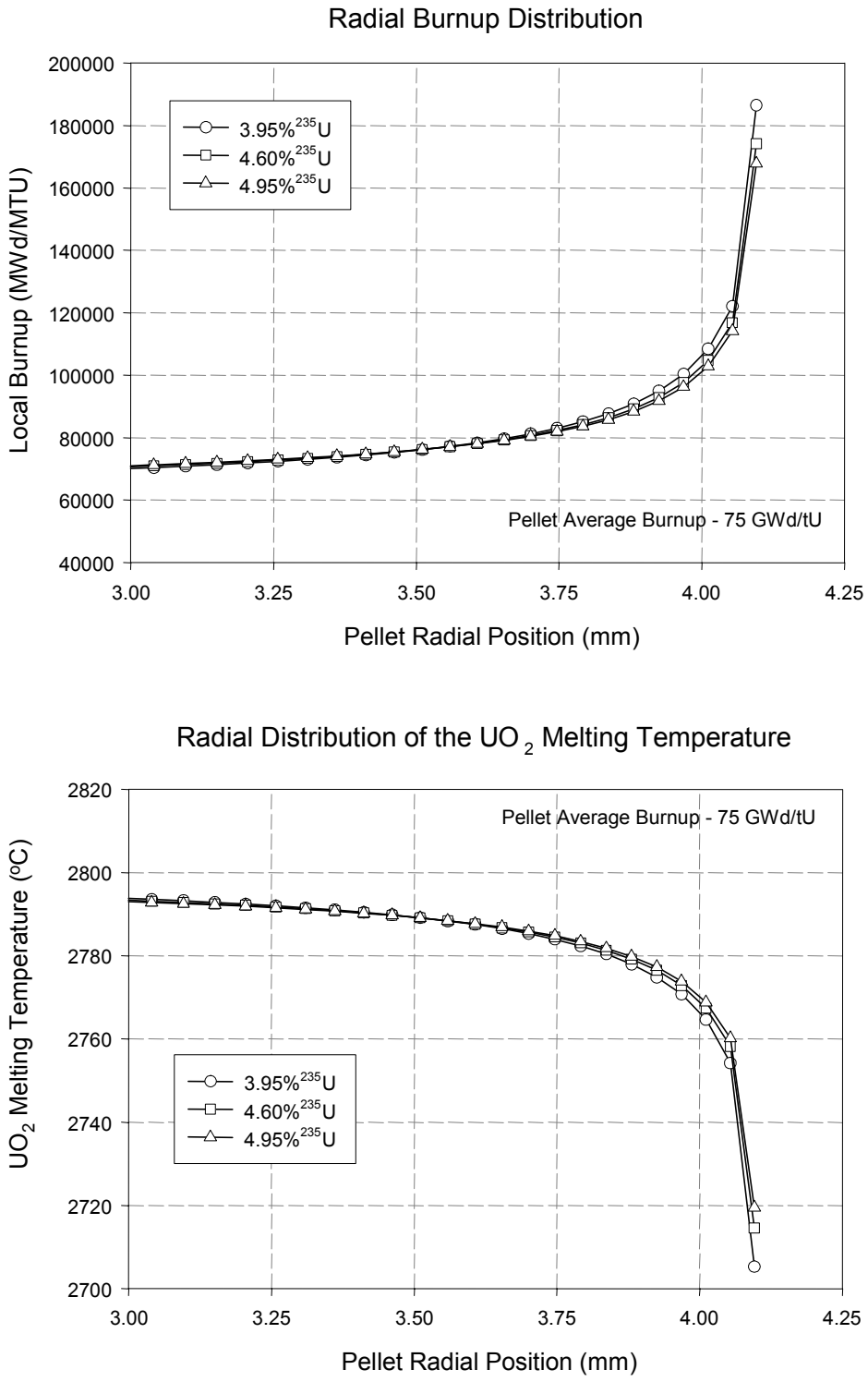

Figure 4-19
The TUBRNP calculated radial burnup distribution (a) and the radial distribution of the UO_2 melting (b) are shown as a function of pellet radial position and ^{235}U enrichment at a pellet average burnup of 75 GWd/tU.

The radial power distribution for a ^{235}U enrichment of 4.95% and a gadolinia content of 8 wt% is shown in Figure 4-20 at a pellet average burnup of 40 GWd/tU and 75 GWd/tU. Profiles for both with and without gadolinia are shown for comparison. These results demonstrate that the radial power distribution in the pellet periphery varies by about 1% with the addition of gadolinia. A difference of about 7% is observed at 40 GWd/tU near the center of the pellet, which is caused by the influence by a small remaining amount of absorbing gadolinia content in that part of the pellet. At a pellet average burnup of 75 GWd/tU, the neutronic effects of the gadolinia are completely removed by burnout of the absorbing gadolinia isotope.

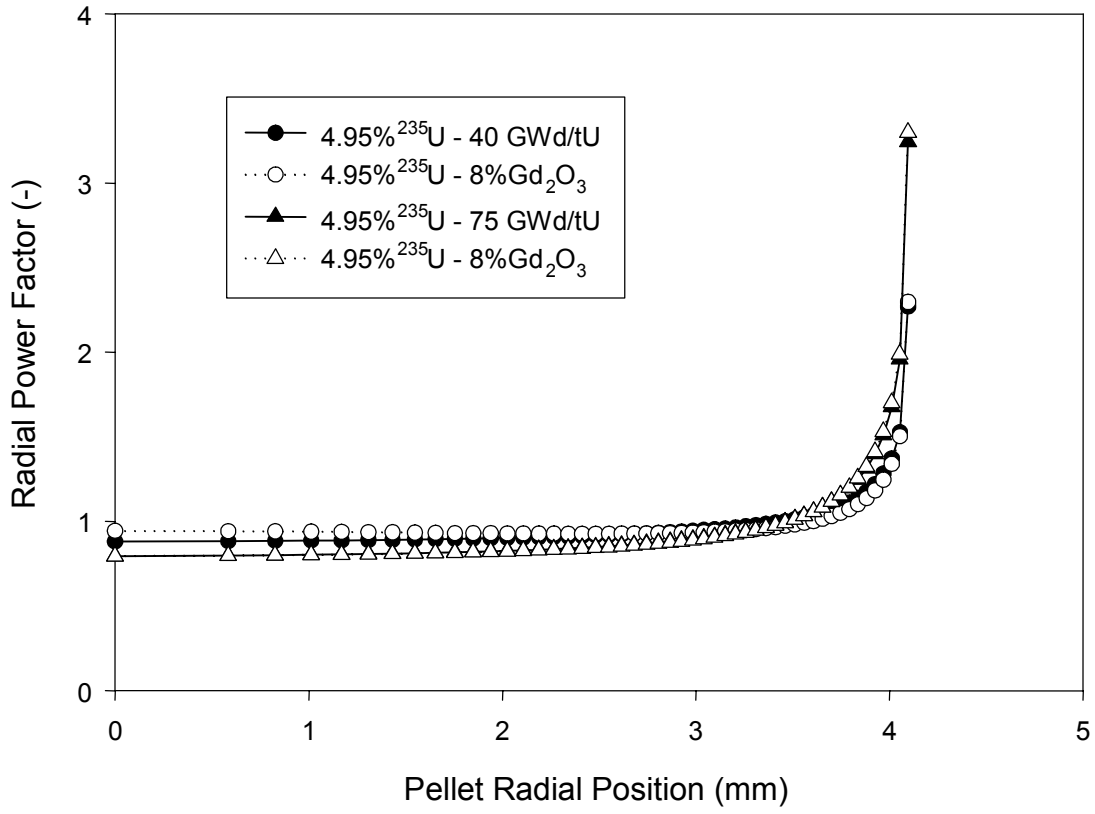

Figure 4-20
Radial Power Factors calculated by the TUBRNP model for 8wt% gadolinia and at pellet average burnup levels 40 GWd/tU and 75 GWd/tU. Profiles for non-gadolinia pellets are shown for comparison.

The radial burnup distribution is impacted by the presence of gadolinia due to the neutron absorption in the pellet. The self-shield effects are more pronounced for pellets with gadolinia isotope additives. Gadolinia suppresses the burnup accumulation in the central part of the pellet and causes an increase in the local burnup near the pellet periphery. The radial burnup distributions calculated by TUBRNP are shown in Figure 4-21a and 4-22a for pellet average burnup levels of 40 GWd/tU and 75 GWd/tU, respectively. The impact of gadolinia on the radial burnup distribution is stronger for the case with the pellet average burnup of 40 GWd/tU. In this case, the local burnup at the centerline is approximately 20% lower for the 8 wt% gadolinia pellet than for a non-gadolinia pellet. At the pellet periphery, this changes to a 20% higher

burnup for the 8 wt% gadolinia case. These differences decrease to 10% for the 75 GWd/tU pellet burnup condition.

A comparison of the 8 wt% gadolinia and the non-gadolinia UO_2 melting temperature distributions, are shown in Figure 4-21b and 4-22b for a pellet average burnup of 40 GWd/tU and 75 GWd/tU, respectively. The radial dependency of UO_2 melting temperature was calculated using Equation 4-2 and the radial burnup distributions shown in Figure 4-21a and 4-22a. It was assumed in the developed of Figure 4-21b and 4-22b that the addition of 8 wt% Gd_2O_3 would not impact the UO_2 melting temperature and only the local burnup distribution causes the melting temperature to depend on radial position. The data used to develop Equation 4-2 included UO_2 material with Gd_2O_3 additives up to 2 wt% and the experimental measurements found no impact of gadolinia on the UO_2 melting temperature. Because of the increase of local burnup in the pellet periphery for the gadolinia pellets, the melting temperature is lower than a non-gadolinia pellet by between 10 to 15°C. This difference is reversed in the central part of the pellet because of the slight burnup depression in this region for the gadolinia pellet. As mentioned previously, the FALCON calculations show that the peak temperature occurs near the pellet periphery, not at the pellet surface. At these locations, the change in UO_2 melting temperature is less than 5°C between the gadolinia and non-gadolinia pellets. This difference is well within the uncertainty of the measured UO_2 melting temperature. Also, this difference is smaller than the margin used to define incipient melting in the FALCON calculations. As shown in Table 4-6, the FALCON calculated peak temperatures are below the UO_2 melting temperature by between 10 and 20°C.

The impact of variations in ^{235}U enrichment and gadolinia content from the values used to develop the core coolability limit shown in Figure 4-16 are small based on changes reflected in the radial power and burnup distribution. The uncertainty in the curve shown in Figure 4-16 associated with variations in the initial ^{235}U enrichment or the presence of gadolinia additives would be less than 5 cal/gm.

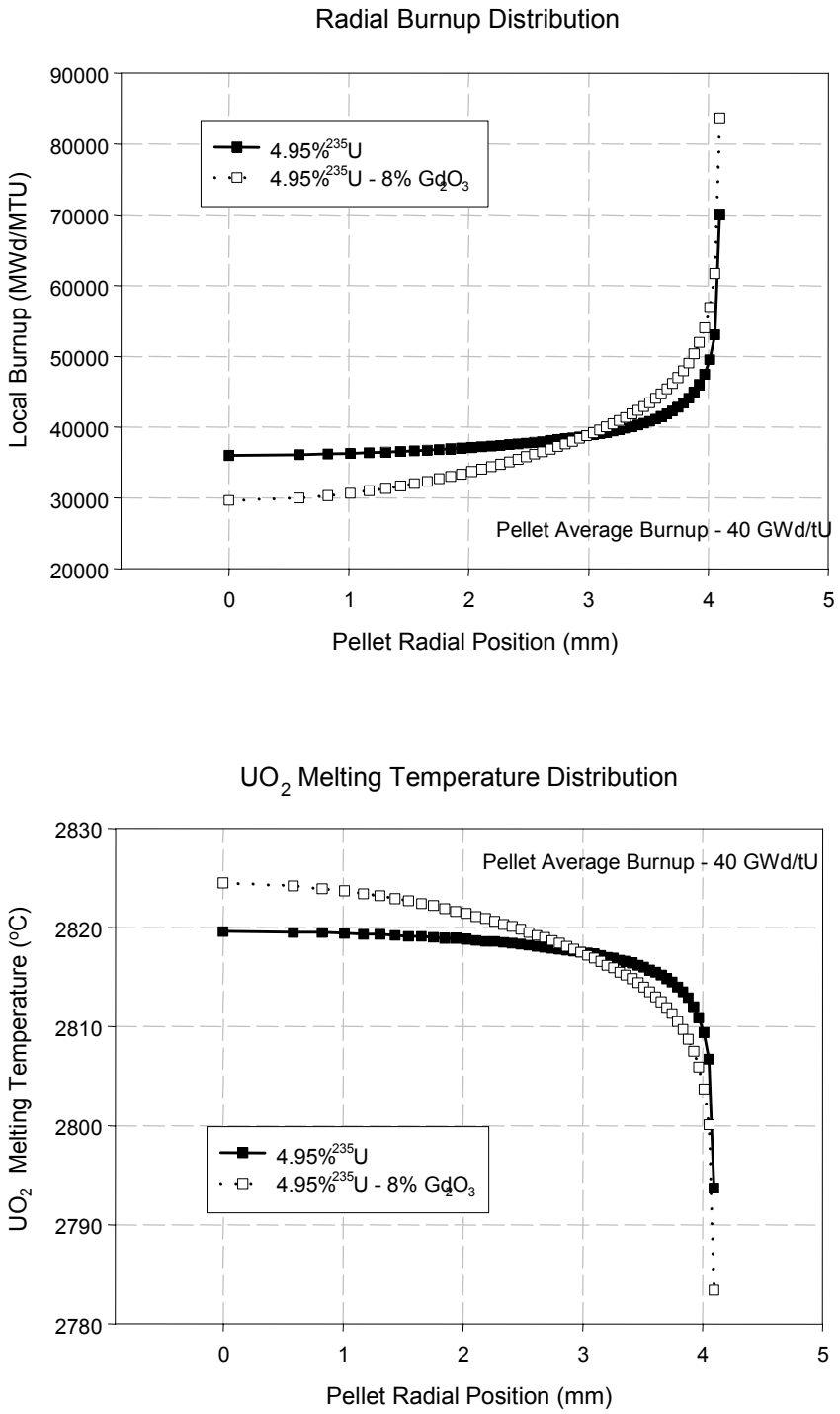

Figure 4-21
The TUBRNP calculated radial burnup distribution (a) and the radial distribution of the UO_2 melting (b) are shown as a function of pellet radial position and gadolinia content at a pellet average burnup of 40 GWd/tU.

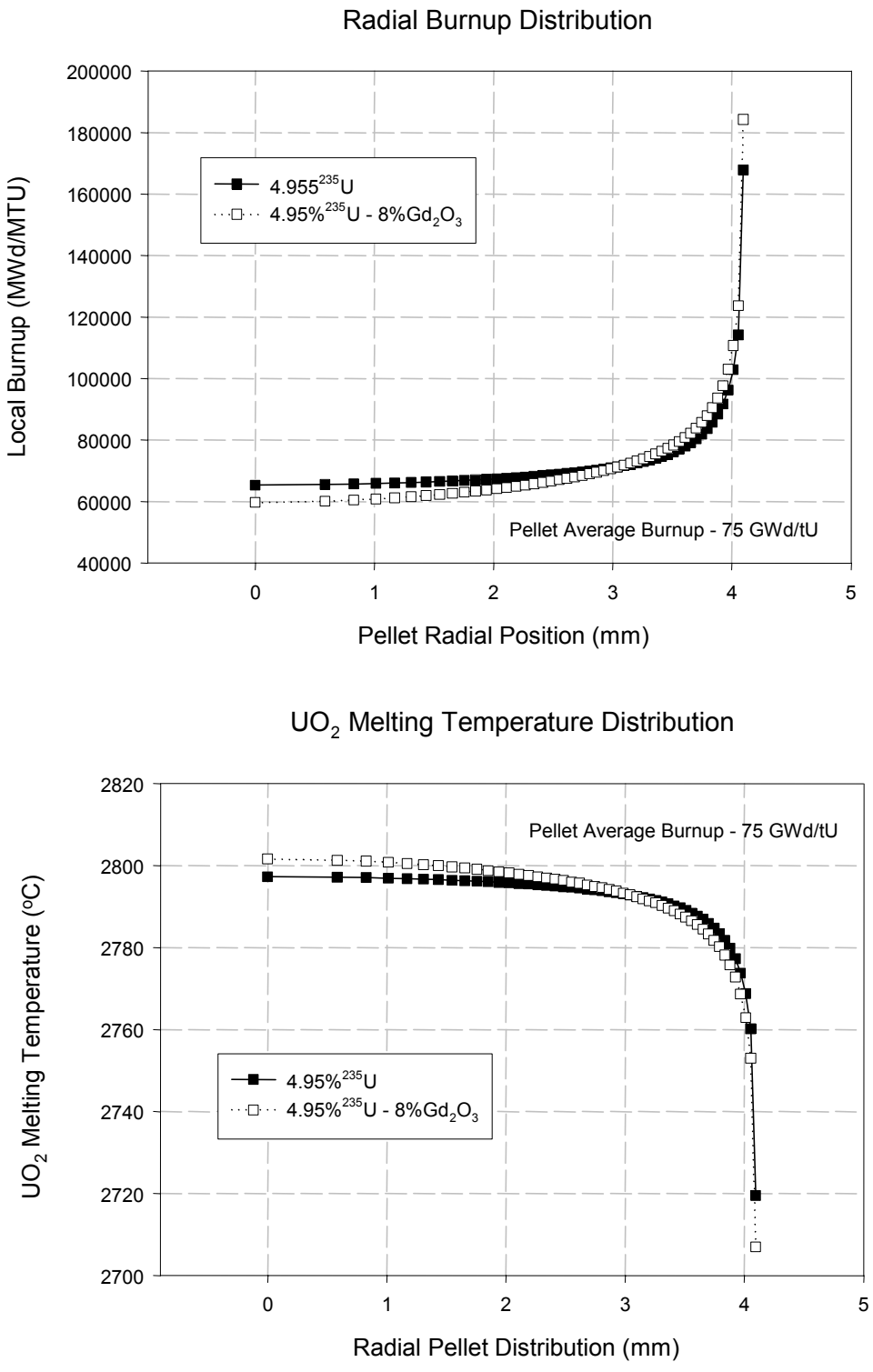

Figure 4-22
The TUBRNP calculated radial burnup distribution (a) and the radial distribution of the UO_2 melting (b) are shown as a function of pellet radial position and gadolinia content at a pellet average burnup of 75 GWd/tU.

4.3.1.3 Transient Pellet-Cladding Gap Conductance

The evolution of the pellet-cladding gap conductance during the power pulse was calculated in FALCON using the Ross and Stoute model for open gap conditions and a modified Mikic-Todreas model for closed gap solid contact conditions [refers]. These models were developed for quasi-steady state conditions and may not be directly applicable to pellet-cladding gap conductance for high contact pressure conditions during a rapid power pulse. The FALCON calculations used to establish the core coolability curve shown in Figure 4-16 are based on a gap conductance model that was unlimited. As a consequence, transient gap conductance values in excess of $1x10^5$ W/m^2-K were calculated using the model in FALCON over a very short period near the end of the power pulse when the contact stress between the pellet and the cladding are high. In comparison, some steady state fuel performance codes limit the maximum gap conductance to values less than $2x10^4$ W/m^2-K [Kramman and Freeburn 1987].

To evaluate the sensitivity of the calculated peak pellet temperatures during the power pulse to the gap conductance, a series of FALCON calculations were performed using an upper limit on the pellet-cladding gap conductance calculated by the model. Calculations were performed for both a rod average burnup of 40 GWd/tU and 75 GWd/tU. Maximum pellet-cladding gap conductance limits ranging between 1,000 W/m^2-K and 60,0000 W/m^2-K were employed in the FALCON analysis. A summary of the results is shown in Table 4-8. The calculated maximum radial average peak fuel enthalpy that produced incipient melting is mostly insensitive to the maximum pellet-cladding gap conductance value above 30,000 W/m^2-K. This arises because the heat conduction within the pellet limits the ability of heat to flow from the pellet to the cladding. Below 30,000 W/m^2-K, some impact on the maximum radial average peak fuel enthalpy is observed because adiabatic heat transfer conditions from the pellet to the cladding are approached.

Table 4-8
Summary of Pellet-Cladding Gap Conductance Sensitivity Evaluation

	Max. Gap Conductance (W/m^2-K)	Maximum Radial Average Stored Energy (cal/gm)	Decrease in Radial Average Stored Energy (cal/gm)
40 GWd/tU	> 100,000	222	Base Case
	60,000	221	1
	30,000	218	4
	15,000	213	9
	1,000	178	44
75 GWd/tU	> 100,000	189	Base Case
	60,000	188	1
	30,000	183	6
	15,000	176	13
	1,000	147	42

The results in Table 4-8 demonstrate that the peak fuel temperatures in the outer pellet region are not sensitivity to the maximum gap conductance under realistic transient heat transfer conditions in an RIA. For near adiabatic heat transfer conditions, the radial average peak fuel enthalpy required to induce melting decreases between 10 and 50 cal/gm.

4.3.1.4 Sensitivity to Power Pulse Width

The power pulses used in the FALCON analyses to establish the core coolability limit shown in Figure 4-16 were generated with a pulse width of 20 milliseconds. However, the power pulse width determined from the results of neutron kinetics analyses, which are used to compare to the core coolability limit, can vary between 10 and 30 milliseconds. A series of sensitivity calculations were performed with FALCON to assess the impact of pulse width on the maximum fuel temperature and the maximum radial average peak fuel enthalpy to produce incipient melting. These results were used to develop the core coolability limit. The FALCON calculations were performed at rod average burnup levels of 40 and 75 GWd/tU and power pulse widths of 10, 15, and 30 milliseconds. The FALCON calculations incorporate the impact of pulse width through the heat conduction processes, which influence the radial temperature profile and the cladding temperature. No additional fission gas bubble expansion or dynamic gas loading effects were used in the PCMI analysis.

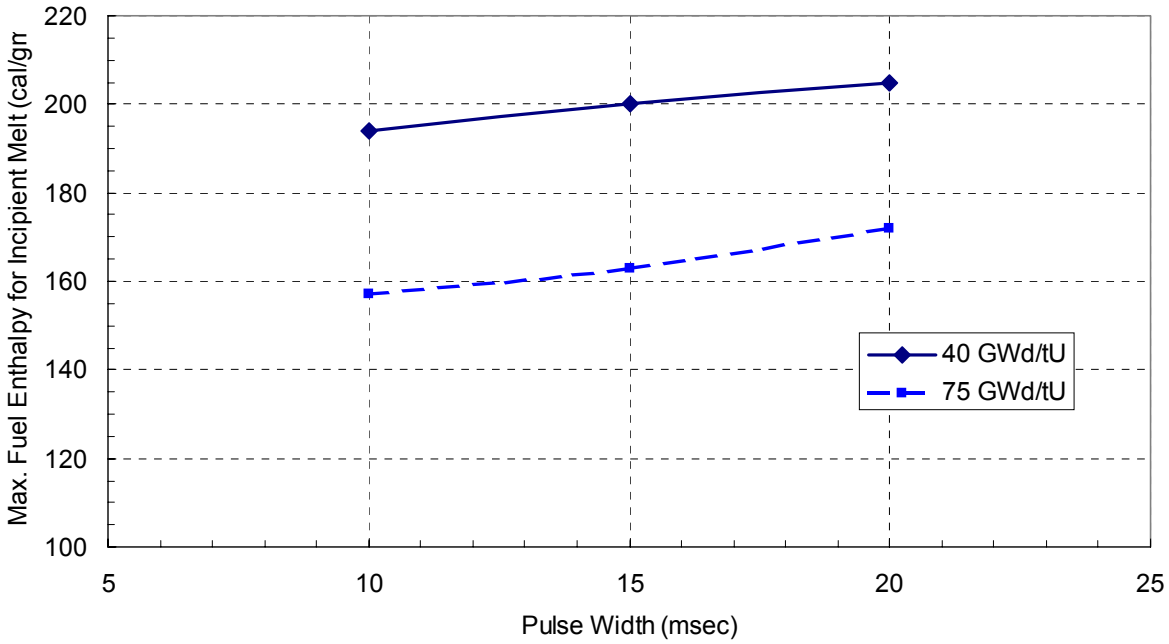

Figure 4-23
The Radial Average Peak Fuel Enthalpy at Incipient Pellet Melting as a Function of Power Pulse Width for Rod Average Burnup Levels of 40 GWd/tU and 75 GWd/tU.

The results of the pulse width sensitivity analysis are shown in Figure 4-23 for a rod average burnup of 40 GWd/tU and 75 GWd/tU. Shown in Figure 4-23 is the radial average peak fuel enthalpy to produce incipient pellet melting as a function of pulse width. The FALCON calculations demonstrate that the core coolability decreases by about 10 to 15 cal/gm for pulse widths below 20 milliseconds. The large impact is at a rod average burnup of 75 GWd/tU because the peak temperature occurs near the pellet surface and is influenced strongly by heat conduction processes for wider pulse widths. Above a pulse width of 20 milliseconds, the core coolability at both 40 and 75 GWd/tU saturate to values very close to those shown in Figure 4-16.

5
CONCLUSIONS

The current regulatory acceptance criteria used in the licensing analysis of the PWR REA are defined in the US NRC regulations to be:

Fuel Rod Failure Threshold: Cladding failure occurs when the calculated heat flux equals or exceeds the departure from nucleate boiling ratio for zero power, low power and full power RIA events in PWRs.

Core Coolability Limit: The maximum radial average peak fuel enthalpy shall not exceed 280 cal/gm at any axial location in any rod.

When combined with neutron kinetics calculations, these acceptance criteria have been used to demonstrate the safe operation of PWRs during postulated RIA events.

The criteria defined above are not burnup dependent and therefore do not consider changes in fuel rod behavior introduced as a consequence of burnup accumulation. During the last 10 years, RIA-simulation tests in the CABRI (France) and NSRR (Japan) facilities using rods from commercial reactors have demonstrated that the regulatory acceptance criteria used for the PWR REA may not be applicable to fuel rod average burnup levels beyond 40 GWd/t. The NRC has evaluated the situation and concluded that the test results coming from these RIA-simulation tests do not constitute a safety concern for currently operating facilities. Nevertheless, the NRC has indicated that the approach to high burnup fuel design operation must consider revised regulatory acceptance criteria for postulated RIA events that incorporate the effects of burnup [Taylor 1994].

Technical evaluation of the RIA issue has been conducted under the auspices of the Robust Fuel Program Working Group 2 with the objective of developing revised RIA acceptance criteria for use with fuel rod designs targeted for operation beyond rod average burnup levels of 62 GWd/tU. The approach used in the technical evaluation combined experimental data from a variety of sources, including integral RIA-simulation tests and separate effects tests, with transient fuel rod analysis calculations. In this way, the effects of burnup on both fuel rod failure and the conditions leading to damaging fuel-coolant interaction were determined and revised acceptance criteria established. The revised acceptance criteria consist of a fuel rod failure threshold and a separate core coolability limit. The fuel rod failure threshold is used to account for radiological release to the environment following cladding failure. The core coolability limit is established to ensure long-term cooling of the reactor after the accident. The use of two separate criteria is consistent with the approach defined in Regulatory Guide 1.77.

5.1 Fuel Rod Failure Threshold

The experimental data from RIA-simulation tests shows that fuel rod failure during a rapid power pulse occurs by one of two modes. If the cladding ductility is high, cladding failure can occur by high temperature processes following departure from nucleate boiling heat transfer. If the cladding ductility is low, the forces resulting from PCMI can cause cladding failure. The transition between these two modes is a function of how the cladding ductility transforms as burnup accumulation proceeds.

Because of inconsistencies in the database caused by the effects of prior irradiation and initial coolant temperature on cladding ductility, the experimental data from RIA-simulation experiments are insufficient to develop directly a fuel rod failure threshold based on PCMI mechanisms. However, the database of RIA-simulation experiments can be used to validate transient fuel rod analysis methods. Such analytical evaluations are required to translate the data from RIA tests to applicable PWR REA conditions.

The development of a complete fuel rod failure threshold that spans the entire range of burnup operation must incorporate both of the possible cladding failure modes. Therefore, the approach to develop a revised fuel rod failure threshold focused on identifying the transition from high temperature induced cladding failure to PCMI-induced cladding failure. The following approach was used to develop the revised fuel rod failure threshold.

Zero/Low Burnup Regime: The experimental data on high temperature failure behavior was reviewed and it was found that for zero and low burnup fuel rods the potential for cladding failure by high temperature oxidation-induced embrittlement increases above a radial average peak fuel enthalpy of 170 cal/gm. Failure below 170 cal/gm has been shown to occur only when the internal rod pressure exceeds the coolant pressure by more than 1 MPa at the initiation of the transient (positive pressure differential conditions). The possibility to have a positive pressure differential at HZP is low at low and intermediate burnup regimes, even for IFBA fuel. Therefore, fuel rod failure by high temperature processes was defined to occur above a radial average peak fuel enthalpy of 170 cal/gm.

Intermediate and High Burnup Regime: Because of the complex manner in which burnup influences fuel rod failure, it was not possible to develop a fuel rod failure threshold directly from the experimental data. An alternative approach that combined analytical modeling and experimental data was used to develop the PCMI part of the failure threshold. The analytical approach is based on the FALCON transient fuel behavior code.

The radial average peak fuel enthalpy required to cause cladding failure by PCMI was calculated by FALCON as a function of rod average burnup using a cladding ductility model based on mechanical properties tests from irradiated low-tin Zr-4 cladding material. The critical strain energy density (CSED) data formed the basis of the cladding ductility model. To account for the accumulation of outer surface corrosion, a conservative oxidation rate was used that bounded a large databoase of low-tin Zr-4 oxide thickness measurements. A maximum cladding outer surface oxide thickness of 100 microns was imposed and the impact of oxide layer spalling on the cladding mechanical properties was not considered. The analytical evaluation included

several fuel rod designs and the design that resulted in the lowest fuel enthalpy levels at failure was selected to develop the failure threshold.

The overall fuel rod failure threshold was obtained by combining the high temperature failure threshold of 170 cal/gm with the fuel enthalpy required to produce cladding failure by PCMI deduced from the analytical evaluation. The result is shown in Figure 5-1 along with the mathematical expression for the failure threshold as a function of rod average burnup.

The failure threshold shown in Figure 5-1 is defined in terms of the radial average peak fuel enthalpy as a function of rod average burnup. Below 36 GWd/tU, the failure threshold is established based on high temperature failure mechanisms. Beyond 36 GWd/tU, the failure threshold is based on cladding failure by PCMI. The decrease in the failure threshold is caused by two factors, the increase in PCMI loading due to gap closure effects and by the decrease in cladding ductility with oxidation.

Because of the conservative oxidation rate and the Zr-4 mechanical property data used in the cladding integrity model, the high burnup portion of the failure threshold shown in Figure 5-1 represents a lower bound curve for advanced cladding alloys that exhibit improved corrosion performance and more ductile behavior at high burnup.

5.2 Core Coolability Limit

The core coolability limit for RIA events represents the ultimate safety limit to ensure that the consequences of the accident do not impair the long-term capability to cool the core or threaten the integrity of the reactor vessel. The current limit was established to preclude the potential for prompt dispersal of molten fuel particles into the coolant, and it was determined from RIA-simulation experiments using zero burnup rods. The data from these tests demonstrate that the dispersal of molten fuel particles may lead to fuel-coolant interaction and the generation of coolant pressure pulses that could damage the reactor core or pressure vessel.

Recent RIA-simulation experiments on rods with burnup levels greater than 30 GWd/tU demonstrate a potential for dispersal of finely fragmented non-molten fuel material following cladding failure. In all cases that resulted in dispersal of non-molten material, the tests were run with a power pulse width less than 10 milliseconds. For pulse widths less than 10 milliseconds, post-test examinations and analytical evaluations have shown that the thermal and mechanical state in the pellet periphery can lead to conditions conducive to material dispersal following cladding failure.

The consequences from fuel-coolant interaction are much less for the dispersal of finely fragmented non-molten material than for the dispersal of molten material. The measured mechanical energy generation from fuel coolant interaction is an order of magnitude larger for molten fuel dispersal than for finely fragmented non-molten fuel dispersal. This arises because less than 10% of the pellet is dispersed as non-molten finely fragmented material and the thermal energy content of non-molten material is less than for molten material.

These factors make the dispersal of finely fragmented non-molten fuel material a radiological release issue and not a coolability issue. Furthermore, the potential is low in a PWR REA event

for dispersal of non-molten fuel material following cladding failure because typical power pulse widths, determined from neutron kinetics calculations, are greater than 10 milliseconds.

Based on the experimental data from zero and low burnup RIA-simulation tests, it is most appropriate to limit the peak pellet temperature to below the UO_2 melting temperature to mitigate the adverse consequences of fuel-coolant interaction in the unlikely event of dispersal of pellet material. Restricting the fuel enthalpy level to values below that necessary to produce fuel pellet melting will ensure that fuel rod geometry is maintained throughout an RIA event.

Because no experiments on high burnup fuel have been conducted that resulted in molten fuel dispersal, an analytical evaluation was used to determine the maximum radial average peak fuel enthalpy that causes the local pellet temperature to reach the melting temperature. The analysis included the effects of burnup on the local UO_2 melting temperature, the radial power distribution, and the UO_2 thermal conductivity. A realistic thermal and mechanical fuel rod analysis was performed using FALCON that included pellet to cladding heat transfer. The outcome is a radial average peak fuel enthalpy that decreases as a function of rod average burnup. The resulting core coolability limit is shown in Figure 5-1 along with the mathematical expression. The maximum radial average peak fuel enthalpy versus rod average burnup curve shown in Figure 5-1 limits the peak fuel pellet temperature to below the UO_2 melting temperature. It is assumed that radial average peak fuel enthalpy levels above the limit shown in Figure 5-1, may lead to fuel melting, fuel material dispersal, and mechanical energy generation by fuel-coolant interaction.

In summary, the core coolability limit shown in Figure 5-1 assures long-term core cooling after a PWR REA event for the following reasons:

- No fuel dispersal leading to fuel-coolant interaction will occur following cladding failure for typical PWR REA power pulse widths.
- In the unlikely event of fuel dispersal, the dispersed material will be below the UO_2 melting temperature, thus limiting the extent of mechanical energy generation by fuel-coolant interaction to below that required for damaging consequences.

The revised acceptance criteria shown in Figure 5-1 are applicable to Zircaloy-clad UO_2 or UO_2-Gd_2O_3 fuel rod designs operated up to a target lead rod average burnup of 75 GWd/tU. The core coolability limit is applicable to both HZP and HFP PWR REA and BWR RDA events. The fuel rod failure threshold can be applied to the HZP PWR REA and the HZP BWR RDA events. Departure from nucleate boiling (DNB) should continue to be used as the failure threshold for both PWR and BWR HFP RIA events. Implied in the use of the fuel rod failure threshold is a limitation on the maximum cladding outer surface zirconium oxide layer of 100 microns, which precludes the adverse effects of oxide layer spallation on the cladding mechanical properties. The fuel rod failure threshold shown in Figure 5-1 is applicable to advanced cladding designs provided the cladding material exhibits superior or equivalent ductility as the Zircaloy cladding properties used to develop the failure threshold.

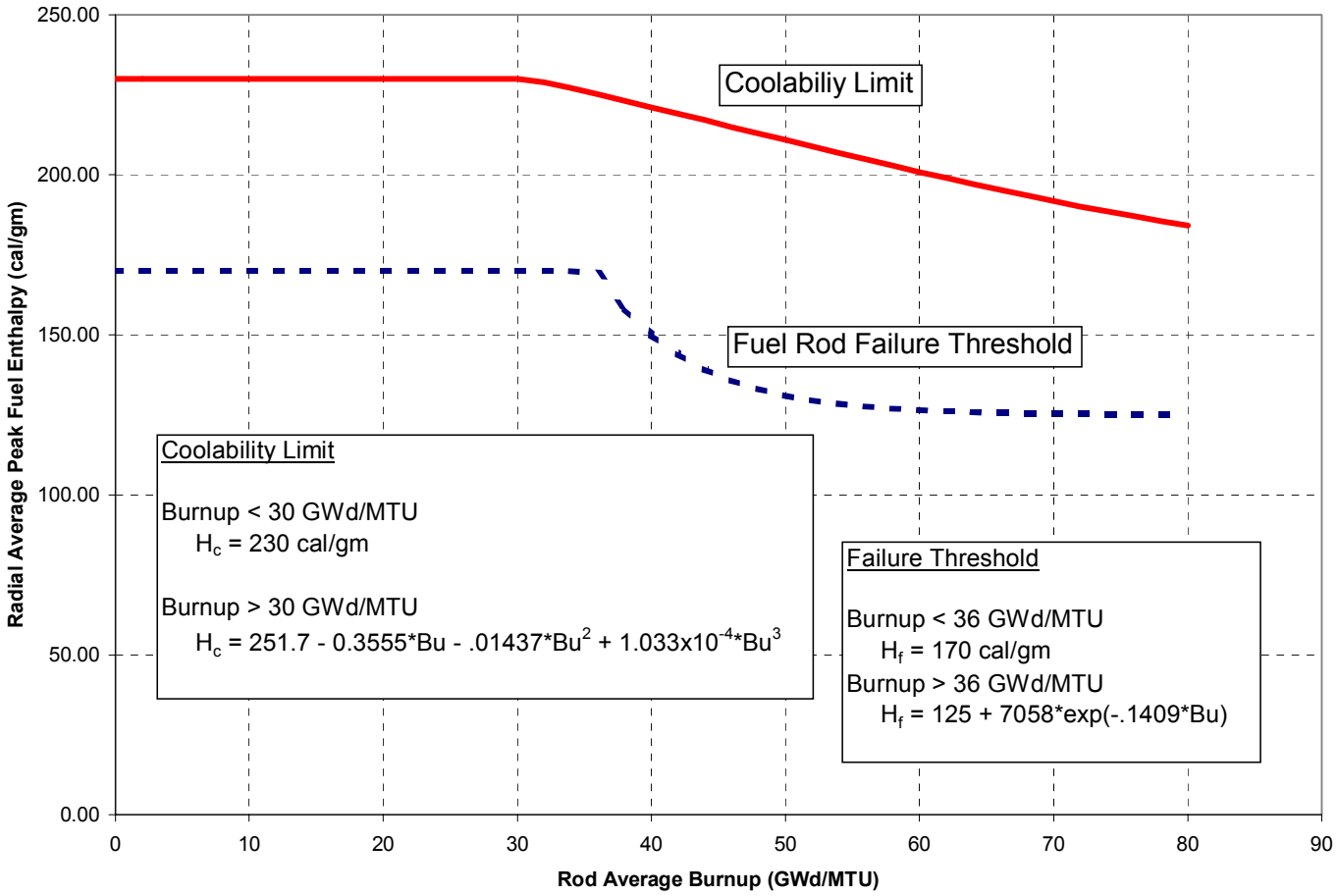

Figure 5-1
Revised Acceptance Criteria for the HZP PWR REA and the HZP BWR RDA events. The criteria are defined in terms of the radial average peak fuel enthalpy as a function of rod average burnup.

6
REFERENCES

1. 10 CFR Part 50 Appendix A, General Design Criteria for Nuclear Power Plants, U.S. Government Printing Office, Washington, 1990.

2. 10 CFR Part 100.11,Determination of Exclusion Area, Low Population Zone, and Population Center Distance, U.S. Government Printing Office, Washington, 1990.

3. Amaya M, et.al., "Thermal Conductivities of Irradiated UO_2 and $(U,Gd)O_2$ Pellets," Nuclear Fuel Behavior Modelling at High Burnup and Its Experimental Support, Proceedings of a IAEA Technical Committee Meeting, Windermere, UK, IAEA-TECDOC-1233, p. 17, June 2000.

4. Andersson, T. and A. Wilson, "Ductility of Zircaloy Canning Tubes in Relation to Stress Ratio in Biaxial Testing," Zirconium in the Nuclear Industry: Fourth International Conference, ASTM STP 681, American Society for Testing and Materials, 1979, pp. 60-71.

5. Asmolov, V. and Yegorova, L., "The Russian RIA Research Program: Motivation, Definition, Execution, and Results," Nuclear Safety, Vol. 37, No. 4, Nuclear Regulatory Commission, Betheseda, Maryland, October - December 1996, 343 - 371.

6. Balfour, M. G. et al., "Final Report: Hot Cell Examination of Zion Fuel, Cycles 1 Through 4," WCAP-10473, Westinghouse Electric Corporation, April 1985.

7. Baron, D., "About the Modelling of Fuel Thermal Conductivity Degradation at High Burnup Accounting for Recovering Processes with Temperature," Proceedings of the NEA/OECD Seminar on Thermal Performance of High Burnup LWR Fuel, Cadarache France, p. 129, March 1998.

8. Bates, D. W., Influence of Stress State and Hydrogen on Deformation and Failure of Zircaloy-4," Thesis, Department of Nuclear Engineering, Pennsylvania State University, December 1998.

9. Bibilashvili, Yu., et al., "Experimental Study of VVER High Burnup Fuel Rods at the BIGR Reactor under Narrow Pulse Conditions," *Proceedings of the ANS International Topical Meeting on Light Water Reactor Fuel Performance*, Park City, Utah, April 10-13, 2000 pp. 306 - 314.

10. Boyack, et.al., "Phenomena Identification and Ranking Tables (PIRTs) for Rod Ejection Accidents in Pressurized Water Reactors Containing High Burnup Fuel," NUREG/CR-6742, September 2001.

11. Collier, J. G., Convective Boiling and Condensation, Second Edition, McGraw-Hill, Inc., 1972.

12. Cook, B. A., S. K. Fukuda, Z. R. Martinson, P. Bott-Hembree, "Reactivity Initiated Accident Test Series Test RIA 1-2 Fuel Behavior Report," NUREG/CR-1842, EG&G, Inc., January 1981.

13. Corsetti, L. V. et al., "Improved BWR and PWR Fyel Designs and Operating Experience at ABB," *Proceedings of the ANS International Topical Meeting on Light Water Reactor Fuel Performance*, Portland, Oregon, March 2-6, 1997 pp. 280-286.

14. Christiansen, J. A., et al., "Uranium Dioxide Thermal Conductivity," *Transactions of the American Nuclear Society*, 7, 1964, p. 391.

15. Chung, H. M., A. M. Garde, and T. F. Kassner, "Development of an Oxygen Embrittlement Criterion for Zircaloy Cladding Applicable to Loss-of-Coolant Accident Conditions in Light-Water Reactors," *Zirconium in the Nuclear Industry: Forth International Conference, ASTM STP 681*, American Society for Testing and Materials, Stratford-upon-Avon, 1978, pp. 600-627.

16. Chung, H. M., and T. F. Kassner, "Deformation Characteristics of Zircaloy Cladding in Vacuum and Steam under Transient-Heating Conditions: Summary Report, NUREG/CR-0344, Argonne National Laboratory, July 1978.

17. Chung, H. M., L. A. Neimark, and T. F. Kassner, “Test Plan for High-Burnup Fuel Behavior Under Loss-of-Coolant Conditions,” *Proceedings of the Twenty-Fourth Water Reactor Safety Meeting*, Vol. 1, Nuclear Regulatory Commission, Bethesda, Maryland, October 21-23, 1996, pp. 173-184.

18. Chung, H. M., "Fundamental Metallurgical Aspects of Axial Splitting in Zircaloy Cladding," *Proceedings of the ANS International Topical Meeting on Light Water Reactor Fuel Performance*, Park City, Utah, April 10-13, 2000 pp. 325 - 344.

19. Cunningham, M. E., M. D. Freshley, and D. D. Lanning, “Development and Characteristics of the RIM Region in High Burnup UO_2 Fuel Pellets," *Journal of Nuclear Materials*, Volume: 188, 1992, pp. 19-27.

20. Cunningham, M. E. et al., " Development and Assessment of the FRAPTRAN Transient Fuel Rod Code," *Proceedings of the Twenty-Eighth Water Reactor Safety Information Meeting*, NUREG/CP-0172, U.S. Nuclear Regulatory Commission, Bethesda, Maryland, October 23-25, 2000, pp. 251-263.

21. Daum, R. S. et al., "*Mechanical Property Testing of Irradiated Zircaloy Cladding Under Reactor Transient Conditions," Fourth Symposium on Small Specimen test Techniques, ASTM 1418*, Reno, NV, January 23-25, 2001.

22. Daum, R. S. et al., "On the Embrittlement of Zircaloy-4 Under RIA-Relevant Conditions," *Zirconium in the Nuclear Industry: Thirteenth International Symposium, to be published*, American Society for Testing and Materials, Annecy, France, 2001.

23. Davidson, S. L. and D. L. Nuhfer, Eds., "VANTAGE+ Fuel Assembly Reference Core Report, WCAP-12610 (Non-Proprietary) Westinghouse Electric Corporation, June 1990.

24. Delette, G., and M. Charles, “Thermal Conductivity of Fully Dense Unirradiated UO_2: A New Formulation from Experimental Results Between 100°C and 2500°C and Associated Fundamental Properties,” Water Reactor Fuel Element Modelling at High Burnup and Its Experimental Support, Proceedings of a IAEA Technical Committee Meeting, Windermere, UK, IAEA-TECDOC-957, p. 203, September 1994.

25. Diamond, D. J., “A Probabilistic Profile for Reactivity Accidents,” Brookhaven National Laboratory, Technical Report FIN W-6382, Contract No. AC02-98CH10886, March 1998.

26. Fan and Koss, Metall. Trans., 16A, 1985, p. 675.

27. Federici, E. et al., "Status of Development of the SCANAIR Code for the Description of Fuel Behavior Under Reactivity Initiated Accidents," *Proceedings of the ANS International Topical Meeting on Light Water Reactor Fuel Performance*, Park City, Utah, April 10-13, 2000 pp. 345 - 358.

28. Fletcher, D. F., "The Particle Size Distribution of Solidified Melt Debris from Molten Fuel-Coolant Interaction Experiments," UKAEA, Culham Laboratory, Elsevier Science Publishers B. V. (North-Holland Physics Publishing Division), August 1987.

29. Forgeron, T. et al., "Experiment and Modeling of Advanced Fuel Rod Cladding Behavior Under LOCA Conditions, Alpha-Beta Phase Transformation Kinetics and EDGAR Methodology," *Zirconium in the Nuclear Industry: Twelfth International Symposium, ASTM STP 1345*, G. P. Sabol and G. D. Moan, Eds., American Society for Testing and Materials, West-Conshohocken, PA, 2000, pp. 256-278.

30. Freeburn, H. R., O. Ozer, and R. Yang, "The Effect of Burnup on UO2 Thermal Conductivity - NRC Review of the ESCORE Model," Enlarged Halden Programme Group Meeting on Fuels and Materials Performance and Computerised Man-Machine Communication, Bolkesjo, Norway, June 9-14, 1991.

31. Fujishiro, T., et al. "Transient fuel behavior of preirradiated PWR fuels under reactivity initiated accident conditions," Journal of Nuclear Materials, Volume 188, 1992, pp. 162-167.

32. Fuketa, T., N. Yamano, and A. Inoue, "Proceedings of the CSNI Specialists Meeting on Fuel-Coolant Interactions," NUREG/CP-0127, NEA/SCNI/R(93)8, Santa Barbara, California, January 5-8, 1993.

33. Fuketa, T., et al., “NSRR/RIA Experiments with High-Burnup PWR Fuels,” *Nuclear Safety*, Vol. 37, No. 4, Nuclear Regulatory Commission, Bethesda, Maryland, October-December, 1996, pp. 328-342.

34. Fuketa, T., Sasajima, H., Mori, Y., Ishijima, K., "Fuel failure and fission gas release in high burnup PWR fuels under RIA conditions," Journal of Nuclear Materials, Volume 248, 1997, pp. 249-256.

35. Fuketa, T, et al., "NSRR Pulse Irradiation Experiments and Tube Burst Tests," *Proceedings of the Twenty-Sixth Water Reactor Safety Information Meeting*, Vol. 3, Nuclear Regulatory Commission, Bethesda, Maryland, October 26-28, 1998, pp. 223-242.

36. Fuketa, T., "Experimental Insights on High-Burnup PWR Fuel Behavior During an RIA," *Proceedings of the Twenty-Third NSRR Technical Review Meeting*, Japan Atomic Energy Research Institute, Tokyo, November 11-12, 1999.

37. Fuketa, T., et al., Behavior of PWR and BWR Fuels During Reactivity-Initiated Accident Conditions," *Proceedings of the ANS International Topical Meeting on Light Water Reactor Fuel Performance*, Park City, Utah, April 10-13, 2000 pp. 359 - 373.

38. Garde, A. M., "Hot Cell Examination of Extended Burnup Fuel From Fort Calhoun," DOE/ET/34030-11, Combustion Engineering, September 1986.

39. Garde, A. M., "Effects of Irradiation and Hydriding on the Mechanical Properties of Zircaloy-4 at High Fluences," *Zirconium in the Nuclear Industry: Eighth International Symposium, ASTM STP 1023*, L. F. P. Van Swam and C. M. Eucken Eds., American Society for Testing and Materials, Philadelphia, 1989, pp. 548-569.

40. Garde, A. M., G. P. Smith, and R. C. Pirek, "Effects of Hydride Precipitate Localization and Neutron Fluence on the Ductility of Irradiated Zircaloy-4," *Zirconium in the Nuclear Industry: Eleventh International Symposium, ASTM STP 1295*, E. R. Bradley and G. P. Sabol Eds., American Society for Testing and Materials, 1996, pp. 407-430.

41. Guedeney, P. et al., "FRAGEMA Fuel Rod Behaviour Characterization at High Burnup," *Proceedings of the ANS International Topical Meeting on LWR Fuel Performance*, Avignon, France, April 21-24, 1991 pp. 627-639.

42. Hagrman, D. T., "MATPRO – A Library of Materials Properties for Light Water Reactor Accident Analysis," SCDAP/RELAP5/MOD/3.1 Code Manual, Vol. 4, NUREG/CR-6150, EGG-2720, June 1995.

43. Heck, C. L., et al., "Realistic Evaluation of Reactivity Insertion Accidents in Boiling Water Reactors," *Proceedings of the CSNI Specialists Meeting on Transient Behavior of High Burnup Fuel*, Cadarache France, September 12-14, 1995, Report NEA/CSNI.R(95) 22, 1996.

44. Hermann, A. et al., Fuel Cladding Integrity at High Burnup (Part I), Hydraulic Burst Tests and Tensile Tests on Large Samples, Revision 1 of TR-108753-P1, 1000605 Final Report, NFIR-III/EPRI, Paul Scherrer Institute, September 2000.

45. Hobbins, R. R., G. R. Smolik, and G. W. Gibson," Zircaloy Cladding Behavior During Irradiation Tests Under Power-Cooling-Mismatch Conditions," *Zirconium in the Nuclear Industry, ASTM STP 633*, A. L. Lowe and G. W. Parry Eds., American Society for Testing and Materials, 1977, pp. 182-208.

46. Ishikawa, M. and S. Shiozawa, "A Study of Fuel Behavior Under Reactivity Initiated Accident Conditions - Review", *Journal of Nuclear Materials*, Volume: 95, 1980, pp. 1-30.

47. Komatsu, J., T. Tachibana, and K. Konashi, "The Melting Temperature of Irradiated Oxide Fuel," *Journal of Nuclear Materials*, Volume: 154, 1988, pp. 38-44.

48. Kramman, M. A., and H. R. Freeburn, Eds., "ESCORE--the EPRI Steady-State Core Reload Evaluator Code: General Description," EPRI NP-5100, Electric Power Research Institute, Palo Alto, California, February 1987.

49. Krankota, J. L., and C. N. Craig, "The Melting Point of Plutonia-Urania Mixed Oxide Fuel Irradiated to High Burnup," GEAP-13515, 1969.

50. Kuo, R. C. et al., Fuel Cladding Integrity at High Burnup (Part II), Uniaxial Tensile Tests and Slotted Arc Tests on Small Samples, Revision 1 of TR-108753-P2, 1000606 Final Report, NFIR-III/EPRI, Institute of Nuclear Energy Research, September 2000.

51. Lassmann K., C. O'Carroll, J. van de Laar, and C. T. Walker, "The Radial Distribution of Plutonium in High Burnup UO_2 Fuels," *Journal of Nuclear Materials*, Volume: 208, 1994, pp. 223-231.

52. Lassmann, K., A. Shubert, J. Van De Laar, "Recent Development of the TRANSURANUS Code with Emphasis on High Burnup Phenomena," Nuclear Fuel Behavior Modelling at High Burnup and Its Experimental Support, Proceedings of a IAEA Technical Committee Meeting, Windermere, UK, IAEA-TECDOC-1233, p. 387, June 2000.

53. Lemoine, F. and M. Balourdet, "RIA Related Analytical Studies and Separate Effects Tests," *Proceedings of the ANS International Topical Meeting on Light Water Reactor Fuel Performance*, Portland, Oregon, March 2-6, 1997 pp. 693-703.

54. Lespiaux, D., J. Noirot, and P. Menut, "Post-Test Examination of High Burnup PWR Fuels Submitted to RIA Transients in the CABRI Facility," *Proceedings of the ANS International Topical Meeting on Light Water Reactor Fuel Performance*, Portland, Oregon, March 2-6, 1997 pp. 650-658.

55. Link, T. M., D. A. Koss, and A. T. Motta, "Failure of Zircaloy Cladding Under Transverse Plane-Strain Deformation," Nuclear Engineering and Design (186) 1998.

56. Lyon, W. F., R. O. Montgomery, D. J. Sunderland, and Y. R. Rashid, "Nuclear Fuel Industry Research Program, Fuel Cladding Integrity at High Burnups, Mechanical Property Data Assessment and Evaluation," EPRI TR-1003134, July 2001.

57. MacDonald, P. E., S. L. Seiffert, Z. R. Martinson, R. K. McCardell, D. E. Owen, and S. W. Fukuda, "Assessment of Light-Water-Reactor Fuel Damage During a Reactivity-Initiated Accident," *Nuclear Safety*, Vol. 21, No. 5, Nuclear Regulatory Commission, Bethesda, Maryland, September-October, 1980, pp. 582-602.

58. MacLachlan, Ann, "Framatome Sees Last CABRI Test as Good News for M5 Cladding, Nuclear Fuel, No. 5, McGraw-Hill Inc., July 24, 2000.

59. MacLachlan, Ann, "Latest CABRI Test Indicates No Fuel Ejected into Reactor Circuit, Inside N.R.C., Vol. 22, No. 26, McGraw-Hill Inc., December 18, 2000.

60. Mardon, J. P. et al., "Update on the Development of Advanced Zirconium Alloys for PWR Fuel Rod Claddings," *Proceedings of the ANS International Topical Meeting on Light Water Reactor Fuel Performance*, Portland, Oregon, March 2-6, 1997 pp. 405-412.

61. Martinson, Z. R. and R. L. Johnson, "Transient Irradiation of 1/4-Inch OD Zircaloy-2 Clad Oxide Fuel Rods to 590 cal/g UO_2," IDO-ITR-102, Phillips Petroleum Company, Atomic Energy Division, November 1968.

62. McGrath, M. A., H. Ruhmann, B. C. Oberlander, and S. Thorshaug, "Investigation into the Effects of In-Pile Dry-Out Transients on Zircaloy Fuel Cladding as Performed in IFA-613," HWR-666, OECD Halden Reactor Project, March 2001.

63. Meyer, R. O., R. K. McCardell, and H. H. Scott, "A Regulatory Assessment of Test Data for Reactivity Accidents," *Proceedings of the ANS International Topical Meeting on Light Water Reactor Fuel Performance*, Portland, Oregon, March 2-6, 1997 pp. 729-744.

64. Meyer, R. O., "Implications from the Phenomenon Identification and Ranking Tables (PIRTs) and Suggested Research Activities for High Burnup Fuel," NUREG-1749, September 2001.

65. Miller, R. W., "The Effects of Burnup on Fuel Failure, I. Power Burst Tests on Low Burnup UO_2 Fuel Rods," IN-ITR-113, Idaho Nuclear Corporation, July 1970.

66. Miller, R. W., "The Effects of Burnup on Fuel Failure, II. Power Burst Tests on Fuel Rods with 13,000 and 32,000 MWd/MTU Burnup," IN-ITR-118, Idaho Nuclear Corporation, April 1971.

67. Miller, R. W. and W. G. Lussie, "The Response of UO_2 Fuel Rods to Power Bursts, 5/16-Inch OD, Pellet and Powder Fuel, Zircaloy Clad," IDO-ITR-103, Phillips Petroleum Company, Atomic Energy Division, January 1969.

68. Montgomery, R. O. and Y. R. Rashid, "Evaluation of Irradiated Fuel During RIA-Simulation Tests", EPRI TR-106387, May 1996.

69. Montgomery, R. O., Y. R. Rashid, O. Ozer, and R. L. Yang, "Assessment of RIA-Simulation Experiments on Intermediate- and High-Burnup Test Rods," *Nuclear Safety*, Vol. 37, No. 4, Nuclear Regulatory Commission, Bethesda, Maryland, October-December, 1996, pp. 372-387.

70. Montgomery, R. O., et al., "Review and Analysis of RIA-Simulation Experiments on Intermediate and High Burnup Test Rods," *Proceedings of the ANS International Topical Meeting on Light Water Reactor Fuel Performance*, Portland, Oregon, March 2-6, 1997 pp. 711-720.

71. Montgomery, R. O., et al., "FALCON – Fuel Analysis and Licensing Code, Volume 2: User's Manual", ANA-97-0230, Anatech Corporation, San Diego, California, December 1997.

72. Murty, K. L. and S. T. Mahmood, "Effects of Recrystallization and Neutron Irradiation on Creep Anisotropy of Zircaloy Cladding," Zirconium in the Nuclear Industry: Ninth International Symposium, ASTM STP 1132, American Society for Testing and Materials, Philadelphia, Pennsylvania, 1991, pp. 198-217.

73. Nakamura, et al., "Boiling Water Reactor Fuel Behavior at Burnup of 26 GWd/tonne U Under Reactivity-Initiated Accident Conditions," Nuclear Technology, Volume 108, October 1994.

74. Newman, L.W., "The Hot Cell Examination of Oconee 1 Fuel Rods after Five Cycles of Irradiation," DOE/ET/34212-50, BAW-1874, Babcock & Wilcox, Lynchburg, Virginia, October 1986.

75. Ozer, O., Y. R. Rashid, R. O. Montgomery, R. Yang, "Evaluation of RIA Experiments and Their Impact on High Burnup Fuel Performance," *Proceedings of the CSNI Specialists Meeting on Transient Behavior of High Burnup Fuel*, Cadarache France, September 12-14, 1995, Report NEA/CSNI.R(95) 22, 1996.

76. Papazoglou, T. P. and H. H. Davis, "EPRI/B&W Cooperative Program on PWR Fuel Rod Performance," NP-2848, Electric Power Research Institute, Palo Alto, California, March 1983.

77. Papin, J., et al., “French Studies on High-Burnup Fuel Transient Behavior Under RIA Conditions,” *Nuclear Safety*, Vol. 37, No. 4, Nuclear Regulatory Commission, Bethesda, Maryland, October 21-23, 1996, pp. 289-327.

78. Papin, J., et al., "The SCANAIR Code for the Description of PWR Fuel Rod Behaviour Under RIA: Validation on Experiments and Extrapolation to Reactor Conditions," *Proceedings of the ANS International Topical Meeting on Light Water Reactor Fuel Performance*, Portland, Oregon, March 2-6, 1997 pp. 659-668.

79. Papin, J., J-C. Melis, and C. Lecomte, "Definition and Status of the CABRI International Program for High Burn-Up Fuel Studies," *Proceedings of the Twenty-Eighth Water Reactor Safety Information Meeting*, NUREG/CP-0172, U.S. Nuclear Regulatory Commission, Bethesda, Maryland, October 23-25, 2000, pp. 185-190.

80. Pettersson, K., G. Vesterlund, and T. Andersson, "Effect of Irradiation on the Strength, Ductility, and Defect Sensitivity of Fully Recrystallized Zircaloy Tube," Zirconium in the Nuclear Industry: Fourth International Conference, ASTM STP 681, American Society for Testing and Materials, 1979, pp. 155-173.

81. Philipponneau, Y., "Catalogue Européen des Propriétés de l'oxyde mixte $(U,Pu)O_2$," Chapite II, Note Technique LPCA n°02.

82. Philipponneau, Y., "Etude sur la Température a Fusion du Combustible Oxyde et sur son Evolution avec la taux de Combustion," Note Technique LPCA n°27.

83. Rashid, Y.R. et.al., “A Cladding Failure Model for Fuel Rods Subjected to Operational and Accident Transients,” Nuclear Fuel Behavior Modelling at High Burnup and Its

Experimental Support, Proceedings of a IAEA Technical Committee Meeting, Windermere, UK, IAEA-TECDOC-1233, p. 187, June 2000.

84. Rashid, Y.R., R.O. Montgomery, and A.J. Zangari, "FREY-01: Fuel Rod Evaluation System, Volume 1: Theoretical and Numerical Bases", EPRI NP-3277-V1R3, August 1994.

85. Rice, J.R., "A Path Independent Integral and the Approximate Analysis of Strain Concentration by Notches and Cracks," Journal of Applied Mechanics, Transactions ASME, 35, June 1968.

86. Rowland, T. C., Demonstration of Fuel Resistance to Pellet-Cladding Interaction, Phase-2, Final Report, GEAP-25163-10, General Electric Company, November 1984.

87. Rusche, B. C. (NRC), Letter to R. Farley (ACRS), “Generic Item IIA-2 Control Rod Drop Accident (BWRs),” June 1976.

88. Sabol, G. P. et al., "In-Reactor Fuel Cladding Corrosion Performance at Higher Burnups and Higher Coolant Temperatures," *Proceedings of the ANS International Topical Meeting on Light Water Reactor Fuel Performance*, Portland, Oregon, March 2-6, 1997 pp. 397-404.

89. Schmitz, F. and J. Papin, "REP-Na 10, Another RIA Test with a Spalled High Burnup Rod and with a Pulse Width of 30 ms," *Proceedings of the Twenty-Sixth Water Reactor Safety Information Meeting*, NUREG/CP-0166, Vol. 3, U.S. Nuclear Regulatory Commission, Bethesda, Maryland, October 26-28, 1998, pp. 243-253.

90. Schmitz, F. and J. Papin, “High Burnup Effects on Fuel Behavior Under Accident Conditions: The Tests CABRI REP-Na”, *Journal of Nuclear Materials*, Volume: 270, 1999, pp. 55-64.

91. Smith, G. P., et al., "Hot Cell Examination of Extended Burnup Fuel from Calvert Cliffs-1," Vol. 2, EPRI TR-103302-V2, Electric Power Research Institute, Palo Alto, California, July 1994.

92. Smith, G. P., et al., "The Evaluation and Demonstration of Methods for Improved Nuclear Fuel Utilization," Final Report, DOE/ET/34013-15, UC-523, CEND-432, ABB Combustion Engineering, Windsor, Connecticut, August 1994.

93. Sontheimer, F., H. Landskron, M. Billaux, “A Fuel Thermal Conductivity Correlation Based on the Latest Experimental Results,” Proceedings of the NEA/OECD Seminar on Thermal Performance of High Burnup LWR Fuel, Cadarache France, p. 119, March 1998.

94. Stelletta, S., and M. Moreau, "Study of the Rod Ejection Transient on a PWR Related to High Burnup Fuel Rupture Disk," *Proceedings of the CSNI Specialists Meeting on Transient Behavior of High Burnup Fuel*, Cadarache France, September 12-14, 1995, Report NEA/CSNI.R(95) 22, 1996.

95. Stelletta, S., and N. Waeckel, "Fuel Failure Risk Assessment Under Rod Ejection Accident in PWRs Using the RIA Simulation Tests Database," *Proceedings of the ANS International Topical Meeting on Light Water Reactor Fuel Performance*, Portland, Oregon, March 2-6, 1997 pp. 721-728.

96. Sugiyama, T., and T. Fuketa, "Mechanical Energy Generation During High Burnup Fuel Failure under Reactivity Initiated Accident Conditions," *Journal of Nuclear Science and Technology*, Volume 37, No. 10, October 2000, pp. 877-886.

97. Swindlehurst, G., Duke Power Company, and R. Deveney, Framatome Fuel Company, Private Communication, June 2001.

98. Taylor, J. M (NRC) Memorandum to the USNRC Chairman Commissioner Rogers and Commissioner de Planque, "Reactivity Transients and Fuel Damage Criteria for High Burnup Fuel," November 9, 1994.

99. Thadani, A. C. (NRC) letter to J.S. Charnley (GE), "Acceptance for Referencing of Licensing Topical Report NEDE-24011-P-A, 'General Electric Standard Application for Reactor Fuel,' Revision 8, Amendment 17, December 1987.

100. Tompson, T. J., and J. G. Beckerley, "The Technology of Nuclear Reactor Safety," Vol. 1, MIT Press, 1964.

101. Tsuruta, T., M.-A. Ochiai, and S. Saito, "Fuel Fragmentation and Mechanical Energy Conversion ratio at Rapid Deposition of High energy LWR Fuels," *Journal of Nuclear Science and Technology*, Volume 22, No. 9, September 1985, pp. 60-72.

102. Turnbull, J.A., "A Comparison Between In-pile and Laser Flash Determinations of UO_2 Thermal Conductivity," OECD Halden Reactor Project, HWR-484, April 1996.

103. U. S. Atomic Energy Commission, Assumptions Used for Evaluating A Control Rod Ejection Accident for Pressurized Water Reactors, Regulatory Guide 1.77, Directorate of Regulatory Standards, May 1974.

104. U. S. Nuclear Regulatory Commission, Standard Review Plan for the Review of Safety Analysis Reports for Nuclear Power Plants, LWR Edition, NUREG-0800, Office of Nuclear Reactor Regulation, July 1981.

105. Van Houton, R., "Fuel Rod Failure as a Consequence of Departure from Nucleate Boiling or Dryout," NUREG-0562, U.S. Nuclear Regulatory Commission, Bethesda, Maryland, June 1979.

106. Van Swam, L. P., and S. H. Shann, "The Corrosion of Zircaloy-4 Fuel Cladding in Pressurized Water Reactors," Zirconium in the Nuclear Industry: Ninth International Symposium, ASTM STP 1132, pp. 758-781, 1991.

107. Vaughan, G. J., "Paper for the Fourth CSNI Specialist Meeting on Fuel-Coolant Interaction in Nuclear Reactor Safety" UKAEA, SRD, Culcheth, England, Bournemouth, UK, April 2-5, 1979.

108. Waeckel, N., C. Bernaudat, and B. Salles, "EdF Proposed Safety Domain for Rod Ejection Accidents in a PWR," *Proceedings of the ANS International Topical Meeting on Light Water Reactor Fuel Performance*, Park City, Utah, April 10-13, 2000 pp. 374 - 382.

109. Wiesenack, W., M Vankeerberghen, R. Thankappan, :UO_2 Conductivity Degradation Based on In-pile Temperature Data," OECD Halden Reactor Project, HWR-469, 1996.

110. Willse, J. T., Private Communication with W, FCF, ENUSA, *ANS International Topical Meeting on Light Water Reactor Fuel Performance*, Park City, Utah, April 10-13, 2000

111. Wilson, H. W., "Westinghouse Fuel Performance in Today's Aggressive Plant Operating Environment," *Proceedings of the ANS International Topical Meeting on Light Water Reactor Fuel Performance*, Portland, Oregon, March 2-6, 1997 pp. 23-30.

112. Wisner, S. B. and R. B. Adamson, "Combined Effects of Radiation Damage and Hydrides on the Ductility of Zircaloy-2," Nuclear Engineering and Design, 185, pp 33-49,1998.

113. Woods, K. N, and W. Klinger, "Siemens Fuel Performance Overview," *Proceedings of the ANS International Topical Meeting on Light Water Reactor Fuel Performance*, Portland, Oregon, March 2-6, 1997 pp. 272-279.

114. Yamanouchi, S., et al. "Melting Temperature of Irradiated UO_2 and OU_2-2wt%Gd_2O_3 Fuel Pellets up to Burnup of about 30 GWd/tU," *Journal of Nuclear Science and Technology*, Volume: 25 No. 6, June 1988, pp. 528-533.

115. Yang, R. L., R. O. Montgomery, N. Waeckel, and Y. R. Rashid, "Industry Strategy and Assessment of Existing RIA Data," *Proceedings of the ANS International Topical Meeting on Light Water Reactor Fuel Performance*, Park City, Utah, April 10-13, 2000 pp. 383 - 401.

116. Yegorova, L., "Data Base on the Behavior of High Burnup Fuel Rods with Zr-1%Nb Cladding and UO2 Fuel (VVER Type) under Reactivity Accident Conditions, Review of Research Program and Analysis of Results," NUREG/IA-0156, Vol. 1, IPSN 99/08-1, NSI RRC 2179, U.S. Nuclear Regulatory Commission, Washington, D. C., July 1999.

117. Zimmermann, C. L., C. E. White, and R. P. Evans, "Experiment Data Report for Test RIA 1-2 (Reactivity Initiated Accident Test Series), NUREG/CR-0765, EG&G Idaho Inc., June 1979.

A
APPENDIX A: DATABASE OF RIA-SIMULATION EXPERIMENTS

Table A-1a
CDC- SPERT Irradiated Rod Tests

Test No.	Burnup	Dep. Eng.	Rad. Avg Eng.	Failure Eng.
571	4550	161	134	NF
568	3480	199	165	147
567	3100	264	219	219
569	4140	348	289	300
703	1140	192	159	NF
709	990	238	198	197
685	13100	186	154	NF
684	12900	200	166	NF
756	32700	176	146	146
859	31800	190	158	85

Table A-1b
CDC-SPERT Unirradiated Rod Tests

Test No.	Burnup	Dep. Eng.	Rad. Avg Eng.	Failure Eng.
694	0	223	185	NF
690	0	256	212	212
639	0	313	259	260
478	0	340	282	282
489	0	201	166	NF
487	0	243	202	201

Table A-2a
NSRR PWR Program

Test No.	Burnup	Dep. Eng.	Rad. Avg. Eng.	Failure Eng.
MH-1	39000	63	49	NF
MH-2	39000	72	55	NF
MH-3	39000	87	67	NF
GK-1	42000	121	93	NF
GK-2	42000	117	90	NF
OI-1	3900	136	105	NF
OI-2	39000	139	107	NF
HBO-1	50000	93	72	60
HBO-2	50000	51	39	NF
HBO-3	50000	95	73	NF
HBO-4	50000	67	52	NF
HBO-5	44000	80	80	77
HBO-6	49000	85	85	NF
HBO-7	49000	88	85	NF
TK-1	38000	125	123	NF
TK-2	48000	107	107	60
TK-3	50000	99	99	NF
TK-4	50000	100	100	NF
TK-5	48000	101	101	NF
TK-6	38000	125	125	NF
TK-7	50000	95	95	86

Table A-2b
NSRR JMTR Program

Test No.	Burnup	Dep. Eng.	Rad. Avg. Eng.	Failure Eng.
JM-1	24000	126	97	NF
JM-2	27000	113	87	NF
JM-3	23000	174	134	NF
JM-4	23000	230	177	177 (hydride blisters)
JM-5	26000	212	163	163 (hydride blisters)
JM-6	15000	178	137	NF
JM-7	13000	168	129	NF
JM-8	20000	183	141	NF
JM-9	23000	187	144	NF
JM-10	20000	192	148	NF
JM-11	30000	189	146	NF
JM-12	36000	202	156	156 (hydride blisters)
JM-13	38000	150	116	NF
JM-14	38000	160	123	123 (hydride blisters)
JM-15	30000	180	139	NF
JM-16	38000	180	139	NF
JMH-1	22000	150	116	NF
JMH-2	22000	190	146	NF
JMH-3	22000	200	154	154 (hydride blisters)
JMH-4	30000	200	150	NF
JMH-5	30000	280	210	185 (hydride blisters)
JMN-1	22000	150	141	141

Table A-2c
NSRR BWR Program

Test No.	Burnup	Dep. Eng.	Rad. Avg. Eng.	Failure Eng.
TS-1	26000	55	42	NF
TS-2	26000	66	51	NF
TS-3	26000	88	68	NF
TS-4	26000	89	69	NF
TS-5	26000	98	76	NF
FK-1	45400	112	112	NF
FK-2	45400	60	60	NF
FK-3	41000	145	145	NF
FK-4	56000	140	140	NF
FK-5	56000	70	70	NF
FK-6	60800	130	130	70
FK-7	60800	130	130	62
FK-8	60800		65	NF
FK-9	60800		93	86

Table A-3
PBF RIA tests

Test No.	Burnup	Rad. Avg. Eng.	Failure Eng.
RIA-ST-2	0	260	260
RIA-ST-3	0	225	225
RIA-ST-4	0	350	350
RIA 1-1	5500	285	285
RIA 1-1	0	285	285
RIA 1-2	4800	185	185

Table A-4
CABRI RIA Tests

Test No.	Burnup	Dep. Eng.	Rad. Avg. Eng.	Failure Eng.
REP Na-1	63000	100	100	15
REP Na-2	33000	203	195	NF
REP Na-3	52000	120	118	NF
REP Na-4	63000	90	70	NF
REP Na-5	63000	105	105	NF
REP Na-6	44000	150	145	NF (MOX Fuel)
REP Na-7	55000	175	160	120 (MOX Fuel)
REP Na-8	60000	94	85	69
REP Na-9	28000	228	299	NF (MOX Fuel)
REP Na-10	63000	90	90	75
REP Na-11	63000	105	105	NF (M5 Cladding)
REP Na-12	65000	90	90	NF (MOX Fuel)

B
APPENDIX B: ZIRCONIUM OXIDE SPALLATION

The following is a definition of oxide spallation in the context of cladding mechanical properties and cladding integrity during normal operation, anticipated operational occurrences, and postulated accidents.

Definition

Oxide Spallation (spalling) - Sufficient loss of the zirconium oxide (ZrO_2) layer integrity to degrade the mechanical properties of the cladding beyond the scatter of the mechanical property data for cladding with uniform oxide layers.

Overview

Spallation is the final step in a four-step process that characterizes the corrosion of Zircaloy-4 cladding in a PWR environment. The four steps are oxide layer growth, formation of radial cracks in the oxide, delamination, and eventual loss of the cracked oxide layer. A schematic diagram depicting the evolution of this process is shown in Figure B-1.

The first step of the oxide spallation process is the formation of a uniform oxide layer of thickness up to approximately 80 μm, depending upon the composition of the material and its prior operating history. Degradation of the oxide layer begins with the formation of radial microcracks (Step 2). This typically occurs at a threshold oxide thickness of approximately 80 to 100 μm as shown in Figure B-1, although some experimental data have shown cracking at thicknesses as low as 55 to 65 μm (Kilp, 1991). Examinations of these regions show the cracks penetrating into the oxide layer toward, but not reaching, the metal/oxide interface. Figure B-2 is an example of observed oxide layer cracking patterns. The precise mechanism behind the formation of the cracks is not well known. However, indications are that the stress distribution due to oxide volumetric growth and Poisson's effect within the oxide layer lead to their formation.

The third step in the oxide spallation process occurs when the oxide layer delaminates axially and circumferentially, forming two or more distinct layers. Such delamination has been observed to penetrate through the oxide layer to depths of 50 to 2 μm above the metal/oxide interface as shown in Figure B-3. The formation of interlayer gaps in delaminated oxide decreases the local thermal conductance, causing an increase in the local cladding temperature. As the local cladding temperature increases near regions of delaminated oxide layers, the solubility limit of hydrogen in the cladding increases permitting the dissolution of hydrides and

the diffusion of hydrogen down the thermal gradients. The net effect is a reduction in the local hydride concentration.

Spallation (Step 4) occurs when the delaminated oxide layers lose their strength, fragment into pieces, and are removed by coolant flow. Figure B-4 illustrates localized spalled areas or blisters transitioning to large spalled regions. As spallation progresses along the surface of a fuel rod, the smaller regions interconnect and to form large regions of the oxide surface layer that are affected by oxide loss. Cracking and spallation of the oxide layer can also be seen in corrosion profilometry measurements. Figure B-5 is an example of an eddy current oxide scan showing incipient oxide cracking and delamination in the upper region of a fuel rod.

As the delaminated oxide layers are removed, heat transfer from the cladding to the coolant improves. This reduces the cladding temperature relative to the unspalled regions, creating thermal gradients that promote the migration of hydrogen. The temperature gradients established by oxide spallation are a function of the unspalled oxide layer thickness, the thickness of the remaining oxide layer after spalling, and the power level. Operation with a large azimuthal temperature gradient may lead to a high concentration of localized hydrides in the spalled region. PIE examination results from cladding with uniform oxide layer thickness values above 100 microns, and which spalled to less than 5 microns, have found localized concentration of hydrides that can occupy 40 to 45% of the cladding wall thickness over an area up to 30º around the circumference. Such localized hydride concentrations decreases the effective cladding strength and elongation.

The oxide spallation process defined above is not intended to include the small oxide loss observed under high magnification SEM or optical examinations. The small non-uniformity in oxide layer thickness due to loss of 1 to 10 microns of oxide has no impact on the cladding thermal or mechanical properties.

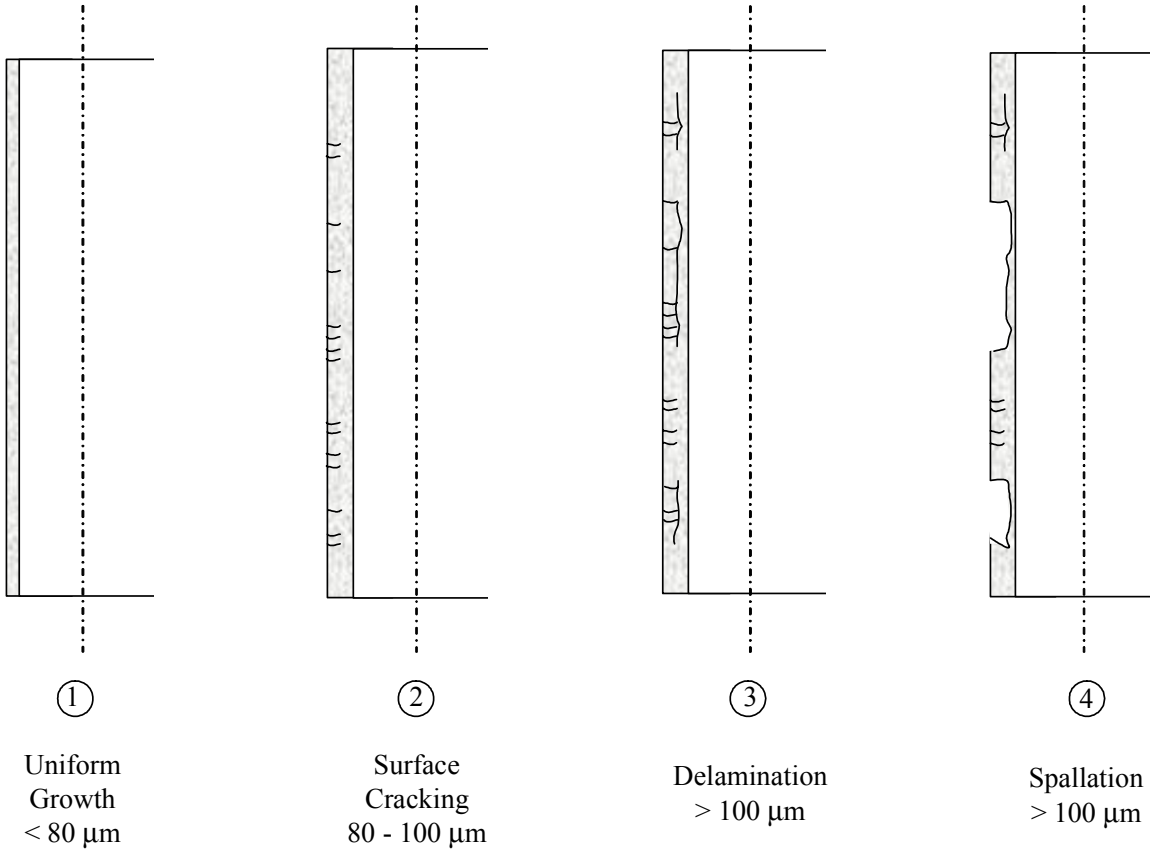

Figure B-1
The Four Stages of the Oxide Spallation Process

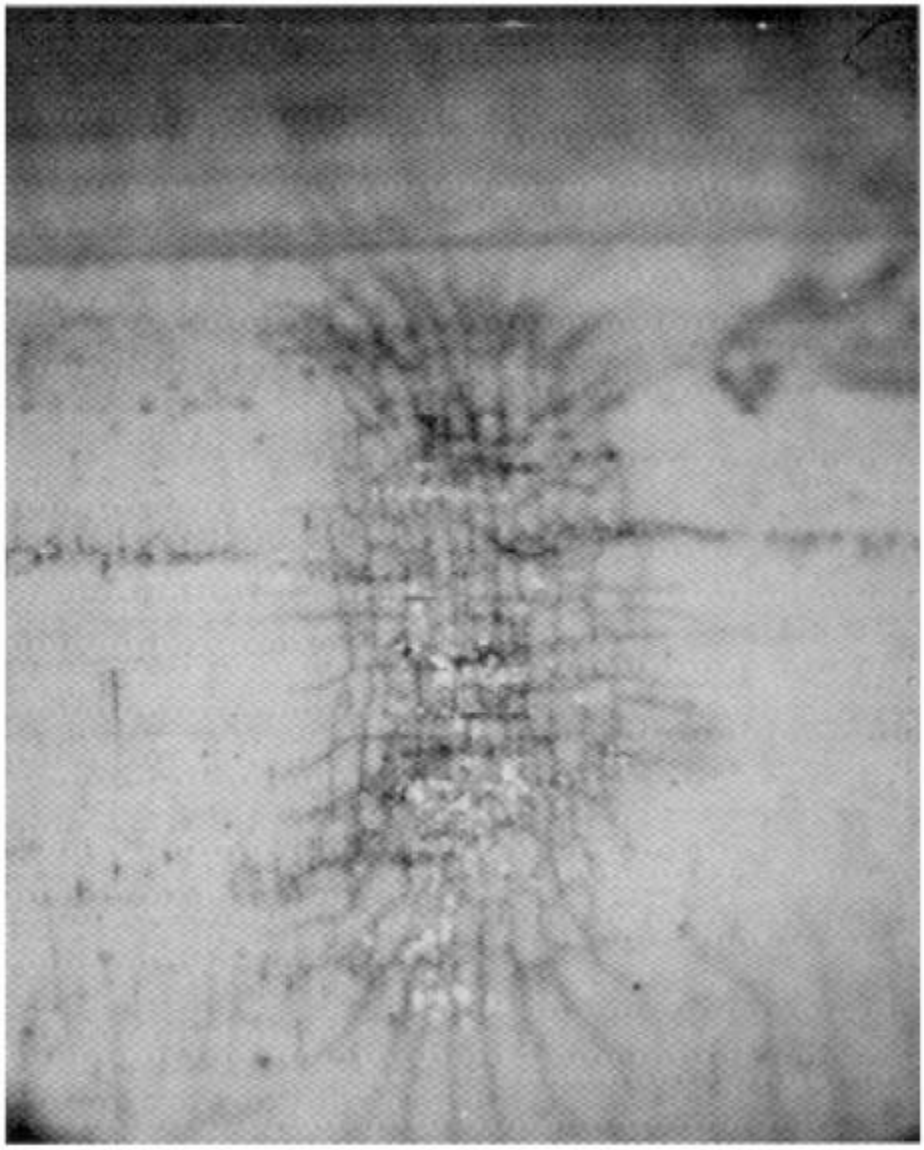

Figure B-2
Spalling Oxide Initiation Site [from Smith 1994]

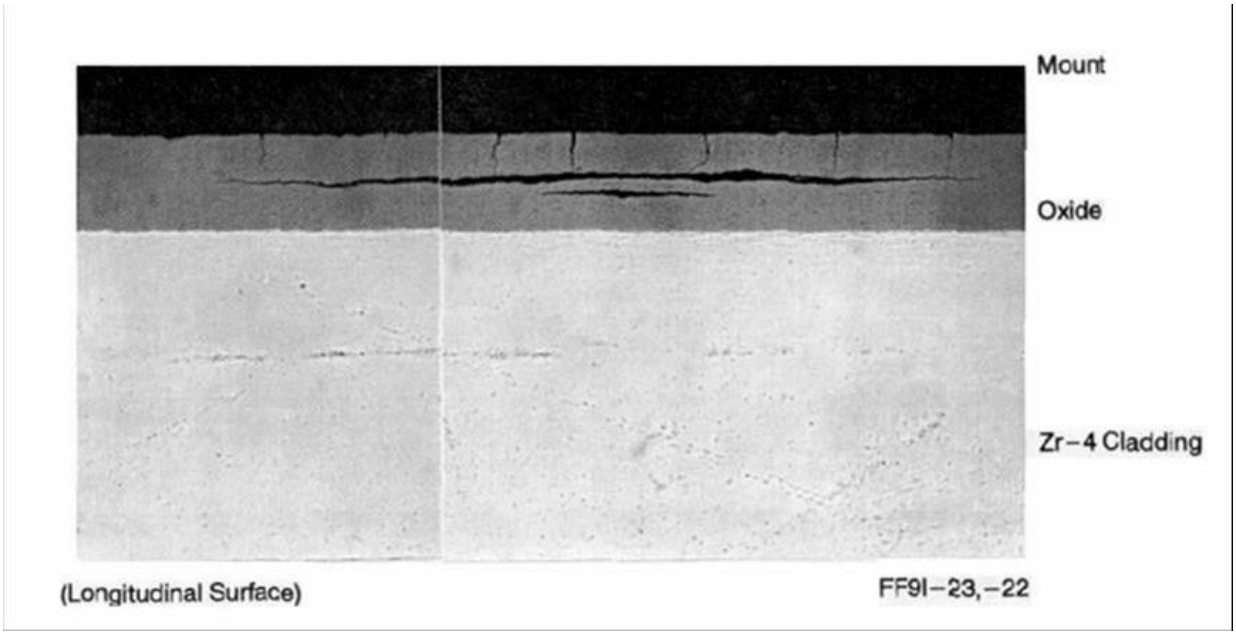

Figure B-3
Delamination of the Oxide Layer [from Smith,1994]

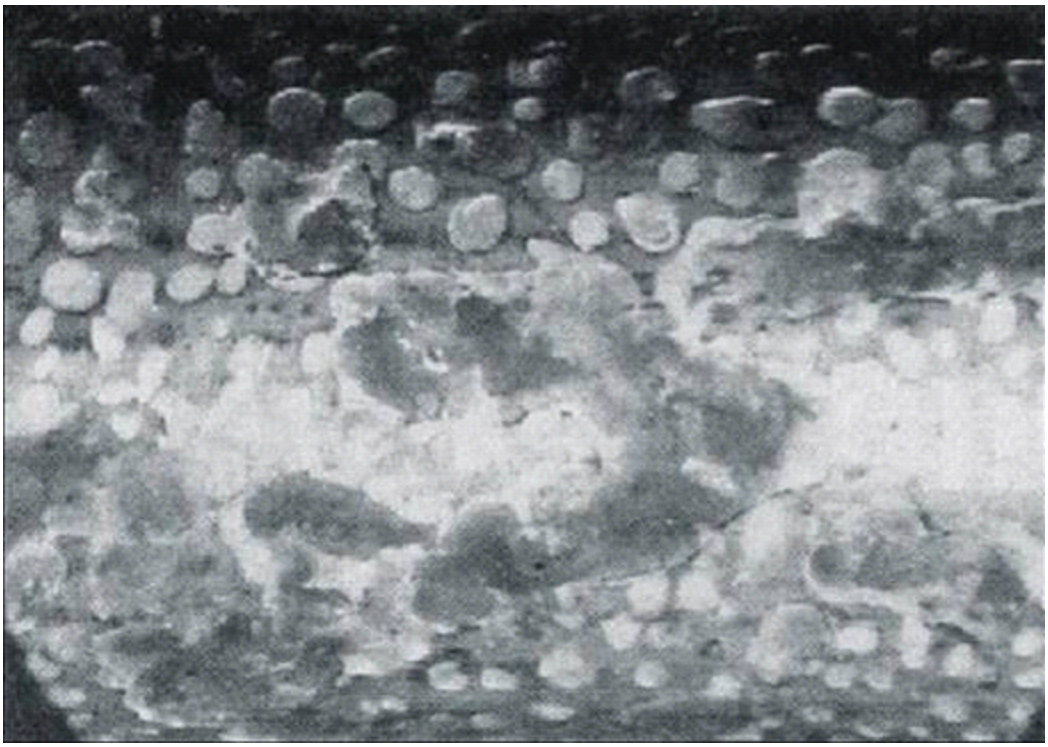

Figure B-4
Small Oxide Blisters Transitioning to Large Spalled Regions [from Van Swam 1991]

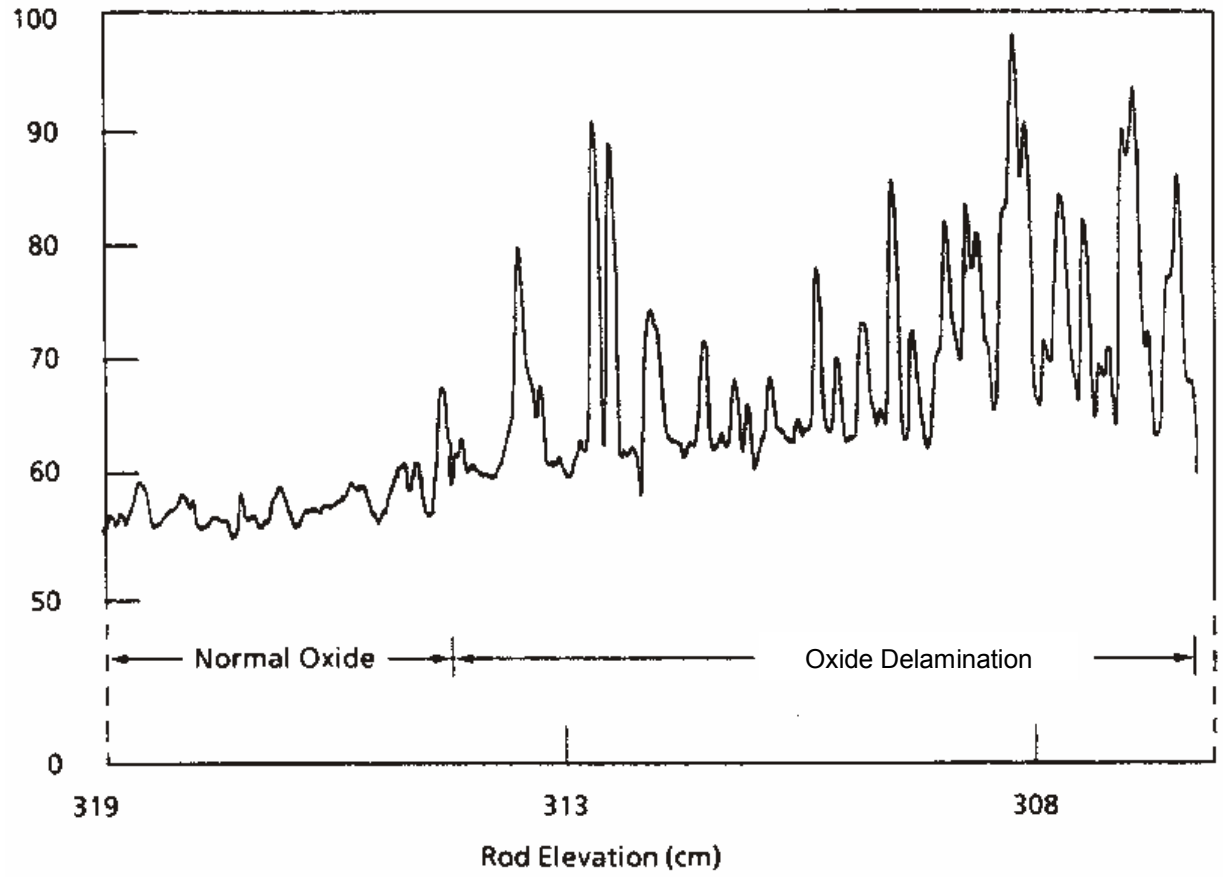

Figure B-5
Eddy Current Scan Showing Incipient Cracking and Delamination

Target:
Nuclear Power

About EPRI

EPRI creates science and technology solutions for the global energy and energy services industry. U.S. electric utilities established the Electric Power Research Institute in 1973 as a nonprofit research consortium for the benefit of utility members, their customers, and society. Now known simply as EPRI, the company provides a wide range of innovative products and services to more than 1000 energy-related organizations in 40 countries. EPRI's multidisciplinary team of scientists and engineers draws on a worldwide network of technical and business expertise to help solve today's toughest energy and environmental problems.

EPRI. Electrify the World

Printed on recycled paper in the United States of America

1002865

EPRI • 3412 Hillview Avenue, Palo Alto, California 94304 • PO Box 10412, Palo Alto, California 94303 • USA
800.313.3774 • 650.855.2121 • askepri@epri.com • www.epri.com